

**Understanding the Effect of Surface Topography on Stiction and Friction
in MEMS**

by

Naveed Mohammed Asgar Ansari

A dissertation submitted to the Graduate Faculty of
Auburn University
in partial fulfillment of the
requirements for the Degree of
Doctor of Philosophy

Auburn, Alabama
December 12, 2011

Keywords: MEMS, Tribology, Topography, Stiction, Friction, Roughness, Thin films

Copyright 2011 by Naveed Mohammed Asgar Ansari

Approved by

William R. Ashurst, Chair, Associate Professor of Chemical Engineering
Christopher B. Roberts, Uthlaut Professor of Chemical Engineering
Steve R. Duke, Alumni Associate Professor of Chemical Engineering
Robert Dean, Associate Professor of Electrical and Computer Engineering

Abstract

The field of micro-electromechanical systems (MEMS) undoubtedly has the potential of producing great technological innovations. However, a precise understanding of the tribological behaviour of MEMS surfaces is needed for the realization of the full potential of a variety of complex, sophisticated and extremely useful MEMS. While on one hand, the number of smaller, more complex and more useful new MEMS prototypes, which are commercially extremely attractive, is continuously increasing, on the other hand, despite years of research, the Micro-electromechanical Systems (MEMS) community is yet to find a solution that sufficiently addresses the reliability issues (stiction, friction and wear) that limit the commercial success of most MEMS prototypes. The main bottleneck, which limits the ability of MEMS community to devise an appropriate solution, is their poor understanding of the factors, especially surface topography, that govern the tribological behaviour of MEMS surfaces. Therefore, there is a serious and urgent need to conduct a systematic investigation for understanding the effects that the surface topography of a MEMS surface has on the stiction and friction experienced by it. Accordingly, the main objective of this study is to understand the effects that the surface topography of a MEMS surface has on the stiction and friction experienced by it.

This study reports on the development of a test platform (TP), which not only overcomes the limitations of the previously reported test platforms but is also a versatile tool that can be used to systematically study the tribology of MEMS surfaces. The details of the design and fabrication of the Test Platform are discussed in the study. Further, in order to be able to fabricate the TP using a facile, inexpensive and less time consuming fabrication process, a single mask scheme is devised in this

study for fabricating the Test Platform. Additionally, in order to ensure that the sidewall surfaces of the microinstruments included in the Test Platform are relatively smooth so that a systematic investigation of the effects that the surface topographies of MEMS surfaces have on their stiction and friction characteristics can be conducted, a polishing technique to smoothen the scalloped as-fabricated sidewalls of the Test Platform is developed in this study.

The designs, actuation procedures and modeling of the various (i.e., seven types of) microinstruments included in the Test Platform are explained in detail in this study. The details of the key features of all the (seven types of) microinstruments are successfully highlighted in this study. Additionally, some of the microinstruments developed in this study are convincingly shown to overcome some of the limitations of the previously reported corresponding microinstruments. Further, all the (seven types of) microinstruments developed in this study are successfully used to investigate two standard test surfaces, namely, surfaces coated with *n*-OTS ($C_{18}H_{37}SiCl_3$) SAM coating (i.e., hydrophobic surfaces) and surfaces having only a layer of native oxide on them (i.e., hydrophilic surfaces). Additionally, the apparent work of adhesion of the OTS SAM coated sidewalls, which has never been reported to-date, is obtained in this study using the Sidewall Beam Array. The apparent work of adhesion of the OTS SAM coated sidewalls is $37.65 \mu J/m^2$. Also, the engineering coefficients of static and kinetic friction of the OTS SAM coated sidewalls, which have also never been reported to-date, are obtained in this study using both the Sidewall Friction Tester as well as the Sidewall Friction and Adhesion Tester. The mean engineering coefficients of static and kinetic friction of the OTS SAM coated sidewalls are 0.15 and 0.11, respectively.

Further, the investigation conducted to study the effect of surface topography reports the successful use of a dodecanethiol-capped gold nanoparticle-based surface texturing technique for tailoring the topographies of the surfaces (in-plane as well

as sidewall) of five Test Platform chips. Additionally, it reports the successful investigation of six Test Platform chips (five textured using the dodecanethiol-capped gold nanoparticle-based surface texturing technique and one untextured (control)) conducted to understand the effect that the surface topography of a surface has on its tribological (i.e., stiction and friction) characteristics. The surface topographies of the surfaces of each of the six Test Platform chips investigated in this study are characterized qualitatively using SEM and quantitatively using AFM. The quantitative characterization of the surface topographies of the surfaces of the six Test Platform chips investigated in this study is used to quantify them in terms of two measurable parameters, namely, the rms roughness and the surface coverage of the interacting asperities present on the surface. Further, in order to understand the effects that the surface topography of a MEMS surface has on its stiction and friction characteristics, three important tribological properties of the surfaces of each of the six Test Platform chips investigated in this study, which are the apparent work of adhesion of the in-plane surfaces, the apparent work of adhesion of the sidewall surfaces and the engineering coefficient of static friction of the sidewall surfaces, are determined. The tribological characterization of the surfaces of the six Test Platform chips investigated in this study provided an experimental confirmation of the already believed theory that the friction experienced by contacting MEMS surfaces shows a strong dependence on the stiction experienced by them. Additionally, it indicated that both the micro-scale as well as the nano-scale topographies of a surface have a strong influence on its stiction and friction characteristics.

In order to mathematically correlate the surface topography of a surface with its stiction and friction characteristics, a dimensionless parameter called Tribotopography number (i.e., τ_{topo}) is formulated in this study. Further, the Tribotopography number is successfully used to develop two mathematical correlations, one between the surface topography of a surface and its apparent work of adhesion, and the other

between the surface topography of a surface and the friction experienced by it. In order to use the two mathematical correlations developed in this study for a particular type of surface, the value of index α , which is the index of the denominator of the fraction that represents the Tribotopography number, for that type of surface must be determined first. The value of index α for silicon-type surfaces (i.e., surfaces, whose tribological behaviours are governed by the same type of interfacial forces that govern the tribological behaviour of silicon surfaces) is determined in this study. This study also reports an analysis (i.e., experimental validation), which substantiates the validities of the two mathematical correlations developed to correlate the surface topography of a surface with its stiction and friction characteristics, respectively. Additionally, it also discusses the constraints, under which, the two mathematical correlations are valid. Lastly, the study reports the results of the investigation conducted to determine the influence of the geometry of the contact interface on the effect that the surface topographies of the surfaces forming the interface have on its tribological characteristics.

Owing to the fact that the surface coverage of the coating can serve as an effective parameter in the comparison between the effectivenesses of various nanoparticle-based (sub-)monolayer coatings, a chapter in this study (i.e., chapter 10) reports a simple experimental technique based on optically determined resonance that can be used for determining the surface coverage of the nanoparticle-based monolayer coatings used to texture MEMS surfaces. The modeling as well as the experimental validation of the technique are presented in that chapter. The factor that defines the resolution of the technique is also discussed in that chapter.

The results obtained during the investigation of the effect of surface topography on the stiction and friction characteristics of a surface revealed that the effectiveness of AuNP-based surface texturing not only depends on the roughness of the uncoated test surfaces but also depends strongly on the surface coverage of the coating (refer to

results reported in Chapter 9). Accordingly, a chapter in this study (i.e., chapter 11) reports on a novel gold nanoparticle (AuNP) coating, which is deposited on microelectromechanical systems (MEMS) surfaces using the gas-expanded liquid technique, and has the potential to be used as an alternative of OTS SAM for reducing the stiction and friction experienced by them. A complete characterization of the AuNP coating is presented in that chapter.

Lastly, one of chapters of this study (i.e. chapter 7) reports on an experimental requirement of the phase shifting interferometry, which is a technique widely used in optical testing, and used in this study for determining the height profiles of actuated cantilever beams. The chapter reports on a class of five frame interferogram-collecting sequence, which, due to its mathematical equivalence with the one suggested by Hariharan *et al.* and ease of execution, is more commonly used, but is much less effective in reducing the height profile errors caused by phase step errors. It presents a mathematical as well as experimental analysis of two distinct classes of the five frame interferogram-collecting sequence used in PSI.

Acknowledgments

Throughout the entire course of my doctoral studies, I have received support, advice and help from numerous people, and they deserve my sincere thanks. First and foremost, I would like to thank my parents and my brother for being patient with, and extending unconditional support to me, during my years as a graduate student. Without them, I would not have sailed through the turbulent phases of my doctoral studies. Next, I would like to extend my sincere thanks to my research advisor Dr. W. R. (Bob) Ashurst (Associate Professor, Department of Chemical Engineering, Auburn University). He has been a true mentor in every sense of the word. Not only was he a constant source of technical and administrative guidance but was also an honest critic and guide for issues related to my personal life. He has become a friend for life. The long conversations that I had with him about issues outside the realm of my doctoral studies as well as life in general are some of the fondest memories I have collected at Auburn.

I would also like to thank the other members of my doctoral research advisory committee, especially Dr. C. B. Roberts (Department Chair and Uthlaut Professor, Department of Chemical Engineering, Auburn University), for their encouragement as well as their inciteful suggestions and advices. Additionally, special thanks are due to three more individuals Mr. B. A. Schwieker (Machinist, Department of Chemical Engineering, Auburn University), who expertly built all the custom designed hardwares that I needed for my experiments, Mr. C. Ellis (Manager, AMSTC's microfabrication lab at Auburn University), who not only allowed me to use the tools of the microfabrication facility but also unconditionally offered his expertise when I needed it, and Karen Cochran (Administrative Assistant II - Academic, Department

of Chemical Engineering, Auburn University), whose expert help in administrative matters saved a lot of my time, and jovial nature made me feel that I belonged to the Chemical Engineering Department.

In addition to thanking the former members of the Ashurst research group, Dr. Adam Anderson (graduated with a Ph. D. in 2009) and Dr. Aimee Poda (graduated with a Ph. D. in 2010), for making my transition into the group smooth and easy, and the special bond they shared with me, I would like to offer special thanks to Dr. Kendall Hurst (graduated with a Ph. D. in 2010) of the Roberts research group for collaborating with me on a research project. Our project was very fruitful and it yielded some very exciting results. Additionally, working on that project helped me to significantly expand my knowledge base.

Lastly, I would like to thank all the friends in Auburn for making my stay here very pleasant and enjoyable. A special person, who deserves a mention here is Payal Agarwal. I am really grateful to her for being there for me like a sister at all times throughout my doctoral studies. I would also like to acknowledge Nidhi Sehgal, who was the first friend I made in Auburn, and has been my closest friend in Auburn since then.

Table of Contents

Abstract	ii
Acknowledgments	vii
List of Figures	xvi
List of Tables	xxvii
1 MEMS Technology	1
1.1 Miniaturization: Exploring the Room at the Bottom	1
1.2 MEMS: A Technological Evolution	2
1.3 Tribology: Role in Hindering the Commercialization of MEMS	6
1.4 Micromachining: Description and Influences on MEMS Surface Characteristics	9
1.4.1 Deposition	9
1.4.2 Lithography	10
1.4.3 Etching	11
1.4.4 Wafer Bonding	12
1.4.5 Chemical Mechanical Planarization (CMP)	12
1.4.6 The LIGA Process	14
1.4.7 Bulk Micromachining	14
1.4.8 Surface Micromachining	15
1.5 Reliability of MEMS: A Challenge for the MEMS Community	18
1.5.1 Interfacial Forces	19
1.5.2 Stiction	31
1.5.3 Friction	34
1.5.4 Wear	35

1.5.5	Fracture and Fatigue	36
2	Previous Studies: A Review	38
2.1	Stiction	38
2.1.1	Release Stiction	38
2.1.2	In-Use Stiction	43
2.2	Friction	45
2.3	Self Assembled Monolayers	48
2.3.1	Chlorosilane Based Self-Assembled Monolayers	51
2.3.2	Limitations Imposed by the Chlorosilane Chemistry	56
2.3.3	Non-Chlorosilane Based Organic Coatings	61
2.3.4	Issues Challenging the Viability of Self-assembled Monolayers	64
2.4	Surface Texturing	68
2.5	Wear	70
2.6	Fracture and Fatigue	72
3	Motivations and Objectives	74
3.1	The Need of an Easy-to-fabricate, Versatile Test Platform	74
3.2	The Variation in the Material Properties of the Structural Film	76
3.3	The Influence of the Multi-grain Nature of the Polysilicon Structural Films on the Topography of Polysilicon MEMS Surfaces	77
3.4	Objectives of this Study	81
4	The Test Platform: Design, Fabrication and Actuation	83
4.1	Design of the Test Platform	83
4.1.1	Structural Film	83
4.1.2	The Layout of the Test Platform	84
4.2	Fabrication of the Test Platform	90
4.2.1	Single Mask Scheme	90
4.2.2	Polishing of the Test Surfaces	91

4.3	Actuation of the Test Platform	95
5	Microinstruments: Design, Testing Procedure and Modeling	97
5.1	Residual Stress Tester (RST)	97
5.1.1	Design	97
5.1.2	Modeling	97
5.1.3	Testing Procedure	101
5.2	Mechanical Strength Tester (MST)	101
5.2.1	Design	103
5.2.2	Testing Procedure	108
5.3	Resonator	110
5.3.1	Design	110
5.3.2	Testing Procedure	112
5.3.3	Modeling	113
5.4	Cantilever Beam Array (CBA)	115
5.4.1	Design	115
5.4.2	Testing Procedure and Analysis	117
5.5	Sidewall Beam Array (SBA)	119
5.5.1	Previously Reported Devices: A Review	120
5.5.2	Design	123
5.5.3	Testing Procedure	124
5.5.4	Modeling	126
5.6	Sidewall Friction Tester (SFT)	129
5.6.1	Previously Reported Devices: A Review	129
5.6.2	Design	132
5.6.3	Modeling	138
5.6.4	Testing Procedure	144
5.7	Sidewall Friction and Adhesion Tester (SFAT)	148

5.7.1	Design	148
5.7.2	Modeling	154
5.7.3	Testing Procedure	161
6	Processes and Techniques Used: Experimental, Analytical, Surface Characterization & Metrology	165
6.1	Process Used to Release the Microinstruments of the Test Platform	165
6.2	Process Used to Obtain Oxide-covered Test Surfaces	166
6.3	Preparation of the OTS SAM Coating Solution	166
6.4	Process Used to Obtain OTS SAM Coated Test Surfaces	167
6.5	Gold Nanoparticle (AuNP) Synthesis	168
6.6	Process Used to Deposit the Dodecanethiol-capped Gold Nanoparticles on the Test Surfaces of the Test Platform	170
6.7	Contact Angle Goniometry	173
6.8	Ellipsometry	173
6.9	Fourier Transform - Infrared Spectroscopy	174
6.10	Microscopy	174
6.10.1	Optical Microscopy	175
6.10.2	Atomic Force Microscopy	175
6.10.3	Scanning Electron Microscopy	176
6.10.4	Transmission Electron Microscopy	176
6.11	Interferometry	177
6.12	Image Analysis Technique Used for Determining the Surface Coverage of the Interacting Asperities	178
7	Experimental Requirement of the Phase Shifting Interferometry	179
7.1	Introduction	179
7.2	Five Frame Interferogram Collecting Sequence for PSI	181
7.3	Experimental Details	183
7.4	Results and Discussion	185

7.5	Conclusions	187
8	Benchmarking the Microinstruments: Highlighting Key Features & Testing Standard Surfaces	188
8.1	The Pattern Matching Technique	188
8.2	Residual Stress Tester	189
8.3	Mechanical Strength Tester	191
8.4	Resonator	194
8.5	Cantilever Beam Array	196
8.5.1	Validating the Authenticity of the Actuation Method Used to Actuate the Cantilever Beams	196
8.5.2	Stress Gradient at the Sacrificial Oxide-Device Layer Interface	201
8.5.3	Determining the Apparent Work of Adhesion of In-plane Surfaces Coated with Standard Coatings	206
8.6	Sidewall Beam Array	209
8.7	Sidewall Friction Tester	217
8.8	Sidewall Friction and Adhesion Tester	228
8.9	Conclusions	239
9	The Effect of Surface Topography	240
9.1	Obtaining Test Surfaces with Distinct Topographies	240
9.2	Characterization of the Tailored Test Surfaces	244
9.2.1	Topography	245
9.2.2	Stiction and Friction	252
9.3	Tribotopography Number (τ_{topo})	262
9.3.1	Formulation	267
9.3.2	Determination of α for Silicon-type Surfaces	272
9.3.3	Validation	277
9.3.4	Significance of the Tribotopography Number (τ_{topo})	282
9.4	Influence of the Geometry of the Contact Interface on the Effect of Surface Topography	284

9.5	Conclusions	285
10	A Simple Experimental Technique to Estimate the Surface Coverage of the Nanoparticle-based Monolayer Coatings Used to Texture MEMS Surfaces	289
10.1	Introduction	289
10.2	Estimation of Surface Coverage	290
10.3	Results	292
10.4	Conclusions	295
11	Surface Texturing: A Potent Alternative to Reduce Stiction and Friction Experienced by MEMS Surfaces	297
11.1	Introduction	297
11.2	Experimental Details	299
11.2.1	Coatings	299
11.2.2	Microinstruments Used	300
11.3	Results and Discussion	302
11.3.1	Topographical Properties of the AuNP Coating	302
11.3.2	Tribological Properties of the AuNP Coating	305
11.4	Conclusions	311
12	Summary	313
12.1	The Test Platform	313
12.2	Microinstruments	315
12.3	Effect of Surface Topography	316
12.4	Other Results	318
	Bibliography	321
	Appendices	337
A	Scripts Used for Actuating the Microinstruments	338
A.1	Script Name: RST Analysis.stp	338
A.2	Script Name: MST Actuation.stp	343
A.3	Script Name: CBA Actuation Method Validity Test.stp	345

A.4	Script Name: CBA Analysis.stp	353
A.5	Script Name: SB Actuation and Analysis.stp	359
A.6	Script Name: Comb - drive Actuator Calibration.stp	362
A.7	Script Name: SFT Normal Arm Comb - drive Actuator Calibration.stp	368
A.8	Script Name: SFT Friction Test.stp	375
A.9	Script Name: SFAT Friction Test.stp	379
A.10	Script Name: SFAT Adhesion Test.stp	382
A.11	Script Name: Pattern Matching Technique Uncertainty.stp	388
A.12	Macro Name: init.mac	390
B	Derivations of the Equations Used to Determine ϕ and $\Delta\phi$	393
B.1	Derivation of the Equation Used to Determine ϕ : Sequence H	393
B.2	Derivation of the Equation Used to Determine ϕ : Sequence NH	393
B.3	Error Analysis of Sequence H	394
B.4	Error Analysis of Sequence NH	396
C	List of Acronyms	398

List of Figures

1.1	(a) A <i>DMD</i> TM commercially manufactured by Texas Instruments. (b) A micro-accelerometer (model: ADXL193) commercially manufactured by Analog Devices using the silicon based <i>i</i> MEMS surface micromachining technology. This device senses acceleration up to $\pm 250g$ and costs about \$7 in 2011.	3
1.2	(a) SEM image of a micro steam engine developed by Sandia National Laboratories [14]. (b) SEM image of an electromechanical locking device developed by Sandia National Laboratories [14].	5
1.3	A simplified schematic illustrating the basic steps involved in surface micromachining. Notice that the “released” microstructure is a cantilever beam.	16
1.4	A schematic diagram exhibiting the shape of the meniscus of a liquid layer trapped between two (a) hydrophilic surfaces and (b) hydrophobic surfaces. The arrows shown in the diagram indicate the direction of the Laplace force acting on the upper (movable) plate with respect to the lower (fixed) plate.	22
1.5	A schematic diagram of (a) a hydrophilic surface and (b) a hydrophobic surface. Also illustrated in both the diagrams, is the definition of contact angle.	24
1.6	A plot illustrating how the Capillary, Van der Waals and Electrostatic forces experienced by a pair of proximate atomically smooth silicon surfaces vary with the distance of separation between them. For reference, the variation in the Casimir forces (i.e., vacuum energy level) experienced by a pair of atomically smooth, perfectly conducting plates with the distance of separation between them is also shown in the plot. Additionally, the range of magnitudes of the restoring forces that are typically generated in most MEMS devices is also indicated on the plot [66].	32
2.1	A P-T diagram depicting the phase paths followed during the critical point drying and the freeze sublimation drying processes. Notice that in both the processes, a longer phase path is intentionally followed to avoid crossing the liquid-vapor line.	42

2.2	A schematic diagram of a typical precursor molecule. The non-polar tail shown in the diagram is a C ₁₈ hydrocarbon chain and the polar head group is a trichlorosilane molecule.	50
2.3	A simplified, conceptual model illustrating the second step of the chlorosilane-based SAM formation process. The first step (not shown) is the complete hydrolysis of the precursor molecules, which results in the formation of 3 HCl molecules per precursor molecule as well as the trisilanol forms (shown in this figure) of the precursor molecules. In the second step, which is shown in this figure, water elimination (condensation) reactions result in Si-O-Si linkages between the adjacent hydrolyzed precursor molecules and/or the native oxide layer present on the substrate. The precursor molecules shown in the figure are octadecyltrichlorosilane (CH ₃ (CH ₂) ₁₇ SiCl ₃) molecules.	53
2.4	(a) AFM image of an OTS coated Si(100) surface. The RMS roughness of the surface based on image statistics is 25 nm. (b) Linescan along the white line drawn across image a. Notice that some of the particulates visible in image a are as wide as 2 micron and as high as 490 nm. . . .	60
3.1	(a) An AFM image of a typical in-plane polysilicon surface. The rms roughness of the surface shown in image a is 3.71 nm. The z-scale of image a is 30.7 nm. (b) Linescan along the white line drawn across image a.	78
3.2	An AFM image of a typical sidewall polysilicon surface [78]. The rms roughness of the surface shown in image a is 13.8 nm. The z-scale of image a is 158.7 nm. (b) Linescan along the white line drawn across image a.	79
4.1	(a) An AFM image of the in-plane surface of the test platform. The rms roughness of the surface shown in image a is 0.097 nm. The z-scale of image a is 1.1 nm. (b) Linescan along the black line drawn across image a.	85
4.2	(a) An AFM image of the sidewall surface of the test platform. The rms roughness of the surface shown in image a is 6.52 nm. The z-scale of image a is 41.8 nm. (b) Linescan along the black line drawn across image a. . .	86
4.3	The layout of the mask used to fabricate the test platform. Notice that the test platform is fabricated on a 1 cm × 1 cm chip. It consists of seven different types of microinstruments, all of which, are labelled in the above figure.	89
4.4	SEM images of (a) An unpolished sidewall surface. (b) A polished sidewall surface.	93
4.5	Photograph of the custom-built probing system used to actuate the microinstruments of the test platform.	96

5.1	(a) Optical image of a released Residual Stress Tester. Notice that the I-beam consists of a horizontal central beam that is connected to two vertical flanges. (b) Magnified optical image of the area that is enclosed in the box in Fig. 5.1a. Notice the pair of movable and anchored patterns labelled in this image.	98
5.2	(a) A schematic diagram (plan view) illustrating the clockwise rotation of the I-beam of the Residual Stress Tester due to the tensile stress present in the released structural film. (b) A schematic diagram (plan view) illustrating the anti-clockwise rotation of the I-beam of the Residual Stress Tester due to the compressive stress present in the released structural film. Shaded regions shown in the diagrams are anchored to the substrate. A ground plane (not depicted) is present underneath the entire device. . . .	100
5.3	Optical image of a released Mechanical Strength Tester.	102
5.4	Photograph of the Micro-manipulator developed to actuate the Mechanical Strength Testers. Notice the “bypass” connection used to electrically ground the probe tip. The two main components of the Micro-manipulator (i.e., the “coarse” manipulator and the “fine” manipulator) are clearly labelled in the photograph.	105
5.5	Photograph showing the five components of the “fine” manipulator. . . .	106
5.6	Orthographic projections (plan view) of the four machined components of the “fine” manipulator. The dimensions indicated in the orthographic projections are in mm.	107
5.7	Optical images illustrating the actuation of a Mechanical Strength Tester. (a) The MST is shown in its pre-actuated state. (b) Optical image collected during the actuation of the MST. Notice that all the six fracture beams are pushed against their corresponding anchored stoppers. (c) Optical image showing the MST in its post-actuated state. Notice that all the fracture beams that were attached to the central shuttle are fractured.	109
5.8	Optical image of a released Resonator.	111
5.9	An optical image showing two adjacent released Cantilever Beam Arrays.	116
5.10	A schematic diagram illustrating the actuation procedure of a cantilever beam. (a) Free-standing (unactuated) cantilever beam. (b) Actuated cantilever beam. (c) Cantilever beam released after actuation (post-actuation state). Notice that the cantilever beam is adhered over a length of $L - s$ at its tip.	118

5.11	A schematic diagram of the sidewall adhesion test microinstrument (plan view). Shaded regions shown in the diagram are anchored to the substrate. A ground plane (not depicted) is present underneath the entire device.	122
5.12	(a) Optical image of a released sidewall adhesion test microinstrument. Anchors that anchor the sidewall test beams are not visible in the image. The total length of the sidewall beams shown in the image is $750\ \mu\text{m}$. (b) Optical image of a released sidewall beam array. The shortest pair of sidewall beams is $750\ \mu\text{m}$ long. The length of sidewall beam pairs is increased in increments of $250\ \mu\text{m}$ and the longest pair of sidewall beams is $2250\ \mu\text{m}$ long.	125
5.13	A schematic diagram (plan view) illustrating the actuation procedure of the sidewall adhesion tester. (Top) The sidewall beams are in the as-fabricated position. (Center) The sidewall beams are in an actuated state, contacting over almost the entire length of their final segments. (Bottom) Final state of the sidewall beams post-actuation when the actuating voltage is reduced to zero. The beams are adhered over a length $L - s$ at their tips.	127
5.14	A schematic diagram of the Sidewall Friction Tester (plan view). Shaded regions shown in the diagram are anchored to the substrate. A ground plane (not depicted) is present underneath the entire device. The diagram is not drawn to scale to better illustrate the important components of the device.	133
5.15	Optical image of a released Sidewall Friction Tester (SFT). Notice the ground plane present underneath the entire device. The total footprint of the microinstrument is $2.8\ \text{mm}^2$	134
5.16	(a) A schematic diagram illustrating the segmental design of the anchored comb fingers of the SFT. The diagram is drawn using a scale of 127000:1. In the as-fabricated (unactuated) position, the anchored and suspended comb fingers overlap over a length of $20\ \mu\text{m}$ (nominal). Notice that the gap between them will decrease to $1\ \mu\text{m}$ (nominal) when their overlap increases beyond $22.8\ \mu\text{m}$ (nominal). (b) Optical image showing a bank of interdigitated anchored and suspended comb fingers. The two segments of the anchored comb fingers are clearly visible in this image. (c) Magnified optical image of the area enclosed in the box in image b. The pointed tips of the suspended comb fingers are clearly visible in this image.	137
5.17	Optical image showing the loading section of an unpolished, released Sidewall Friction Tester. The loading section is in its as-fabricated (unactuated) position. Notice that the anchored posts are not aligned with the as-fabricated position of the normal arm (i.e., b is greater than a). The gap between the anchored posts and the corresponding sidewall surfaces of the loading beam is $6\ \mu\text{m}$ (nominal) in the as-fabricated position.	139

5.18	Optical image of a released Sidewall Friction and Adhesion Tester (SFAT). Notice the ground plane present underneath the entire device. The total footprint of the microinstrument is 0.47 mm^2	149
5.19	(a) Optical image showing the normal arm of a released Sidewall Friction and Adhesion Tester (SFAT). (b) Optical image showing the tangential arm of a released Sidewall Friction and Adhesion Tester (SFAT). Notice that both the normal and the tangential arm have one push drive and one pull drive each.	151
5.20	(a) Optical image showing one bank of interdigitated comb fingers each of the normal and tangential arms of a released Sidewall Friction and Adhesion Tester (SFAT). The two segments of the anchored comb fingers are clearly visible in this image. (b) Magnified optical image showing the comb fingers of the tangential arm of the SFAT, that are enclosed in the box in Fig. 5.20a. (c) Magnified optical image showing the comb fingers of the normal arm of the SFAT, that are enclosed in the box in Fig. 5.20a. The pointed tips of the suspended comb fingers are clearly visible in both Fig. 5.20b and Fig. 5.20c.	153
5.21	Optical image showing the loading section of a released Sidewall Friction and Adhesion Tester. The loading section is in its as-fabricated (unactuated) position. Notice the gap between the loading block and the friction block. It is designed to be $4 \mu\text{m}$ (nominal) in their as-fabricated positions. The anchored and suspended patterns that are used to track the displacements of the normal and tangential arms are clearly labelled in the image.	155
6.1	AFM image of a $25 \mu\text{m}^2$ area of the OTS SAM coated Si(100) monitor chip, which is processed simultaneously with the OTS SAM coated Test Platform chip. Notice that only four extremely small polymerized particles are present in the $25 \mu\text{m}^2$ area shown in the scan. The rms roughness of the area shown in the image is 0.23 nm	169
6.2	A TEM image showing the dodecanethiol-capped gold nanoparticles used to tailor the surface topographies of the test surfaces investigated in this study. The size of the dodecanethiol-capped gold nanoparticles shown in the image is determined to be $5.48 \pm 1.16 \text{ nm}$	171
7.1	Error in ϕ ($\Delta\phi$) for different imposed percentage error ($\%\epsilon$) in α	186
8.1	A plot showing the experimentally determined axial and lateral displacements of the central shuttle of one of the MSTs of the OTS SAM coated Test Platform chip versus the corresponding voltage applied to the micro-manipulator that is used to actuate it. Notice the discontinuities in the plot that represents the axial displacement data. Also, the lateral displacements of the central shuttle are negligible throughout the actuation of the MST.	192

8.2	A plot of the square of the observed resonance frequency of the Resonators investigated in this chapter versus their corresponding value of the term that is written in brackets on the right hand side of Eq. 5.3.6. The (●) represent the experimentally observed resonance frequencies and (—) is a line fitted to the experimentally obtained data. Notice the high R^2 value of the linear fit. The slope of the fitted line is the experimentally obtained value of E of the structural film of the native oxide covered Test Platform chip.	197
8.3	(a) Interferogram of a polysilicon-based CBA, collected before actuation. (b) Interferogram of the CBA shown in Fig. 8.3a, collected after actuation. This CBA was actuated manually.	198
8.4	(a) Interferogram of a polysilicon-based CBA, collected before actuation. (b) Interferogram of the CBA shown in Fig. 8.4a, collected after actuation. This CBA was actuated electrostatically.	199
8.5	(a) Interferogram showing a released cantilever beam array of the Test Platform chip coated with OTS SAM. Notice the presence of fringes on all the cantilever beams, which indicates that they are not parallel to the substrate. (b) Height profile of beam 5 labelled in Fig. 8.5a. The height profile is obtained experimentally, using phase shifting interferometry. It indicates that beam 5 is inclined upwards, and has a convex shape. . . .	203
8.6	(a) Interferogram showing a released cantilever beam array of a Test Platform chip, which is not polished. Notice that the number of fringes present on the cantilever beams shown in this image is less, which indicates that they are not parallel to the substrate. (b) Height profile of beam 5 labelled in Fig. 8.5a. The height profile is obtained experimentally, using phase shifting interferometry. It indicates that beam 5 is inclined upwards, and has a convex shape.	204
8.7	(a) Interferogram showing released sidewall adhesion test microinstruments. Notice the fringes on the sidewall beams, which clearly indicate that the sidewall beams are freestanding and also not parallel to the substrate (b) Height profile of the initial segment of the topmost sidewall beam shown in Fig. 8.7a. The height profile is obtained using phase shifting interferometry. It clearly indicates that the sidewall beam is inclined upwards and exhibits a take-off angle of 1 mrad.	211
8.8	Interferogram showing the initial segment of an actuated sidewall adhesion test microinstrument. Voltage applied to the actuation electrode is 52 V. Notice the increased number of fringes visible on the actuated sidewall beams as compared to that of fringes visible on the unactuated sidewall beams shown in Fig. 8.7a, which is a manifestation of levitation. Also notice that the exact same number of fringes are visible on both the actuated sidewall beams.	213

- 8.9 (a) Interferogram showing the final segment of an actuated sidewall adhesion test microinstrument. Voltage applied to the actuation electrode is 70 V. The two sidewall beams are stuck to each other over a length of 50 μm at their tips. Notice that while the fringes on the two sidewall beams are equal in number, they are slightly mismatched in phase. (b) Interferogram, showing the final segment of the same sidewall adhesion test microinstrument that is shown in Fig. 8.9a, collected post-actuation. Notice that no “scissoring” is visible on the two sidewall beams, which are stuck over a length of 25 μm at their tips. 215
- 8.10 A plot showing the experimentally determined axial (■) and lateral (◆) displacements of the tangential arm of the test device versus square of the corresponding voltages (V_t^2) applied to its pull drive. Notice that the data representing the axial displacements is clearly divided into two segments, which have significantly different slopes. The transfer functions G_{t1} and G_{t2} are extracted from the corresponding linear fits (∩) of the experimental axial displacement data. δ_a , which is determined optically, is the distance by which the tangential arm should be pulled to its left to align the normal arm with the anchored posts and V_a is the corresponding voltage that should be applied to the pull drive of the tangential arm. . . 219
- 8.11 A plot showing the experimentally determined axial (■) and lateral (◆) displacements of the normal arm of the test device versus square of the corresponding voltages (V_n^2) applied to its pull drive. Notice that the data representing the axial displacements is clearly divided into three segments, which have significantly different slopes. The transfer functions G_{n1} and G_{n2} are extracted from the corresponding linear fits (∩) of the experimental axial displacement data. δ_c is the distance by which the normal arm should be axially displaced in order to bring the loading beam in contact with the anchored post and V_c is the corresponding voltage that should be applied to the normal comb-drive actuator. Notice that even at voltages greater than V_c , the lateral displacements of the normal arm are negligible. . . . 221
- 8.12 An interferogram, showing the loading section of the test device, collected after bringing the loading beam in contact with the anchored post. A voltage of 45 V is applied to the pull drive of the normal comb-drive actuator before collecting this interferogram. Notice the absence of fringes on the normal arm as well as on the loading section. The step edge at the sidewall interface is determined using HSI to be 20 nm. 223

8.13	A plot showing the onset of slip at an OTS SAM coated sidewall interface. The displacement of the loading beam, which is determined by considering its position when the normal arm is aligned with the anchored post as the initial position, is plotted against the voltage applied to the tangential comb-drive actuator. A normal load of $8.05 \mu\text{N}$, which corresponds to a Hertzian contact pressure of 224 MPa, is applied at the sidewall interface. Notice that the first slip occurred at $V_{t,s}$ of 32.8 V and the second slip occurred at $V_{t,s}$ of 34.8 V.	225
8.14	A plot showing the experimentally determined axial (■) and lateral (◆) displacements of the tangential arm of one of the OTS SAM coated Sidewall Friction and Adhesion Testers versus square of the corresponding voltages (V_t^2) applied to its push drive. Notice that the data representing the axial displacements is clearly divided into two segments, which have significantly different slopes. The transfer functions G_{t1} and G_{t2} are extracted from the corresponding linear fits () of the experimental axial displacement data.	230
8.15	A plot showing the experimentally determined axial (■) and lateral (◆) displacements of the normal arm of one of the OTS SAM coated SFAT versus square of the corresponding voltages (V_n^2) applied to its push drive. Notice that the data representing the axial displacements is clearly divided into three segments, which have significantly different slopes. The transfer functions G_{n1} and G_{n2} are extracted from the corresponding linear fits () of the experimental axial displacement data. δ_c is the distance by which the normal arm should be axially displaced in order to bring the loading block in contact with the friction block and V_c is the corresponding voltage that should be applied to the normal comb-drive actuator.	232
8.16	An interferogram showing the sidewall interface formed in one of the OTS SAM coated Sidewall Friction and Adhesion Testers. A voltage of 50 V is applied to the push drive of the normal arm to bring the loading block in contact with the friction block, before collecting this interferogram. Notice the absence of fringes on the loading and friction blocks shown in the interferogram. The step edge at the sidewall interface is determined using HSI to be 75 nm.	234
8.17	A plot showing the onset of slip at an OTS SAM coated sidewall interface investigated using the SFAT developed in this study. The displacement of the friction block is plotted against the voltage applied to the tangential comb-drive actuator. A normal load of $1.82 \mu\text{N}$, which corresponds to an apparent contact pressure of 0.26 MPa, is applied at the sidewall interface. Notice that the first slip occurred at $V_{t,s}$ of 52 V and the second slip occurred at $V_{t,s}$ of 57 V.	236

9.1	SEM images of the substrates of the five textured Test Platform chips investigated in this chapter. The numbers indicated on the SEM images are the sample numbers of the corresponding textured Test Platform chips. Notice the monotonous increase in the amount of the nanoparticles present on the textured surfaces shown in the SEM images from the image a to image e.	246
9.2	AFM images of the substrates of the Test Platform chips investigated in this chapter. The numbers indicated on the AFM images are the sample numbers of the corresponding textured Test Platform chips.	251
9.3	Bar graph showing the rms roughnesses of the in-plane surfaces of the Test Platform chips investigated in this chapter.	253
9.4	A schematic explaining the observed variations in the roughnesses of the substrates of the Test Platform chips investigated in this chapter. The red lines shown in all the diagrams represent the surface profile of the (untextured or textured) substrates shown in them.	254
9.5	A plot showing the variations in the apparent works of adhesion of the in-plane as well as sidewall surfaces with the variations in their surface topographies. The data points plotted in the plot are arithmetic means of several measurements. The error bars shown in the plot indicate the maximum and minimum values of the apparent works of adhesion exhibited by the in-plane and sidewall surfaces of that Test Platform chip.	259
9.6	A plot showing the variation in the engineering coefficient of static friction of a sidewall surface with the variation in its surface topography. The data points plotted in the plot are arithmetic means of 225 measurements. The error bars shown in the plot indicate the maximum and minimum values of the engineering coefficient of static friction exhibited by the contacting sidewall surfaces of that Test Platform chip.	263
9.7	(a) A SEM image showing the edge of a released cantilever beam of sample no. 4. (b) A SEM image of a region of the substrate, which is underneath the cantilever beam shown in Fig. 9.7a. The SEM image shown in this image is collected after breaking the cantilever beam shown in Fig. 9.7a apart using a probe tip (Signatone 20T). Notice that the surfaces shown in both the image a as well as the image b have exactly identical nanoparticle coatings on them.	264

9.8	A plot of the apparent works of adhesion exhibited by the six in-plane surfaces investigated in this chapter versus their rms roughnesses. The data points plotted in the plot are arithmetic means of 40 measurements. The error bars shown in the plot indicate the maximum and minimum values of the apparent work of adhesion exhibited by the in-plane surface of that Test Platform chip. Notice that the plot indicates that there exists an optimum rms roughness, at which, the in-plane surface experiences minimum stiction.	266
9.9	A plot, in which, the ordinates of Eq. 9.3.23 are plotted against its abscissae. The data points (■) plotted in Fig. 9.9 are obtained using the mean values of \mathcal{W} reported in Table 9.5. The error bars shown in the plot indicate one standard deviation of the sample of 40 measurements used to determine that data point. A line () fitted to the data points (■) is also shown in the plot. Notice the high R^2 value of the linear fit.	278
9.10	A representative AFM image of the sidewall surface of the control (un-textured) sample. The rms roughness of the surface shown in the image is 6.52 nm. The z-scale of the image is 41.8 nm.	279
9.11	A plot showing the μ_s of the sidewall surfaces of all the six Test Platform chips, determined using both the SFTs as well as the SFATs. The data points plotted in the plot are arithmetic means of several measurements. The error bars shown in the plot indicate the maximum and minimum values of the engineering coefficient of static friction exhibited by the sidewall surfaces of that Test Platform chip. Notice the close agreements between the μ_s determined using the SFTs and those determined using the SFATs.	286
10.1	(a) A high resolution AFM image of the top surface of one of the Resonators of the coated Test Platform chip. The rms roughness of the surface shown in image a is 2.06 nm. The z-scale of image a is 13.8 nm. (b) Linescan along the white line drawn across image a.	293
11.1	(a) AFM image of the native oxide covered uncoated substrate of the control chip I. The rms roughness of the surface shown in image a is 0.097 nm. (b) Linescan along the white line drawn across image a.	303
11.2	(a) AFM image of the AuNP coated substrate of the test chip. The rms roughness of the surface shown in image a is 8.3 nm. (b) Linescan along the white line drawn across image a.	304
11.3	(a) An interferogram showing a tested Cantilever Beam Array of the control chip I. (b) Experimentally determined height profile of beam 2 labelled in image a. The height profile is determined using phase shifting interferometry. Notice that the crack of beam 2 labelled in image a is less than 100 μm	306

11.4	(a) An interferogram showing a tested Cantilever Beam Array of the test chip. (b) Experimentally determined height profile of beam 4 labelled in image a. The height profile is determined using phase shifting interferometry. Notice that the crack of beam 4 labelled in image a is close to 850 μm	307
11.5	(a) Optical image showing the five longest sidewall beam pairs of a released Sidewall Beam Array of the test chip, collected before actuating the Sidewall Beam Array. Notice that the sidewall beams of each of the five sidewall beam pairs shown in this image are apart from each other. (b) Optical image of the Sidewall Beam Array shown in image a, collected after actuating it. Notice that the sidewall beams of the three shorter sidewall beam pairs shown in this image peeled apart completely, while those of the two longer sidewall beam pairs remained stuck, after actuation.	308
11.6	A plot of the (mean) μ_s of the AuNP coated contacting sidewalls versus the corresponding voltage applied to the comb-drive actuator of the normal arm. The arrows shown in the plot indicate the direction, in which, the normal load applied at the sidewall interface of the SFAT used for this study is changed. Notice that the (mean) μ_s of the AuNP coated contacting sidewalls changed irreversibly when a voltage of 77 V is applied to the normal comb-drive actuator.	312
A.1	A screenshot of the user-interface of MEMScript.	339

List of Tables

2.1	A comparison between the film properties of OTS, FDTS and oxide surface films [6, 35, 64, 80, 99].	57
8.1	This table reports the measured lever arms as well as the measured displacements of corresponding MSTs at the instant of fracture of the tested fracture beams. It also reports the strains that exist in the tested fracture beams at the instant of their fracture. Each value reported in the table is an arithmetic mean of 16 measurements, and the corresponding std. dev. is one standard deviation of the sample consisting of those measurements.	193
8.2	This table reports the drive signals used to actuate the Resonators of the native oxide covered Test Platform chip along with their optically observed resonance frequencies. Each resonance frequency reported in the table is an arithmetic mean of five measurements, which are made using five distinct Resonators having the same supporting beam length.	195
8.3	Comparison between the apparent work of adhesion of OTS SAM coated in-plane surfaces calculated using different methods. The OTS SAM coated cantilever beam used for this analysis exhibited a crack length of 835.3 μm . The method used for determining the apparent work of adhesion of the in-plane surfaces investigated in this study is highlighted in the table.	207
8.4	Comparison between the apparent work of adhesion of in-plane surfaces of OTS SAM coated surfaces and that of surfaces with only native oxide on them. The apparent works of adhesion of in-plane surfaces reported in this table are determined using the CBAs. All the values reported in the table are arithmetic means of 40 measurements and sd is one standard deviation of the sample consisting of those measurements.	208
8.5	Comparison between the apparent work of adhesion of sidewall surfaces of OTS SAM coated surfaces and that of surfaces with only native oxide on them. The apparent works of adhesion of sidewall surfaces reported in this table are determined using the SBAs. All the values reported in the table are arithmetic means of several measurements and sd is one standard deviation of the sample consisting of those measurements.	216

8.6	Comparison between the engineering coefficients of static and kinetic friction of OTS SAM coated surfaces and those of surfaces with only native oxide on them. The engineering coefficients of friction reported in this table are determined using the Sidewall Friction Tester. All the values reported in the table are arithmetic means of 200 measurements and the std. dev. is one standard deviation of the sample consisting of those measurements.	227
8.7	Comparison between the engineering coefficients of static and kinetic friction of OTS SAM coated surfaces and those of surfaces with only native oxide on them. The engineering coefficients of friction reported in this table are determined using the Sidewall Friction and Adhesion Tester. All the values reported in the table are arithmetic means of 325 measurements and the std. dev. is one standard deviation of the sample consisting of those measurements.	238
9.1	This table lists the decrease in the resonance frequencies (Δf_R) and the corresponding increase in the effective masses (ΔM_{eff}) of the Resonators with 500 μm long supporting beams, of each of the five textured Test Platform chips. Each value reported in the table is an arithmetic mean of five measurements, which are obtained using five distinct Resonators that are fabricated at different locations on the corresponding Test Platform chip.	249
9.2	Comparison between the mean apparent works of adhesion of the in-plane surfaces of the six Test Platform chips investigated in this chapter to study the effect of topography. The apparent works of adhesion of in-plane surfaces reported in this table are determined using the CBAs. All the values reported in the table are arithmetic means of 40 measurements.	256
9.3	Comparison between the mean apparent works of adhesion of the sidewall surfaces of the six Test Platform chips investigated in this chapter to study the effect of topography. The apparent works of adhesion of in-plane surfaces reported in this table are determined using the SBAs. All the values reported in the table are arithmetic means of several measurements.	257
9.4	Comparison between the mean engineering coefficients of static friction of the sidewall surfaces of the six Test Platform chips investigated in this chapter to study the effect of topography. The engineering coefficients of static friction reported in this table are determined using Sidewall Friction Testers. All the values reported in the table are arithmetic means of 225 measurements.	260

9.5	This table reports the \mathcal{W} (arithmetic mean), r_{rms} , Ω_{rms} and Θ of all the five textured in-plane surfaces investigated in this study. The values of Θ and Ω_{rms} reported in this table are determined using the untextured (control) in-plane surface as the reference surface. Accordingly, \mathcal{W}^o and r_{rms}^o used are $38700 \mu\text{J}/\text{m}^2$ and 0.14 nm , respectively. The r_{rms} of each of the five textured in-plane surfaces as well as the r_{rms}^o are obtained from their corresponding representative AFM images. $n_{asperities}$ for each of the five textured in-plane surfaces as well as for the reference surface are determined using the image analysis technique explained in section 6.12. The threshold value used in the image analysis technique is the kelvin radius of water at the relative humidity of 45%.	274
9.6	This table reports the r_{rms} , Ω_{rms} , Θ and τ_{topo} of the sidewall surface of the control (untextured) sample. The r_{rms} reported in this table is obtained using the AFM image shown in Fig. 9.10. The Ω_{rms} and the Θ reported in the table are obtained using the in-plane surface of the control (untextured) sample as the reference surface. The table also reports the apparent works of adhesion of the sidewall surface of the control sample, determined using its τ_{topo} and obtained experimentally.	281
10.1	This table reports the optically observed resonance frequencies of the two sets of Resonators tested in this study. Each resonance frequency reported in the table is an arithmetic mean of five measurements, which are made using five distinct Resonators having the same supporting beam length. .	296
11.1	Comparison between the critical tribological properties of the native oxide covered hydrophilic surfaces of the control chip I, the OTS SAM coated hydrophobic surfaces of the control chip II and the AuNP coated surfaces of the test chip. All the values reported in the table are arithmetic means of several measurements and sd is one standard deviation of the sample consisting of those measurements.	310

Chapter 1

MEMS Technology

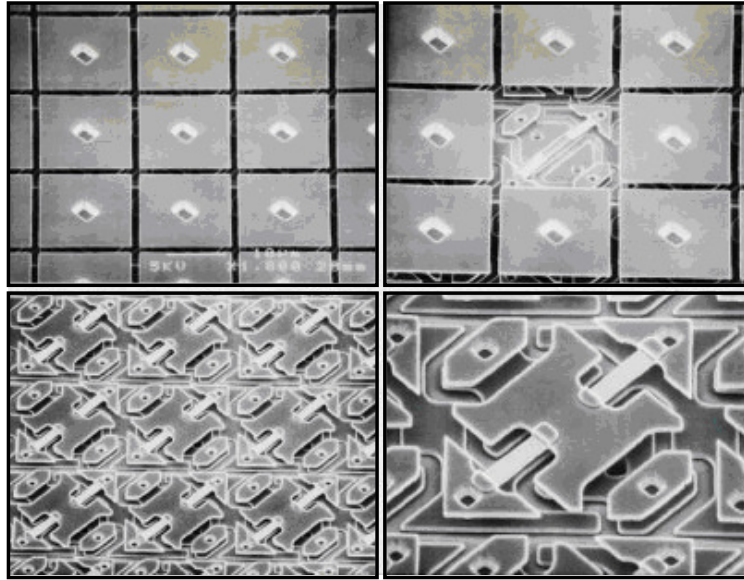
1.1 Miniaturization: Exploring the Room at the Bottom

Miniaturization is extremely beneficial in many technological applications, in all the branches of fundamental (i.e., physics, chemistry and biology) and applied (i.e., engineering) sciences [1]. A good example, which substantiates this, is the increased efficiency and speed of microprocessors used presently, which are direct consequences of the miniaturization of transistors used in them [2]. While there are several such useful consequences of miniaturization, as pointed out by Feynman half-a-century ago in his historic lecture “There’s plenty of room at the bottom”, the one that has materialized most prominently over the last two decades is the evolution of the field of Micro-electromechanical systems (MEMS) [1, 3]. However, although MEMS technology has evolved significantly in the past few years, it has seen limited commercial success due to the poor reliability of most of the invented MEMS prototypes. Since the primary motivation behind this study is to enhance our understanding of the tribological characteristics of MEMS interfaces so that an appropriate strategy to improve the reliability and hence, enable the commercialization of useful MEMS prototypes, could be devised, it is only logical to begin this report by answering the following questions: what are MEMS, why are they technologically attractive and why is it important to enable their commercialization?

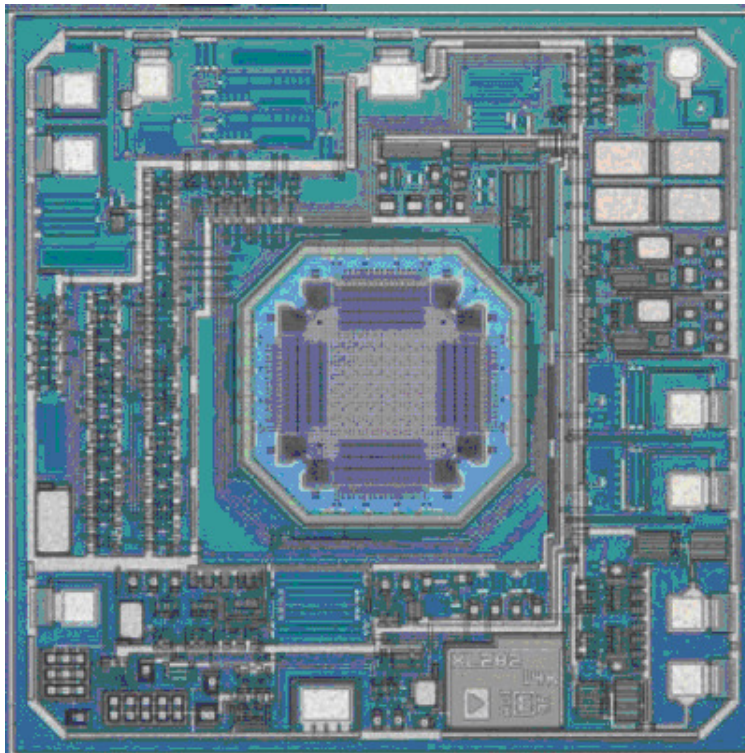
1.2 MEMS: A Technological Evolution

Micro-electromechanical systems (MEMS) are miniature devices, in which, mechanical components, with dimensions ranging from a few to a few hundred microns, and electrical components are directly integrated together. They are used either individually to sense, control and activate mechanical processes at the micro-scale or in arrays to generate effects at the macro-scale. The idea of MEMS was first conceived in the mid 1960's, when Nathanson and colleagues at the Westinghouse Research Laboratory devised a complete oscillator by combining a simple mechanical resonator with an early electronic transistor on the same silicon wafer [3]. However, it took a quarter of a century for the scientific community to produce the first commercial MEMS device and even to-date the technology has been used successfully in only a few commercialized applications. The working of most of those applications is based on the mechanical response of a MEMS device (with no contacting parts) to an environmental change [4, 5].

The first MEMS device that was commercialized was an *i*MEMS accelerometer, which integrated a small, reliable MEMS sensor structure with a signal conditioning circuitry on a single chip [6]. It was produced in 1991 by Analog Devices [6]. Other MEMS devices that have been commercialized since then include relatively simple sensing mechanisms like accelerometers, gyroscopes and pressure sensors [7, 8]. Presently, the accelerometer technology, which is used in airbag-deployment systems, anti-skid breaking systems and four-wheel drive systems in the automobile industry, is on the order of a billion dollars-a-year industry, dominated by Lucas NovaSensor and Analog Devices. The most recently commercialized MEMS device is the Digital Mirror Device (*DMD*TM) developed by Texas Instruments, which has useful applications in digital light processing (DLP) equipments such as television sets and projectors [9–11]. Figures 1.1a and 1.1b show two of the most widely used commercially available MEMS devices.



(a)



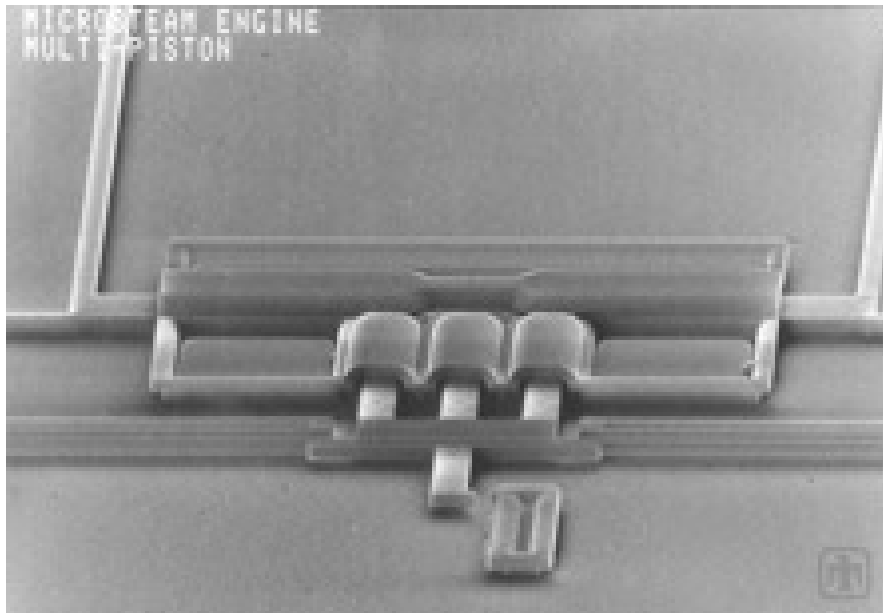
(b)

Figure 1.1: (a) A *DMD*TM commercially manufactured by Texas Instruments. (b) A micro-accelerometer (model: ADXL193) commercially manufactured by Analog Devices using the silicon based *i*MEMS surface micromachining technology. This device senses acceleration up to $\pm 250g$ and costs about \$7 in 2011.

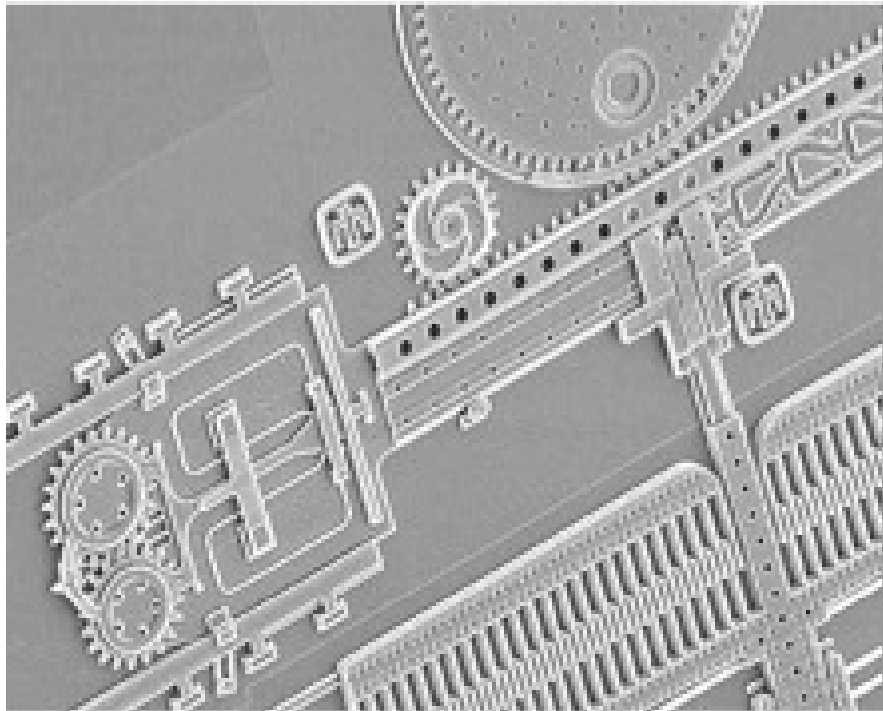
MEMS are technologically as well as commercially very attractive primarily because they are inherently smaller, lighter, faster and generally more precise than their macro-counterparts. However, for some applications such as car airbag deployment systems, RF switches and RF filters, they are commercially attractive because of their low cost [3]. While some these attributes that make MEMS technologically and commercially attractive, such as low cost, small size and light weight, are direct consequences of the micromachining processes and the relatively inexpensive structural material (i.e., silicon) used to fabricate them, others, such as high speed and precision, are consequences of their small size [9, 12, 13].

Leveraging the infrastructure of the integrated circuit (IC) industry and the advancements in the micromachining technologies, the MEMS community have devised an extensively large number of useful MEMS prototypes. However, to-date, only a few of those MEMS prototypes have been commercialized and the rest, such as those shown in Figs. 1.2a and 1.2b, still remain in the category of potential MEMS due to their poor reliability. Since those potential MEMS devices are also technologically and commercially very attractive and have extremely useful applications in a wide variety of electronically controlled equipments such as robots, industrial process controllers and instruments, toasters, automobiles, bathroom scales, displays, printers and storage devices, there is an urgent and serious need to devise strategies that can enable their commercialization [4]. Figure 1.2a shows a SEM image of a micro steam engine developed by Sandia National Laboratories, which has the potential to be a breakthrough invention in the field of micro-scale power generation. Figure 1.2b shows a SEM image of another MEMS prototype developed by Sandia National Laboratories, which is a strong potential candidate for applications that involve precise positioning.

Presently, the potential MEMS devices that are most promising and on the verge of commercialization belong to the two emerging and exciting branches of Bio-MEMS



(a)



(b)

Figure 1.2: (a) SEM image of a micro steam engine developed by Sandia National Laboratories [14]. (b) SEM image of an electromechanical locking device developed by Sandia National Laboratories [14].

and Microfluidics. Bio-MEMS and Microfluidic devices are portable, potentially low cost, integrated packages, which also offer an additional advantage of requiring only small amounts of sample and reagents due to their small sizes. While the only commercially available Bio-MEMS devices presently are Biosensors, which are used for detecting from pH of a biological system to small molecules such as oxygen and glucose, the range of applications in which potential Bio-MEMS can be used extends from tools for molecular biology, cell biology and biochemistry to breakthrough medical devices such as micromachined neural prostheses, micro-pumps and micro-needles used for drug delivery [15–20]. Additionally, extensive research to develop Bio-MEMS implants that can record from, sense, stimulate and deliver to biological systems, is also being conducted [17, 20]. A good example of this is the retinal implant reported by Peachey *et al.*, which employs a semiconductor based microphotodiode array to restore the impaired visual function [19]. Microfabricated biocapsule reported by Desai *et al.* is also a promising possible application of potential Bio-MEMS [18]. It has novel implications in the field of immunoisolation [18].

1.3 Tribology: Role in Hindering the Commercialization of MEMS

While at the laboratory scale, a wide variety of complex MEMS prototypes including sensors, actuators, valves, nozzles, turbines, pumps and gear trains have been conceptualized and tested, at the commercial scale, only the sensors have been extensively employed [3]. The issues that have historically hindered the commercialization of most useful MEMS prototypes include generation of low force/torque by the MEMS prototype, unavailability of technology to couple the different micro-components of the MEMS prototype to produce useful work and poor reliability of the MEMS prototype [3]. While the five-level poly-crystalline silicon (polysilicon) micromachining process (i.e., “SUMMiT™ V”) developed recently at Sandia National Laboratories

has resolved the first two issues, which in turn has initiated the realization of the concept of mechanical power transmission using MEMS as well as significantly increased the number of possible applications of potential MEMS, poor reliability still remains a major hindrance in the commercialization of most complex and useful MEMS prototypes [3].

The poor reliability of most MEMS prototypes is generally attributed to their susceptibility to failures induced by surface phenomena such as stiction, friction and wear [9,12,21]. Indeed, stiction is responsible for hampering the functioning of several micro - and nano - machines because their moving parts adhere spontaneously upon contact [6]. This is a direct consequence of the fact that the relative significance of surface forces increases drastically at the scale of MEMS (i.e., micro-scale). To better understand the increase in the relative significance of surface forces at the micro-scale, consider the adhesion force experienced by the stainless steel grinding media used in ball mills. If the diameter of the grinding media is 10 cm and its surface is dirty (i.e., apparent work of adhesion of its surface is 0.1 Jm^{-2}), it experiences an adhesion force (i.e., 12 mN) that is three orders of magnitude smaller than the force of gravity (i.e., 41000 mN) experienced by it. Contrastingly, if the diameter of the same grinding media is $1 \mu\text{m}$, it experiences an adhesion force that is more than a million times greater than the force of gravity experienced by it. The increased relative significance of the adhesion force experienced by the stainless steel grinding media at the micro-scale is a consequence of the fact that the adhesion force falls linearly with the size of the grinding media whereas the gravitational force falls with its size cubed [22].

The stainless steel grinding media illustration also emphasizes that we cannot always intuitively transfer our understanding of the macroscopic mechanical systems to the micro-domain. Therefore, dedicated systematic investigations should be conducted to understand the laws that govern the behaviour of objects at the micro-scale. A complete understanding of the behaviour of micron-size objects requires

knowledge of all the factors that influence it as well as in-depth understanding of the mechanisms underlying them. However, although surface phenomena such as stiction, friction and wear were identified as factors that dominate the behaviour of micron-size objects half-a-century ago, the mechanisms underlying their manifestations at the micro-scale are still poorly understood [1]. Our current knowledge base is so incomplete that it can neither reasonably accurately predict nor satisfactorily explain all the interactions that occur between two micron-size surfaces when they are brought together, separated and rubbed against each other (collectively called as tribology) [6, 23–31]. Making this already dire situation worse is the demand for sophisticated and compact MEMS, which is increasing with every passing day. Therefore, an increasing number of scientists are now opting to investigate the factors and the associated mechanisms that lead to stiction, friction, lubrication and wear at the micro-scale. Understanding the tribology of micron-size surfaces is critical not only for the commercialization of an astronomical spectrum of sophisticated, complex and useful MEMS prototypes but also for finding the solutions of many other basic and applied problems in the field of micro- and nano-technology [6, 23–31].

The factors that strongly influence the tribological properties of MEMS surfaces include environmental factors such as temperature, pressure and relative humidity of the operating environment and surface characteristics such as topography and chemistry of MEMS surfaces [3, 6, 13, 32]. While the environmental factors are imposed by the targeted application, the chemistry and topography of MEMS surfaces are defined by the treatments, to which, they are subjected to during and post-fabrication. While the chemistry of MEMS surfaces can be manipulated significantly, their topography can be changed only limitedly, and is mainly defined by the micromachining processes used to fabricate the MEMS. The following section will briefly describe the various micromachining processes used in the fabrication of MEMS and elaborate their influences on the characteristics of the micromachined MEMS surfaces.

1.4 Micromachining: Description and Influences on MEMS Surface Characteristics

The three processes that constitute the realm of micromachining are Deposition, Lithography and Etching. They are usually used in conjunction with Wafer Bonding and Chemical Mechanical Planarization (CMP) to enable fabrication of extremely complex structures, which have useful applications in a wide variety of fields. Each of the above mentioned five processes are known to have a strong influence on the characteristics of MEMS surfaces [3, 32, 33].

1.4.1 Deposition

Deposition, which is one of the three key processes used in micromachining, is used to deposit structural, sacrificial or protective films of different thicknesses and different materials. The three most commonly used deposition processes are the chemical vapor deposition (CVD) process, the ion beam sputtering (IBS) process and the thermal oxidation process [30, 31, 34–36]. Examples of deposited structural films include metallic copper films, which are deposited using ISB and poly-crystalline silicon (polysilicon) films, which are deposited using CVD [3, 30, 31, 36]. Examples of sacrificial films include metal oxide and silicon oxide films, which are generally grown on the substrate thermally and phosphosilicate glass (PSG) films, which are deposited using CVD [31, 34]. Examples of deposited films that are used as protective, lubricating or surface modifying layers in MEMS include films of organic precursors such as octadecyltrichlorosilane (OTS), which are deposited using either a vapor phase process such as CVD or a solution phase process [30, 31, 35, 37, 38].

The parameters of the deposition process as well as that of the subsequent annealing process strongly influence the structural characteristics of the deposited films such as the type, size, shape and arrangement of its crystals [3, 36]. These structural

characteristics, in turn, define the surface characteristics such as texture, topography and roughness of the surfaces of the deposited films [3, 36]. The same structural characteristics also define some of the mechanical properties such as the Young's modulus of the deposited films, the residual stress in the deposited films and the residual stress gradient across the thicknesses of the deposited films [39, 40]. These mechanical properties, in turn, determine the usefulness of the deposited films in addition to determining their mechanical strength and wear properties [39, 40].

1.4.2 Lithography

Lithography is the second key process used in micromachining. It is an essential component of all the micromachining techniques and is required in the fabrication of every MEMS device [7, 41]. It is used to define the in-plane shapes of the various components of a MEMS device [7, 41]. It consists of a series of steps, which begins with, coating of the layer that is to be patterned with a film of radiation sensitive material (resist). Next, the resist layer is exposed to a radiation of specific wavelength, through a pattern (mask). Exposure to radiation makes the exposed regions of the resist layer either soluble or insoluble in the corresponding developing solution. Finally, the soluble portions of the resist layer are dissolved in the corresponding developing solution and the corresponding regions on the underlying substrate are exposed for etching [7, 41–46]. All the steps involved in lithography significantly affect the final shape of the components of a MEMS device and the surface topography of their sidewall surfaces. An under/over exposed resist layer, an under/over developed resist layer and a non-uniform resist layer can all lead to formation of irregularities on the sidewall surfaces of a MEMS device.

1.4.3 Etching

Etching is the third key process used in micromachining. Like lithography, etching is also an essential component of all the micromachining techniques and is required in the fabrication of every MEMS device [7, 41]. It is used to define the three-dimensional geometry of a MEMS device [33, 45, 47–56]. In some cases, it is also used to release a MEMS device [45, 55, 56]. Etching processes can be broadly classified into two categories: wet etching processes and dry etching processes. Each wet as well as dry etching process can be further classified either as anisotropic or as isotropic etching process. Anisotropic wet etching of polysilicon structural layers is commonly accomplished using either aqueous potassium hydroxide (KOH) or ethylenediamine pyrocatechol (EDP), and anisotropic dry etching of polysilicon structural layers is commonly accomplished using gases such as oxygen (O_2), sulfur hexafluoride (SF_6) and C_4F_8 [33, 45, 47–56]. Isotropic dry etching of silicon and polysilicon structural layers is commonly accomplished using Xenon difluoride (XeF_2) vapors [57]. Hydrogen Fluoride (HF) vapors, Hydrofluoric acid (HF) solutions of various concentrations as well as HF solution buffered with ammonium fluoride (NH_4F) are etchants commonly used for isotropic etching of sacrificial layers [56]. In case of etchants with known etching rates, the extent of etching is usually controlled using a timed etch [55]. For etchants whose etch rates are not known precisely, an etch stop is used to terminate the etching [7, 45]. A silicon layer heavily doped with either boron or phosphorous is a commonly used etch stop [7, 45]. Silicon nitride and silicon oxide layers are other commonly used etch stops.

The type as well as the parameters of an etching process determine the mechanisms that are involved in it. Etching mechanisms vary from physical removal due to bombardment, which is a directional mechanism to chemical reactions followed by removal of the reaction products, which is either directional (e.g., selective etching of particular crystal planes) or isotropic [33, 47–55, 57–62]. Both the etching mechanism

involved as well as the environment to which the MEMS surfaces are exposed during etching strongly influence their surface characteristics. A prime example of this is the difference between the chemistry as well as the topography of in-plane surfaces, which are masked during etching, and the corresponding sidewall surfaces, which are exposed to the etching environment, of every MEMS device.

1.4.4 Wafer Bonding

Wafer bonding is a technique that is used to adhere two or more wafers together. It is almost always used with the three key micromachining processes, in the fabrication of MEMS devices. While in some applications, it is used to join two silicon substrates to provide mechanical support to, thermal isolation to, heat sink for or make electrical connections to the microfabricated devices, in other applications, it is used to create sealed chambers in the bulk-micromachined micro-valves and micro-pumps [63]. Additionally, it is also used to manufacture silicon-on-insulator (SOI) substrates, which are used to fabricate microelectronics as well as MEMS [63]. Wafer bonding is usually carried out at elevated temperatures, exposure to which, alters the physical as well as chemical characteristics of most thin film coatings, which are deposited on MEMS surfaces to improve their reliability [6, 35, 37, 64]. Therefore, depending on the thin film coating that is deposited on MEMS surfaces and the temperature at which wafer bonding is performed, wafer bonding can also significantly influence the characteristics of MEMS surfaces.

1.4.5 Chemical Mechanical Planarization (CMP)

Chemical mechanical planarization is a technique that is used to planarize or polish the in-plane surface of a wafer. It was originally used in the sub-micron circuit technology for globally planarizing the surface of the topmost layer of a substrate wafer [3]. It was first employed in MEMS micromachining for smoothing polysilicon

film surfaces, to improve the optical quality of surface micromachined mirror devices fabricated using them [3]. Presently, it is more extensively used in surface micromachining of MEMS that are fabricated using multiple structural layers [3]. The four attributes that make CMP an integral component of the micromachining technology are as follows: First, it can be used to polish and produce surfaces that can be used in optical applications. Second, it can be used in surface micromachining of MEMS that are fabricated using multiple structural layers to reduce polysilicon film-to-film mechanical interference caused by topography introduced during the process flow. Third, it can be used in surface micromachining of MEMS that are fabricated using multiple structural layers to eliminate several fabrication issues related to photolithography and film definition. Fourth, it enables monolithic integration of electronic components and surface micromachined structures [3]. While CMP has no influence on the characteristics of sidewall surfaces, by definition, it strongly influences the characteristics of in-plane surfaces.

It is clear from the discussion in this section that each of the five processes discussed here, which are either essential or extremely useful components of the micromachining technology, significantly influence the performance and reliability of MEMS devices through the surface characteristics of their contacting surfaces [32]. Fairly complex microstructures are fabricated by performing several rounds of the deposition-lithography-etching cycle in conjunction with CMP. Leveraging the mature infrastructure for deposition, lithography and etching from the IC industry, the micromachining technology has rapidly expanded and branched into three major branches, namely, the LIGA process, Bulk micromachining and Surface micromachining. For the sake of completeness, a brief description of all the three micromachining techniques is provided in the following sections.

1.4.6 The LIGA Process

LIGA is a German acronym for **L**ithographie, **G**alvanoformung (electrodeposition) und **A**bformung (molding). The LIGA process was developed in the 1980's for the mass production of microstructures with high aspect ratios, since those could not be fabricated using the other two micromachining techniques [42]. It employs the combination of X-ray lithography, electroforming and molding to fabricate microstructures and can be used to fabricate a wide variety of high aspect ratio microstructures. It enables fabrication of three dimensional microstructures, which have arbitrary lateral shapes, lateral dimensions of few micrometers and structural heights of several hundred micrometers [46]. It allows usage of any metal or alloy as the structural layer since in principle all metals and alloys can be electroplated [42]. Additionally, it can also be used to fabricate microstructures using ceramic as well as plastic structural layers [46]. Titanium and SiO₂, which can be easily etched using HF solution, are commonly used as the sacrificial layers in the microstructures fabricated using the LIGA process [42, 46].

1.4.7 Bulk Micromachining

Bulk micromachining is a technique, using which, microstructures are fabricated in the silicon substrate itself, rather than on top of it. Consequently, the technique is also known as substrate micromachining [41]. It was developed in the 1960's. It can be used to fabricate both stationary structures as well as structures that can move with respect to the frame of the substrate [7, 45]. A useful advantage of bulk micromachining is that since it relies on undercutting rather than sacrificial layer etching for releasing the microstructures, significantly larger gaps between the suspended free-standing structures and the substrate can be created using it than those created using the other two micromachining techniques [7, 45]. Additionally, since it

obviates the use of SiO_2 as sacrificial material, it can be used to fabricate devices that employ silica as a functional material [7, 45].

1.4.8 Surface Micromachining

Surface micromachining is a technique, which is used to fabricate microstructures above the substrate, by selectively etching the sacrificial layer sandwiched between the substrate and the deposited patterned structural film. The microstructures fabricated using the surface micromachining technique are anchored to the substrate but can move freely with respect to it. Their in-plane dimensions are defined using the lithography and the etching processes, their thickness is defined by the thickness of the deposited structural film and their offset from the substrate (i.e., gap between the top surface of the substrate and the bottom surface of the microstructures) is defined by the thickness of the deposited or grown sacrificial film. Although surface micromachining was first demonstrated in the 1960's, using deposited thin metal films, its use by the MEMS community increased significantly only after the introduction of polycrystalline silicon (polysilicon) as the structural material for MEMS, in the 1980's [3, 41]. Presently, it is the most extensively used of the three micromachining techniques [6]. It is used to fabricate static and dynamic MEMS using low-pressure chemical vapor deposited (LPCVD) polysilicon films, LPCVD silicon nitride films as well as polyimide films as structural films [6, 41]. One of the several advantages of surface micromachining is that it enables fabrication of integrated micro-systems, which couple surface micromachined sensors and actuators with integrated electronics, on the same chip [3]. Figure 1.3 is a simplified schematic illustrating the basic steps involved in surface micromachining. A brief description of the basic steps involved in the surface micromachining of polysilicon-based microstructures is also presented here to contrast them with, and impress the relative simplicity and facileness of, those involved in the surface micromachining of the microinstruments used in this study.

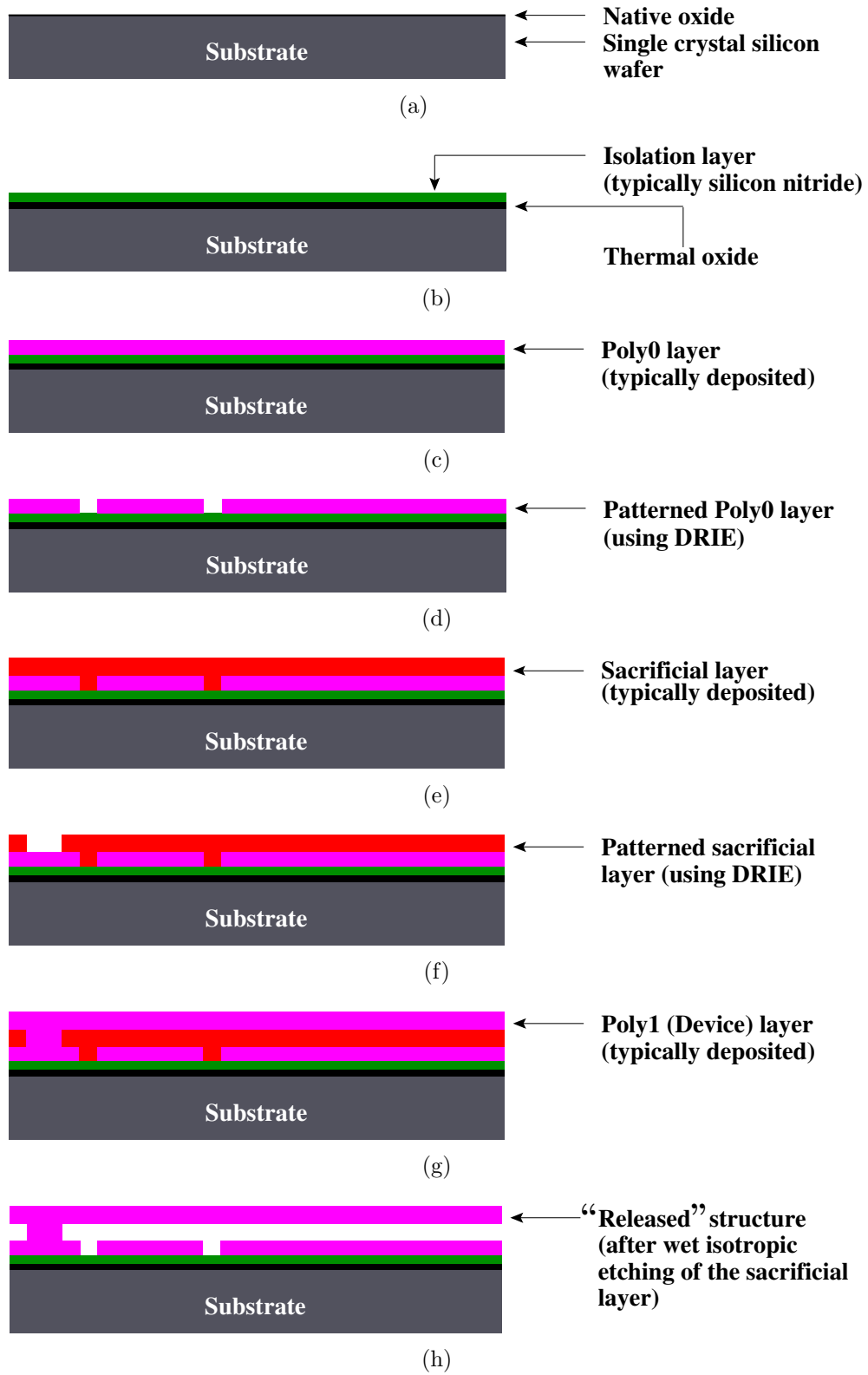


Figure 1.3: A simplified schematic illustrating the basic steps involved in surface micromachining. Notice that the “released” microstructure is a cantilever beam.

The substrate, which is used most commonly in the fabrication of polysilicon-based surface micromachined microstructures is single-crystal-silicon wafer. Surface micromachining of polysilicon-based microstructures begins with cleaning of the substrate, after which, the cleaned surfaces of the substrate are oxidized thermally. An electrical isolation layer (typically silicon nitride) is then deposited on the SiO_2 layer grown thermally on the substrate. Next, the first structural layer (typically polysilicon) “poly0” is deposited on top of the electrical isolation layer. Then, using photolithography and etching, the poly0 layer is patterned to define the ground planes as well as the actuation pads of the microstructures. After patterning the poly0 layer, a sacrificial (spacer) layer (typically silicon oxide or PSG) is deposited over it. In the next step, the sacrificial layer is also patterned using photolithography and etching, to reveal access windows to the underlying ground plane. Then, the second structural layer (typically polysilicon) “poly1” is deposited on top of the patterned sacrificial layer. Since the deposition of poly1 layer is conformal, it results in the formation of a link between the poly0 and the poly 1 layers, through the access windows etched in the sacrificial layer. This connection between the poly0 and the poly1 layers not only anchors the microstructures to the substrate but is also used to electrically ground them through the ground plane. Finally, using photolithography and etching, the microstructures, of desired designs, are defined in the poly1 layer. This step completes the surface micromachining of polysilicon-based microstructures but the microstructures do not become functional until the sacrificial layer is completely removed from underneath them, which is usually accomplished by etching the sacrificial layer using an isotropic wet chemical etching process. The suspended free-standing microstructures obtained after the complete removal of the sacrificial layer from underneath them are termed as “released” microstructures.

1.5 Reliability of MEMS: A Challenge for the MEMS Community

Commercialization of a MEMS device demands that the device should not only operate predictably and reliably in a variety of commonly encountered environments but also perform efficiently even when subjected to extreme operating conditions or put to service after a prolonged storage. Therefore, despite of having several other commercially and technically attractive attributes such as high surface area to volume ratio, small and precise size and geometry, of getting batch (parallel) processed, of getting fabricated in a high throughput, high yield process and of getting integrated with the required electronic circuitry on the same chip, most MEMS prototypes fail to be commercially viable. Their reliability issues, which take over from the point of releasing of microstructures, overshadow all the attributes that are bestowed on them by micromachining and limit the extension of benefits of those attributes only up to the point of their fabrication [16]. While usually, the commercialization of MEMS prototypes is primarily hindered by the quality concern associated with their poor reliability, in the case of MEMS prototypes, which have applications in life-critical systems such as those used in space applications and car airbags, it is primarily hindered by the safety concern, which is associated with their poor reliability in addition to the quality concern associated with it [65].

As mentioned earlier, the reliability and lifetime of a MEMS device depend on the operating environment to which it is exposed and the mode in which it is operated as well as the surface characteristics of its contacting surfaces, which in turn depend on its design, the processes used to fabricate it and the treatments to which it is subjected [32]. All of these factors have a strong influence on the magnitude of surface phenomena that ensue at interfaces between MEMS surfaces and are known to be the main causes behind the failure of most MEMS devices. The operating environment and the mode of operation of a MEMS device are defined/fixed by the targeted application but the characteristics of the surfaces of a MEMS device can be

manipulated desirably, to improve its reliability. However, in order to be able to effectively improve the reliability of MEMS devices by manipulating the characteristics of their surfaces, it is essential to know which of the characteristics of the surfaces of a MEMS device have a strong influence on the surface phenomena that ensue at interfaces between them, as well as understand why they have that strong influence. While it is known that the two characteristics of MEMS surfaces that strongly affect the magnitude of surface phenomena that ensue at interfaces between them are their topography and chemistry, the mechanisms underlying the effects of topography and chemistry of MEMS surfaces on the surface phenomena that ensue at interfaces between them are still poorly understood [31]. Therefore, improving its presently poor understanding of the effects of surface characteristics of contacting MEMS surfaces on the surface phenomena that lead to failure of MEMS is the biggest challenge currently faced by the MEMS community in improving the reliability and enabling the commercialization of most useful MEMS prototypes. A brief overview of the various phenomena that lead to failure of MEMS is provided in the following section.

1.5.1 Interfacial Forces

As the size scale shrinks from macroscopic to microscopic, the increasing ratio of surface area to volume also increases the ratio of magnitude of surface forces to that of volumetric forces. As explained earlier using the stainless steel grinding media illustration, when the characteristic dimension of an object decreases from a few centimeters to a few micrometers, its surface area and hence the associated surface forces such as capillary forces, Van der Waals (VDW) forces and electrostatic forces experienced by it, which are proportional to the square of its characteristic dimension, increase from being several orders of magnitude smaller to being several orders of magnitude larger than its volume and the associated volumetric forces such as inertial forces,

gravitational forces and electromagnetic forces experienced by it, which are proportional to the cube of its characteristic dimension, respectively [21, 28]. Therefore, in the micro-domain, the surface forces become interestingly critical and have a much greater significance and dominance than the corresponding body forces. On the other hand, due to the increasing demand for tinier, more compact and more sophisticated gadgets and leveraging the significant advances made in the field of micromachining over the last two decades, an increasing number of MEMS devices with even smaller dimensions, which range from a couple to a few thousand microns, are being developed [6, 21]. While those MEMS devices are commercially and technologically very attractive and have a wide variety of useful applications, the reduced/extremely small kinetic energies, start-up forces and torques involved in their operation, and available to overcome the retarding resistive forces experienced by them, make surface forces, which already have a high relative significance at the micro-scale, an even major threat to their reliability and lifetime [21, 66].

Depending on the operational parameters (i.e., electrostatic signals used for actuation) used, the surface characteristics of contacting surfaces (i.e., topography, surface chemistry), the material properties of contacting surfaces (i.e., Young's modulus, shear modulus, fracture strength, hardness) and the environmental properties (i.e., temperature, humidity) of the operating environment, some of the various surface forces that ensue at interfaces between the contacting surfaces of a MEMS device will have a stronger influence on the tribological properties of its contacting surfaces than others [3, 67, 68]. The various surface forces that ensue at interfaces between contacting MEMS surfaces include capillary forces, Van der Waals (VDW) forces and electrostatic forces, which are long range attractive forces and can strongly influence the tribological properties of the interface even when the two surfaces forming it are significantly apart, as well as short range interactions such as hydrogen bonds, chemical bonds and metallic bonds, which are effective only when the two surfaces forming

the interface are in close proximity [68]. Interfacial interactions originating from diffusion and alloying are generally very slow and weak at room temperature and hence do not have a significant effect on the tribological properties of contacting surfaces of MEMS operated at room temperature [68]. The following section provides an insight into the different types of interfacial forces that influence the tribological properties of MEMS interfaces.

Capillary Forces

The capillary forces that ensue at interfaces between the contacting surfaces of a MEMS device are a manifestation of the surface tension of the liquid, to which, the MEMS device is exposed during the release procedure [68]. The surface tension forces are nonexistent as long as the device is completely submerged in the liquid [36]. They begin to ensue when the upper surfaces of the device are removed from the liquid and the device is exposed to the liquid-vapor interface, and even after the released free-standing device is completely removed from the liquid, a thin layer of the liquid remains trapped between each pair of adjacent fixed and movable plates present in the device and a pressure differential known as “Laplace Pressure” (P_L) exists across both the menisci of each trapped layer of the liquid [31, 36, 69]. The Laplace Pressure across any liquid meniscus is determined using the Laplace-Young equation (i.e., Eq. 1.5.1) shown below, where, γ_l is the surface tension of the trapped liquid (with respect to air), r_1 is the radius of curvature of the liquid meniscus that is perpendicular to the two plate surfaces, between which, the liquid is trapped and r_2 is the radius of curvature of the liquid meniscus that is parallel to them [67].

$$P_L = P_1 - P_2 = \gamma_l \left(\frac{1}{r_1} - \frac{1}{r_2} \right) \quad (1.5.1)$$

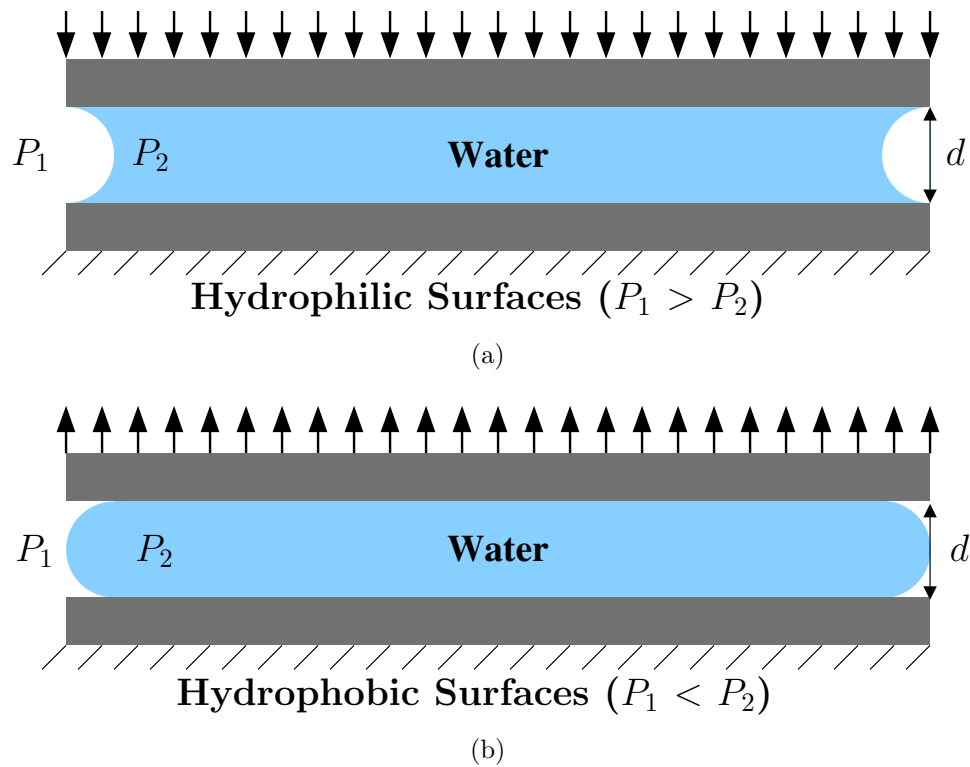


Figure 1.4: A schematic diagram exhibiting the shape of the meniscus of a liquid layer trapped between two (a) hydrophilic surfaces and (b) hydrophobic surfaces. The arrows shown in the diagram indicate the direction of the Laplace force acting on the upper (movable) plate with respect to the lower (fixed) plate.

Since the lateral dimensions of most MEMS structures are significantly larger than the spacings between them (i.e., $r_2 \gg r_1$), Eq. 1.5.1 can be reduced to Eq. 1.5.2 [67].

$$P_L = \gamma_l \left(\frac{1}{r_1} \right) \quad (1.5.2)$$

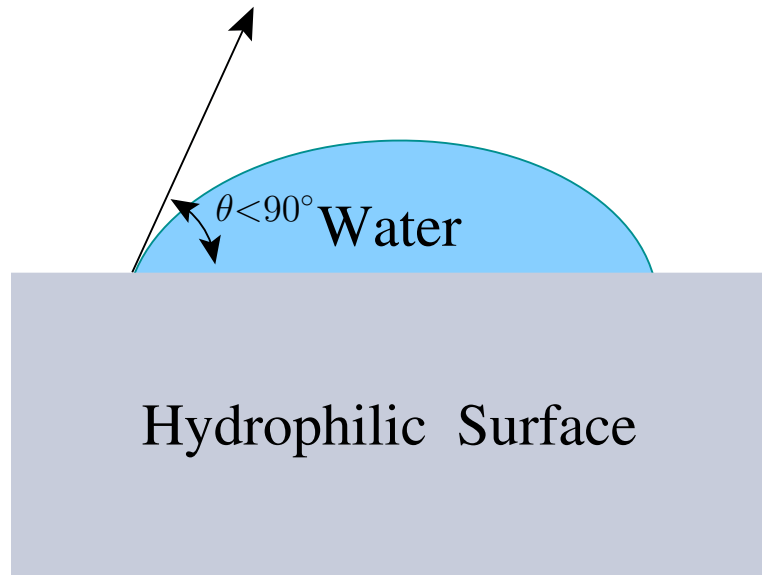
Further using Eq. 1.5.3 shown below, where, θ_1 and θ_2 are the contact angles made by the trapped liquid on the two surfaces, between which, it is trapped, and d is the distance of separation between those two surfaces, Eq. 1.5.2 can be expressed in terms of measurable quantities, as shown in Eq. 1.5.4 [67].

$$d = r_1(\cos \theta_1 + \cos \theta_2) \quad (1.5.3)$$

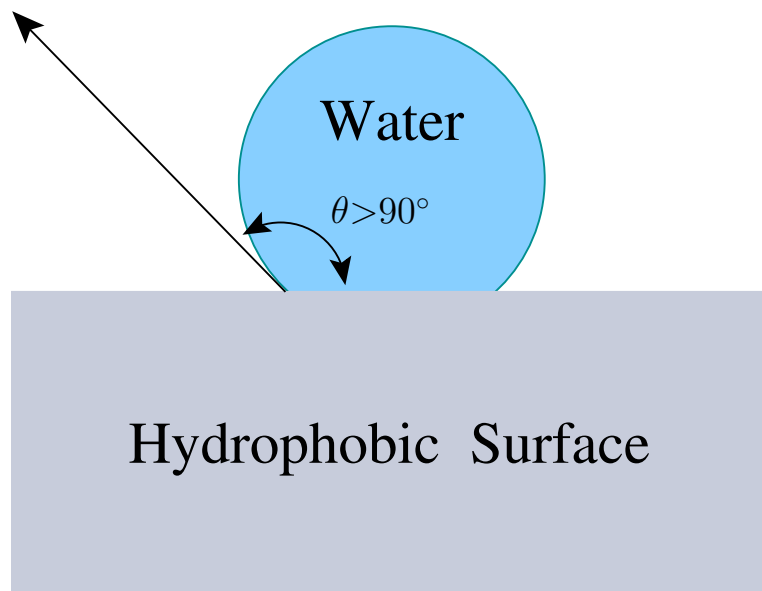
$$P_L = \gamma_l \left(\frac{1}{r_1} \right) = \gamma_l \frac{\cos \theta_1 + \cos \theta_2}{d} \quad (1.5.4)$$

Depending on the contact angles made by the trapped liquid on the surfaces of the fixed and movable plates (i.e., θ_1 and θ_2), the Laplace pressure may either pull the movable plate towards the fixed plate or push it away from it, as shown in Fig. 1.4.

Surfaces on which, the contact angle (θ) made by a droplet of water is less than 90° , are considered as hydrophilic, and those on which, it is greater than 90° are considered as hydrophobic [6]. Figure 1.5 illustrates how a droplet of water resides, and the corresponding contact angles it makes, on a hydrophilic surface as well as on a hydrophobic surface. As evident from Fig. 1.4, capillary forces can lead to failure of only those MEMS devices that have hydrophilic surfaces [68, 70]. A good example of a hydrophilic surface is a silicon surface covered with a thin layer of native oxide. Hydrophilic surfaces have high surface energies owing to the presence of free hydroxyl groups on them [67]. Additionally, they are known to adsorb from one to several monolayers of water from the ambience [68]. The water films physisorbed on hydrophilic MEMS surfaces do not desorb even when the surfaces are exposed to dry



(a)



(b)

Figure 1.5: A schematic diagram of (a) a hydrophilic surface and (b) a hydrophobic surface. Also illustrated in both the diagrams, is the definition of contact angle.

or vacuum ambients. Their complete desorption is reported to require temperatures as high as 600°C [68]. Owing to these surface characteristics, hydrophilic surfaces are always completely wetted by the solvents used in the release procedure, due to which, when a MEMS device that has hydrophilic surfaces is pulled out of the rinse liquid used in the final rinse step of the release procedure, its surfaces that are adjacent to each other experience a strong capillary force, which acts to pull them together [67]. The capillary force (F_{cp}) experienced by adjacent hydrophilic MEMS surfaces when they are pulled out from a liquid, is given by Eq. 1.5.5 shown below, where, A_l is the overlapping surface area of the two surfaces, between which, the liquid is trapped [66].

$$F_{cp} = \frac{A_l \gamma_l}{r_1} \quad (1.5.5)$$

In order to arrest the capillary pull that is exerted by the trapped layers of the rinse liquid, MEMS devices are usually subjected to drying treatments to remove the trapped rinse liquid, immediately after they are pulled out from the rinse liquid. However, while on one hand, the lowering of the vapor pressure of the rinse liquid caused by the pressure differential that exists across the menisci of the trapped rinse liquid and the concentrated soluble impurities that are dissolved in it, makes it extremely difficult to completely remove the trapped rinse liquid from the narrow gaps between adjacent hydrophilic MEMS surfaces, on the other hand, even when the trapped liquid is dried completely, the capillary pull experienced by the adjacent hydrophilic MEMS surfaces is not averted completely because liquid droplets from the ambience condense into the narrow gaps between them and continue to exert a capillary pull on them [68]. If the MEMS surfaces are extremely smooth, the capillary forces exerted on them by the condensed liquid droplets show no dependence on the partial pressure that the vapors of the condensed liquid have in the ambience. However, if they are rough, the capillary forces exerted on them by the condensed

liquid droplets show a strong exponential dependence on the partial pressure that the vapors of the condensed liquid have in the ambience [66, 71]. This is a direct consequence of the exponential dependence of the Kelvin radius (r_k) on the relative partial pressure that the vapors of the condensed liquid have in the ambience, which is illustrated by Eq. 1.5.6 shown below, where, V_l is the molar volume of the condensed liquid, R is the universal gas constant (i.e., its value is $8.314 \text{ Jmol}^{-1}\text{K}^{-1}$), T is the temperature of the ambience in $^\circ\text{K}$, p_i is the pressure inside the condensed drop of the liquid and p_o is the pressure of its vapors in the ambience [66, 71]. If the liquid is water, then the ratio p_i/p_o represents the relative humidity of the ambience [66].

$$r_k = \frac{\gamma_l V_l}{RT \ln(p_i/p_o)} \quad (1.5.6)$$

Van der Waals (VDW) forces

Van der Waals forces (F_{vdw}), which are exerted by proximate or contacting surfaces on each other, are a manifestation of the interactions that occur between the dipoles that are either present or induced in the surface atoms of those surfaces [13, 70]. Unlike capillary forces, which ensue only at interfaces formed by hydrophilic surfaces, they ensue at all interfaces irrespective of the chemistries of the surfaces forming them. They are attractive in nature, and act to bring the proximate surfaces in contact. Depending on the distance of separation between two surfaces, the VDW forces experienced by them are classified as either non-retarded (short-range) or retarded (long-range) VDW forces. If the distance of separation between the two surfaces is 20 nm or less, the VDW forces experienced by them fall in the non-retarded regime [13, 68]. The VDW forces exchanged between two surfaces can be estimated using Eqs. 1.5.7, 1.5.8a and 1.5.8b, where, H_1 and H_2 are the Hamakar constants corresponding to the retarded and non-retarded regimes respectively, for the pair of those two surfaces, h is the distance of separation between them, w and l are the

overlapping width and length of the two surfaces respectively, h_c is the hard-wall spacing between them at contact and $z(x)$ is an arbitrary function that depends on the surface topographies of the two surfaces [68]. As evident from Eqs. 1.5.7, 1.5.8a and 1.5.8b, roughness of a surface significantly complicates the estimation of VDW forces experienced by it and a mathematical function that precisely represents its topography is required to accurately estimate them.

$$F_{vdw,retarded} = - \int_0^l \frac{H_1 w}{[h - z(x)]^4} dx \quad h - z(x) > 20 \text{ nm} \quad (1.5.7)$$

$$F_{vdw,non-retarded} = - \int_0^l \frac{H_2 w}{6\pi [h - z(x)]^3} dx \quad h - z(x) > h_c \quad (1.5.8a)$$

$$= - \int_0^l \frac{H_2 w}{6\pi h_c^3} dx \quad h - z(x) \leq h_c \quad (1.5.8b)$$

Electrostatic Forces

Like the capillary and VDW forces, the electrostatic forces (F_e) experienced by proximate or contacting MEMS surfaces are also attractive in nature and act to bring them in contact. They can be induced by the release procedure induced electrostatic charging of the surfaces, the difference in the material work functions of the surfaces forming an interface or a voltage externally applied across the interface [13, 68, 70]. While the difference between the work functions of contacting MEMS surfaces usually does not exceed 1 V at equilibrium, the potential differences induced by the electrostatic charging of MEMS surfaces, at the interfaces formed by them, can be in kV range [68, 70]. MEMS surfaces can get electrostatically charged either during the etching of the sacrificial layers or during the drying of the microstructures [68, 70]. Large electric fields associated with electrostatic actuation can also result in

electrostatic charging of MEMS surfaces by causing a significant amount of charge to get trapped in the thin insulator films (i.e., silicon nitride or silicon oxide) present on them [70]. The thin physisorbed film of water present on MEMS surfaces also acts as an insulating film and traps charges [68]. Additionally, it is known that even in the absence of an externally applied electric field, charges present in the ambience accumulate on, and migrate across, the insulating films present on MEMS surfaces [13]. Electrostatic forces experienced by proximate or contacting MEMS surfaces can be estimated using Eqs. 1.5.9a and 1.5.9b, where, ϵ is the effective dielectric constant of the insulating film that is sandwiched between the two surfaces, w and l are the overlapping width and length respectively of the two surfaces, V is the potential difference across the interface formed by them, h is the distance of separation between them, $z(x)$ is an arbitrary function that depends on their surface topographies and h_c is the hard-wall spacing between them at contact [68]. Again, Eqs. 1.5.9a and 1.5.9b indicate that the roughnesses of contacting MEMS surfaces significantly complicate the accurate estimation of electrostatic forces that exist at interfaces formed by them.

$$F_e = -\frac{\epsilon w V^2}{2} \int_0^l \frac{dx}{[h - z(x)]^2} \quad h - z(x) > h_c \quad (1.5.9a)$$

$$= -\frac{\epsilon w V^2}{2} \int_0^l \frac{dx}{h_c^2} \quad h - z(x) \leq h_c \quad (1.5.9b)$$

Hydrogen Bonding

Hydrogen bonds are formed between the surface groups of two surfaces only when the distance of separation between them is extremely small. Accordingly, the attractive forces associated with hydrogen bonding are not involved in bringing MEMS surfaces together as they begin to act only after the MEMS surfaces are already in

close proximity. However, they do contribute in keeping the MEMS surfaces adhered to each other. Although, while like the VDW forces, hydrogen bonding occurs at all interfaces irrespective of the chemistries of the surfaces forming them, like the capillary forces, its contribution in the total interfacial force is significant only at interfaces formed by hydrophilic surfaces. Hydrophilic surfaces have a high density of groups that have a strong tendency to form hydrogen bonds, such as free or polarized -OH groups [13]. A completely hydrated silica surface has 5 free silanol groups per nm^2 . The strengths of most hydrogen bonds are in the range of 10-40 kJ/mol [13].

Solid Bridging

A Solid Bridge is a specific type of interfacial bond. Unlike other interfacial bonds, which are formed between the surface atoms/molecules or surface functional groups of proximate surfaces, a solid bridge cements together proximate MEMS surfaces that are separated by narrow gaps by forming a bridge of solid residue between them. The constituents of a solid bridge are the non-volatile impurities, which precipitate out of the rinse liquid when it is evaporated during the drying of microstructures [70]. Those non-volatile impurities get accumulated in the narrow gaps between proximate MEMS surfaces, and act as an adhesive, which adheres them together [70]. The non-volatile impurities, which form a solid bridge between proximate MEMS surfaces, are either present in the rinse liquid itself and directly introduced with it when it is used during the release procedure, or formed by the dissolution of particles, sacrificial films or structural films in the rinse liquid, during the release procedure [13,70]. Formation of a silica residue by the dissolution of polysilicon structural films in deionized (DI) water, which is used for rinsing during the release procedure, has been confirmed by Alley et al. using Auger electron spectroscopy [13,70]. The silica residue is formed by the reaction of oxygen dissolved in the DI water with H-terminated surfaces of polysilicon structural films that are exposed during the etching of the sacrificial

layers. Additionally, formation of fluorocarbon containing residues during the etching of silicon dioxide sacrificial layers using HF has been confirmed by Gould and Irene using *in-situ* ellipsometry and contact angle measurements [36, 40, 70]. It is difficult to estimate the adhesive strength of a solid bridge, since it depends on the amount as well as the density of the residue forming the bridge, both of which, are highly variable and very difficult to determine accurately [13, 68, 70].

In addition to the attractive interfacial forces discussed in this section, a repulsive interfacial force, which is induced by the deformation of the contacting asperities of the two surfaces forming the interface, also exists at the interface, and tries to push the two surfaces forming the interface apart from each other [13, 68]. Accordingly, the net interfacial force (i.e., attractive or repulsive) experienced by the two surfaces forming an interface is an outcome of the balance between the attractive and repulsive forces acting concomitantly on them. A plot illustrating how the more dominant interfacial forces vary with the distance of separation between the two surfaces forming the interface is shown in Fig. 1.6. The plots shown in Fig. 1.6 represent the capillary, VDW and electrostatic forces experienced by a pair of atomically smooth silicon surfaces, which are completely wetted by DI water, at room temperature. The h_c for most materials is in the range of 2 - 7 Å and specifically for atomically smooth silicon surfaces, it is 5 Å [13, 70]. The H_1 and H_2 for a system consisting of a pair of clean Si surfaces with air sandwiched between them as the dielectric are 1.8 eVnm and 1.7 eV respectively [68, 70]. For reference, the variation in the Casimir forces (i.e., vacuum energy level) experienced by a pair of atomically smooth, perfectly conducting plates with the distance of separation between them is also shown in Fig. 1.6. The Casimir forces (i.e., vacuum energy level) plotted in Fig. 1.6 are determined using Eq. 1.5.10, where, A_p is the overlapping area of the pair of plates that experience the Casimir forces, \hbar is the reduced Planck constant, c is the speed of light in vacuum and h is the distance of separation between the two plates [72]. Figure 1.6 clearly indicates that

at small separations, the dominant attractive interfacial forces are several orders of magnitude greater than the typical restoring forces that are generated in most MEMS devices.

$$F_{cas} = \frac{A_p \hbar c \pi^2}{240 h^4} \quad (1.5.10)$$

1.5.2 Stiction

Stiction, which is a term coined by the magnetic recording media industry, is used in the MEMS community to refer to unintentional and undesirable adhesion of compliant MEMS structures [73, 74]. Since MEMS structures have lateral dimensions that typically range from 50 - 500 μm and thicknesses that typically range from 0.1 - 10 μm , and are offset from the substrate typically by 0.1 - 5 μm , they have large surface-area-to-volume ratios, which as explained in section 1.3, significantly increases the influence of surface/interfacial forces on their tribological behaviour [6, 9, 32, 66, 74–77]. Particularly, the interfacial forces experienced by the proximate surfaces of a MEMS device, whose microstructures have hydrophilic surfaces, are several orders of magnitude greater than the forces required to bend and bring them in contact. In essence, the combination of the increased relative significance of the interfacial forces at the scale of MEMS devices, the compliant nature of MEMS structures and the small internal restoring forces that can be typically generated by most MEMS devices makes proximate MEMS surfaces extremely susceptible to severe stiction. Stiction is encountered by MEMS devices during the release procedure, which is classified as release stiction, as well as after it, which is classified as in-use stiction [67, 78, 79]. Practically, every MEMS device is susceptible to either release and/or in-use stiction.

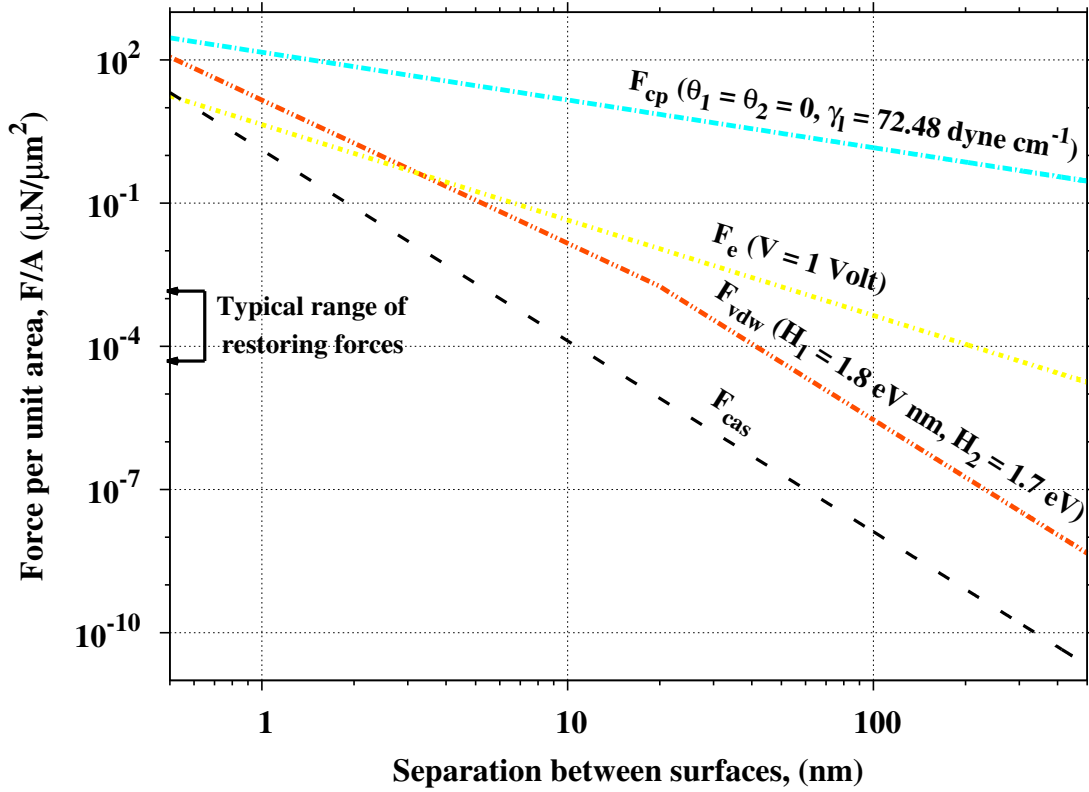


Figure 1.6: A plot illustrating how the Capillary, Van der Waals and Electrostatic forces experienced by a pair of proximate atomically smooth silicon surfaces vary with the distance of separation between them. For reference, the variation in the Casimir forces (i.e., vacuum energy level) experienced by a pair of atomically smooth, perfectly conducting plates with the distance of separation between them is also shown in the plot. Additionally, the range of magnitudes of the restoring forces that are typically generated in most MEMS devices is also indicated on the plot [66].

Release Stiction

Release stiction, which limits the yield of MEMS devices, is encountered when microstructures are dried following their release. It is usually the first reliability issue encountered with all MEMS devices. After the MEMS devices are micromachined, the sacrificial layers, which encompass their structural layers, are usually dissolved in a liquid etchant (this step is called as the release step) to render their movable microstructures free-standing (released). The released microstructures are oxidized, subjected to a series of rinsing using different solvents and finally removed from the liquid used for the final rinse, and dried. During drying, the microstructures get exposed to a liquid-vapor interface. Exposure of adjacent MEMS surfaces to the liquid-vapor interface that is created by the evaporating rinse liquid during drying induces strong capillary forces between them. The induced capillary forces act to bring the two surfaces together, in the same manner as that illustrated in Fig. 1.4a, and are usually stronger than the internal restoring forces that are generated by most MEMS devices. As the separation between the two surfaces decreases, the strength of other interfacial forces acting between them also increases, eventually causing the two surfaces to adhere permanently and result in device failure [77].

In-use Stiction

In-use stiction, which limits the lifetime and reliability of MEMS devices, occurs when during storage or normal operation, the MEMS surfaces come in close proximity of each other and experience attractive surface forces that are greater than the internal restoring forces generated by the corresponding microstructures [9, 76]. During normal operation, MEMS surfaces may come into contact either unintentionally due to overdriving electrical signals or mechanical instabilities such as excess acceleration, or intentionally such as in applications which employ MEMS devices that consist of microstructures that impact or shear against each other [11, 76]. Additionally, during

storage as well as normal operation, exposure of MEMS devices, which have components that are designed to touch each other, to environmental factors such as high relative humidity (RH) leads to the formation of liquid bridges between their proximate surfaces, which in turn, leads to the induction of strong attractive interfacial forces between the proximate surfaces [76]. Most of the engineering solutions used to address release stiction do not prevent adhesion from occurring during the operation or storage of MEMS devices, and therefore cannot be used to address in-use stiction. In-use stiction is commonly quantified by measuring the apparent work of adhesion employing cantilever beam arrays [76].

1.5.3 Friction

The contact loads experienced by most MEMS interfaces during operation are comparable to the adhesive forces existing at them [35,37,80]. Owing to the comparable magnitudes of the contact loads and the adhesive forces experienced by MEMS interfaces, and the fact that the adhesive forces existing at MEMS interfaces also act as normal loads, the total normal load experienced by a MEMS interface strongly depends on the stiction between the surfaces forming it. Consequently, the friction forces exerted by a pair of contacting MEMS surfaces on each other also show a strong dependence on the stiction between them [35,37,80]. Friction, like the stiction experienced by MEMS devices, poses a severe threat to the commercial viability of several useful MEMS prototypes. However, understandably, unlike stiction, friction affects the performance and reliability, and limits the lifetime, of only those MEMS devices, which consist of components that are designed to impact or rub against each other during operation [81]. Friction between contacting surfaces is reported to negatively impact the dynamical behaviour of MEMS actuators and result in undesirable modes of operation, if the drive signals used to actuate the MEMS actuators are not optimized [66,82]. It has also been reported to increase the power requirements and

decrease the power output as well as efficiency of MEMS actuators [66, 82]. MEMS devices, which cannot generate sufficient driving forces to overcome the friction forces experienced by their contacting components, do not function at all [81]. Additionally, in all MEMS devices that have contacting components, friction leads to wear of contacting surfaces, which eventually results in device failure [66]. Although, the friction forces experienced by contacting MEMS surfaces significantly impact both the reliability and the performance of MEMS devices that have contacting components, relatively fewer investigations to determine the factors that influence them, and study the mechanisms underlying their manifestation, have been conducted to-date [64].

1.5.4 Wear

While stiction between proximate surfaces mainly determines the reliability of MEMS devices and friction experienced by contacting surfaces mainly determines the efficiency of MEMS devices, wear of contacting surfaces mainly determines the lifetime of MEMS devices [12]. In order to leverage the highly matured infrastructure of the IC industry, MEMS devices are predominantly fabricated using silicon-based structural films. While, owing to (among other reasons) its high Young's modulus and low density, silicon (monocrystalline and polycrystalline) is a good structural material for MEMS devices that do not have contacting components, silicon-based MEMS devices that have contacting components have a very limited lifetime because silicon surfaces that contact (either intermittently such as at rotor-stator interface or continuously such as at rotor-hub interface) each other during operation exhibit severe wear even under moderate contact loads [11, 81, 83–85]. The hubs on microgears get visibly cluttered with wear debris after only a few hundred thousand cycles. MEMS devices such as microgears, linear racks, rotating platforms and pop-up mirrors, which have components that experience high shear during operation, seldom last for more than a few million cycles before the build-up of wear debris and increased friction irreversibly

binds them [11, 83]. The high wearability of MEMS surfaces that are derived from silicon-based structural films is attributed to their high roughness, which significantly reduces the real area of contact between them, and is responsible for the generation of enormous contact pressures (even at moderate contact loads) at the interfaces formed by them [11, 81, 83–85]. Although, wear of contacting surfaces is what predominantly limits the lifetime of MEMS devices, relatively fewer studies have been conducted to-date to understand the mechanisms that result in the wear of contacting MEMS surfaces.

1.5.5 Fracture and Fatigue

Although, silicon (monocrystalline and polycrystalline) is a hard and brittle material, to-date, fracture (without wear) of silicon-based components has never been reported as the cause of failure of a MEMS device. Fatigue, which is a phenomenon due to which materials subjected to alternating stresses degrade and fail pre-maturely, on the other hand, has been reported to cause pre-mature failure of silicon-based MEMS devices. For example, it is being considered as one of the possible failure mechanisms that may be responsible for the limited lifetime of Texas Instrument’s DMD [11]. Fatigue results in initiation of new flaws and/or growth of existing flaws, and limits the long-term durability of MEMS. Fatigue induced damage results in loss of stiffness, which degrades the performance of MEMS devices such as filters and other timing critical MEMS devices as well as MEMS sensors such as accelerometers that rely on the invariance of the compliance of microstructures. Given the unsusceptibility of bulk silicon to stress-corrosion cracking (at measurable rates) in water or moist air, the ideal brittle nature of silicon due to its low dislocation mobility, the limited fracture toughness of silicon-based structural films and the apparent absence of extrinsic toughening mechanisms in the popular types of silicon-based structural films produced using Low Pressure Chemical Vapor Deposition (LPCVD), one would

expect to not observe cyclic fatigue in the thin structural films that are derived from silicon. However, the thin silicon films that are used as structural layers in MEMS are observed to be susceptible to both fatigue crack initiation as well as fatigue crack growth in moist air [86–92].

Chapter 2

Previous Studies: A Review

2.1 Stiction

The term “stiction” is used by the MEMS community to refer to the deleterious effects associated with adhesion, and the associated static friction, experienced by MEMS components [6]. While stiction between proximate surfaces itself causes the failure of the majority of MEMS prototypes, the two surface phenomena that cause the failure of most of the remaining MEMS prototypes, namely the friction experienced by, as well as wear of, contacting MEMS surfaces, also strongly depend on the stiction experienced by the contacting surfaces of those MEMS prototypes [35,37,80]. Therefore, stiction between proximate surfaces is considered as the biggest obstacle in the commercialization of MEMS prototypes, and hence, the most challenging reliability issue faced by the MEMS community. Accordingly, most of the studies conducted to-date to improve the reliability of MEMS devices have focussed on inventing strategies that can significantly reduce the stiction experienced by proximate MEMS surfaces. The following sections provide a summary of the technological advances aimed at alleviating the issue of stiction that plagues the commercialization of MEMS.

2.1.1 Release Stiction

As mentioned previously, stiction (specifically release stiction) is the first reliability issue encountered by every MEMS device. The engineering solutions developed to address the issue of release stiction involve the use of either release or drying techniques that eliminate the exposure of MEMS components to the liquid-vapor

interface, such as polymer-support ashing, dry-release methods such as hydrofluoric acid (HF) vapor etching, critical point drying (CPD) and freeze sublimation drying (FSD) [4, 56, 93, 94]. Polymer-support ashing and HF vapor etching are techniques used to release the microstructures, and critical point drying and freeze sublimation drying are techniques used following the release step, to dry the microstructures. All the engineering solutions that are commonly used to eliminate release stiction add either additional and/or non-standard processing steps to the release procedure.

Vapor HF etching is a dry-release process. It completely eliminates the possibility of released MEMS structures getting exposed to the liquid-vapor interface as well as the need of rinse cycles that are used in conventional release procedures to displace solvents, by employing a gaseous isotropic etchant for etching the sacrificial layers. Usually, the chips that are released using HF vapor etching are placed upside-down about 5 - 10 cm above a solution of conc. Hydrofluoric acid, and heated to maintain a temperature difference of about 10 - 11.5 °C between the sacrificial layers being etched and the etching solution. The sacrificial layers are etched by the HF vapors that are present in the vapor space between the etching solution and the chip being released [56, 95–97]. Polymer-support ashing is a fairly complex, wet-release process. It consists of, in addition to the steps that constitute the conventional release procedure, additional steps, which involve deposition, patterning and eventual removal of a polymer layer. The polymer-support ashing process begins with partially releasing the microstructures, which is accomplished by etching the sacrificial layer using a timed etch. Next, a thin polymer film is deposited onto the partially released microstructures. The deposited polymer film is patterned into support posts that can hold the microstructures in place when the remainder of the sacrificial layer is also etched away. Next, the sacrificial layer is completely etched away and the microstructures are pulled out of the liquid. The polymer-support posts fabricated on the microstructures prevent the proximate surfaces of the microstructures from

adhering under the influence of capillary forces, which are experienced by them when the microstructures are exposed to the liquid-vapor interface. Finally, the polymer-support posts are burned away, typically by ashing in an oxygen plasma [76,94]. The microstructures left behind after the ashing of the polymer-support posts are completely released and free-standing. It is clear from the above description that the microstructures released using the polymer-support ashing process do not experience release stiction. In other words, the polymer-support ashing process eliminates the need of using a special drying technique to avoid release stiction.

MEMS devices that are dried using either the critical point drying technique or the freeze sublimation drying technique are first released by etching their sacrificial layers using an isotropic wet etchant. After the devices are completely released, they are rinsed with a series of solvents, and finally stored (in a submerged state) under the rinse liquid that is used in the final rinse cycle until they are subjected to the drying process. If the released MEMS devices are to be dried using the critical point drying technique, then, the rinse liquid, under which they are stored, is displaced with a short-alcohol (i.e., methanol, ethanol, isopropanol). Next, the devices are carefully removed from the short alcohol solution and placed in a high-pressure chamber that is already filled with the same short-alcohol, without exposing them to the liquid-vapor interface. Next, the high-pressure chamber is sealed and the short-alcohol solution present in it is completely displaced with liquid carbon dioxide (CO_2). Following this, the chamber is, first isothermally pressurized up to a pressure greater than the critical pressure of CO_2 , and then, isobarically heated up to a temperature greater than the critical temperature of CO_2 , to transform the liquid CO_2 present in it into a supercritical fluid. After the CO_2 present in the high-pressure chamber is completely transformed into a supercritical fluid, it is slowly vented out of the chamber until the pressure of the chamber reduces to atmospheric pressure. The venting of CO_2 from the high-pressure chamber is performed isothermally to ensure that the physical state

of the CO₂ present inside the chamber never crosses the vapor-liquid line. After the high-pressure chamber is completely vented, it is opened and the dried free-standing MEMS devices are removed [93]. The freeze sublimation drying technique is very similar to the critical point drying technique. It also begins with released MEMS devices that are kept submerged under the rinse liquid used in the final rinse cycle until they are subjected to the drying process. The rinse liquid, in this case, is displaced through a series of gradual dilutions, with a solvent (i.e., t-butyl alcohol, cyclohexane, water/isopropanol mixture), which has a high solid pressure even at near room temperatures (i.e., 10 - 28 °C). Next, instead of heating, the solvent, in this case, is frozen with the released MEMS devices submerged in it, and maintained in that state until the drying process is complete. The vapor above the solidified solvent is continuously pumped away, using a vacuum pump, until the entire solid solvent is completely sublimated. This leaves behind dry free-standing MEMS devices [4,40,68]. An expected, well-known disadvantage of the freeze sublimation drying technique is that certain solvents can undergo a significant volume change when they are frozen, and in doing so, can exert a significant amount of stress on, and damage the MEMS devices submerged in them [76]. Figure 2.1 is a P-T diagram, which depicts the phase paths that are followed during the critical point drying and the freeze sublimation drying processes.

In theory, all the techniques discussed in this section should be equally effective in eliminating release stiction. However, in practice, they exhibit varied degrees of success. Additionally, the implementation of each of them is non-trivial, and requires specialized and costly equipments. Moreover, since the mechanism underlying each of them can be effective only during either the release or the drying of microstructures, all of them can only prevent release stiction. None of them have a lasting effect, which can prevent proximate device surfaces from adhering during MEMS storage or operation. In other words, none of them can prevent in-use stiction. The techniques

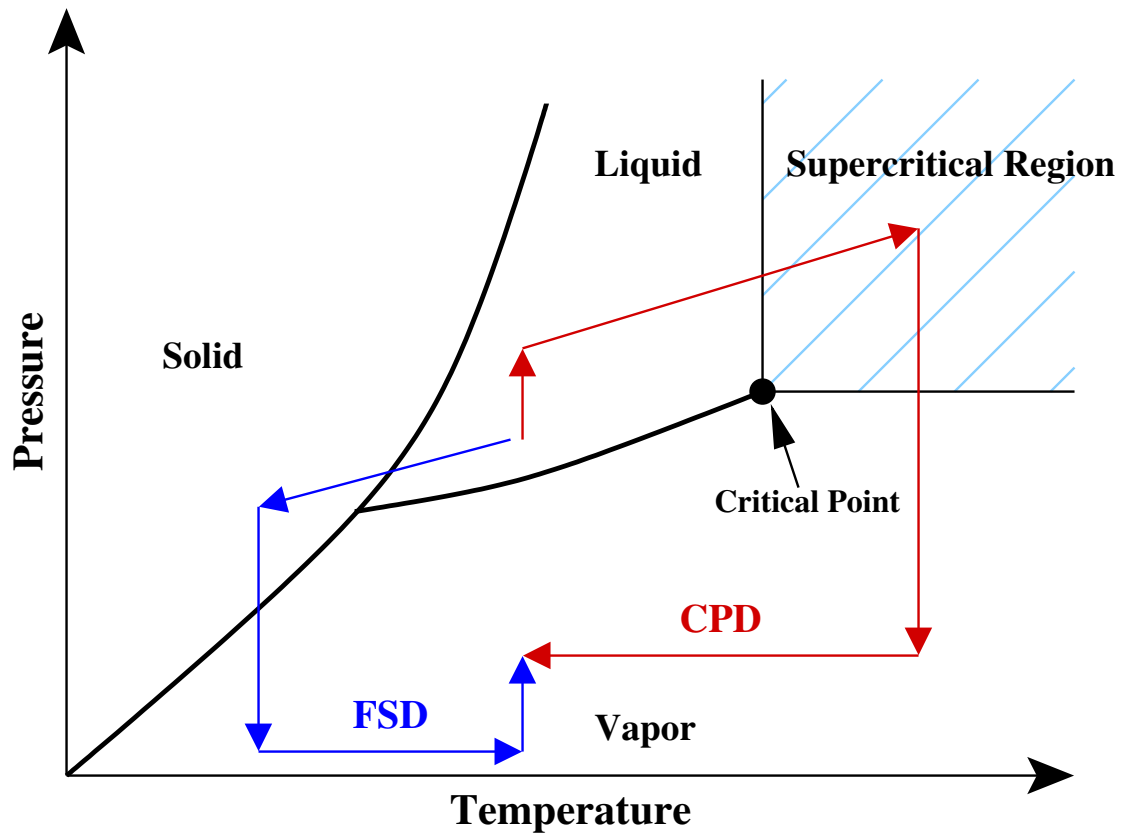


Figure 2.1: A P-T diagram depicting the phase paths followed during the critical point drying and the freeze sublimation drying processes. Notice that in both the processes, a longer phase path is intentionally followed to avoid crossing the liquid-vapor line.

that are used to address the issue of in-use stiction are discussed in greater detail in the following sections.

2.1.2 In-Use Stiction

As explained in section 2.1.1, since release stiction occurs only during the release step, most of the engineering solutions used to address it, while eliminate it with varying degrees of success, are not effective beyond the point of release of MEMS devices. Therefore, they do not address the issue of in-use stiction, which by definition, is experienced by MEMS devices after their release, either during storage or during operation. Engineering solutions that are used to address the in-use stiction experienced by MEMS devices include approaches that permanently change either the topography and/or the chemical composition of their surfaces, and have lasting effects. The approaches are broadly classified into two categories: physical modification approaches and chemical modification approaches. In the physical modification approaches, which are used to alter the topography of MEMS surfaces, microstructure surfaces are textured to reduce the area of contact of surfaces that may touch each other during storage or operation [66, 80, 98]. The various methods that are used to permanently alter the topography of MEMS surfaces are discussed in greater detail in section 2.4. The chemical modification approaches, which are used to alter the chemistry of MEMS surfaces, involve grafting of hydrophobic molecules to MEMS surfaces to alter the shape of meniscus made by water droplets on them [64, 70, 99]. They are aimed at eliminating the most prominent cause of stiction (i.e., capillary forces).

One of the first strategies investigated to address the in-use stiction experienced by MEMS devices employed a combination of both physical as well as chemical surface modification approaches [100, 101]. It involved treating the surfaces of silicon-based MEMS devices with NH_4F or HF [100, 101]. This treatment etches away the

hydrophilic native surface oxide and terminates the treated silicon surfaces with hydrogen [100, 101]. Since Si-H bond is essentially non-polar, the treated surfaces are hydrophobic in nature. Additionally, since NH_4F preferentially etches (111) crystallographic planes slower than the others, the treated surfaces also have a rougher topography, and hence, a reduced area of contact. The two factors combined together result in them experiencing a reduced in-use stiction. While this strategy is viable for MEMS encapsulated in an inert (non-oxidizing) ambient, the treatment does not have lasting effects on MEMS operated in oxidizing ambients (i.e., air). This is because the H-terminated silicon surfaces slowly re-oxidize in air, thereby leading to a recurrence of in-use stiction several weeks after the treatment [100]. Therefore, for MEMS operated in oxidizing ambients, this strategy only delays the occurrence of in-use stiction. Another strategy, which employs only the chemical modification approach, involves depositing a low surface energy plasma-polymerized fluorocarbon film on MEMS surfaces. A conformal fluorocarbon film is deposited on all the MEMS surfaces including those that are underneath the microstructures if the deposition is performed in the field-free zone of the plasma reactors used for depositing the fluorocarbon films [76, 102]. However, deposition of a thick film on the top surfaces of the microstructures is required to obtain a uniform coating on the surfaces underneath them, which, is highly undesirable, since a thick as well as unidentical coating alters the mechanical characteristics of the coated MEMS devices [103]. Also, this strategy requires the microstructures to be released using some other release process before they can be coated with the fluorocarbon film, indicating that it does not address the issue of release stiction. A more effective chemical modification approach based strategy is to deposit a hydrophobic molecular thin film on MEMS surfaces. Indeed, it has been confirmed by many research groups that self-assembled monolayers (SAMs) deposited using the solution-based process are very effective in reducing both release

as well as in-use stiction experienced by MEMS, if the coating is performed properly [13, 28, 35, 37, 64, 67, 73, 78, 80, 99, 104–107]. Tribology-related characteristics of several different SAMs are reported and compared in the literature. They will be discussed in greater detail in section 2.3.

In-use stiction is influenced by a wider spectrum of factors and has a larger time frame to occur than release stiction. Consequently, researchers have a poorer understanding of in-use stiction, and hence, have achieved lesser success in addressing the issue of in-use stiction than in addressing the issue of release stiction. This is evident from the fact that while atleast some of the engineering solutions devised to address release stiction are able to completely eliminate it, all the engineering solutions devised to address in-use stiction can at best only reduce it. Additionally, none of the several treatments used to mitigate in-use stiction address all the factors that strongly influence it. Therefore, in-use stiction still remains the focus of intense research in the MEMS community.

2.2 Friction

Friction was first studied in the late fifteenth century, by Leonardo de Vinci, who postulated that friction between two contacting surfaces is proportional to the normal load applied at their interface [108]. Later in 1699, a french engineer named Amonton reaffirmed Leonardo de Vinci's postulate and further postulated that friction between two surfaces is independent of the area of contact between them [108]. The distinction between static and dynamic friction was first made in 1781, by Coulomb, who, in addition to verifying the postulates proposed by Amonton and Leonardo de Vinci, proposed two explanations of the physics underlying the phenomena of friction [108]. One explanation suggested that the interlocking of the asperities present on the contacting surfaces is the source of friction between them while the other suggested that

the molecular adhesion between the contacting surfaces is responsible for it [108]. Owing to the observed independence of the friction experienced by contacting surfaces on the area of contact between them, initially, the former explanation was accepted and the latter was rejected [108]. However, later in the 1940's, due to the revelation of the fact that the real area of contact between surfaces is significantly lesser than the observed area of contact between them, the latter explanation was accepted and the former was rejected, since the latter explanation no more contradicted the observation that the friction experienced by contacting surfaces does not depend on the apparent area of contact between them [108]. Since then, several studies have been conducted to better understand the physics underlying the phenomena of friction, and determine the various factors that influence it.

Despite of several studies conducted to understand the mechanisms underlying the friction experienced by contacting MEMS surfaces, it still remains a relatively poorly understood tribological property. Even today, the coefficient of friction of contacting surfaces is determined using empirical models. While for materials with known mechanical properties, the plastic deformation theory may be used to estimate the coefficient of friction, for other materials, the coefficient of friction can only be determined experimentally, using Coulomb's friction model, which states that the friction force between two surfaces is proportional to the normal load applied at their interface and the constant of proportionality is their coefficient of static friction [65]. Therefore, even today, there is a need for in-depth understanding of the factors that lead to friction between contacting surfaces so that the physics underlying it can be quantified using an appropriate model. Further, most materials exhibit different friction behaviour at different scales. While the macro-scale experiments conducted using a pin-on-disc tribometer confirm that at the macro-scale the friction force exerted by most materials obeys the Amonton's law, the nano-scale experiments conducted using an atomic force microscope indicate that the friction force experienced by nanoscopic

contacts varies locally [109]. The local variations in the nano-scale friction directly correspond to the local slopes of the contacting surfaces, and are attributed to the anisotropy in their surface roughnesses, which are a direct consequence of the techniques used to prepare them [109]. Additionally, studies conducted at the micro-scale indicate that friction between microscopic contacts exhibits two regimes [109]. In one regime, it obeys the Amonton's law, and the corresponding coefficient of friction is constant and shows no dependence on the normal load applied at the contact interface, in the other regime, the coefficient of friction of contacting surfaces shows a strong dependence on the normal load applied at their interface [109]. Therefore, to better understand the mechanisms that lead to friction between contacting MEMS surfaces, the investigations should be conducted at the micro-scale, using dedicated test devices, which physically more appropriately represent the real MEMS devices.

Friction at MEMS interfaces, like stiction, is strongly influenced by the characteristics of the surfaces forming the interface. For example, the tribochemical reactions (chemical reactions induced at an interface by the rubbing of the surfaces forming the interface) between the surface molecules of contacting surfaces are reported to have a strong effect on the friction experienced by them [11]. Similarly, the native surface oxide present on MEMS surfaces is observed to have a significant influence on the friction behaviour of contacting MEMS surfaces [65]. A study, which investigated the effect of ambience on the friction force exerted by contacting MEMS surfaces on each other, reported that contacting MEMS surfaces experience less friction in air than in vacuum [65]. The study attributed the observed results to the lubricating effect of the contaminants that deposit on the contacting surfaces from the ambience, since the replenishment of contaminants, which may wear-off during sliding, is expected to be less in vacuum than in air [65]. Other studies have reported that while at higher normal loads, the friction force experienced by contacting MEMS surfaces depends only on the normal load externally applied at their interface, at lower normal loads, which

are more representative of the loads experienced by contacting MEMS surfaces during operation, it also shows a strong dependence on the stiction between them. The strong influence that stiction between contacting MEMS surfaces has on the friction experienced by them at lower normal loads is the reason why the structure of water molecules physisorbed on contacting MEMS surfaces also has a strong influence on the friction between them [32,67]. It is also the reason why friction between contacting MEMS surfaces is also strongly altered by the same factors (i.e., environmental factors such as RH, surface modifications, etc.) that alter the stiction between them. Consequently, the same surface modifications that are known to successfully address in-use stiction are used to reduce the friction experienced by contacting MEMS surfaces, to improve the reliability of MEMS devices [44]. Although past studies have revealed the various factors that influence the friction force existing at MEMS interfaces, to-date, the mechanisms underlying the influence of those factors are at best only postulated.

2.3 Self Assembled Monolayers

As mentioned in section 2.1.2, one of the most effective anti-stiction treatments employs the chemical modification approach to successfully address both release as well as in-use stiction, and involves deposition of a thin molecular film onto microstructure surfaces. The deposited molecular film is called a self-assembled monolayers (SAM) since during its deposition, the precursor molecules first attach themselves to the microstructure surfaces and then align and orient themselves with each other, thereby forming a thin film with a certain degree of order at the molecular level. The precursor molecules that are typically used to form anti-stiction SAMs on microstructure surfaces have a polar head, which chemically binds to the microstructure surface and a non-polar tail, which points away from it. Figure 2.2 is a schematic representation of a typical precursor molecule. The non-polar tails of

the precursor molecules that constitute a SAM align and orient themselves together, thereby assembling a thin surface film that consists of close-packed non-polar chains, which terminate with non-polar groups. Accordingly, the SAMs typically have a very hydrophobic surface, due to which, they are very effective in reducing stiction experienced by MEMS surfaces.

Indeed, several studies have demonstrated that SAM coatings deposited using a solution-based process successfully address several of the tribological issues that plague MEMS, if the coating process is appropriately integrated with the MEMS release process [6, 64, 80, 99, 107, 110–113]. Specifically, SAMs are reported to reverse the shape of the meniscus formed, during the drying process that follows the release process, by the liquid layer trapped between proximate microstructure surfaces. This effect, which is reported to completely eliminate release stiction, has been verified by measuring the contact angle made by water droplets on SAM-coated surfaces. Water contact angle is reported to increase from $<30^\circ$ on native oxide covered silicon surfaces to 110° on SAM-coated surfaces [6]. SAMs are reported to also reduce the in-use stiction (quantified by measuring the apparent work of adhesion using CBAs) experienced by native oxide covered silicon MEMS surfaces by four orders of magnitude [6]. Additionally, SAMs deposited on the contacting surfaces of the microengines are reported to significantly reduce the friction experienced by them. This has been qualitatively determined by monitoring the input signals (or mechanical probing) required to start the microengines [6]. Moreover, some of the SAMs can even survive the typical packaging processes (some SAMs are thermally stable up to temperatures as high as 400°C in several, including oxygen containing, environments) used in the MEMS industry [6]. This further enhances their usability for improving the reliability of MEMS devices.

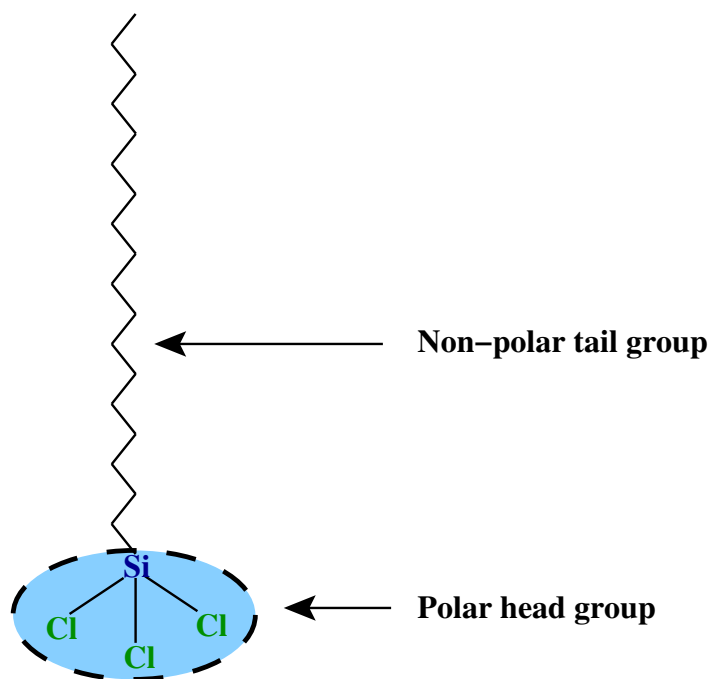
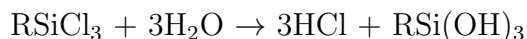


Figure 2.2: A schematic diagram of a typical precursor molecule. The non-polar tail shown in the diagram is a C_{18} hydrocarbon chain and the polar head group is a trichlorosilane molecule.

To-date, several different classes of precursor molecules have been explored for the formation of SAMs on MEMS surfaces. Examples include alkyl- and perfluoroalkyl-trichlorosilanes (R-SiCl₃), dichlorosilanes, alkane-thiols and several other classes of organic molecules. Among the various explored classes of precursor molecules, the class that is by-far the most widely used is chlorosilanes.

2.3.1 Chlorosilane Based Self-Assembled Monolayers

Coating a MEMS surface with chlorosilane-based SAMs requires the presence of free hydroxyl groups on it. Formation of chlorosilane-based SAMs is a two-step process. In the first step, which takes place in the precursor (coating) solution itself, the precursor (i.e., chlorosilane) molecules are completely hydrolyzed. For example, a trichlorosilane precursor molecule will react with three molecules of water (present in the precursor solution) and get hydrolyzed into its trisilanol form along with producing three molecules of hydrochloric acid. A balanced chemical reaction depicting the first step of trichlorosilane-based SAM formation process is shown below.



The water molecules required to hydrolyze the chlorosilane precursor molecules are usually supplied to the coating solution by exposing it to the ambient humidity (and not added to it), since the organic solvents generally used to prepare the coating solution are typically fairly hygroscopic and absorb sufficient water molecules from the ambient air. However, in order to obtain a good coating, it is necessary to ensure that while the coating is being performed, the relative humidity (RH) of the ambience is in the range of 40-70%. If the RH of the ambience is too low (i.e., <40%), then the amount of water molecules that get absorbed in the coating solution is too little to hydrolyze the entire amount of precursor molecules needed to obtain a SAM with complete surface coverage. On the other hand, if the RH of the ambience is too high (i.e., >70%), then more than required water molecules are taken up by

the solvent from the ambience. This results in bulk polymerization of the precursor molecules, in the coating solution itself, which has detrimental effects on the MEMS being coated. In the second step of the chlorosilane-based SAM formation process, the silanol forms of the precursor molecules interact with the hydrophilic surface layer, such as the native oxide layer, present on the MEMS surfaces. Typically, the hydrophilic surface layer (i.e., native oxide) present on the MEMS surfaces has a layer of water molecules physisorbed on it. Therefore, the hydrolyzed precursor molecules that interact with the MEMS surfaces orient themselves in such a way that their polar head-groups are directed towards the surface, and interact with the polar water layer present on it, while their non-polar tail-groups are isolated from the polar water layer and directed away from it. The hydrolyzed precursor molecules then diffuse along the microstructure surface and/or interact with the neighbouring hydrolyzed precursor molecules until they lock themselves in a place by cross-linking with the neighbouring hydrolyzed precursor molecules and/or the microstructure surface [114]. The cross-linking involves condensation reactions between the hydroxyl groups of the neighbouring hydrolyzed precursor molecules or the hydroxyl groups of the hydrolyzed precursor molecules and the hydroxyl groups of the hydrophilic layer present on the MEMS surface, which eliminate water and result in the formation of Si-O-Si bonds at the SAM-native oxide interface and between the precursor molecules adsorbed adjacent to each other on the microstructure surface. Although the actual mechanism of the second step of the chlorosilane-based SAM formation process is still debated in the research community, the simplified conceptual model illustrating it, shown in Fig. 2.3, is most widely accepted [115,116].

SAMs were first considered for alleviating the stiction experienced by proximate MEMS surfaces by Alley *et al.*, in the 1990's [70]. In particular, Alley *et al.* examined a SAM coating derived using octadecyltrichlorosilane (OTS) as the precursor, using arrays of polysilicon cantilever beams. They reported that the OTS SAM significantly

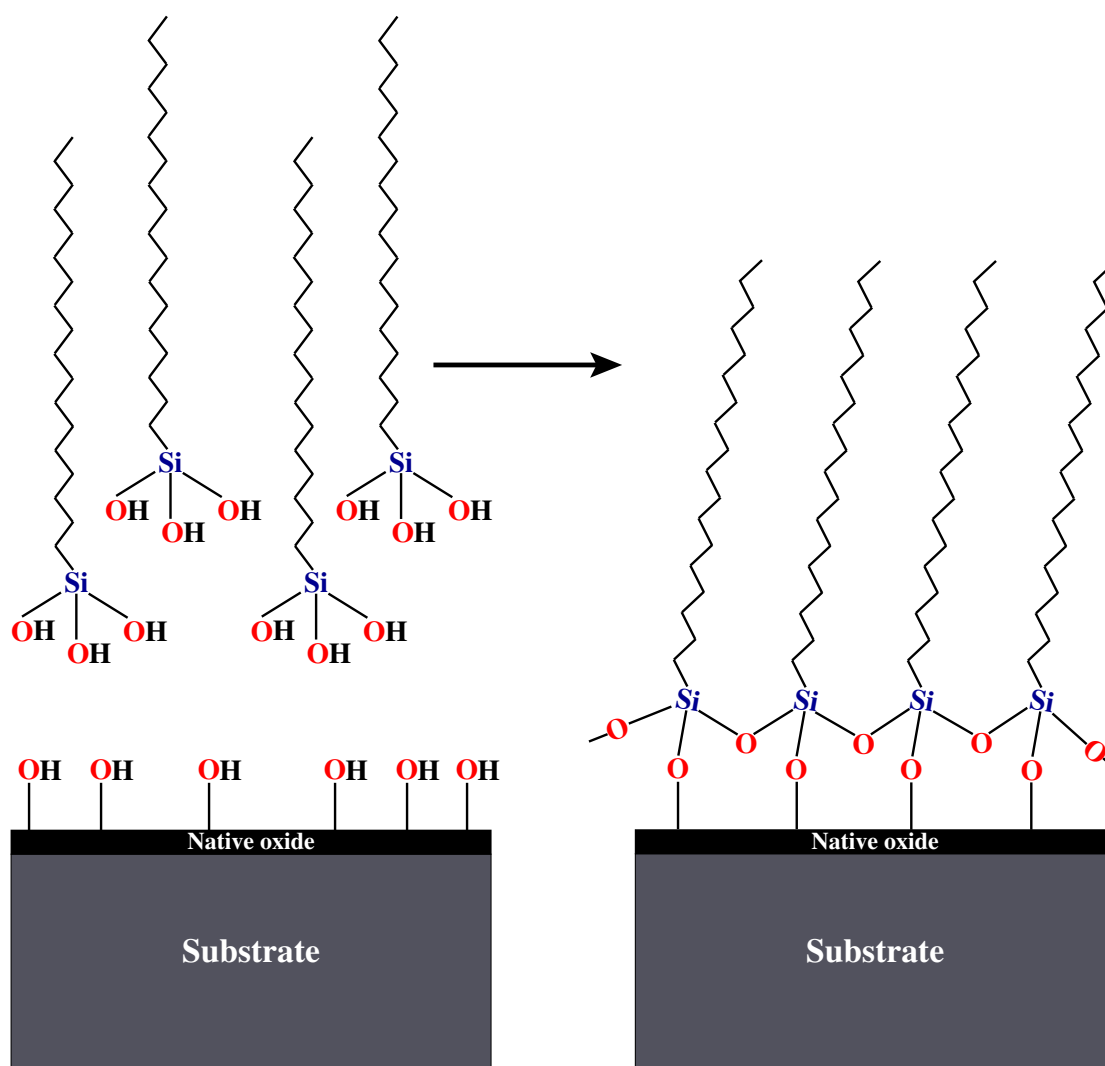


Figure 2.3: A simplified, conceptual model illustrating the second step of the chlorosilane-based SAM formation process. The first step (not shown) is the complete hydrolysis of the precursor molecules, which results in the formation of 3 HCl molecules per precursor molecule as well as the trisilanol forms (shown in this figure) of the precursor molecules. In the second step, which is shown in this figure, water elimination (condensation) reactions result in Si-O-Si linkages between the adjacent hydrolyzed precursor molecules and/or the native oxide layer present on the substrate. The precursor molecules shown in the figure are octadecyltrichlorosilane ($\text{CH}_3(\text{CH}_2)_{17}\text{SiCl}_3$) molecules.

reduced release stiction. However, they could not quantify the reduction in the release stiction due to the high stiffnesses of the cantilever beams used in their study. Based on the ability of the OTS SAM to reduce release stiction, Alley *et al.* further suggested that OTS SAM can also be an effective post-release (in-use) anti-stiction lubricant. Since then, several other research groups have investigated the effectiveness of OTS SAMs in addressing the tribological issues of MEMS. Deng *et al.* demonstrated that SAM-coated polysilicon wobble motors are less prone to release stiction and additionally their contacting surfaces have significantly improved wear properties [110, 111]. They reported that motors coated with OTS SAM operated for nearly 80 million cycles, over a period of nine months, indicating low wear and good durability of the OTS SAM present on motor surfaces that were in continuous moving contact. Also, Cléchet *et al.*, who investigated the lubricating properties of an OTS SAM coated on oxidized Si(100) surfaces using a conventional pin-on-disc tribometer, reported that the coefficient of dynamic friction, which is typically 0.6 - 0.7 for silicon surfaces with only native oxide on them, is reduced to about 0.12 when the same silicon surfaces are coated with an OTS SAM [117]. Houston *et al.* were the first to integrate the steps involved in the OTS SAM formation process with those involved in the process used to release MEMS devices [13,64]. They reported that the release stiction experienced by MEMS test devices was effectively eliminated, and the apparent work of adhesion (in-use stiction) exhibited by them was reduced by three orders of magnitude, by coating their native oxide covered surfaces with an OTS SAM [13,64].

While OTS is the most widely investigated precursor molecule, many other precursor molecules of the forms RSiCl_3 , $\text{R,R}'\text{SiCl}_2$, R_2SiCl_2 and $\text{R,R}',\text{R}''\text{SiCl}$ have also been investigated for the formation of ordered hydrophobic SAMs on oxidized silicon surfaces, where, R, R' and R'' represent distinct aliphatic hydrocarbon chains. In fact, it has been demonstrated that the most hydrophobic SAMs are those that are derived

from fluorinated alkyltrichlorosilane precursors [118]. Indeed, the critical surface tension exhibited by a 1H,1H,2H,2H-perfluorodecyltrichloro silane (FDTS) SAM (i.e., 6 mJ/m²) is significantly lesser than that exhibited by Teflon (i.e., 15 mJ/m²) and OTS SAMs (i.e., 22 mJ/m²) [119]. Therefore, a FDTS SAM coating is expected to be more effective in addressing the tribological issues of MEMS than an OTS SAM coating. Indeed, the apparent work of adhesion exhibited by the FDTS SAM coated MEMS surfaces is lower than that exhibited by the OTS SAM coated MEMS surfaces [80]. A comparison between the film properties of the most widely investigated SAMs is shown in Table 2.1 [6, 35, 64, 80, 99].

Besides the alkyl- and perfluoroalkyl- trichlorosilane precursor molecules, the dialkyldichlorosilane class of precursor molecules has also been considerably explored for the formation of SAMs on oxidized silicon surfaces. The most widely investigated dialkyldichlorosilane precursor molecule is the dimethyldichlorosilane ((CH₃)₂SiCl₂, DDMS) molecule. Several studies comparing the film properties of the DDMS SAM with those of the OTS SAM as well as their effectivenesses as anti-stiction coatings for MEMS have been reported in literature [35, 105]. While the coating processes used to deposit the DDMS and OTS SAMs are identical to each other, there are important differences in the properties of the SAMs formed. The main advantages of the DDMS SAM over the OTS SAM are its higher thermal stability in air as compared to the OTS SAM and the lesser tendency of its precursor molecules as compared to the OTS precursor molecules to polymerize in the coating solution itself. The main drawbacks of the DDMS SAM are the higher coefficient of friction and the higher apparent work of adhesion (in-use-stiction) exhibited by the DDMS SAM coated surfaces as compared to the OTS SAM coated surfaces. Other precursor molecules of the form R₂SiCl₂ that have been investigated for the formation of SAMs on oxidized silicon surfaces are dichlorodiethylsilane ((C₂H₅)₂SiCl₂, DDES) and dichlorodipropylsilane ((C₃H₇)₂SiCl₂, DDPS) [105]. Studies reported in the literature indicate that unlike

their trichlorosilane counterparts, an increase in the chain length of the symmetric dialkyldichlorosilane precursor molecules neither increases the water contact angle nor improves the anti-stiction properties of the SAMs formed using them. Moreover, the thermal stabilities (in air) of the DDES and the DDPS SAMs are inferior than that of the DDMS SAM. In essence, DDMS is clearly the most effective member of the symmetric dialkyldichlorosilane class of precursor molecules, for the formation of anti-stiction SAMs.

2.3.2 Limitations Imposed by the Chlorosilane Chemistry

While on one hand, properly formed chlorosilane-based SAM coatings are very effective in improving the tribological behaviour of the MEMS surfaces coated with them, on the other hand, their formation process has a number of limitations intrinsically related to the chemistry involved in their formation, which motivates the MEMS community to search for an alternative to replace them. Irrespective of the precursor used, the first step in the formation of any chlorosilane-based SAM is the hydrolysis of one or more Si-Cl bonds of the precursor molecules. The hydrolysis reaction generates one equivalent of HCl for each Si-Cl bond that is hydrolyzed in this step. The presence of HCl, which is formed as a by-product in the first step of the chlorosilane-based SAM formation process, in the chlorosilane-based SAM coating solution makes it corrosive for integrated MEMS devices that have exposed metallic components [10]. Therefore, integrated MEMS devices, which invariably contain metallic components, cannot be exposed to chlorosilane-based SAM coating solutions, and hence, chlorosilane-based SAMs are not a viable alternative to improve their reliability. Additionally, the formation of chlorosilane-based SAMs on MEMS surfaces requires the presence of free -OH groups on them. Therefore, the surfaces of all MEMS devices are always oxidized before coating them with a chlorosilane-based SAM. This is usually accomplished by growing a thin layer of chemical oxide (i.e., 20 Å thick)

Table 2.1: A comparison between the film properties of OTS, FDTS and oxide surface films [6, 35, 64, 80, 99].

Surface Film	Contact Angle		App. Work of Adhesion (mJ/m ²)	Coeff. of Static Friction	Thermal Stability in Air (°C)	Degree of Particulate Formation
	Water	Hexadecane				
OTS	110°	38°	0.012	0.07	225	High
FDTS	115°	68°	0.005	0.10	400	Very High
Oxide	0-30°	0-20°	20.000	1.10	-	-

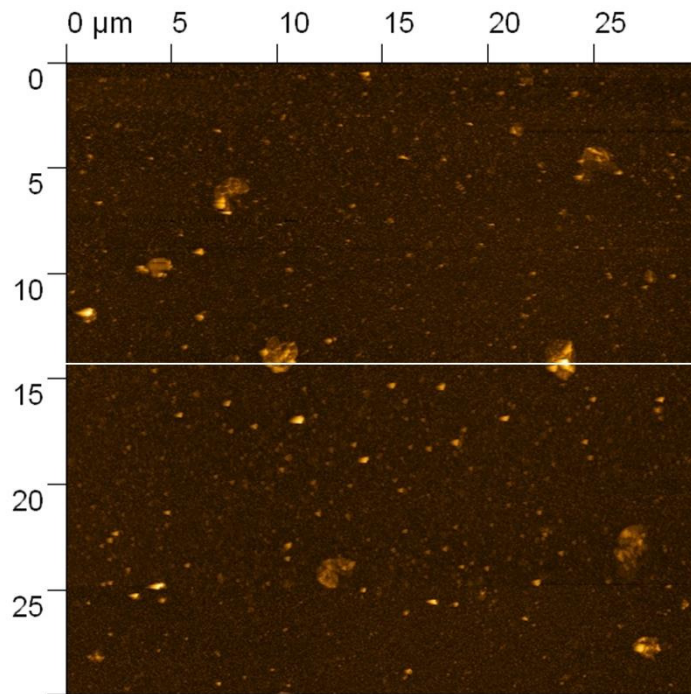
on them, by exposing the MEMS device to an oxidizing agent such as hydrogen peroxide during the release process. Since the oxide layer grown on MEMS surfaces is electrically insulating, and conformally present on all them, it is a concern in case of some MEMS devices because it can trap charges, which can lead to unpredictable performance and/or failure of those MEMS devices [113].

The ability, and the tendency of the chlorosilane (precursor) molecules to polymerize in the coating solution itself (bulk polymerization) is another limitation of the chlorosilane-based SAM formation process [107,120]. Polymerization of precursor molecules in the coating solution results in the formation of large agglomerates in it, which get deposited on the MEMS surfaces being coated during the coating process. The agglomerates (i.e, polymerized clusters of SAM precursor molecules) can be several microns in diameter, and can mechanically interfere with the operation of a MEMS device, thereby affecting its performance and reliability. Figure 2.4a is an AFM image of an OTS coated Si(100) surface, which has polymerized agglomerates of precursor molecules deposited on it [35]. The linescan shown in Fig. 2.4b confirms that some of the agglomerates visible in Fig. 2.4a are as wide as $2\ \mu\text{m}$ and as high as 490 nm. Unfortunately, presently, there is no method available to satisfactorily remove the polymerized clusters, once they are deposited on the substrate or the surfaces of microstructures. However, since the ability/tendency of the precursor molecules to polymerize stems from the presence of more than one functional groups in them, using precursor molecules that have only one Si-Cl bond reduces the likelihood of them polymerizing in the coating solution itself. This is in fact the motivation behind the exploration of precursor molecules of the form $\text{R,R}'\text{SiCl}_2$, R_2SiCl_2 and $\text{R,R}',\text{R}''\text{SiCl}$ for the formation of chlorosilane-based SAM coatings on MEMS surfaces.

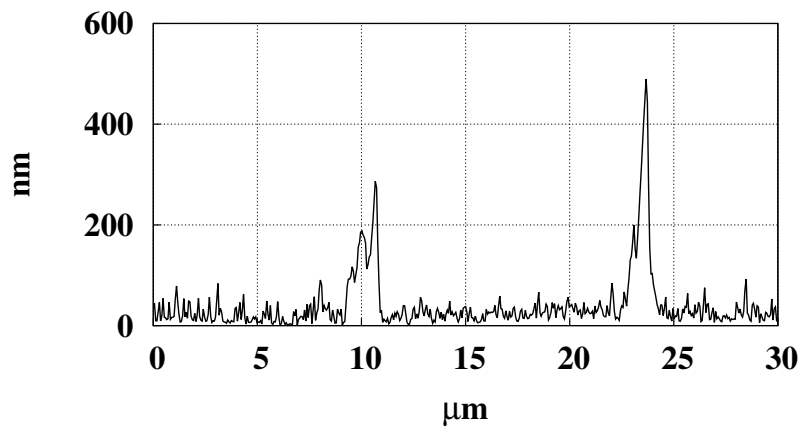
Besides the limitations discussed above, which are implicitly imposed by the chemistry of the reactions involved in the formation of the chlorosilane-based SAM coatings, the coating process is very cumbersome too. In order to obtain a good

quality chlorosilane-based SAM, the SAM coating solution must be freshly prepared and appropriately conditioned immediately before the coating is performed. This requirement is due to the sensitivity of the chlorosilane-based SAM coating solution to the ambient relative humidity and the ability/tendency of the chlorosilane precursor molecules to polymerize in the coating solution itself in the presence of excess relative humidity. As mentioned earlier, a hydrolysis step is required for the formation of the chlorosilane-based SAMs, and the water, which is a reagent, necessary for that step is made available in the chlorosilane-based SAM coating solution through mass transfer of the water vapor present in the ambient air. Therefore, it is necessary to control the relative humidity of the ambience such that while the water present in the chlorosilane-based SAM coating solution is sufficient to hydrolyze the required number of precursor molecules, it is insufficient to promote their bulk polymerization. In essence, great care and control must be exercised during the coating process to obtain a good quality chlorosilane-based SAM.

Some of the issues associated with the solution-phase process used to deposit the chlorosilane-based SAMs can be eliminated by carrying out the deposition in the vapor phase. It has been demonstrated that the tridecafluoro-1,1,2,2-tetrahydrooctyltrichlorosilane ($\text{CF}_3(\text{CF}_2)_5(\text{CH}_2)_2\text{SiCl}_3$, FOTS) SAMs deposited using the vapor-phase SAM formation process exhibit a similar apparent work of adhesion as that exhibited by the FOTS SAMs deposited using the solution-phase SAM formation process [38]. Although the vapor-phase chlorosilane-based SAM formation process does not eliminate the formation of HCl as the by-product, it reduces the threat that HCl poses to the exposed metallic components of integrated MEMS devices. The HCl generated during the vapor-phase deposition of chlorosilane-based SAMs is a gas, which does not corrode metals. Additionally, the stoichiometry of precursor and water molecules can be more precisely controlled in the vapor-phase SAM formation process. Accordingly,



(a)



(b)

Figure 2.4: (a) AFM image of an OTS coated Si(100) surface. The RMS roughness of the surface based on image statistics is 25 nm. (b) Linescan along the white line drawn across image a. Notice that some of the particulates visible in image a are as wide as 2 micron and as high as 490 nm.

the vapor-phase SAM formation process enables the suppression of the bulk polymerization of precursor molecules. Further, the vapor-phase chlorosilane-based SAM formation process eliminates the use of organic solvents, the need of freshly preparing and conditioning the SAM coating solution immediately before performing the coating and the need of controlling the relative humidity of the ambience. Accordingly, it is relatively much simpler than the corresponding solution-phase SAM formation process. Since the vapor-phase depositions of SAMs are performed in low pressure CVD-style reactors, it is possible to perform in-situ plasma cleaning of the samples before the deposition as well as in-situ measurements of the film growth during the deposition. The monitoring capability provided by the vapor-phase SAM formation process enables tuning of the process, which results in excellent process uniformity as well as reproducibility [38]. However, the vapor-phase SAM formation process also has a few drawbacks. It does not eliminate the need of an oxide layer to be present on the surfaces to be coated with the chlorosilane-based SAM. Also, it necessitates the use of an alternate process to release the microstructure before they can be coated with a SAM. Additionally, the vapor-phase SAM formation process is a feasible alternative only for those precursors that have sufficient vapor-pressures at the desired temperatures.

2.3.3 Non-Chlorosilane Based Organic Coatings

In order to eliminate the need of an oxide layer to be present on the surfaces to be coated with a SAM, several non-chlorosilane-based organic coatings have been investigated as potential surface modifications, for addressing the tribological issues of MEMS. None of those coatings require an inter-linking oxide layer. They attach alkyl chains to the silicon surface either directly or through an intermediate head group. For example, Bansal *et al.* utilized the surface reactions of alkyl-lithium (e.g., $C_{18}H_{37}Li$) and alkyl-Grignard (e.g., $C_{18}H_{37}MgBr$) with Cl-terminated Si surfaces to form densely

packed alkyl monolayers on silicon surfaces, in a two step process [6, 121]. In the first step, a H-terminated Si surface was transformed into a Cl-terminated Si surface by exposing it to a solution of PCl_5 in chlorobenzene at an elevated temperature, and in the presence of a catalytic amount of a radical initiator [121]. The second step was the surface reaction between the Cl-terminated Si surface and the chosen reagent. When an alkyl-lithium reagent was used, LiCl was eliminated, forming a direct alkyl-Si linkage. When an alkyl-Grignard reagent was used, MgBrCl was eliminated, also forming a direct alkyl-Si linkage. Bansal *et al.* characterized the $-\text{C}_{18}\text{H}_{37}$ functionalized Si surfaces by determining the asymmetric methylene stretching peaks exhibited by them using Multiple-internal-reflection Fourier-transform infrared spectroscopy (FTIR) [121]. They reported that the asymmetric methylene stretching peaks exhibited by the $-\text{C}_{18}\text{H}_{37}$ coatings obtained using both the alkyl-Li as well as the alkyl-Grignard reagents indicated the presence of highly crystalline environments of packed alkyl chains on the corresponding coated Si surfaces [121]. Zhu and co-workers have also developed a two step process, which attaches alkyl chains to a Cl-terminated silicon surface via Si-O or Si-N linkages [122–124]. In particular, they explored the surface reactions of molecules of the form R-NH₂ and R-OH with Cl-terminated Si surfaces, in vacuum as well as in a solution. Again, the first step was to produce a Cl-terminated Si surface. Zhu and co-workers obtained Cl-terminated Si surfaces by exposing the H-terminated Si surfaces to Cl₂ gas in vacuum, while simultaneously either heating them and maintaining their temperature at about 80 °C or illuminating them with a tungsten filament. The second step was the surface reaction between the Cl-terminated Si surface and the chosen precursor (i.e., R-NH₂ or R-OH). The surface reaction was accomplished either in the vapor-phase by exposing the Cl-terminated Si surface to the vaporized precursor molecules (i.e., R-NH₂ or R-OH) in vacuum or in the solution-phase by keeping the Cl-terminated Si surface in the solution that contains the desired precursor molecules. When a molecule of the form R-NH₂ is

used as the precursor, the surface reaction results in bridge bonding of the -N- of the precursor molecules to two adjacent Si atoms on the Si surface, and generation of two HCl molecules from every molecule of the precursor that is attached to the Si surface. When a molecule of the form R-OH is used as the precursor, the surface reactions result in the formation of O-Si bonds between the precursor molecules and the Si surface, and generation of one HCl molecule from every molecule of the precursor that is attached to the Si surface. Zhu and co-workers used X-ray photoelectron spectroscopy (XPS) and interfacial force microscopy (IFM) to characterize the coated Si surfaces. They reported that the films obtained using both types of precursors (i.e., R-NH₂ and R-OH) had packed alkyl chains and ordering, similar to those of the films obtained using the methods discussed earlier in this section [125].

While all the non-chlorosilane-based organic coatings discussed up to this point do seem to have a promising potential for addressing some of the tribological issues of MEMS, none of them have yet been tested on test devices that are representative of real MEMS. The only new class of non-chlorosilane-based organic coatings that has been examined using MEMS test devices is the class that is derived using alkenes as precursor molecules. The process to coat MEMS devices with alkene-based organic coatings was developed by Ashurst *et al.*, who in particular, investigated a coating derived using 1-octadecene (C₁₆H₃₃CH=CH₂) as the precursor molecule [37]. Ashurst *et al.* reported that not only are the tribological properties of an octadecene coating comparable to those of an OTS SAM, but also its formation process does not have any of the drawbacks that are inherent in the chlorosilane-based SAM formation process [37]. An alkene-based thin film is formed on the surfaces of a MEMS device by free radical mediated reactions between the precursor molecules and the H-terminated surfaces of the MEMS device [37, 106]. The H-terminated surfaces are obtained prior to keeping the MEMS device in the alkene-based coating solution, by etching away the native oxide present on the surfaces of the MEMS device using a solution of either

conc. HF or NH_4F . Accordingly, the formation of alkene-based thin film coatings on MEMS surfaces does not result in the generation of HCl as a by-product. Also, it does not require the presence of an inter-linking oxide layer on the surfaces that are to be coated. Additionally, the limited functionality of the alkene molecules limits their ability/tendency to polymerize in the coating solution itself (i.e., bulk polymerize). Indeed, surfaces coated with a 1-octadecene-based coating are reported to have fewer particulates (polymerized agglomerates of precursor molecules) deposited on them as compared to those coated with chlorosilane-based SAMs [37]. Moreover, since water does not play any role in the formation of alkene-based coatings, the coating process used to coat MEMS surfaces with alkene-based coatings is essentially insensitive to the relative humidity of the ambience. Therefore, there is no need to freshly prepare and condition an alkene-based coating solution immediately before performing the coating. In essence, the process used to form alkene-based coatings on MEMS surfaces is much simpler and robust as compared to the chlorosilane-based SAM formation process. An additional advantage in using alkene-based coatings is that they can be formed selectively only on exposed silicon surfaces by generating the radicals required for their formation using a radical initiator.

2.3.4 Issues Challenging the Viability of Self-assembled Monolayers

While reports introducing new SAMs, and confirming the effectivenesses of the already devised SAMs in addressing the tribological issues of MEMS, are abundant in literature, a relatively inadequate amount of research has been devoted to addressing the several challenges that limit the viabilities of the existing SAM coating processes [6, 35, 37, 38, 64, 67, 73, 80, 99, 102–107, 111, 113, 117, 121–127]. Although some progress has been made in improving the viabilities of the existing SAM coating processes, several basic issues remain unaddressed [6, 104]. The following sections provide a

brief introduction of the main issues that challenge the viability of self-assembled monolayers.

Reproducibility

The “portability” of the SAM coating processes between different laboratories has been an issue since the very conceptualization of the idea of SAMs [6]. While some of the research groups have been consistently reporting good quality SAM coatings, others have struggled to obtain even acceptable coatings [6]. This has been attributed to the large number of process variables involved in the SAM coating processes, which make them extremely susceptible to operator errors at many of their critical steps [6]. Indeed, recently developed SAM coating processes, which consist of fewer processing steps, are reported to be more reproducible across laboratories and operators [6]. Additionally, the advancement in technology, which has enabled process automation as well as sensing for real-time process monitoring, has also resulted in significant improvement in the reproducibility of the SAM coating processes [6]. However, the issue of “portability” of SAM coating processes is still not resolved completely [6]. While to address the issue of “portability” of SAM coating processes, the ideal process would be a novel dry (vapor-phase) SAM coating process that is designed to eliminate many of the steps required by any wet-chemistry-based SAM coating process, vapor-phase SAM formation processes have their own drawbacks, as explained in section 2.3.2.

Scale-up

Another challenging issue, which limits the viability of the SAM coating processes, is the scale-up of those processes from the scale of single dies to the scale of whole wafers, and eventually to the scale of multi-wafer cassettes [6, 104]. Presently,

most of the laboratory scale studies are conducted on $1\text{ cm} \times 1\text{ cm}$ size dies. Scaling-up the release and the SAM coating processes from the scale of individual individual dies to the scale of whole wafers and eventually to the scale of multi-wafer cassettes is an extremely challenging engineering task. The main challenges include complete displacements of the solvents from one step to the next, without exposing the MEMS devices to the liquid-vapor interface as well as without excessive use of solvents and excessive generation of the associated chemical waste [6,104]. Again, dry vapor-phase SAM formation processes would be much easier to scale-up than the wet solution-phase SAM formation processes.

Wear of Self-assembled Monolayer Coatings

The durability of the SAM coatings is also a concern [10,126,128]. All SAM coatings are essentially physically thin (i.e., typically, few nm thick), and mechanically softer than the surfaces they are deposited on. Therefore, they wear off, when the surfaces coated with them are operated under high contact loads (i.e., typically, on the order of MPa or higher) for an extended amount of time [10,126,128]. One strategy that can be used to address this issue is to deposit thicker coatings (i.e., multi-layer coatings) on the microstructures. This would ensure that the underlying microstructure surface will not get exposed even when the top layer of the coating completely wears off. In other words, the presence of multiple layers will extend the overall lifetime of the coating. For devices that are encapsulated in a sealed environment, a more beneficial strategy is to fill the vapor space above the devices with an excess amount of vaporized precursor molecules. The equilibrium between the precursor molecules present in the vapor-phase and those adsorbed on the device surfaces causes a continuous mass transfer (of the precursor molecules) from the vapor-phase onto the device surfaces, which ensures that a near-monolayer coverage of the coating is maintained on the coated surfaces for a longer time even if the coating

keeps wearing off with time. This strategy is indeed employed in the *DMD*TM, which is a commercialized MEMS device developed by Texas Instruments [10].

Undesired Electrical Properties of Self-assembled Monolayer Coatings

Depending on the electrical signals used to actuate the MEMS device, the SAM coating deposited on its surfaces may act as an insulator and lead to stiction between its contacting surfaces. The touch-mode electrostatic actuators studied by Cabuz *et al.* are a prime example of the MEMS devices, whose contacting surfaces experience severe in-use stiction due to the undesired insulating properties of the SAM deposited on them [6, 112, 113]. The contacting surfaces of an OTS SAM coated touch-mode electrostatic actuator studied by Cabuz *et al.* remained stuck even after the bias voltages applied to it were turned-off [112, 113]. Cabuz *et al.* reported that the charges trapped in the OTS SAM coating were responsible for the in-use stiction experienced by the OTS SAM coated touch-mode electrostatic actuator. Their conclusion was based on the observation that the contacting surfaces of the touch-mode electrostatic actuator, which was coated with a less insulating FDTS SAM, did not experience any in-use stiction at all [112, 113].

As evident from the discussion in this section, while every self-assembled monolayer coating has certain specific advantages, due to which, it perfectly satisfies the requirements of certain specific applications, no single self-assembled monolayer coating satisfies the requirements of all the applications. Therefore, despite the availability of a large number of monolayer coatings, no one coating can be identified as the best surface coating. Infact, the SAM-based surface modification approach itself cannot be claimed as the best approach to address all the tribological issues of MEMS.

2.4 Surface Texturing

Surface texturing was one of the first strategies devised by the MEMS community to alleviate the stiction (both release as well as in-use) experienced by proximate MEMS surfaces. The rationale behind devising a surface texturing based strategy was that it will roughen the surfaces of a MEMS device and consequently reduce the area of contact between its contacting surfaces. However, over the last two decades, the MEMS community has shown a greater inclination towards the SAM-based surface modification approaches, and very limited research has been conducted to investigate the surface texturing based surface modification approaches. To date, no study has investigated the effect of surface texturing on the friction experienced by, and the wear of, contacting MEMS surfaces, and only a few studies investigating the effectiveness of surface texturing in alleviating the (in-plane) stiction experienced by proximate MEMS surfaces have been reported in literature.

Until recently, etching using an anisotropic wet etchant such as ammonium fluoride (NH_4F) was the only method known to the MEMS community for texturing MEMS surfaces. Anisotropic wet etchants preferentially etch certain crystal facets faster than the others, and hence roughen the surfaces being etched using them. The surface texturing accomplished using anisotropic wet etchants has been reported to reduce the (in-use) stiction experienced by (in-plane) MEMS surfaces only by a moderate factor of 20 [127]. In 2006, when DelRio *et al.* studied the effect of the presence of silicon carbide (SiC) particles (diameter ranging between 20-50 nm) on polysilicon-based contacting MEMS surfaces on the (in-use, in-plane) stiction experienced by them, and reported that the deposition of nanoparticles (NPs) on contacting MEMS surfaces can significantly reduce the stiction between them, NPs emerged as a new tool that can be used to texture MEMS surfaces [27]. However, the nanoparticles that textured the MEMS test surfaces that were used in the investigations conducted by DelRio *et al.* were adventitiously formed on them (i.e., the particles were not

deposited intentionally) by a side reaction during the sacrificial layer growth, and a process to controllably deposit NPs on MEMS surfaces was not available at that time [24, 27]. Therefore, in order to be able to use NPs for texturing MEMS surfaces, a process that would deposit a conformal and uniform nanoparticle coating on MEMS surfaces was needed. The conventional drop-casting and solvent evaporation techniques were not preferred because not only they do not result in the deposition of conformal and uniform coatings but also their underlying mechanisms cause deformation of the microstructures being coated, which ultimately leads to device failure. Consequently, the unavailability of a process that could be used to deposit conformal and uniform nanoparticle coatings on MEMS surfaces delayed the use of nanoparticles for texturing MEMS surfaces till 2009. In 2009, extending the process developed by the Roberts research group at Auburn University, which precipitates metallic NPs dispersed in a solution using the gas-expanded liquid technique and deposits them as uniform, conformal, wide area thin films, Hurst *et al.* developed a novel surface texturing technique, which could be used to deposit a conformal and uniform coating of gold nanoparticles (AuNPs) on MEMS surfaces [24, 129]. The surface texturing technique developed by Hurst *et al.* was completely compatible with the techniques conventionally used to fabricate and release MEMS devices, and hence, could be easily integrated with them [24, 130]. Additionally, it enabled engineering of both the surface topography as well as the surface chemistry of MEMS surfaces, which was not possible with the other surface texturing techniques used to-date [24]. Hurst *et al.* studied the effect of texturing polysilicon-based (in-plane) MEMS surfaces using dodecanethiol-capped AuNP (precipitated from CO₂ expanded hexane) on the stiction experienced by them, and reported that the native oxide covered polysilicon-based (in-plane) MEMS surfaces exhibited a factor of 100 reduction in in-use stiction, when they were textured using AuNPs [24].

2.5 Wear

Wear, in general, shortens the lifetimes of all the MEMS devices that have contacting surfaces. The extent of wear dictates which of those devices are mechanically and/or commercially viable. While the primary mechanisms (i.e., adhesion, abrasion, corrosion, surface fatigue, deformation, impact and fretting) underlying the wear of macroscopic mechanical systems are fairly well-understood, those underlying the wear of MEMS surfaces are extremely poorly understood [32]. Therefore, all the studies that have been conducted to investigate the wear of contacting MEMS surfaces were aimed at deciphering the mechanisms that govern it. Legtenberg *et al.* studied the wear characteristics of several structural films that are commonly used in the fabrication of MEMS devices. They suggested that while asperity fracture could be the dominating mechanism underlying the wear of structural films composed of brittle materials such as diamond-like carbon (DLC), SiO₂, Si₃N₄ and single-crystal silicon (SCS), asperity deformation could be the dominating mechanism underlying the wear of polysilicon structural films [44]. In spite of two decades of research, the mechanisms that govern the wear of MEMS surfaces are still not understood satisfactorily. However, the studies conducted have revealed the various factors that influence it. In addition to the details of the mechanical contacts between their contacting surfaces, the environmental conditions, to which, the MEMS devices are exposed during operation have a strong influence on the wear of their contacting surfaces. Several studies have confirmed that the mechanism that leads to the wear of rubbing MEMS surfaces in dry air (i.e., <1% RH) is different from the mechanism that leads to the wear of rubbing MEMS surfaces in humid air [65]. The tribochemical reactions that occur at the interfaces between rubbing MEMS surfaces are also reported to have a significant influence on their wear [11]. Tanner reported that the tribochemical reactions influence both the wear rate as well as the mechanisms that lead to wear, of MEMS surfaces [11]. Patton *et al.* reported that the native oxide layer present on

microstructure surfaces acts as a lubricant, and resists the wear of rubbing MEMS surfaces [65, 131]. They additionally reported that even the contaminants that deposit on MEMS surfaces from the ambience have a lubricating effect on the rubbing MEMS surfaces [65, 131]. Their conclusions were based on the observation that rubbing MEMS surfaces exhibited greater durability in air than in vacuum [65, 131].

While a fraction of the current research addressing the issue of wear in MEMS is still focussed on understanding the fundamental causes of the wear of contacting MEMS surfaces, a significant amount of research is also devoted to searching and integrating harder materials into the micromachining processes commonly used to fabricate MEMS [6, 134–139]. Owing to its excellent performance in demanding mechanical and high temperature applications, silicon carbide (SiC) has emerged as the most promising hard material for MEMS applications [132, 133]. However, since the current infrastructure of the MEMS industry is unable to enable the usage of SiC structural films, most of the present studies that are aimed at exploring SiC for MEMS applications investigate the effectiveness of SiC thin films either deposited or grown on silicon-based MEMS surfaces [6, 134–139]. The methods commonly used for forming thin SiC coatings on silicon-based MEMS surfaces are conventional chemical vapor deposition (CVD) using separate sources for Si (i.e., SiH_4) and C (i.e., C_3H_8), reaction of buckminsterfullerene (i.e., C_{60}) with silicon and low pressure CVD pyrolysis of disilabutane ($\text{CH}_3\text{SiH}_2\text{CH}_2\text{SiH}_3$, DSB) [6, 134–139]. Of the three methods that are commonly used to form SiC thin films, the method, which involves low pressure CVD pyrolysis of disilabutane ($\text{CH}_3\text{SiH}_2\text{CH}_2\text{SiH}_3$, DSB), is the most preferred for polysilicon-based MEMS devices because not only it results in a SiC coating, which is continuous, pinhole free and conformally coated on all the surfaces of the MEMS device (including undersides), but also the coating is formed at low pressures and relatively moderate temperatures [6]. Several studies have investigated the relevant film properties of SiC thin films, and reported that the thin SiC coatings

deposited on silicon surfaces exhibit the same desirable properties as exhibited by the bulk SiC material, which include exceptional electrical properties, high corrosion resistance and most importantly, excellent tribological properties such as high wear resistance [6, 134]. The high wear resistance of the SiC thin film coatings was also reported by Sundararajan *et al.*, who determined it using an atomic force microscope (AFM), and attributed it to the higher hardness and fracture toughness of the SiC thin film coatings [140].

2.6 Fracture and Fatigue

As mentioned in section 1.5.5, fracture of the structural film has never been reported as the cause of failure of a MEMS device. However, fatigue has been reported to cause pre-mature failure of several silicon-based MEMS devices. The use of strength-based design approach for developing MEMS fails to prevent their premature failure caused by fatigue, even at stresses as low as 50% of the strength of the structural material, when they are cyclically loaded [86, 89]. Therefore, it is equally important to understand the mechanisms that cause fatigue-related failure of the structural films that are used to fabricate MEMS as it is to determine their mechanical properties, to improve the reliability of MEMS. Presently, as in the case of wear, the mechanisms that lead to fatigue-related failure of silicon-based MEMS are extremely poorly understood. Therefore, the current research that addresses the fatigue-related failures of MEMS is also focussed on understanding the mechanisms underlying them, in addition to devising solutions to suppress them [86, 90–92]. Muhlstein *et al.* recently proposed a mechanism to explain the fatigue exhibited by the silicon-based MEMS that were cyclically stressed in the presence of air [86, 90–92]. According to the mechanism proposed by Muhlstein *et al.*, which is called as the reaction-layer fatigue, subcritical environmentally-assisted cracks grow in the surface oxide (reaction) layer, which is invariably formed on the silicon surfaces that are exposed to air, until

a crack of critical length is formed in it, after which, the critical crack instantly leads to the rupture of the MEMS component. Muhlstein *et al.* additionally reported that the formation of an alkene-based monolayer film on the surfaces of a MEMS device prevents the formation of the oxide (reaction) layer on them, on exposure to air, and hence, suppresses the fatigue failure of the MEMS device [92].

Chapter 3

Motivations and Objectives

3.1 The Need of an Easy-to-fabricate, Versatile Test Platform

Over the last two decades, while on one hand, the advancements in micromachining technologies and the increasing demand for more complex, compact and sophisticated devices have prompted an increase in the development of MEMS prototypes possessing contact-mode structures, such as microrelays, stepper motors, gas bearings, micromotors and microengines, on the other hand, their poor reliability and limited lifetime have hindered their commercialization and limited their usage to laboratory-scale studies [78, 141–143]. As discussed in the previous chapters, owing to the substantially increased influence of surface forces at the micro-scale, the factors that are mainly responsible for the poor commercial viability of MEMS with contacting surfaces are surface phenomena, such as stiction, friction and wear, that govern the tribological behaviour of MEMS interfaces [78, 126, 141, 143–145]. However, despite over two decades of research encompassing the full spectrum from modeling to experimental characterization, our knowledge of the factors that influence, and the mechanisms that govern, the tribological behaviour of MEMS interfaces is still insufficient [141, 145]. Indeed, not much has been achieved in terms of addressing the tribological issues that are the major bottlenecks to the realization of the full potential of the MEMS technology, at the commercial scale. In essence, with the present state-of-the-art in MEMS technology, a comprehensive understanding of the factors that influence, and the mechanisms that govern, the tribological behaviour of MEMS interfaces and a prompt formulation and accurate evaluation of the strategies that can improve the reliability of MEMS devices are still needed.

This requires development of dedicated microinstruments, which can be used to carry out systematic investigations at the length scales representative of MEMS, since the relative significance of surface forces changes drastically with the length scale [141, 142, 144, 145]. Also, studies conducted using an atomic force microscope (AFM) investigate the tribological characteristics of only single asperity contacts while contacts between MEMS surfaces involve multiple asperities, and those conducted using a surface force apparatus (SFA) investigate the tribological characteristics of atomically smooth surfaces while contacting MEMS surfaces have finite surface roughnesses [145–147]. Further, a relatively large contribution to surface forces from the regions outside the area of direct contact as well as mixed plastic/elastic contact mechanics complicate matters even more in the case of MEMS interfaces [67, 70, 142]. Another motivation behind using MEMS devices to study tribology is that they can reveal insights that are needed to decipher the fundamental differences in the tribological behaviour of surfaces at different length scales. Many tribological effects, such as thermal activation induced reduction of friction (thermolubricity) and near-zero friction among incommensurate atomic lattices (superlubricity), that are observed at the nano-scale have never been observed at the macro-scale, which indicates that at some point during the transition from the nano-scale to the macro-scale, the characteristic tribological behaviour of surfaces changes radically [145]. MEMS devices seem to operate at length scales that are precisely in the range where this change occurs.

While the stiction and friction experienced by MEMS surfaces limit the yield and worsen the reliability of MEMS devices, the wear of contacting MEMS surfaces limits their lifetime. Therefore, it is equally important to understand the mechanisms that lead to, and determine the factors that influence, each of the three tribological characteristics (i.e., stiction, friction and wear) of MEMS interfaces. Additionally, in order to improve the reliability of MEMS devices, it is essential to also understand the

inter-play between the three prominent tribological properties (i.e., stiction, friction and wear) of MEMS interfaces. This requires that the microinstruments that are used to study each of them are fabricated on the same chip, so that, the inconsistencies associated with the uncontrollable variations in the experimental conditions can be eliminated. Further, in order to be able to accurately correlate the effects that a particular surface treatment has on the three prominent tribological properties of MEMS surfaces too, the different microinstruments that are used to investigate the effects should be fabricated on the same chip, so that, the test surfaces that will be tested using each of them will have identical surface characteristics. Therefore, there is a need to develop a versatile test platform, which could be used to systematically investigate all the more prominent tribological properties of MEMS surfaces on the same chip, so that, a meaningful and reliable correlation between the effects that a particular factor has on all of them could be established.

Historically, the test platforms that have been used to study the tribological properties of MEMS surfaces have had extremely complicated designs [6]. Additionally, their fabrications have involved extremely sophisticated fabrication processes, which were not only expensive but also time consuming [6]. However, the design of a test platform should be such that it can be easily fabricated using a facile and inexpensive fabrication scheme, in a reasonable, less amount of time. This is an important requirement because most researchers in university-scale settings are known to be usually short of the two resources, namely, time and money. Besides, this would also make the design of the test platform portable across different laboratories.

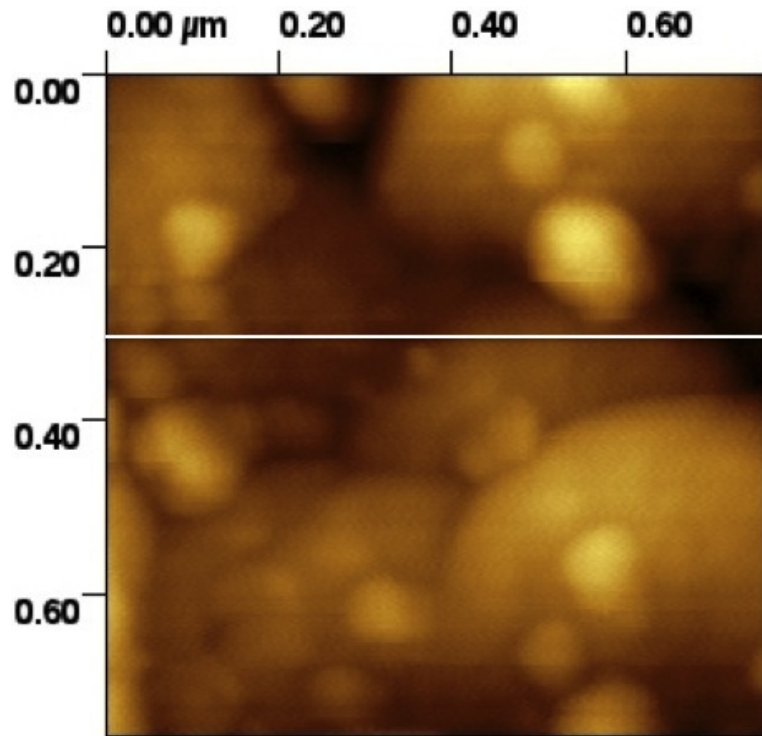
3.2 The Variation in the Material Properties of the Structural Film

Most of the MEMS test devices that have been previously used to study the tribology of MEMS interfaces were fabricated using polysilicon structural layers. It

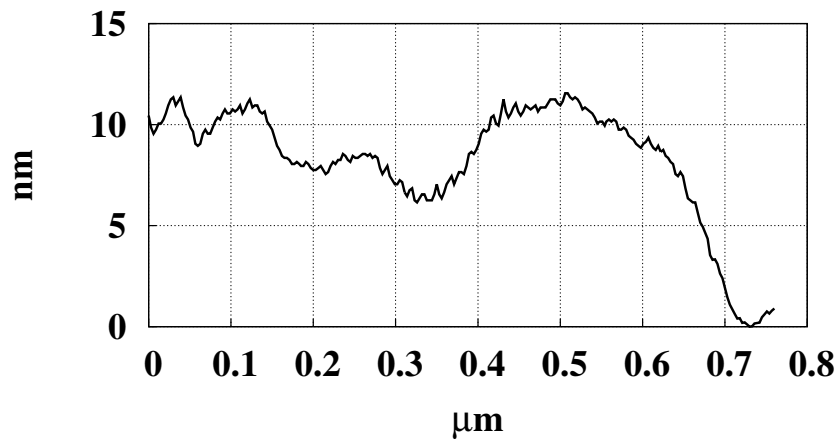
has been reported by several studies that the material properties, such as the residual stress and the elastic modulus (E), of the polysilicon structural layers as well as the stress gradient across their thicknesses are extremely sensitive to the conditions (i.e., temperature, pressure, precursor gas flow rates, etc.) used to deposit and anneal them [36, 39, 40, 148]. Consequently, they are known to vary from fabrication to fabrication, and sometimes, even from chip to chip. If the furnace used to deposit and anneal the polysilicon structural films is not tuned properly, the material properties of the polysilicon structural films vary even on the same chip [9, 149]. Since the material properties of the structural films, such as their elastic modulus, are used in the determination of the tribological properties of the test surfaces, variation in them not only limits the flexibility of the design of the test platform but also results in inconsistent and unreliable estimation of the tribological properties [23, 85, 126, 141, 143, 145, 150, 151]. It makes it impossible to compare and correlate the effects of the different surface treatments that are tested as strategies to address the tribological issues of MEMS. Therefore, a test platform should be fabricated using structural films, whose material properties do not vary at all, so that, consistent and reliable results can be obtained. Consequently, such a test platform would enable meaningful comparisons between the results obtained using different chips. This will not only allow us to establish a reliable correlation between the effects of several factors that influence the tribological characteristics of MEMS interfaces but also facilitate systematic investigations of the strategies that are proposed to improve them.

3.3 The Influence of the Multi-grain Nature of the Polysilicon Structural Films on the Topography of Polysilicon MEMS Surfaces

Since the taller asperities are the real points of contact between two surfaces, the real area of contact between them is determined by their roughnesses, material

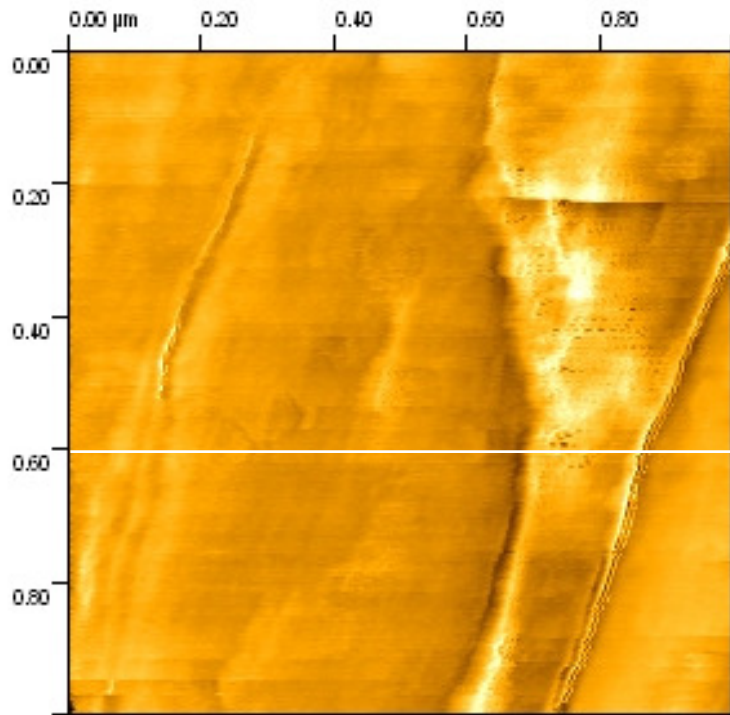


(a)

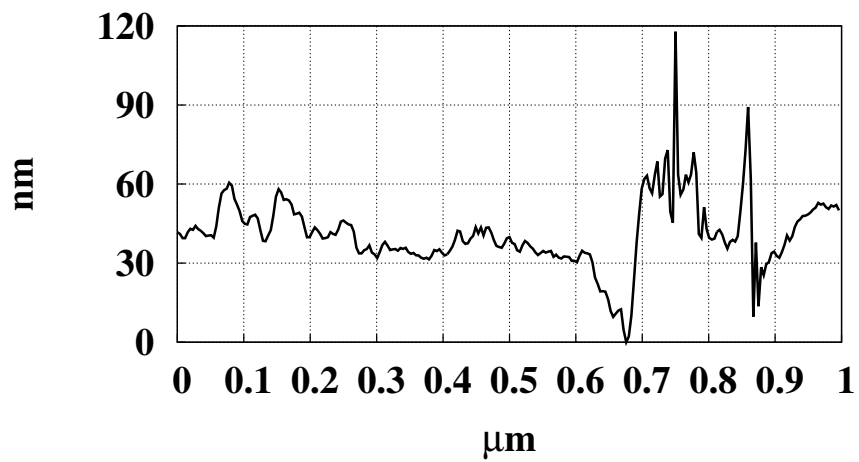


(b)

Figure 3.1: (a) An AFM image of a typical in-plane polysilicon surface. The rms roughness of the surface shown in image a is 3.71 nm. The z-scale of image a is 30.7 nm. (b) Linescan along the white line drawn across image a.



(a)



(b)

Figure 3.2: An AFM image of a typical sidewall polysilicon surface [78]. The rms roughness of the surface shown in image a is 13.8 nm. The z-scale of image a is 158.7 nm. (b) Linescan along the white line drawn across image a.

properties and the shapes of the asperities present on them. Consequently, since the topographies of the contacting surfaces have a strong influence on the area of contact between them, they also have a strong influence on the tribology of the interface formed by them [70, 148, 152]. However, as mentioned in section 2.4, very limited research has been conducted to-date to understand the effect that the surface topography of MEMS surfaces has on their tribological characteristics. Further, it has been reported that the topography of polysilicon MEMS surfaces not only depends on the processes used in the fabrication of MEMS devices but also depends on the orientations as well as the boundaries of the grains present in the structural films [78]. The AFM images of the in-plane (rms roughness is 3.71 nm) and sidewall (rms roughness is 13.8 nm) polysilicon MEMS surfaces shown in Fig. 3.1a and Fig. 3.2a, respectively, also substantiate the grain boundary and grain orientation dependence of the topography of polysilicon MEMS surfaces. The linescans shown in Fig. 3.1b and Fig. 3.2b clearly indicate that while the relative heights of the adjacent grains is the source of the topography of in-plane polysilicon surfaces, the grain boundaries are the main source of the topography of sidewall polysilicon surfaces. Owing to its dependence on the characteristics of the grains present in the structural film, the topography of polysilicon MEMS surfaces varies locally, due to which, it is more than often considered responsible for the scatter observed in the experimental results [23, 85, 126, 143, 145, 150]. Indeed, the (grain-characteristic induced) variation of the topography of MEMS test surfaces from device to device makes it really difficult to obtain a statistically significant data-set. Therefore, not only is there a need to understand the effect that the surface topography of a MEMS surface has on its tribological properties but also there is a need to develop test platforms using structural films that are not composed of multiple grains. Such a test platform will not only enable us to obtain statistically significant data-sets but also enable the

determination of the exact effects of the various surface treatments that are used as strategies to improve the reliability of MEMS devices.

3.4 Objectives of this Study

The field of MEMS undoubtedly has the potential of producing great technological innovations. However, a precise understanding of the tribological behaviour of MEMS surfaces is needed for the realization of the full potential of a variety of complex, sophisticated and extremely useful MEMS. Therefore, the main objective of this study is to enhance our overall understanding of the factors that influence the tribological characteristics of MEMS surfaces.

Specifically, the first main goal of this study is to develop a test platform, which not only overcomes the limitations of the previously reported test platforms but is also a versatile tool that can be used to systematically study the tribology of MEMS surfaces. Achieving this goal will involve designing of several different microinstruments, which will either be used to determine the material properties (i.e., residual stress, fracture strength, elastic modulus) of the structural film or be used to determine the tribological properties (i.e., work of adhesion, coefficient of friction) of the test surfaces (i.e., in-plane as well as sidewall). It will also involve devising of a single mask scheme to fabricate the designed test platform using a SOI wafer. The last part of this goal will involve formulation of the actuation schemes that will be required to actuate the various microinstruments of the developed test platform.

The second main goal of this study is to understand the effect that the surface topography of MEMS surfaces (in-plane as well as sidewall) has on the stiction and friction experienced by them. Achieving this goal will involve tailoring of the topography of the test surfaces of the test platform to obtain test surfaces with several (specifically, six) distinct surface topographies. Further, the apparent works of adhesion and the coefficients of friction (i.e., static as well as dynamic) of the various

tailored test surfaces will be determined. Finally, correlations between the surface topography of a MEMS surface and its apparent work of adhesion as well as its coefficient of static friction will be established.

Chapter 4

The Test Platform: Design, Fabrication and Actuation

4.1 Design of the Test Platform

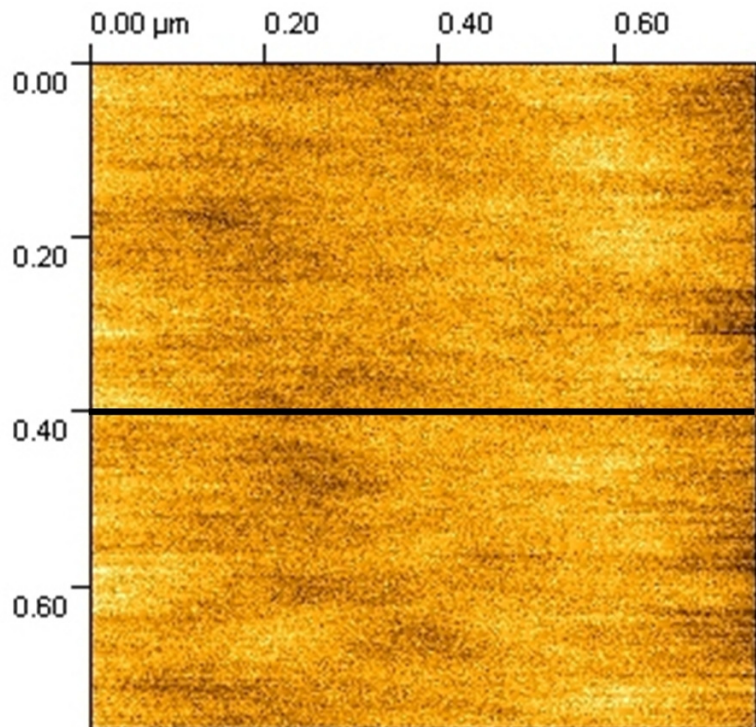
4.1.1 Structural Film

In order to address the issues of the grain-characteristic induced variation of the topography of polysilicon MEMS test surfaces and the deposition-condition induced variation of the material properties of the polysilicon structural films, I have designed a test platform that can be fabricated using a silicon-on-insulator (SOI) wafer. The SOI wafer, which is used to fabricate the microinstrument, consists of a 2 μm (nominal) thick device layer, which is a n-type Si(100) film and has a resistivity of 0.001 - 0.005 $\Omega\text{-cm}$, a 2 μm (nominal) thick sacrificial layer, which is a buried-oxide (BOX) film and a substrate, which is a 500 μm (nominal) thick n-type Si(100) wafer and has a resistivity of 0.001 - 0.005 $\Omega\text{-cm}$. Accordingly, both the substrate as well as the structural film (i.e., device layer) used to fabricate the test platform used in this study are single crystal silicon films, which do not have the polysilicon structural film-like multi-grain morphology. The absence of grain boundaries in the substrate as well as the structural film used to fabricate the test platform is substantiated by the AFM images of the in-plane (rms roughness is 0.097 nm) and sidewall surfaces (rms roughness is 6.52 nm) of the test platform, which are shown in Fig. 4.1a and Fig. 4.2a, respectively. The linescan (i.e., Fig. 4.1b) taken across the AFM image of the in-plane surface (i.e., Fig. 4.1a) clearly indicates that unlike the in-plane polysilicon surfaces, the in-plane surfaces of the test platform are extremely smooth, and exhibit a significantly small peak to valley ratio. In fact, a large fraction of this already small

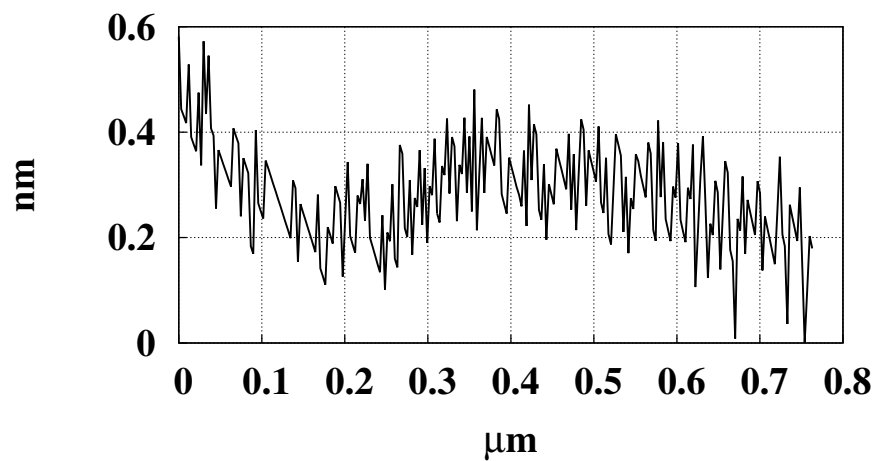
peak to valley ratio is due to the inherent noise of the AFM. Although the linescan (i.e., Fig. 4.2b) taken across the AFM image (i.e., Fig. 4.2a) of the sidewall surface of the test platform indicates that it is rougher than, and exhibits a peak to valley ratio higher than, the in-plane surface of the test platform, it must be noted that the rougher topography of the sidewall surface of the test platform is not induced by the grain boundaries, but is a consequence of the etching process used to fabricate the test platform. Further, it is a known fact that the material properties of the single crystal silicon films do not vary at all. Therefore, the use of a SOI wafer to fabricate the test platform ensures that the material properties of its structural film does not vary from chip to chip, not even from one fabricated batch to another.

4.1.2 The Layout of the Test Platform

In order to be able to systematically investigate, and establish a meaningful and reliable correlation between, the effects that a particular factor has on the different tribological properties (i.e., stiction, friction and wear) of MEMS surfaces, I have included seven different types of microinstruments in the test platform. Their dimensions are determined keeping in mind that fabricating all of them on the same chip should not cause any issues during the release of the test platform. Fabricating all the microinstruments, which are used to determine the different properties (i.e., material or tribological) of MEMS surfaces, on the same chip ensures that the test surfaces examined using each of them have identical surface characteristics, and are exposed to identical experimental conditions. Figure 4.3 is the layout of the mask used to fabricate the test platform. As seen in Fig. 4.3, the test platform is fabricated on a $1\text{ cm} \times 1\text{ cm}$ chip. All the seven different types of microinstruments that are included in the test platform are labelled in Fig. 4.3. The design, actuation procedure and modeling of each of them is discussed in greater detail in the following chapter.

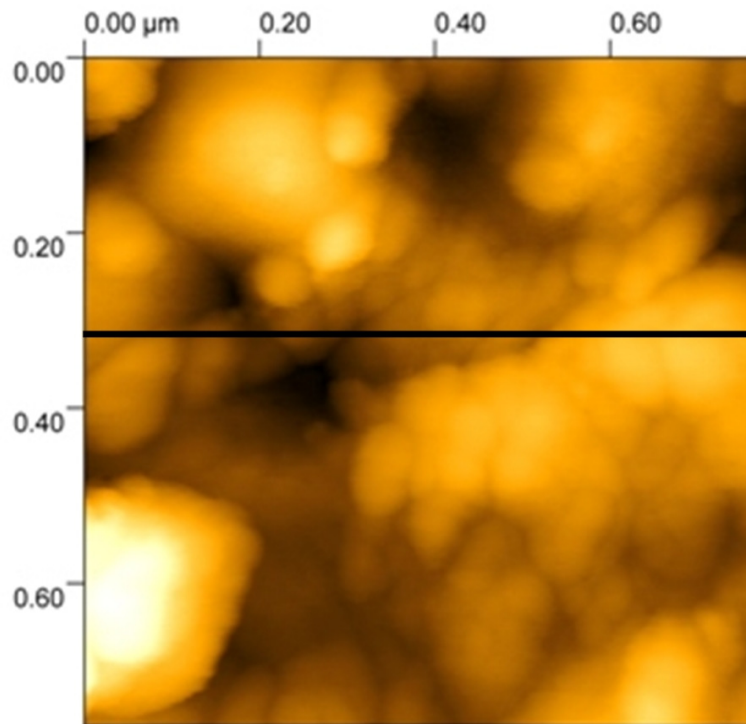


(a)

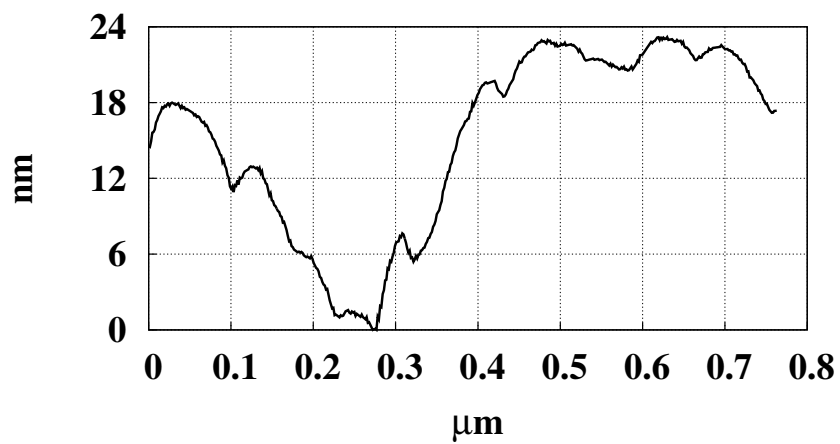


(b)

Figure 4.1: (a) An AFM image of the in-plane surface of the test platform. The rms roughness of the surface shown in image a is 0.097 nm. The z-scale of image a is 1.1 nm. (b) Linescan along the black line drawn across image a.



(a)



(b)

Figure 4.2: (a) An AFM image of the sidewall surface of the test platform. The rms roughness of the surface shown in image a is 6.52 nm. The z-scale of image a is 41.8 nm. (b) Linescan along the black line drawn across image a.

The test platform (TP) has microinstruments that can be used to determine several different material properties of the structural film. The Residual Stress Tester (RST) can be used to determine the residual stress present in a released device layer (structural film). The Mechanical Strength Tester (MST) can be used to determine the fracture strength of the device layer. The “Resonator” can be used to determine the elastic modulus of the device layer. Additionally, the test platform has a microinstrument (i.e., Cantilever Beam Array (CBA)) that can be used to study the stiction characteristics of the in-plane surfaces. Although, most of the tribological studies reported to-date have been conducted using in-plane surfaces, in devices belonging to several of the emerging classes of MEMS such as microgears and microsliders, more vertical (sidewall) surfaces come into contact during operation than horizontal (in-plane) surfaces [142]. Additionally, it is clearly evident from the AFM images shown in Fig. 4.1a and Fig. 4.2a that the in-plane and sidewall surfaces are significantly different topographically. The rms roughness of the sidewall surface shown in Fig. 4.2a is 6.52 nm, which is significantly higher than that of the single crystal silicon in-plane surface shown in Fig. 4.1a, which is 0.18 nm. Linescans (Fig. 4.1b and Fig. 4.2b) taken across the AFM images (Fig. 4.1a and Fig. 4.2a, respectively) along the white lines shown in the images further highlight the difference in the topography of in-plane and sidewall surfaces. Owing to the different processing environments, to which, the sidewall and in-plane surfaces are exposed during micromachining, they are expected to be different, both topographically as well as chemically. The sidewall surfaces are revealed using reactive ion etching (RIE), during which, they are exposed to reactive gases and high energy ions unlike the in-plane surfaces, which are protected by photoresist or other masking layers during the etching process. This results in the formation of polymer-like materials on them, due to which, they exhibit a different chemistry than the in-plane surfaces. The significantly different topographies of the sidewall and in-plane surfaces are also a consequence of the same etching process.

Since topography strongly influences the tribological behaviour of MEMS interfaces, findings of investigations carried out using in-plane interfaces are not applicable to sidewall interfaces [78, 79, 126, 142]. Therefore, microinstruments in which sidewalls form the test interface are needed to study the tribological behaviour of sidewall interfaces. The test platform developed in this study conveniently addresses this need. It has different microinstruments for studying the stiction characteristics of in-plane and sidewall surfaces. While, as mentioned before, the CBA can be used to study the stiction characteristics of the in-plane surfaces, the stiction characteristics of the sidewall surfaces can be studied using the Sidewall Beam Array (SBA). Lastly, the test platform has two different microinstruments (i.e., the Sidewall Friction Tester (SFT) and the Sidewall Friction and Adhesion Tester (SFAT)) that can be used to study the friction as well as wear characteristics of the sidewall surfaces. The purpose behind including two different microinstruments for studying the friction and wear characteristics of sidewall surfaces is to determine the influence of the geometries of the surfaces forming the contact interface on the effect of surface topography. While in the SFT, the contact interface is formed between the plane (vertical) surface of a suspended beam and the cylindrical surface of an anchored post, in the SFAT, it is formed between the plane (vertical) surfaces of two suspended shuttles.

As seen in Fig. 4.3, the test platform is designed to have multiple copies of the seven main microinstruments. The purpose behind including multiple copies of each microinstrument in the test platform is to obtain statistically significant (experimental) data-sets. Further, the copies of each microinstrument are judiciously distributed over the entire real estate of the test platform in order to determine the local variations in the experimentally obtained results. This enables the elimination of the positional bias from the experimentally obtained results. Additionally, the copies of each microinstrument are divided into two groups, which are oriented orthogonally to

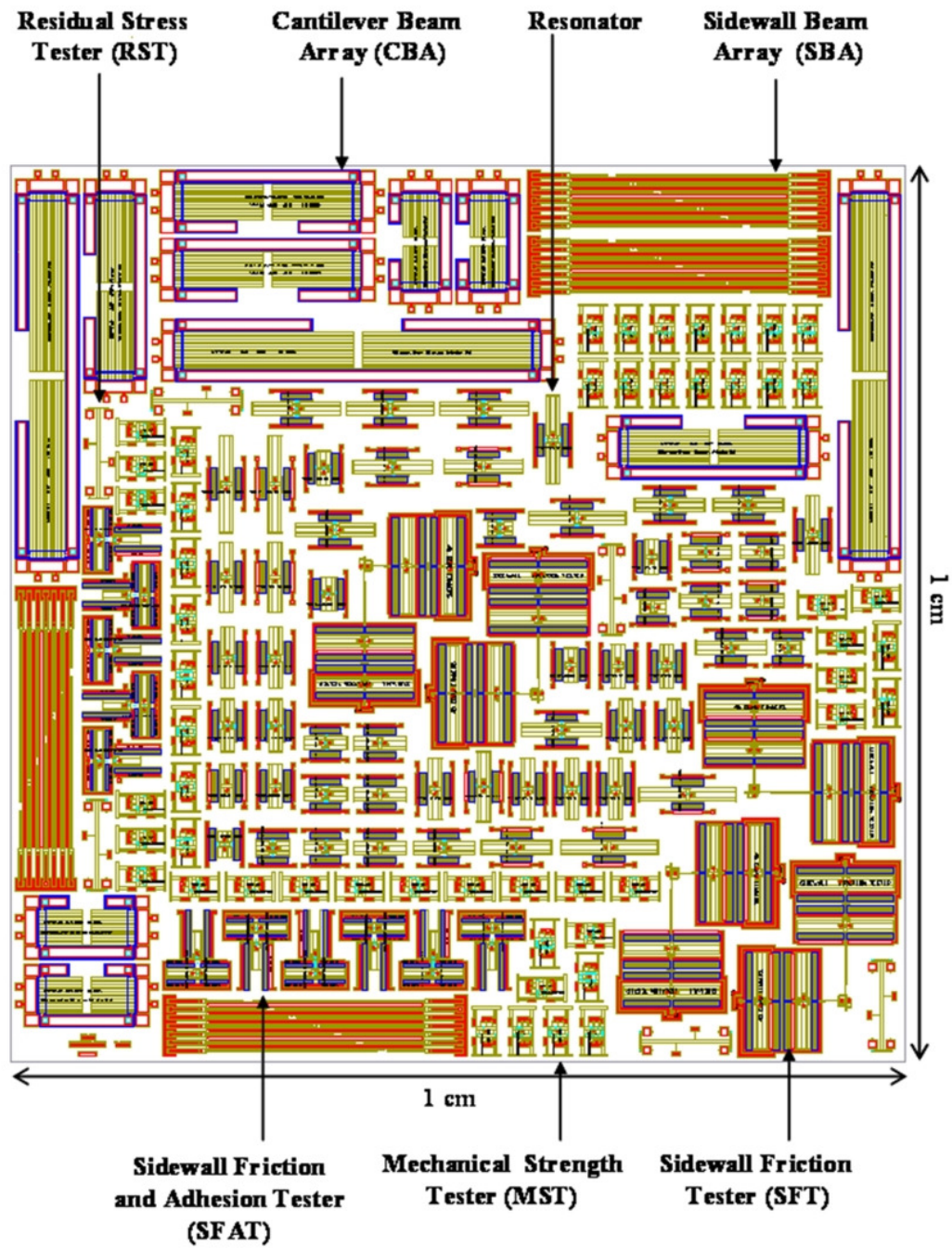


Figure 4.3: The layout of the mask used to fabricate the test platform. Notice that the test platform is fabricated on a 1 cm \times 1 cm chip. It consists of seven different types of microinstruments, all of which, are labelled in the above figure.

each other in the test platform. The purpose behind this is to determine the crystal-plane induced variations in the experimental results. Lastly, all the microinstruments of the test platform are judiciously organized in order to make the most efficient use of the total real estate area of the test platform. In summary, the test platform developed in this study (i.e., TP) is a carefully designed, versatile tool, which enables systematic and reliable studies of the tribology of MEMS interfaces.

4.2 Fabrication of the Test Platform

4.2.1 Single Mask Scheme

In order to be able to fabricate the TP using a facile, inexpensive and less time consuming fabrication process, the microinstruments are designed in such a way that they can all be fabricated in a single-mask scheme. The TP is fabricated using the standard surface micromachining tools. The fabrication process begins with cleaning of the SOI wafer using a RCA1 solution (i.e., consists of 5 parts by volume of deionized H₂O, 1 part by volume of NH₄OH and 1 part by volume of H₂O₂). The cleaned wafer is dehydrated at 120°C for about 30 min., so that, it can be primed with hexamethylenedisilazane (HMDS). Priming of the device layer with HMDS, for 10 min., ensures good adhesion between the device layer and the photoresist layer, which is used as a mask to pattern it. After priming, the device layer is spin coated with a 2 μm thick layer of positive photoresist AZ 5214 E-IR. Next, the photoresist layer is patterned by exposing it through a hard (chrome on quartz) mask, to the h-line (wavelength of the radiation is 404.7 nm) of the mercury vapor lamp and developing the exposed photoresist layer in an aqueous solution of AZ 400K for 2 min. The primary flat of the photoresist coated SOI wafer is placed at 45° to the edges of the hard mask while exposing the photoresist layer to the UV-radiation. The exposure energy used is 50 mJ/cm² and the composition of the developing solution used is one part by volume of AZ 400K in four parts by volume of deionized water. Patterning of

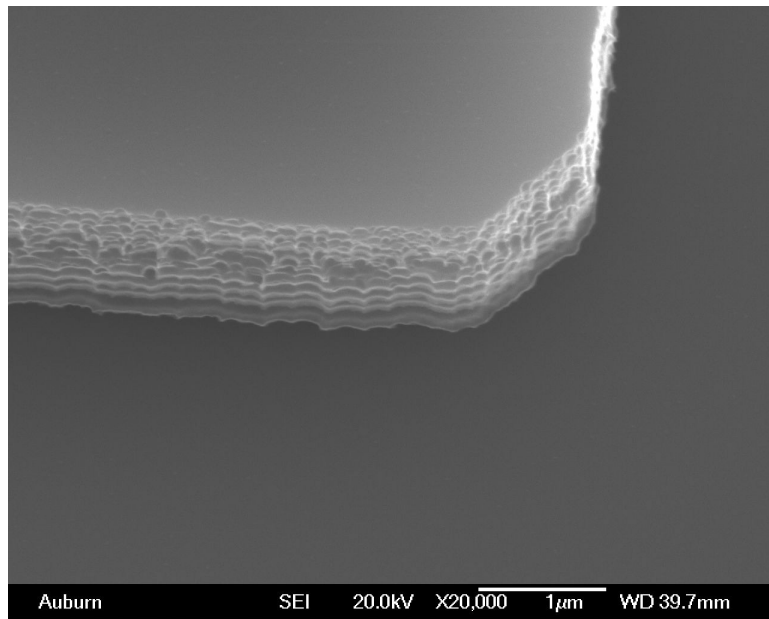
the photoresist layer (i.e., photolithography) transfers the layout of the test platform from the hard mask onto it. Next, the SOI wafer with a patterned photoresist layer on it is dipped in a 1:50 (v:v) solution of HF acid in deionized (DI) water for 10 sec. This etches away the native oxide present on the exposed regions of the device layer. Next, using the patterned photoresist layer as the etch mask, the device layer is etched using the Bosch process, in a deep reactive ion etching (DRIE) system. This anisotropic etching of the device layer defines the three dimensional geometries of the microinstruments of the test platform. Since the Bosch process etches the silicon relatively much faster than the SiO_2 , the sacrificial layer can be conveniently used as an effective etch stop. However, inefficient tuning of the DRIE system used by me necessitated intermittent monitoring of the etched depth of the device layer. Finally, after the entire thickness of the device layer is etched, the wafer is carefully diced into individual test platforms (chips).

4.2.2 Polishing of the Test Surfaces

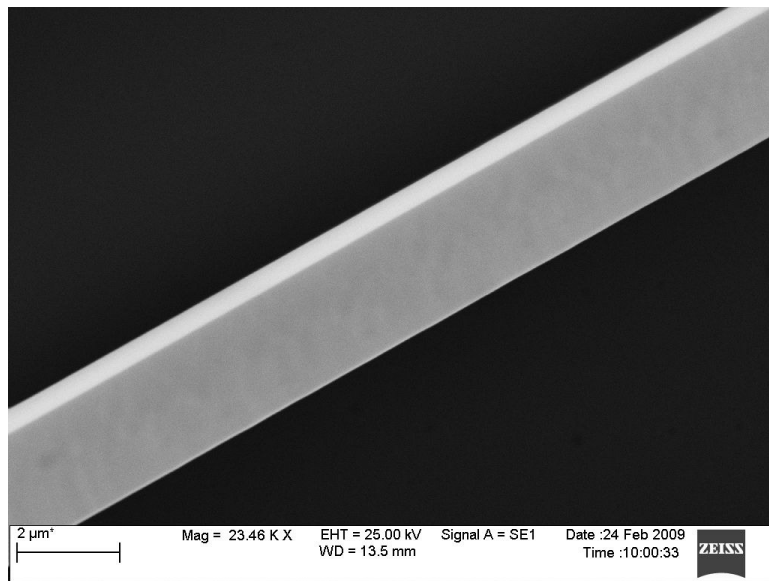
The Bosch process, which is used to define the three dimensional geometries of the microinstruments of the test platform, is known to result in the formation of scallops on the surfaces that are revealed by it [33, 48–50, 52, 53]. Accordingly, the sidewall surfaces of the as-fabricated test platform have a scalloped profile. However, since the in-plane surfaces of the test platform are masked during the etching process, either by the photoresist or by the sacrificial layer, they are not affected by the Bosch process. Figure 4.4a is a SEM image showing the edge of an as-fabricated cantilever beam. A large number of scallops are clearly visible on the as-fabricated sidewall surface shown in Fig. 4.4a. Fig. 4.4a also clearly indicates that the in-plane surfaces (top surface of the cantilever beam in the figure) of the test platform are not affected by the Bosch process. Since one of the objectives of this study is to study the effect that the surface topography of MEMS surfaces has on their stiction and friction

characteristics, it is essential to examine test surfaces, whose surface topographies span the range that includes the surface topographies (i.e., from rms roughness 0.2 nm to rms roughness 15 nm) of the surfaces of most MEMS prototypes. However, the scallops present on the as-fabricated sidewall surfaces of the test platform make the sidewall surfaces significantly rougher (i.e., typical rms roughness is greater than 30 nm) than even the most rough MEMS surfaces. Therefore, a polishing process is devised to smoothen the as-fabricated sidewall surfaces of the test platform.

Three different approaches were tried to polish the test surfaces of the test platform. The first approach involved etching of the as-fabricated test platform in a wet isotropic silicon etchant, which consisted of HNO_3 , HF and H_2O . Several different compositions of the etching solution were examined in order to determine the composition that etches the single crystal silicon structural film of the test platform at the desired etching rate. After finalizing the composition of the isotropic etching solution, the test platform was etched using it. A timed etch was used to ensure that only a thin layer of silicon gets etched from the test surfaces. Unfortunately, this isotropic etching approach did not have any significant effect on the roughness of the sidewall test surfaces. On the contrary, the top surface of the device layer became rough after this treatment. Therefore, this approach was discarded. In the second approach, the test platform was subjected to multiple cycles of polishing, each of which consisted of growing a layer of native oxide on the test surfaces by placing the test platform in hot H_2O_2 for 10 min., and subsequently etching it by dipping the test platform in conc. HF. Even this approach was found to be ineffective, since even after subjecting the test platform to 100 cycles of polishing, no significant change was observed in the scalloped profile of the sidewall test surfaces. Therefore, a third polishing approach based on the thermal oxidation of silicon was investigated to smoothen the as-fabricated sidewall surfaces of the test platform. Considering that the rate of growth of the thermally grown SiO_2 is significantly higher on the asperities than on



(a)



(b)

Figure 4.4: SEM images of (a) An unpolished sidewall surface. (b) A polished sidewall surface.

the flatter surfaces and silicon from the surface layer is consumed by the growing thermal SiO_2 film, it was expected that this approach would considerably smoothen the scalloped sidewall surfaces. Indeed, 2 cycles of polishing using this approach yielded relatively much smoother sidewall surfaces. A SEM image of a sidewall polished using this approach is shown in Fig. 4.4b.

The thermal oxidation (i.e., third) approach based polishing process begins with cleaning of the test platform in piranha (i.e., consists of 2 parts by volume of conc. H_2SO_4 and 1 part by volume of H_2O_2), for 2 min., after which, the test platform is dried by blowing it with a stream of N_2 . Next, a layer of thermal oxide is grown on the exposed silicon surfaces of the test platform using the dry oxidation process, at 1100°C in laboratory air (i.e., pP of O_2 is 0.21 atm) for 75 min. This results in the formation of a 125 - 140 nm thick layer of SiO_2 on the exposed silicon surfaces of the microinstruments of the test platform. The thickness of the thermal oxide layer grown on the exposed silicon surfaces of the test platform is measured using ellipsometry, on a Si(100) monitor chip processed simultaneously with the test platform. Next, the thermally grown oxide layer is completely etched away from the surfaces of the test platform using a timed etch (i.e., 5 - 6 sec.), and conc. HF solution as the etchant. The thickness of the residual thermal oxide left behind on the surfaces of the test platform after this treatment is measured, on the simultaneously processed Si(100) monitor chip using ellipsometry, to ensure that the timed etch is sufficient to completely etch away the entire layer of thermally grown oxide. This completes one cycle of polishing. The scalloped sidewall surfaces of the test platform used in this study are polished using two cycles of polishing. The parameters of the oxidation process (i.e., temperature, time/cycle and no. of cycles) are optimized using the following three criteria: One, the total amount of thermal oxide grown on the exposed silicon surfaces of the test platform should sufficiently smoothen its scalloped sidewall surfaces. Two, the amount of thermal oxide grown in each cycle should be minimized

to avoid chipping of the edges of the microstructures as well as pit formation on the surfaces of the microstructures. Three, the number of polishing cycles should be minimized to avoid induction of stresses in the structural film due to exposure to high-temperature cycling.

4.3 Actuation of the Test Platform

The TPs used in this study are actuated using a custom-built probing system (Probe Station). A photograph of the probing system is shown in Fig. 4.5. The probing system is equipped with the long-working-distance, incoherent light interference microscope similar to that reported by Sinclair *et al.* in [153], which is mounted on a vibration isolation table (Newport Electronics, Inc., ST Series) to dampen the noise associated with the ground vibrations. The Mitutoyo M Plan Apo objectives (10X - 100X) are used as the objective lens in the microscope and a green LED (with λ_{max} of 525 nm, Nichia corp.) monochromated using a monochromator that transmits 532 nm is used as the illumination source. The probing system is also equipped with a charge-coupled device (CCD)-IRIS camera (Sony, XCD-SX910) to collect digital images. Additionally, it has six probe modules, which are used to establish mechanical and/or electrical contacts with the microinstruments. Lastly, it has an in-built vacuum pump, which is used to generate the vacuum suction that holds the probe modules and the TP in place during the actuation of the microinstruments. To automate the actuation of the various microinstruments of the Test Platform, the testing procedures are executed using a scripting environment called MEMScript. All the scripts that are used for this study are reported in Appendix A. The scripts used for testing the microinstruments not only actuate them but also collect and store the required data.

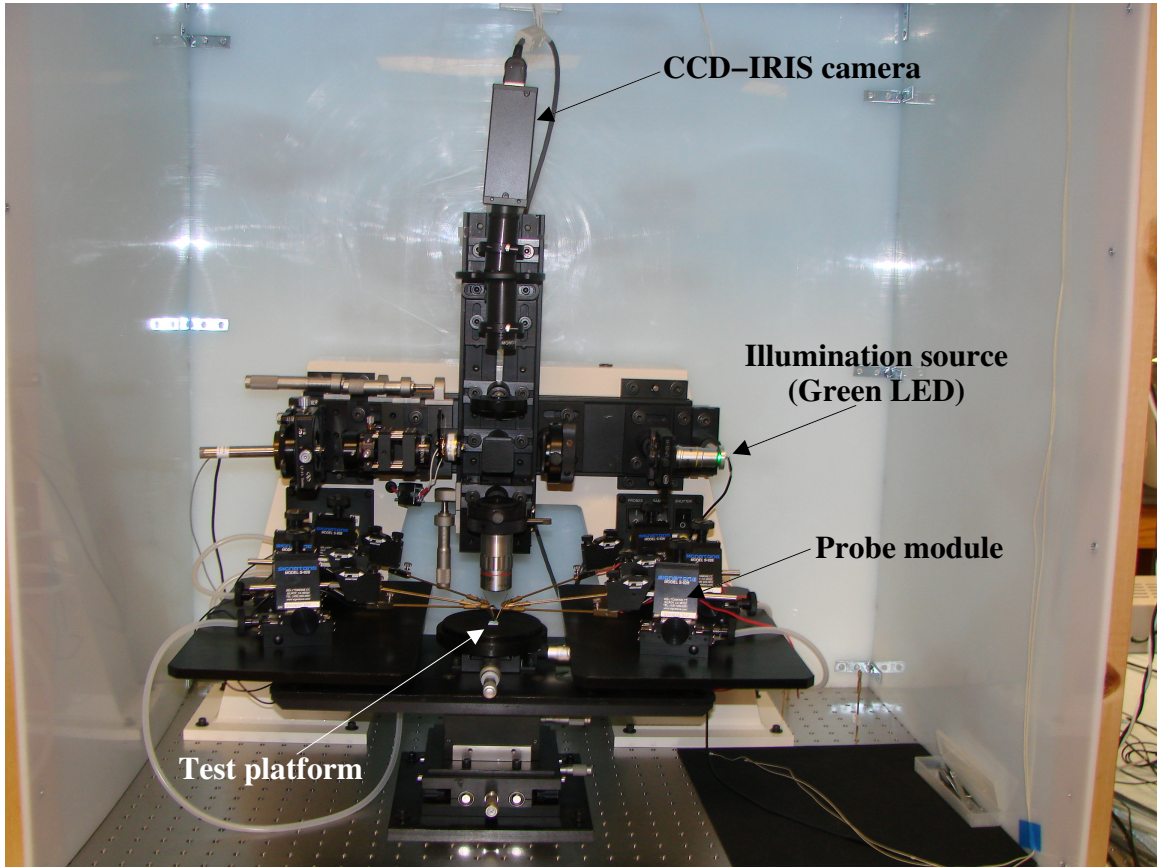


Figure 4.5: Photograph of the custom-built probing system used to actuate the microinstruments of the test platform.

Chapter 5

Microinstruments: Design, Testing Procedure and Modeling

5.1 Residual Stress Tester (RST)

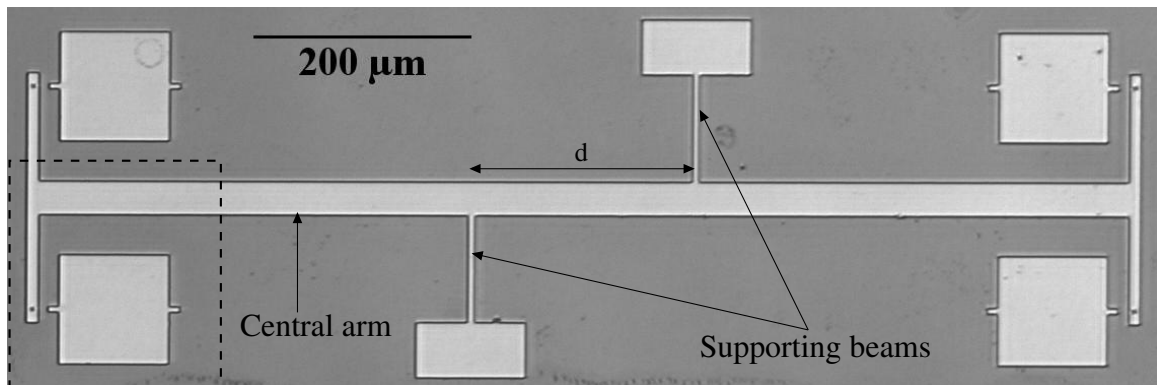
The Residual Stress Tester (RST) can be used to determine the residual stress present in a released structural film.

5.1.1 Design

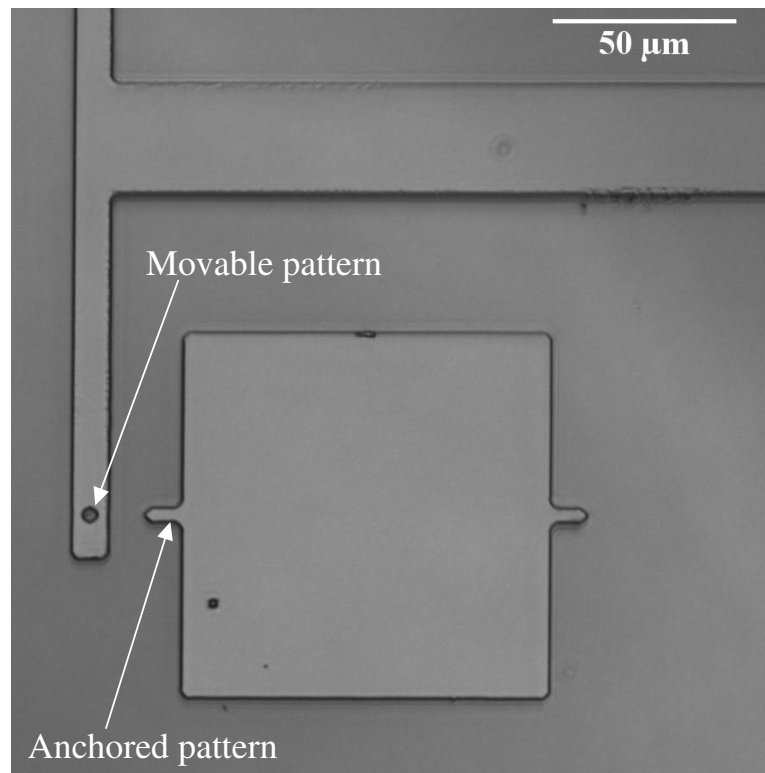
Figure 5.1a is an optical image of a released Residual Stress Tester (RST). As seen in Fig. 5.1a, the main component of the Residual Stress Tester is an I-shaped beam, which is suspended when released. The suspended I-shaped beam is supported by the two thin cantilever beams that are labelled as “supporting beams” in Fig. 5.1a. The two supporting beams are equidistant from the midpoint of the central arm, and are connected to it at a distance d (designed to be $200\ \mu\text{m}$) apart. Both the supporting beams are $100\ \mu\text{m}$ (nominal) long and $5\ \mu\text{m}$ (nominal) wide. Two movable patterns are made on each of the two flanges of the I-shaped beam. On each flange, the two movable patterns are located close to the two ends of the flange, respectively. An anchored pattern corresponding to each movable pattern is designed besides the movable pattern, at a distance of $10\ \mu\text{m}$ (nominal) from it. A pair of movable and anchored patterns can be clearly seen in Fig. 5.1b, which is a magnified optical image of the area that is enclosed in the box in Fig. 5.1a.

5.1.2 Modeling

Since the two supporting beams are connected to the I-shaped beam at points that are off-axis, the forces exerted by them due to the residual stress present in the



(a)



(b)

Figure 5.1: (a) Optical image of a released Residual Stress Tester. Notice that the I-beam consists of a horizontal central beam that is connected to two vertical flanges. (b) Magnified optical image of the area that is enclosed in the box in Fig. 5.1a. Notice the pair of movable and anchored patterns labelled in this image.

structural film, on the I-shaped beam are also off-axis (although equal in magnitude and opposite in direction). Therefore, a torque is induced at the center of the I-shaped beam of the Residual Stress Tester, which causes the I-shaped beam to rotate in the $x - y$ plane when the Residual Stress Tester is released. Depending on the nature of the residual stress (i.e., tensile or compressive) present in the structural film, the I-shaped beam will rotate either clockwise or anti-clockwise. If the residual stress present in the structural film is tensile, the I-shaped beam will rotate clockwise, as shown in Fig. 5.2a. If the residual stress present in the structural film is compressive, the I-shaped beam will rotate anti-clockwise, as shown in Fig. 5.2b.

Since (see Fig. 5.1a) $d/2 \gg w$, which is the width of each supporting beam, the strain induced in both the supporting beams, when the Residual Stress Tester is released, by the residual stress present in the structural film can be approximated by Eq. 5.1.1.

$$\epsilon_R = \theta \frac{d}{2} \quad (5.1.1)$$

Here, ϵ_R is the strain induced in the supporting beams by the residual stress present in the released structural film, θ is the amount (in radians), by which, the I-shaped beam of the Residual Stress Tester rotates, when it is released and d is the distance between the two points, at which, the two supporting beams are connected to the I-shaped beam of the Residual Stress Tester. The residual stress present in the released structural film, that induces a strain of ϵ_R in the supporting beams can be given by Eq. 5.1.3.

$$\sigma_R = E\epsilon_R \quad (5.1.2)$$

E is the elastic modulus of the structural film. Substituting Eq. 5.1.1 in Eq. 5.1.2 gives Eq. 5.1.3, which can be used to determine the residual stress present in the

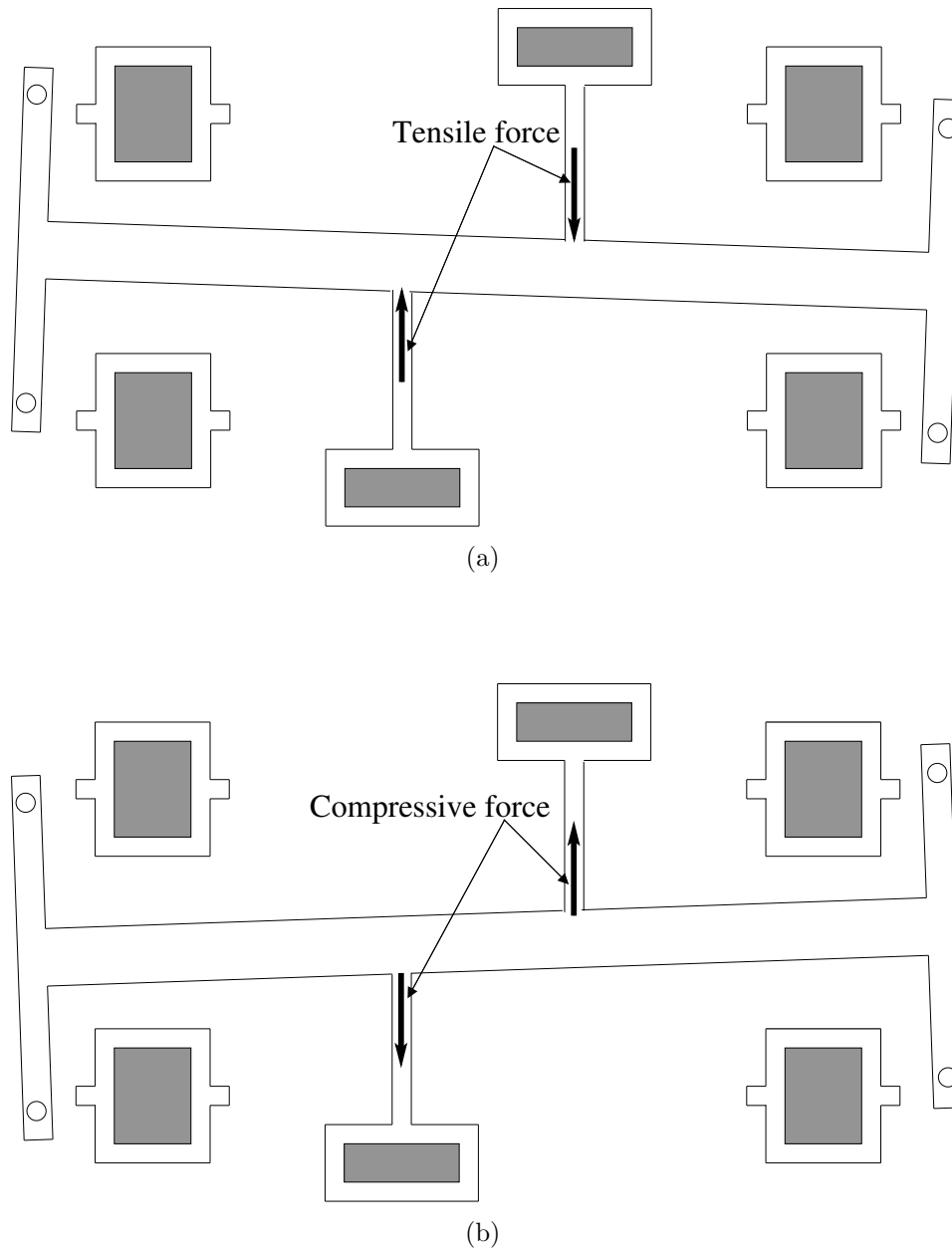


Figure 5.2: (a) A schematic diagram (plan view) illustrating the clockwise rotation of the I-beam of the Residual Stress Tester due to the tensile stress present in the released structural film. (b) A schematic diagram (plan view) illustrating the anti-clockwise rotation of the I-beam of the Residual Stress Tester due to the compressive stress present in the released structural film. Shaded regions shown in the diagrams are anchored to the substrate. A ground plane (not depicted) is present underneath the entire device.

released structural film of the TP.

$$\sigma_R = \frac{E\theta d}{2} \quad (5.1.3)$$

5.1.3 Testing Procedure

A Mitutoyo M Plan Apo 20 objective is used as the objective lens in the microscope, during the testing of Residual Stress Testers. The d for each tested Residual Stress Tester is optically determined, with a resolution of $0.23 \mu\text{m}$. The rotation (i.e., θ) of a released Residual Stress Tester is determined by determining the change in the position of either of the four movable patterns relative its corresponding anchored pattern, when the Residual Stress Tester is released. The change in the position of a movable pattern relative to its corresponding anchored pattern is determined using a pattern matching. The resolution of the pattern matching technique used to determine θ is experimentally determined to be 10 nm . Accordingly, θ can be determined with a resolution of $20 \mu\text{rad}$. The script used to test the Residual Stress Tester is given in Appendix A.1.

5.2 Mechanical Strength Tester (MST)

The Mechanical Strength Tester (MST) can be used to determine the fracture strength of the structural film. It can also be used to investigate the effect of a surface treatment on the fracture strength of the structural film. Accordingly, it can be used to determine the fracture strength of the composite structural film, which is formed when the original structural film is coated with a uniform conformal coating.

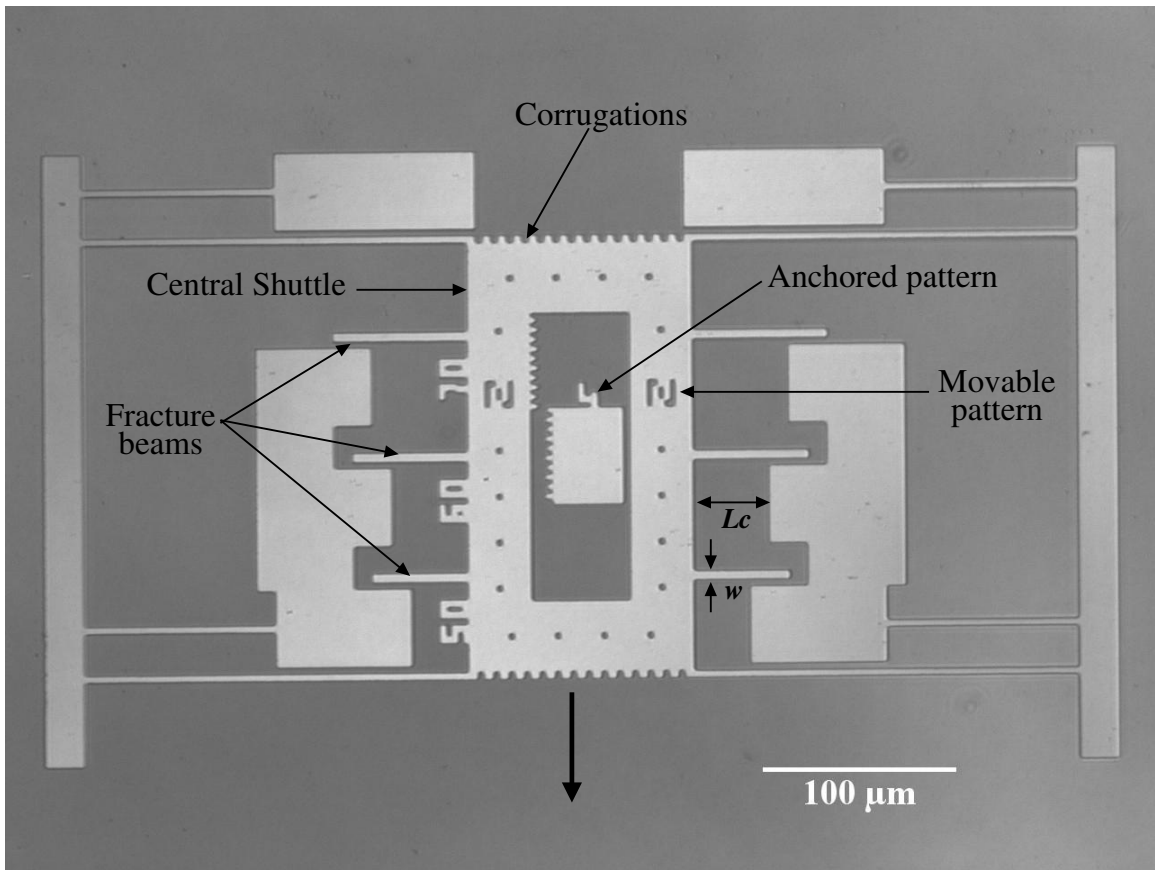


Figure 5.3: Optical image of a released Mechanical Strength Tester.

5.2.1 Design

Test Device

The fundamental design of the Mechanical Strength Tester is inspired from that of the fracture strength test device developed by Jones [154]. Figure 5.3 is an optical image of a released Mechanical Strength Tester. As seen in Fig. 5.3, the Mechanical Strength Tester has a symmetric design. It consists of a central suspended shuttle, which is supported by two identical folded beam flexures. One folded beam flexure is connected to each of the two longer edges of the central shuttle. The two shorter edges of the central shuttle are designed to be corrugated in order to ensure that the probe tip that is used to actuate the Mechanical Strength Tester does not slide along the edge that is pushed by it. This ensures that throughout the actuation of the Mechanical Strength Tester, the motion of its central shuttle is strictly restricted only along the direction of actuation, and the lever arm (i.e., L_c) of each of the actuated fracture beams stays constant. Further, the Mechanical Strength Tester has two identical sets of three fracture beams each. One set of three fracture beams is protruding out of each of the two longer edges of the central shuttle. The three fracture beams that belong to same set all have different lengths. Their lengths are $50 \mu\text{m}$, $60 \mu\text{m}$ and $70 \mu\text{m}$, respectively. The widths of all the six fracture beams of the Mechanical Strength Tester are same. However, the TP has three distinct sets of Mechanical Strength Testers. While the widths of all the fracture beams belonging to a particular set are same, those of the fracture beams belonging to different sets are different. The widths of the fracture beams belonging to the three distinct sets of Mechanical Strength Testers that are included in the TP are $3 \mu\text{m}$ (nominal), $4 \mu\text{m}$ (nominal) and $5 \mu\text{m}$ (nominal), respectively. The Mechanical Strength Tester also has an anchored scale, which is placed in the cavity of the central suspended shuttle. This scale is included in the Mechanical Strength Tester to aid the measurement of the

displacement of the central shuttle during the actuation of the Mechanical Strength Tester. However, in all the experiments conducted for this study, the displacement of the central shuttle of the Mechanical Strength Tester is measured using the movable and anchored patterns labelled in Fig. 5.3 and a pattern matching technique.

Micro-manipulator

A specialized micro-manipulator is developed to actuate the Mechanical Strength Testers for this study. The micro-manipulator, in its assembled form, is shown in Fig. 5.4. It consists of two main components: the “coarse” manipulator and the “fine” manipulator. The *coarse* manipulator is a micropositioner (Model # S - 926) obtained from Signatone. It is used as the holder for the *fine* manipulator as well as for positioning the probe tip in contact with the Mechanical Strength Tester that is to be actuated. The *fine* manipulator consists of five components, which are taken apart and shown clearly in Fig. 5.5. The probe holder is used to hold the probe tip that is used to push the central shuttle, and (using a connector) is screwed into the front-end of the open-loop piezo module. The open-loop piezo module (Melles Griot, travel range is 0 - 30 μm and operating voltage is 0 - 100 V) is used to generate the force that is required to push the central shuttle. It is controlled using the MEMScript. The use of a piezoelectric actuator to actuate the Mechanical Strength Tester enables a controlled and precise pushing of the central shuttle. It allows the central shuttle to be displaced in extremely small, precise and equal nanometer-scale steps. The connecting shaft (using a connector) is screwed into the back-end of the open-loop piezo module at one end, and inserted into the *coarse* manipulator at the other. It is used as the connection between the *fine* manipulator and the *coarse* manipulator, which is used as the holder for the *fine* manipulator. The probe holder and the connecting shaft are made from a single holder (U-P style) bought from Signatone. The orthographic projections (plan view) of the four machined components (i.e., the

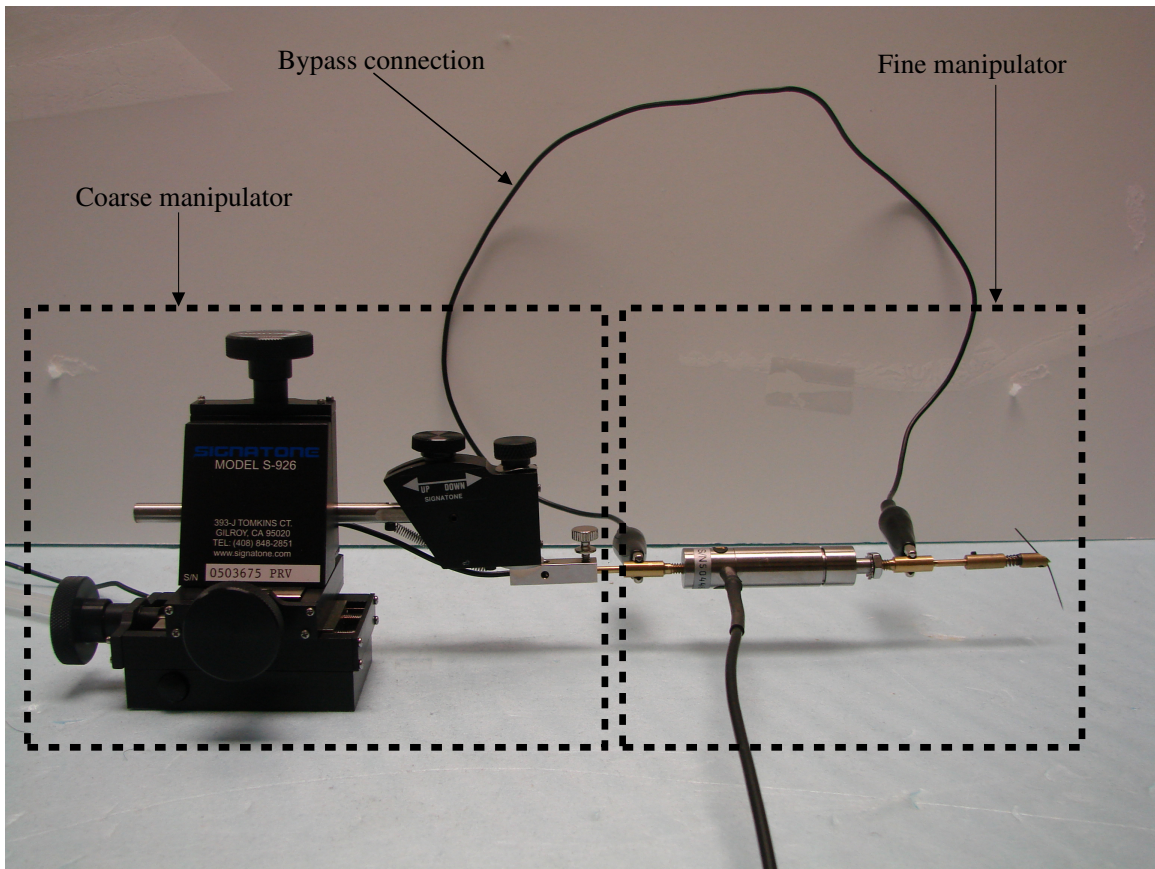


Figure 5.4: Photograph of the Micro-manipulator developed to actuate the Mechanical Strength Testers. Notice the “bypass” connection used to electrically ground the probe tip. The two main components of the Micro-manipulator (i.e., the “coarse” manipulator and the “fine” manipulator) are clearly labelled in the photograph.

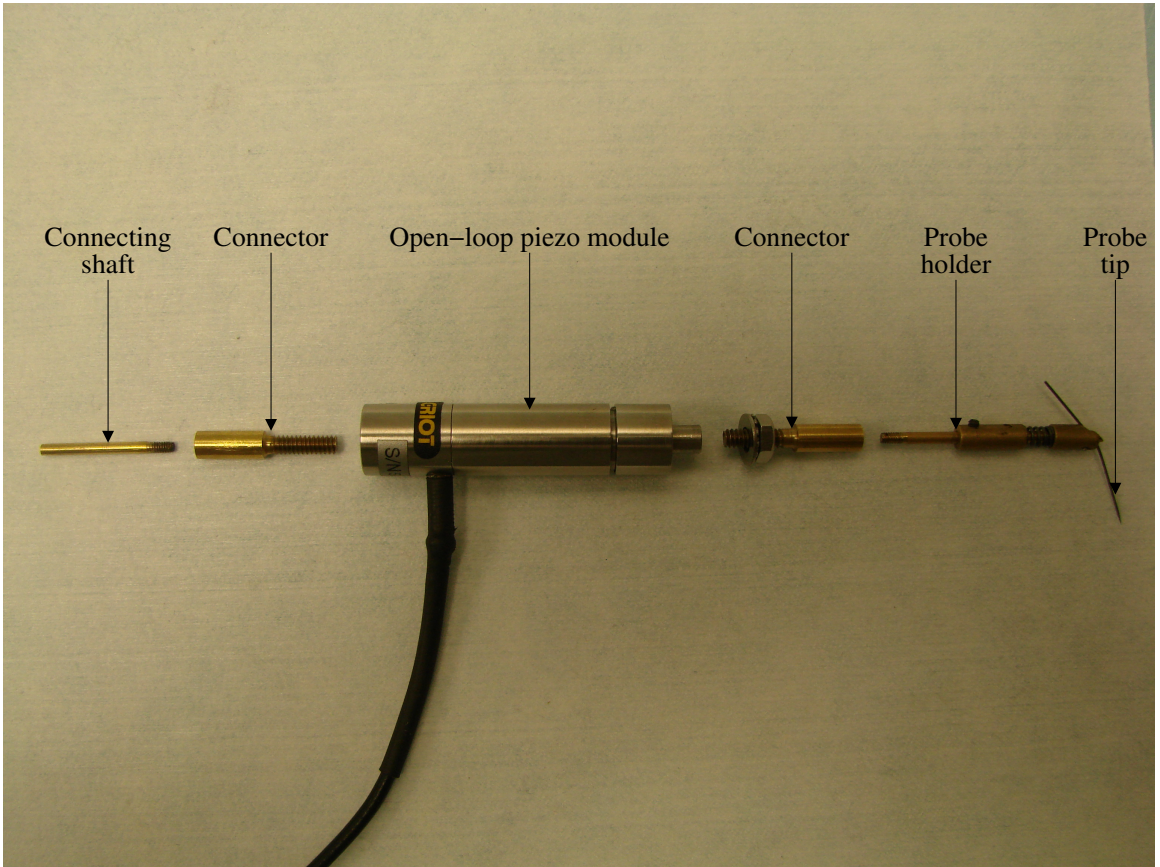


Figure 5.5: Photograph showing the five components of the "fine" manipulator.

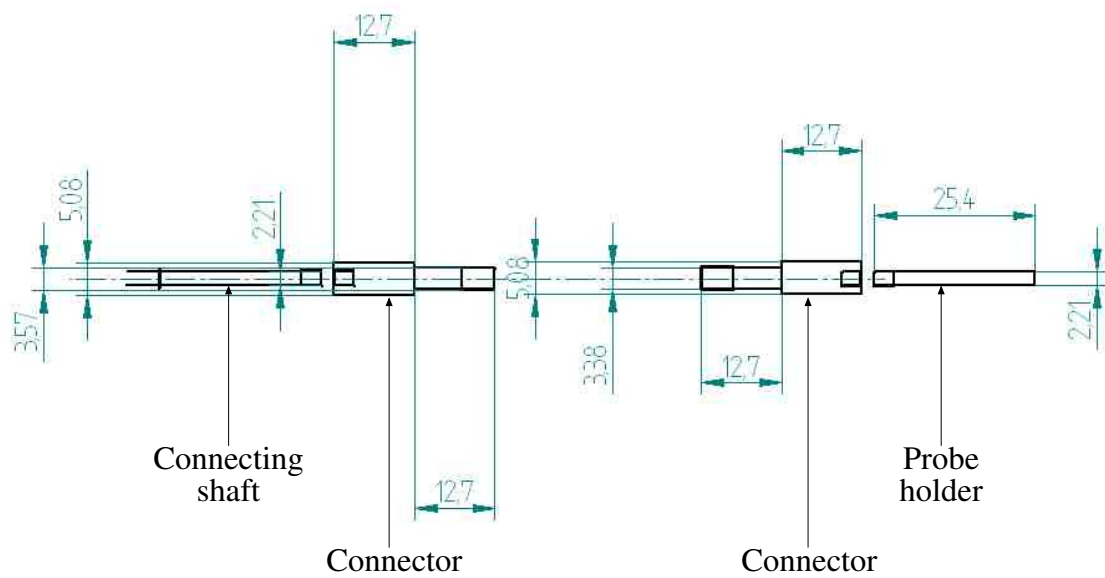


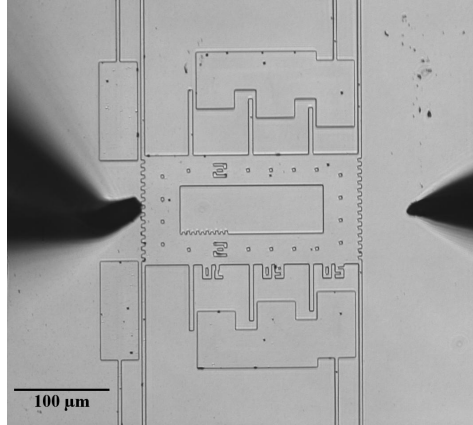
Figure 5.6: Orthographic projections (plan view) of the four machined components of the “fine” manipulator. The dimensions indicated in the orthographic projections are in mm.

probe holder, the two connectors and the connecting shaft) of the “fine” manipulator are shown in Fig. 5.6. The probe tip is electrically grounded using the “bypass” connection shown in Fig. 5.4.

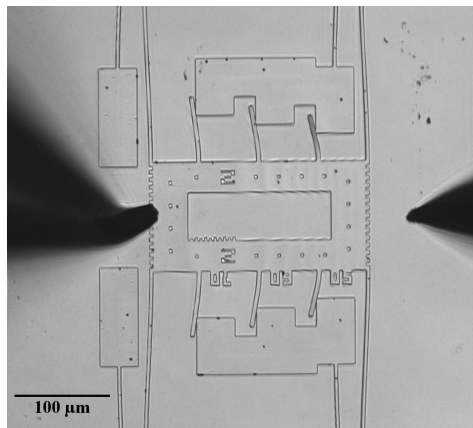
5.2.2 Testing Procedure

Mechanical Strength Testers are actuated using the Micro-manipulator shown in Fig. 5.4. The probe tip used in the Micro-manipulator, to push the central shuttle of the Mechanical Strength Tester, is a Signatone SE-20T probe tip. To actuate a Mechanical Strength Tester, first, it is brought in contact with the anchored stopper blocks using the “coarse manipulator”, at which point, its position is considered as the initial position, then, a DC voltage is applied to the open-loop piezo of the *fine* manipulator, and the substrate and the probe tip are electrically grounded. The voltage applied to the open-loop piezo is increased from 0 V at a rate of 0.5 V/s up to 100 V. This stimulates the fine manipulator to push the central shuttle of the Mechanical Strength Tester in the direction of the arrow shown in Fig. 5.3. As the displacement of the central shuttle increases, the fracture beams that are protruding out of the central shuttle are pushed against their corresponding anchored stopper blocks. The central shuttle is pushed until all the fracture beams attached to it are broken. Optical images illustrating the actuation procedure of the Mechanical Strength Tester are shown in Fig. 5.7. The displacement of the central shuttle is determined at every push, throughout the actuation of the Mechanical Strength Tester. An optical pattern matching technique, which has a resolution of 20 nm (A Mitutoyo M Plan Apo 10 objective is used as the objective lens in the microscope), is used to determine the displacement of the central shuttle. The script that is used to actuate Mechanical Strength Testers is given in Appendix A.2.

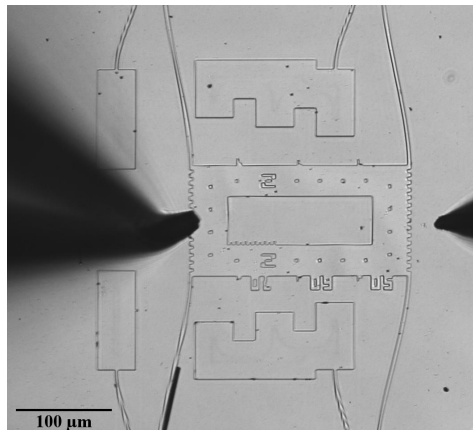
The Mechanical Strength Tester developed in this study can be modeled using an analysis similar to that reported in [154], by Jones. Accordingly, the fracture



(a)



(b)



(c)

Figure 5.7: Optical images illustrating the actuation of a Mechanical Strength Tester. (a) The MST is shown in its pre-actuated state. (b) Optical image collected during the actuation of the MST. Notice that all the six fracture beams are pushed against their corresponding anchored stoppers. (c) Optical image showing the MST in its post-actuated state. Notice that all the fracture beams that were attached to the central shuttle are fractured.

strength (σ_f) of the structural film can be determined using Eq. 5.2.1, where, E is the elastic modulus of the structural film, w is the width of the fractured beam, δ_f is the distance, by which, the shuttle is displaced when the fracture beam gets fractured and L_c is the distance between the shuttle and the anchored stopper corresponding to the fractured beam [154].

$$\sigma_f = \frac{3Ew\delta_f}{2L_c^2} \quad (5.2.1)$$

Rearranging Eq. 5.2.1 gives Eq. 5.2.2, which can be used to determine the strain (ϵ_f) induced in the structural film at the time of its fracture. The fracture strain of a structural film is a fundamental property characteristic of its material, and more often reported in literature than the fracture strength.

$$\epsilon_f = \frac{3w\delta_f}{2L_c^2} \quad (5.2.2)$$

5.3 Resonator

The Resonator can be used to determine the elastic modulus (E) of a structural film. It can also be used to determine the surface coverage (i.e., projected surface area) of nanoparticle-based thin film coatings, which are deposited on MEMS surfaces to texture them.

5.3.1 Design

Figure 5.8 is an optical image of a released Resonator. As seen in Fig. 5.8, the Resonator also has a symmetric design. It consists of two banks of interdigitated movable and anchored comb fingers. Each bank of comb fingers has 30 movable comb fingers and 29 anchored comb fingers. The movable comb fingers of the two banks of comb fingers are connected through a shuttle, which is suspended when the Resonator is released. The suspended shuttle is supported by two identical folded beam flexures, one of which, is attached to each of its two sides. Each of the two folded beam flexures

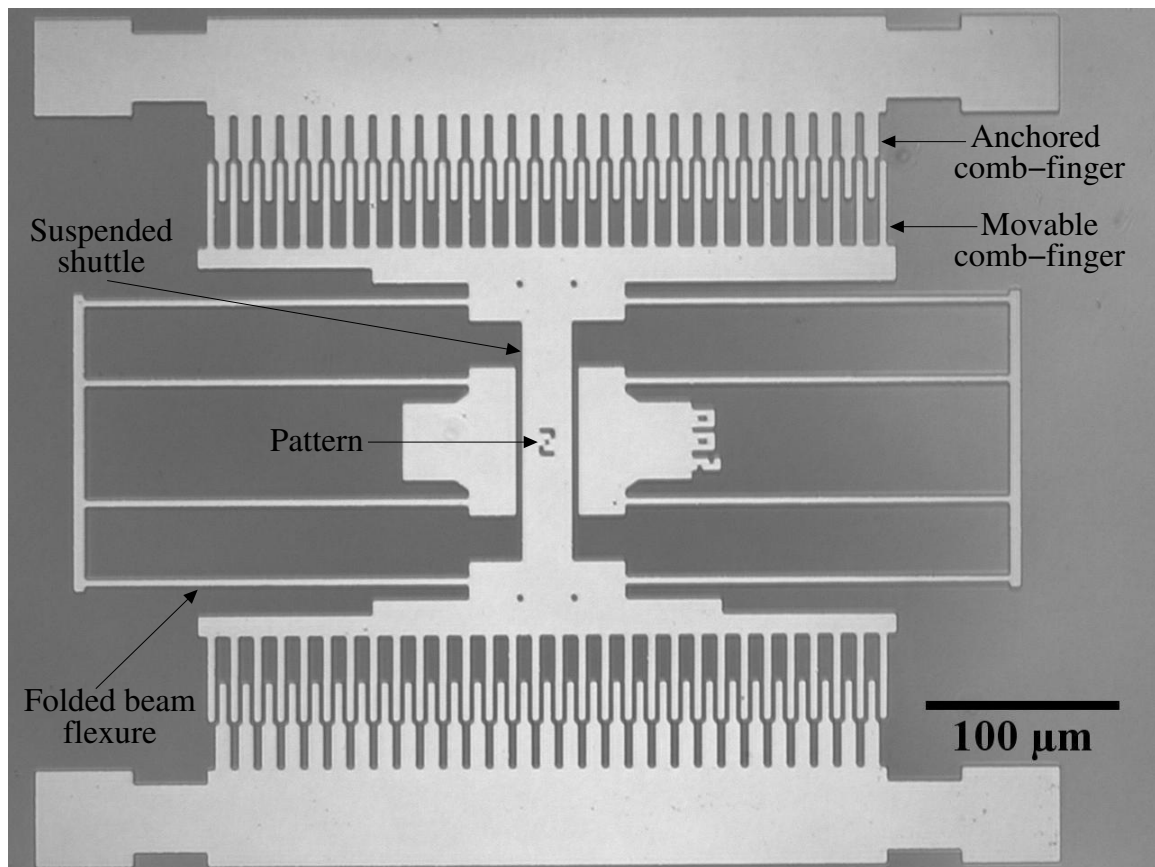


Figure 5.8: Optical image of a released Resonator.

consist of four identical supporting beams, which are connected to each other by a truss. The width of each of the eight supporting beams of the Resonator is $3\ \mu\text{m}$ (nominal). However, the Test Platform has nine distinct sets of Resonators, and the lengths of the supporting beams of the Resonators belonging to different sets are different. The lengths of the supporting beams of the Resonators belonging to those nine distinct sets are $100\ \mu\text{m}$ (nominal), $150\ \mu\text{m}$ (nominal), $200\ \mu\text{m}$ (nominal), $250\ \mu\text{m}$ (nominal), $300\ \mu\text{m}$ (nominal), $350\ \mu\text{m}$ (nominal), $400\ \mu\text{m}$ (nominal), $450\ \mu\text{m}$ (nominal) and $500\ \mu\text{m}$ (nominal), respectively. The purpose behind including Resonators with nine different supporting beam lengths in the Test Platform is to have test devices, whose resonance frequencies span a wide range. A specific pattern (labeled in Fig. 5.8) is made on the shuttles of all the Resonators of the Test Platform in order to monitor their displacements during actuation.

5.3.2 Testing Procedure

The Resonators are actuated electrostatically. Electrical contacts are made by touching the actuation pads, which are fabricated in the microinstrument, with sharp tungsten probe tips (Signatone SE-20T). The drive-signals applied to actuate a Resonator are generated using an arbitrary waveform generator (Keithley, Model # 3390, 50 MHz), and amplified using a high-voltage amplifier (TEGAM, 2350S). To actuate a Resonator, an AC drive signal with a DC bias is applied across either of the two banks of comb fingers and the substrate, the movable structure and the other bank of comb fingers are electrically grounded. The DC biases used to actuate the Resonators with different supporting beam lengths range from 25 V to 150 V. The corresponding AC drive signals used to actuate the Resonators with different supporting beam lengths range from 20 V to 40 V, respectively. In order to determine the resonance frequency of a Resonator, the frequency of the AC drive signal applied to it is increased from close to zero until it crosses the resonance frequency of the resonating structure. The

resonance frequency of a Resonator is detected optically, with a resolution of ± 5 Hz, by monitoring the amplitude of the oscillation of the pattern made on the shuttle.

5.3.3 Modeling

The resonance frequency of a resonating structure such as the Resonator developed in this study is mathematically expressed by the harmonic oscillator equation, which is given by below:

$$f_R = \frac{1}{2\pi} \sqrt{\frac{k_x}{M_{eff}}} \quad (5.3.1)$$

Here, f_R is the resonance frequency of the Resonator, k_x is the combined stiffness of both the folded beam flexures, which support the suspended shuttle, and M_{eff} is the effective mass of the resonating structure. Solving the Euler-Bernoulli beam equation for the supporting beams of the Resonator indicates that k_x , which is the combined stiffness of the two folded beam flexures that support the suspended shuttle, can be given by Eq. 5.3.2.

$$k_x = \frac{24EI}{L^3} \quad (5.3.2)$$

Here, E is the elastic modulus of the structural film, I is the area moment of inertia experienced by the supporting beams of the Resonator about the axis that is perpendicular to their plane of bending and L is the length of the supporting beams of the Resonator. Since the slopes of all the sidewalls of the Test Platform are close to 90° , the cross-sections of all the supporting beams of the Resonator can be considered as rectangular. Therefore, I can be given by Eq. 5.3.3.

$$I = \frac{tw^3}{12} \quad (5.3.3)$$

Here, t is the thickness of the structural film and w is the width of the supporting beams. Substituting Eq. 5.3.3 in Eq. 5.3.2 gives,

$$k_x = 2Et \left(\frac{w}{L} \right)^3 \quad (5.3.4)$$

Substituting Eq. 5.3.4 in Eq. 5.3.1 gives,

$$f_R = \frac{1}{2\pi} \sqrt{2E \frac{tw^3}{M_{eff} L^3}} \quad (5.3.5)$$

Squaring Eq. 5.3.5 gives Eq. 5.3.6, which can be used to determine the elastic modulus (i.e., E) of the structural film.

$$f_R^2 = E \left(\frac{tw^3}{2\pi^2 M_{eff} L^3} \right) \quad (5.3.6)$$

f_R , which is the resonance frequency of the Resonator, is determined experimentally, t , w and L , which are the thickness, width and length of the supporting beams of the Resonator, respectively, are measured optically, with a resolution of $\pm 0.465 \mu\text{m}$ (A Mitutoyo M Plan Apo 10 objective is used as the objective lens in the microscope). The effective mass of the resonating structure (i.e., M_{eff}) can be given by the Rayleigh equation shown below:

$$M_{eff} = M_s + \frac{1}{4}M_t + \frac{12}{35}M_b \quad (5.3.7)$$

Here, M_s , M_t and M_b are the masses of the shuttle, the two trusses and the eight supporting beams of the Resonator, respectively. M_s , M_t and M_b are determined using the dimensions of the corresponding components of the Resonator, which are measured optically, with a resolution of $\pm 0.465 \mu\text{m}$ (A Mitutoyo M Plan Apo 10 objective is used as the objective lens in the microscope).

5.4 Cantilever Beam Array (CBA)

The Cantilever Beam Array can be used to determine the apparent work of adhesion of contacting in-plane surfaces.

5.4.1 Design

Cantilever beams were first used for determining the interfacial work of adhesion of in-plane surfaces by Mastrangelo *et al.*, in 1992 [155]. Since then, the cantilever beam array is considered as the standard test device for studying the stiction characteristics of in-plane surfaces [78]. It has been widely used by several researchers for understanding the mechanisms underlying the stiction experienced by proximate MEMS surfaces as well as for studying the effects of different surface treatments [6, 13, 24, 25, 35, 37, 38, 64, 67, 69, 70, 70, 71, 73, 78, 80, 93, 94, 99–103, 107, 111, 130, 149, 152, 155–158]. Historically, the cantilever beam arrays that have been used for studying stiction consisted of cantilever beams with increasing lengths [24, 37, 64, 78, 80, 94, 99–101, 158]. While the advantage of using cantilever beam arrays that consist of cantilever beams with increasing lengths is that they eliminates the need of a metrology technique to determine the detachment length, the drawback of using them is that each array can be used to obtain only one data point [13, 64, 94, 100, 101]. Additionally, since the purpose behind using cantilever beam arrays that consist of cantilever beams with increasing lengths is to eliminate the need of a metrology technique, the apparent work of adhesion of in-plane surfaces (\mathcal{W}_{ip}) is quantified by visually determining the detachment length [6, 13, 35, 37, 64, 78, 94, 100, 101]. This method of quantifying stiction involves determination of the shortest stuck cantilever beam (arc-shaped beam) [6, 13, 35, 37, 64, 78, 94, 100, 101]. However, deBoer *et al.* reported that using cantilever beams that are adhered over long attachments lengths to determine the apparent work of adhesion of in-plane surfaces yields significantly more accurate results [152]. They demonstrated that quantification of stiction using S-shaped beams

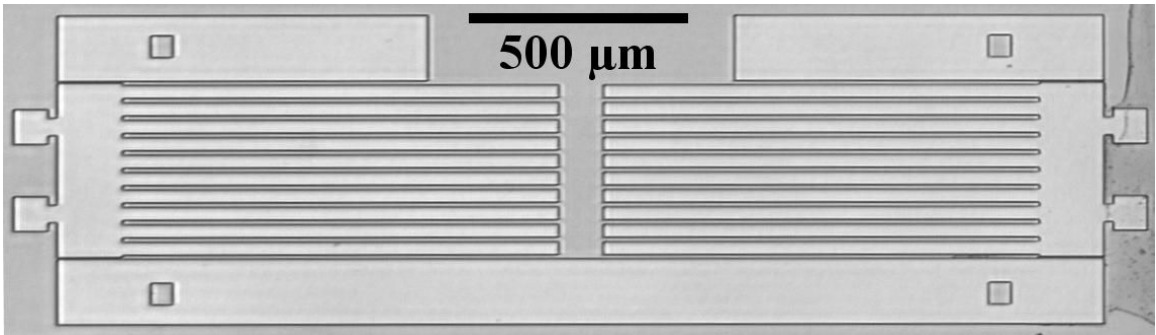


Figure 5.9: An optical image showing two adjacent released Cantilever Beam Arrays.

is much less sensitive to variations in surface topography or to details of capillary drying than that using arc-shaped beams [152]. Therefore, in order to overcome the limitations of the cantilever beam array that consists of cantilever beams with increasing lengths, the CBAs that are included in the TP are designed to have 10 cantilever beams each, all of the same length. An optical image showing two adjacent released CBAs is shown in Fig. 5.9. The crack length of each cantilever beam of the CBA is determined using interferometry. Therefore, each cantilever beam of the CBA can be used to obtain a data point. Accordingly, each CBA of the TP can be used to obtain ten data points. This not only allows the collection of a statistically significant data set but also enables the analysis of the local variation in the adhesion of studied in-plane surfaces. Further, to be able to use the S-shaped cantilever beams, which enable a more accurate estimation of \mathcal{W}_{ip} , for quantifying the entire spectrum of \mathcal{W}_{ip} , three distinct sets of eight CBAs each are included in the TP. While all the cantilever beams belonging to a particular set have the same length, those belonging to different sets have different lengths. The three sets of CBAs that are included in the TP consist of cantilever beams with lengths of 500 μm (nominal), 1000 μm (nominal) and 2000 μm (nominal), respectively. The widths of all the cantilever beams of the TP are 30 μm (nominal).

5.4.2 Testing Procedure and Analysis

The cantilever beams (CBs) are actuated manually using a sharp tungsten probe tip (Signatone SE-SMS). A schematic diagram illustrating the actuation procedure of the cantilever beams is shown in Fig. 5.10. To actuate a cantilever beam, first, its tip is brought in contact with the substrate by pushing with the probe tip and then, the cantilever beam is pushed along its length progressively at points closer to its anchor until it is in contact with the substrate over almost its entire length, leaving a length between 50 - 60 μm near the anchor, as shown in Fig. 5.10b. At this point, the probe

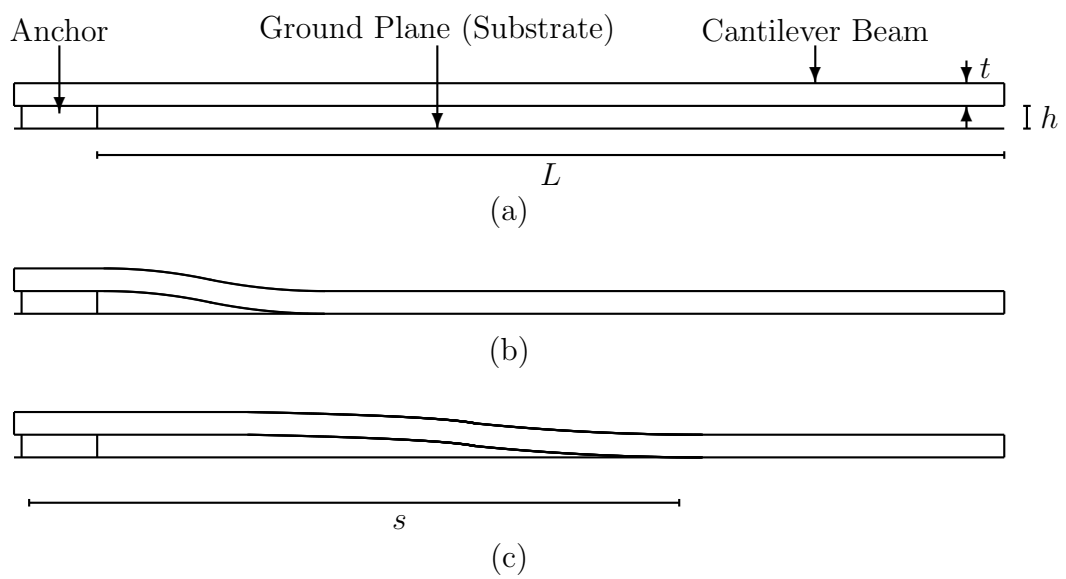


Figure 5.10: A schematic diagram illustrating the actuation procedure of a cantilever beam. (a) Free-standing (unactuated) cantilever beam. (b) Actuated cantilever beam. (c) Cantilever beam released after actuation (post-actuation state). Notice that the cantilever beam is adhered over a length of $L - s$ at its tip.

tip is carefully and slowly retracted, which allows the cantilever beam to peel apart up to a certain characteristic length called as the crack length s , under the influence of its restoring force (i.e., see Fig. 5.10c). The crack length exhibited by a cantilever beam depends on the interfacial properties of the two contacting in-plane surfaces, which in the case of the TP, are the bottom surface of the cantilever beam (i.e., device layer) and the top surface of the substrate. The crack length of each actuated cantilever beam is determined optically using phase shifting interferometry. The long-working-distance, incoherent light interference microscope of the Probe Station is used to collect the interferograms. The apparent work of adhesion of the in-plane surfaces of the TP is determined using Eq. 5.4.1, which is derived by Hurst *et al.* in [175].

$$\mathcal{W}_{ip} = \frac{3Et^3}{2s^4} \left(a_3^2 + a_3 a_2 + \frac{1}{3} a_2^2 \right) \quad (5.4.1)$$

Here, E is the elastic modulus of the structural film (device layer), t is the thickness of the cantilever beam (in the case of the TP, thickness of the structural film), s is the crack length and a_3 and a_2 are parameters extracted from a 3^{rd} order polynomial fitted to the height profile of the actuated cantilever beam, which is determined experimentally using phase shifting interferometry. The script used to determine the height profile of an actuated cantilever beam is given in Appendix A.4. This script also extracts the crack length of the actuated cantilever beam from its experimental height profile, and calculates the apparent work of adhesion of the tested in-plane surfaces using it.

5.5 Sidewall Beam Array (SBA)

The Sidewall Beam Array can be used to determine the apparent work of adhesion of contacting sidewall surfaces.

5.5.1 Previously Reported Devices: A Review

While the cantilever beam array (CBA) is widely used as a standard test device to investigate stiction between in-plane surfaces, there is no consensus on a standard device to study stiction between sidewalls. Historically, the devices that have been used to study stiction between sidewalls can be primarily classified into two categories: devices that measure adhesion force and devices that measure adhesion energy. The first device that was designed to measure adhesion force between sidewall surfaces was reported by Timpe *et al.* [142]. The device consisted of two suspended shuttles, each connected to two comb drives. One comb drive connected to each shuttle was used to bring the shuttles into contact while the other comb drive was used to pull them apart. The difference in the voltages applied to the two sets of comb drives at the instance of contact and separation of shuttles, respectively were used to determine the adhesion force between sidewalls. Since the instance of contact and separation of shuttles was detected optically, the resolution with which the adhesion force between sidewalls could be measured was limited [79, 159]. Also, the electrostatic forces generated by the comb drives, which were used to determine the adhesion force between sidewalls, were calculated theoretically and not obtained experimentally. In order to improve the resolution of adhesion force measurement, van Spengen *et al.* and Friedrich *et al.* used the change in the experimentally measured capacitance of the detection drive to determine the instance of contact and separation of sidewall test surfaces [79, 159]. While the test device designed by Friedrich *et al.* was similar to that reported by Timpe *et al.*, that designed by van Spengen *et al.* consisted of only one suspended shuttle, which was made to contact and separate from the sidewall surface of a fixed post [79, 159]. While the devices reported by van Spengen *et al.* and Friedrich *et al.* could measure sidewall adhesion force with a high resolution of few nN, both required external and extremely sophisticated electronic capacitance readout system. Also,

both these devices are prone to levitation, which should be accurately accounted for in the determination of sidewall adhesion force.

Considering the magnitude of adhesion force between MEMS sidewalls, which ranges from few ten nN to few hundred nN, its sensitivity to sidewall topography and the dependence of sidewall topography on the conditions used to deposit and anneal the device layers, measuring the adhesion energy of contacting sidewalls seems to be a better alternative. The first and only device reported to-date, which measures the apparent adhesion energy needed to separate contacting sidewalls, was designed by Ashurst *et al.* [78]. The device consisted of two suspended, parallel cantilevers, which were electrostatically brought into contact along their sidewalls, and the apparent adhesion energy was determined using the energy minimization approach suggested by Mastrangelo *et al.* [78]. Although the device was successfully used to determine the apparent adhesion energy of octadecane coated as well as oxide coated sidewall surfaces, it had two major design limitations [78]. First, owing to the residual stress gradients in the polycrystalline (polysilicon) device layers, the test beams were curled down [78]. As a result, the longer test beams were touching the substrate at their tips, which made them unusable [78]. Second, the post-actuated beams that were stuck together exhibited random and irreproducible “scissoring” (misalignment in the z plane), which limited the accuracy with which the apparent adhesion energy could be determined [78]. The microinstrument developed in this study for studying the stiction characteristics of sidewall surfaces not only addresses some of the limitations of the test microinstrument reported by Ashurst *et al.* but is also much easier to fabricate. The details of the design, fabrication and modeling of the microinstrument are described in the following sections.

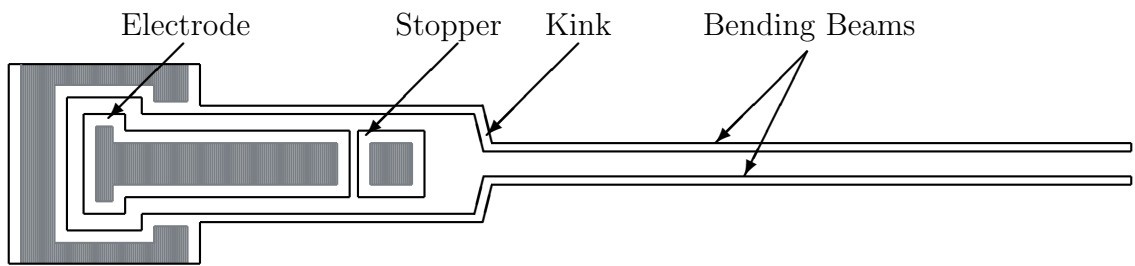


Figure 5.11: A schematic diagram of the sidewall adhesion test microinstrument (plan view). Shaded regions shown in the diagram are anchored to the substrate. A ground plane (not depicted) is present underneath the entire device.

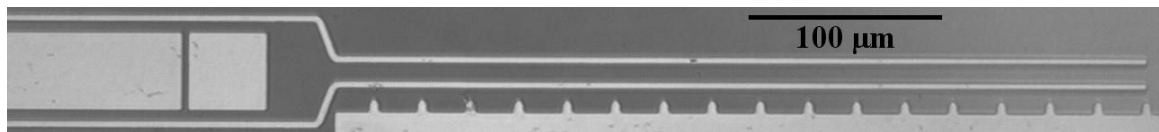
5.5.2 Design

The fundamental design of the sidewall adhesion test microinstrument developed in this study is inspired from that of the microinstrument designed by Ashurst *et al.* [78]. Accordingly, the same rationale that was used, by Ashurst *et al.* in [78], to justify the use of two cantilever beams as the sidewall beams of their sidewall adhesion test microinstrument also explains the design of the Sidewall Beam Array, in which too, two cantilever beams are used as the sidewall beams. A schematic diagram (plan view) to illustrate the microinstrument is shown in Fig. 5.11. The microinstrument consists of two cantilever beams (sidewall beams), which are suspended parallel to each other. Each sidewall beam (SB) consists of two segments; the initial segment, which has a fixed length of $320\ \mu\text{m}$ and the final segment, which is connected to the initial segment using a kink. The sidewall beams (SBs) are $3\ \mu\text{m}$ (nominal) wide and, over their entire final segment, $10\ \mu\text{m}$ (nominal) apart from each other. They are designed to contact along their sidewalls when an increasing voltage is applied to the actuating electrode, which is located between their initial segments. The actuating electrode is $40\ \mu\text{m}$ (nominal) wide and $295\ \mu\text{m}$ (nominal) long. It is centered between the initial segments of the sidewall beams and anchored to the substrate over the shaded region shown in Fig. 5.11. In order to accommodate the electrode, the initial segments of the sidewall beams are spaced $52\ \mu\text{m}$ apart and, are kinked inward so that the spacing between their final segments is small enough to ensure that they contact over much of their lengths with the application of only moderate voltages to the electrode. A stopper with nominal dimensions of $40\ \mu\text{m} \times 40\ \mu\text{m}$ is fabricated, in front of the electrode between the initial segments of the sidewall beams, to avoid short-circuit between the sidewall beams and the electrode in the event of a catastrophic failure. An optical image of a released sidewall adhesion tester is shown in Fig. 5.12a. In order to be able to accurately determine the crack length of the actuated adhered sidewall beams, anchored scales are fabricated on

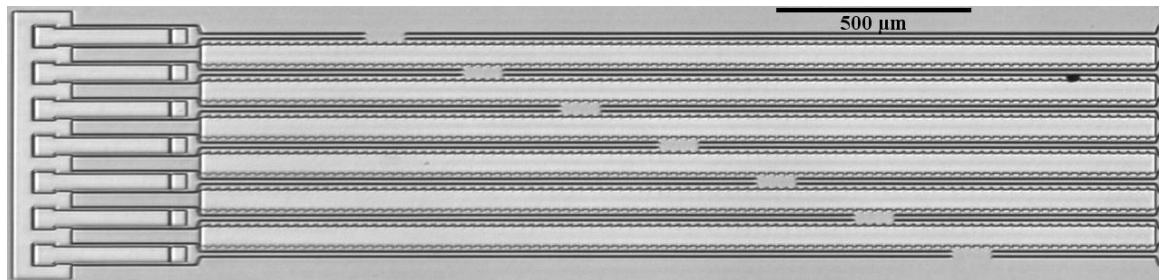
both the sides of the pair of sidewall beams. One of those anchored scales is clearly visible, at the bottom, in Fig. 5.12a. The distance between the adjacent markers (i.e., protrusions) of the scale is $25\ \mu\text{m}$. In order to ensure that surfaces with a wide range of adhesion energies could be investigated using the sidewall adhesion tester, an array (i.e., Sidewall Beam Array) consisting of seven sidewall adhesion testers is designed. The length of the final segment of the sidewall beams varies from $420\ \mu\text{m}$ to $1920\ \mu\text{m}$ in the array. An optical image of the Sidewall Beam Array (SBA) is shown in Fig. 5.12b.

5.5.3 Testing Procedure

The sidewall adhesion test microinstrument is actuated electrostatically. Electrical contacts are made by touching the actuation pads, which are fabricated in the microinstrument, with sharp tungsten probe tips (Signatone SE-20T). The voltages applied to the electrode of the sidewall adhesion test microinstrument are generated using a digital-to-analog converter (DAC) and amplified using a high-voltage amplifier (TEGAM, 2350S). A schematic diagram (plan view) illustrating the actuation procedure of the microinstrument is shown in Fig. 5.13. To actuate the sidewall adhesion test microinstrument, the sidewall beams and the ground plane (substrate) are electrically grounded and, a DC voltage is applied to the electrode. The voltage applied to the electrode is increased from 0 V at the rate of 1 V/s to 90 V. As the applied voltage is increased, the two sidewall beams are drawn together like tweezers and at 90 V, they are in contact over much of the length of their final segments, leaving a length between 100 and $125\ \mu\text{m}$ near electrode not contacting. The actuation voltage is then ramped down to 0 V at the rate of 1 V/s, which allows the sidewall beams to peel apart under the influence of their restoring forces. The sidewall beams peel apart up to a certain characteristic length called as the crack length (s), which depends on the interfacial properties of the two contacting surfaces. The crack length



(a)



(b)

Figure 5.12: (a) Optical image of a released sidewall adhesion test microinstrument. Anchors that anchor the sidewall test beams are not visible in the image. The total length of the sidewall beams shown in the image is $750\ \mu\text{m}$. (b) Optical image of a released sidewall beam array. The shortest pair of sidewall beams is $750\ \mu\text{m}$ long. The length of sidewall beam pairs is increased in increments of $250\ \mu\text{m}$ and the longest pair of sidewall beams is $2250\ \mu\text{m}$ long.

of each actuated adhered pair of sidewall beams is determined using the anchored scales fabricated on both the sides of the pair of sidewall beams. Each division of the anchored scale, which is $25 \mu\text{m}$ long, is further divided into five sub-divisions using a scale ruler and the crack length is determined optically with a resolution of $\pm 2.5 \mu\text{m}$. To determine the crack length, the adhered beams are brought into focus successively from their anchored ends to their tips. This real-time dynamic focussing of the adhered beams accentuates the sharpness of the crack tip and enables the determination of its location within 12 pixels. Once the crack length is known, the apparent work of adhesion of the sidewall surfaces is determined using the same analysis as that reported by Ashurst *et al.* [78]. The script used to actuate a pair of sidewall beams is given in Appendix A.5. This script can also be used to determine the crack length of the actuated sidewall adhesion tester, and calculate the apparent work of adhesion of tested sidewall surfaces using it.

5.5.4 Modeling

In order to evaluate the interfacial adhesion between the sidewall surfaces, a mechanical energy minimization model is employed. The objective of the model is to minimize the energy of the system (U_T), which is a sum of the mechanical strain energy (U_E) stored in each bending beam and the interfacial adhesion energy (U_S) of the fractions of the sidewall beams adhered beyond the crack length.

$$U_T = 2U_E + U_S \quad (5.5.1)$$

Each sidewall beam is considered as a cantilever beam, which bends (from side to side) in the x - y plane. Accordingly,

$$U_E = \frac{EI}{2} \int_0^s \left(\frac{d^2u}{dx^2} \right)^2 dx \quad (5.5.2)$$

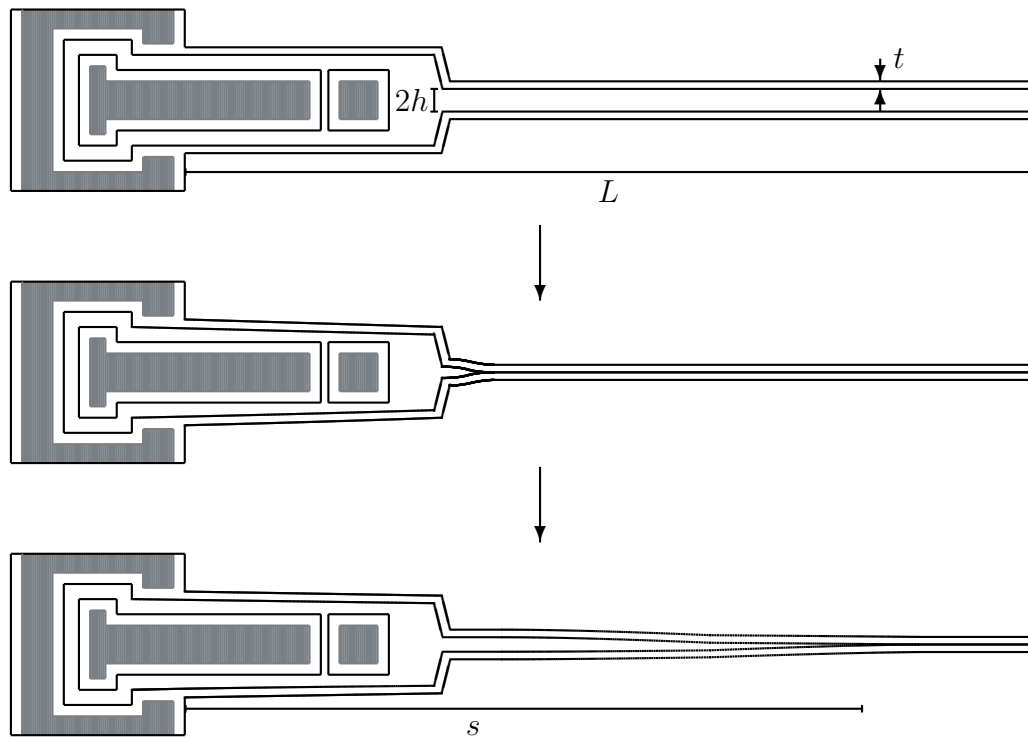


Figure 5.13: A schematic diagram (plan view) illustrating the actuation procedure of the sidewall adhesion tester. (Top) The sidewall beams are in the as-fabricated position. (Center) The sidewall beams are in an actuated state, contacting over almost the entire length of their final segments. (Bottom) Final state of the sidewall beams post-actuation when the actuating voltage is reduced to zero. The beams are adhered over a length $L - s$ at their tips.

where, u is the deflection of the sidewall beam in the x - y plane. Since in their final state post-actuation, the sidewall beams are S-shaped, their deflection can be defined by Eq. 5.5.3.

$$u = \frac{hx^2}{s^2} \left(3 - 2\frac{x}{s} \right) \quad (5.5.3)$$

I is the moment of inertia in the bending plane and for the sidewall beams is given by Eq. 5.5.4.

$$I = \frac{wt^3}{12} \quad (5.5.4)$$

E is the elastic modulus of the structural film (device layer), which for the microinstrument developed in this study, is a 2 μm thick (nominal) Si(100) film. h is the distance through which each beam bends (half the distance between the unactuated sidewall beam pair in as-fabricated position), x is the position along the beam (the anchor point corresponds to $x = 0$), s is the crack length, w is the width of the sidewall beams (for the microinstrument developed in this study, w is the thickness of the device layer), t , as indicated in Fig. 5.13, is the thickness of the sidewall beams. As suggested by Ashurst *et al.* in [78], the kink can reasonably be neglected in the modeling of the sidewall adhesion test microinstrument. Also, since the slopes of all the sidewalls of the test platform are close to 90° , the torsional compliance of the sidewall beams is also neglected in their modeling. U_S is given by Eq. 5.5.5.

$$U_S = -\mathcal{W}_s w(L - s) \quad (5.5.5)$$

Here, \mathcal{W}_s is the apparent work of adhesion of the sidewall surfaces and $L - s$ is the fraction of their lengths, over which, the sidewall beams are adhered post-actuation. Minimizing U_T with respect to crack length s and solving for \mathcal{W} gives Eq. 5.5.6.

$$\mathcal{W}_s = \frac{3Et^3h^2}{s^4} \quad (5.5.6)$$

It should be noted that Eq. 5.5.6 yields the *apparent* work of adhesion, since, the model uses the *apparent* area of contact (in Eq. 5.5.5), which is different from the real area of contact due to the finite roughness and topography of the contacting sidewall surfaces.

5.6 Sidewall Friction Tester (SFT)

The Sidewall Friction Tester can be used to study the friction and wear characteristics of contacting sidewall surfaces.

5.6.1 Previously Reported Devices: A Review

Initial studies that investigated the friction and wear behaviour of MEMS surfaces used polycrystalline silicon (polysilicon) based, surface micromachined rotating microinstruments such as microturbines, electrostatic micromotors and micro-engines [82, 83, 147, 160, 161]. While studying the dynamic behavior of a rotating microinstrument gave a good notion of the friction and wear behaviour of the surfaces of that particular device, the results could not be generalized because the contact geometries and hence the contact pressures at the contact interfaces could not be determined accurately [85, 143]. Therefore, Senft and Dugger designed and surface micromachined a polysilicon based sidewall friction and wear test device, which had a well-defined contact geometry [85]. The device consisted of two orthogonal comb-drive actuators, one of which was used to apply the normal load at the contact interface, while the other was used to shear the contact interface [85]. The contact interface was formed by bringing the flat sidewall surface of a suspended beam in contact with the cylindrical sidewall surface of an anchored post [85]. Although Senft and Dugger's test device had a well-defined contact geometry, the contact pressure could still not be determined accurately because the device had an asymmetric design, which resulted in moments that could not be accurately accounted for. Additionally,

the onset of slip was detected optically, which limited the resolution, with which, the friction force could be measured [85]. In order to improve the accuracy of the estimation of contact pressure, Tas *et al.* reported a polysilicon based sidewall friction and wear test device, whose design did not induce any unaccounted moments [150]. As a result, the contact pressure at the interface, which was formed between two flat sidewall surfaces in their device, could be determined accurately. However, even Tas *et al.* detected the onset of slip optically [150]. Timpe *et al.* also reported two different polysilicon based sidewall friction and wear test devices, which enabled accurate estimation of the contact pressure owing to their symmetric designs [23,143,162]. The contact geometry in one of their devices was flat-on-flat, while that in the other was flat-on-cylinder [23,143,162]. Timpe *et al.* too detected the onset of slip optically, which limited the resolution of their measurements [79,159]. In order to improve the resolution of measurements, Asay *et al.*, who used a polysilicon microdevice similar to that reported by Timpe *et al.*, used a pattern-matching algorithm, which enabled displacement measurements with a resolution of 40 nm, and van Spengen *et al.*, who used a polysilicon microdevice similar to that reported by Senft and Dugger, used an external electronic capacitance readout system, which measured the change in the capacitance of the detection drive during the experiment with a resolution of 10 aF [126,128,145]. While the device used by Asay *et al.* did not have any design limitations, that used by van Spengen *et al.* encountered levitation and had a design limitation, which precluded accurate determination of the normal load applied to the contact interface [145]. Additionally, the electronic capacitance readout system employed by them necessitated averaging of 1000 measurements to obtain an acceptable signal-to-noise ratio [145].

One common hitch of all the studies mentioned above is that in all of them the stiffnesses of the suspension springs and the electrostatic forces generated by

the actuators were calculated using the designed dimensions and not determined experimentally, which might have resulted in inaccurate determination of the friction coefficients [23, 85, 126, 143, 145, 150]. Additionally, the sidewall friction and wear test devices used in all of them were fabricated using polysilicon structural films. Therefore, owing to the variable material properties and surface roughness of polysilicon structural films, the results obtained in all of the above mentioned studies showed significant device to device scatter, which made it difficult to draw a meaningful conclusion [23, 85, 126, 143, 145, 150]. Only four single-crystal-silicon (SCS) based friction test devices have been reported to date [141, 151, 163–165]. The first single-crystal-silicon (SCS) based friction test device was reported in 1995, by Prasad *et al.*, who used it to study the friction characteristics of oxide coated sidewalls [164]. Later in the last five years, three more single-crystal-silicon (SCS) based friction test devices have been reported by Hwang *et al.*, who used it to study the friction characteristics of oxide coated sidewalls, Guo *et al.*, who also used it study the friction characteristics of oxide coated sidewalls, and Wu *et al.*, who used it to study the stick-slip behaviour of SCS sidewalls, respectively [141, 151, 163, 165]. The single-crystal-silicon (SCS) based friction test device reported by Guo *et al.* had an asymmetric design [163]. Accordingly, it has the same limitations as the friction test device reported by Senft and Dugger [85]. Additionally, all the single-crystal-silicon (SCS) based friction test devices reported to date were fabricated using relatively complicated fabrication schemes. The device reported by Prasad *et al.* was fabricated using SCREAM, those reported by Guo *et al.* and Wu *et al.* were fabricated using the silicon on glass (SOG) fabrication process and that reported by Hwang *et al.* was fabricated using a two step surface micromachining scheme [141, 151, 163–165]. Also, the sidewall test surfaces of all the single-crystal-silicon (SCS) based friction test devices reported to date had significant roughnesses [141, 151, 163–165]. The SCS based sidewall friction tester developed in this study not only addresses some of the limitations of the previously

reported devices, but is also much easier to fabricate and has relatively smoother sidewalls [78,141]. The details of the design, fabrication and modeling of the SFT are described in the following sections.

5.6.2 Design

The fundamental design of the Sidewall Friction Tester (SFT) developed in this study is inspired from that of the microinstrument designed by Senft and Dugger [85]. A schematic diagram (plan view) illustrating the SFT is shown in Fig. 5.14. The SFT consists of two identical comb-drive actuators, which are integrated in such a way that they can produce motion in orthogonal directions. One of the comb-drive actuators (normal arm) is used to form the sidewall interface by bringing the flat sidewall surface of a suspended beam in contact with the cylindrical sidewall surface of an anchored post. The normal arm is also used to apply the normal load at the sidewall interface. The other comb-drive actuator (tangential arm) is used to shear the sidewall interface. Each of the two comb-drive actuators have one push drive and one pull drive (see Fig. 5.14), which allows the loading beam that forms the sidewall interface to be moved both forward as well as backward from its unactuated positions in both the orthogonal directions. In both the arms of the SFT, the shuttles are suspended using four identical folded beam flexures. Each folded beam flexure consists of four identical supporting beams, which are connected to each other by a truss. The supporting beams are $500\ \mu\text{m}$ (nominal) long and $3\ \mu\text{m}$ wide (nominal). The SFT has two anchored posts, which are fabricated exactly opposite to each other (see Fig. 5.14), so that, both the sidewall surfaces of the loading beam can be tested. An optical image of a released SFT is shown in Fig. 5.15.

Each of the four drives (i.e., two push drives and two pull drives) have four identical banks of interdigitated anchored and suspended comb fingers. Each bank has 44 suspended and 45 anchored comb fingers, which are $45\ \mu\text{m}$ (nominal) long

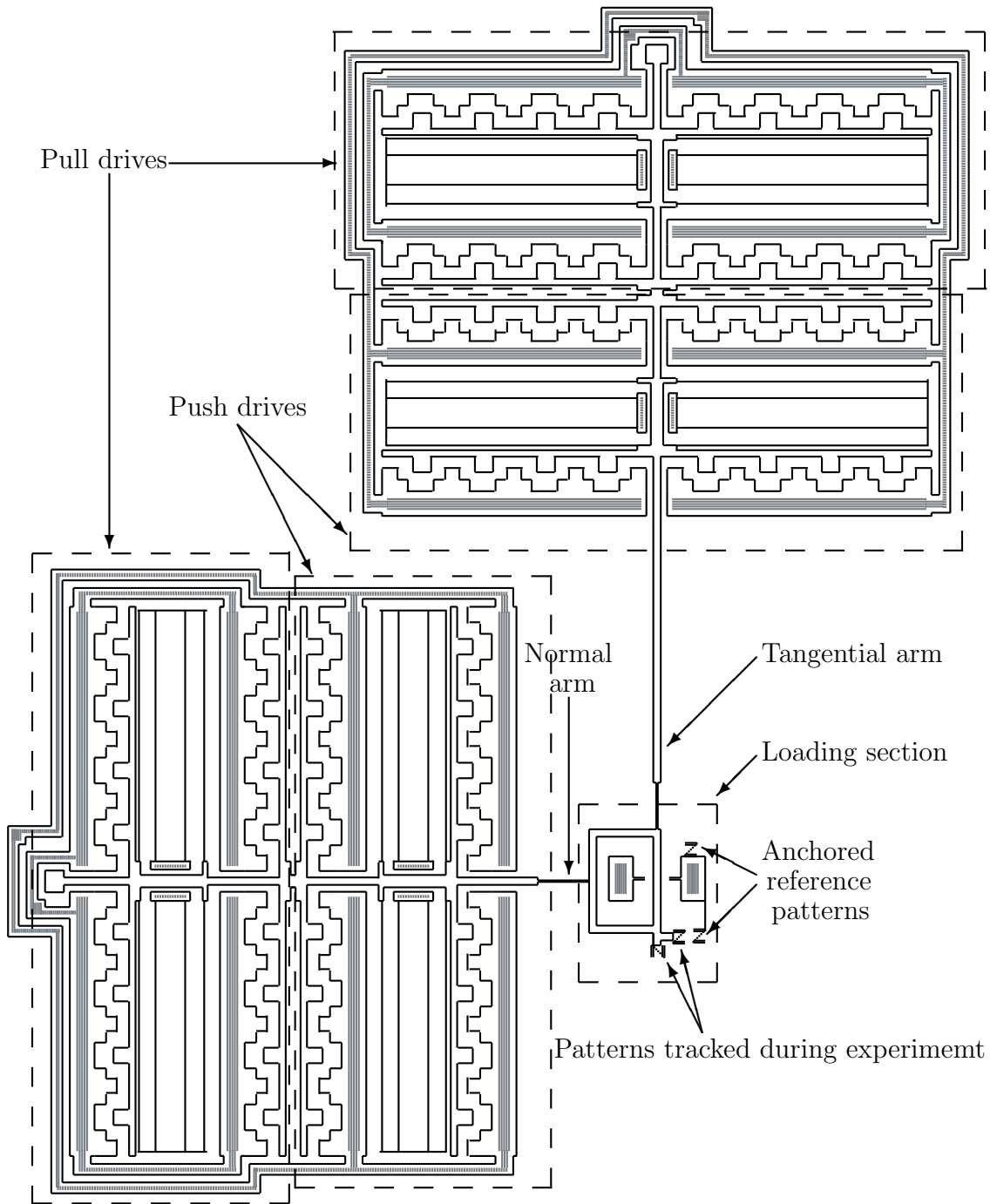


Figure 5.14: A schematic diagram of the Sidewall Friction Tester (plan view). Shaded regions shown in the diagram are anchored to the substrate. A ground plane (not depicted) is present underneath the entire device. The diagram is not drawn to scale to better illustrate the important components of the device.

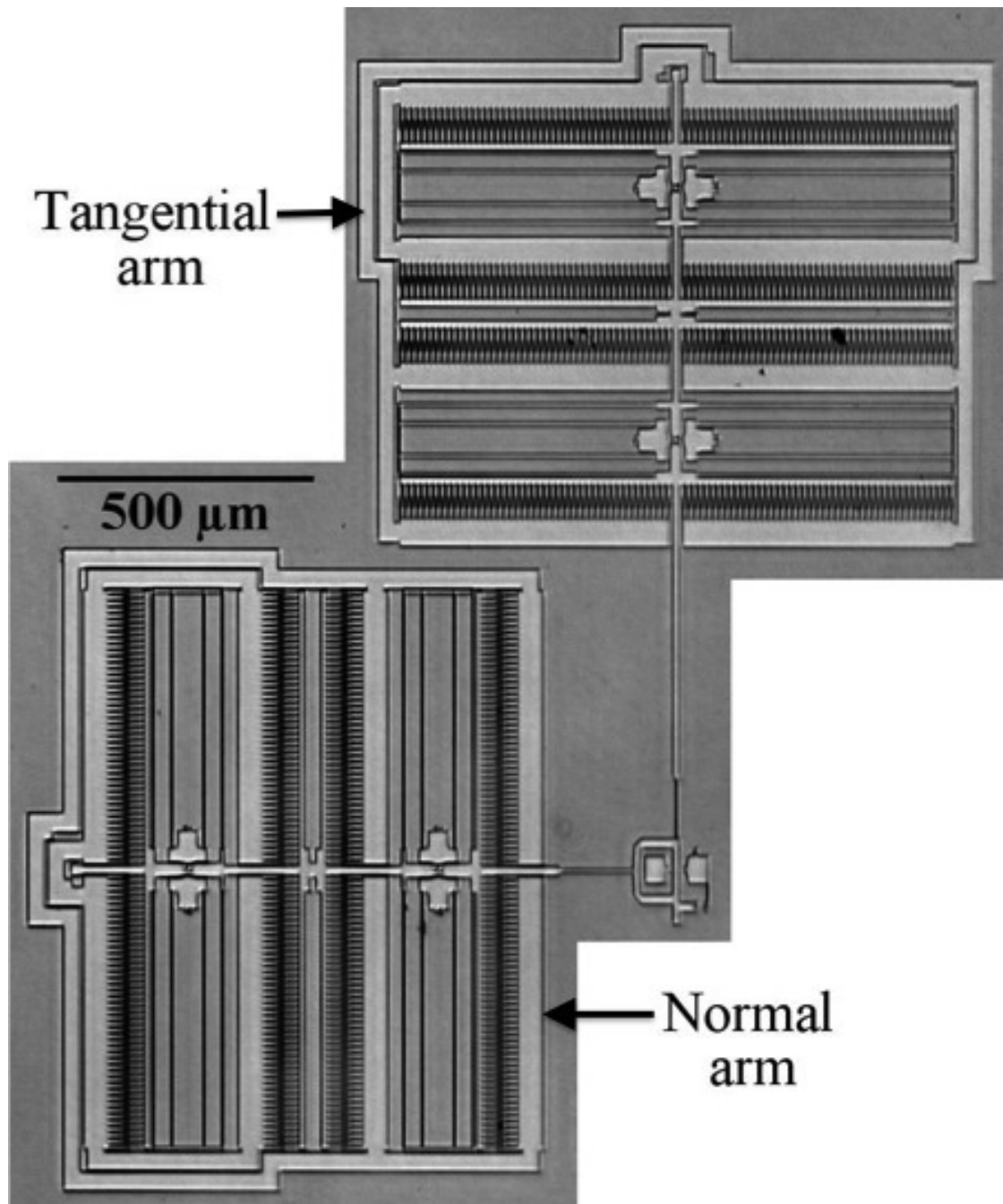
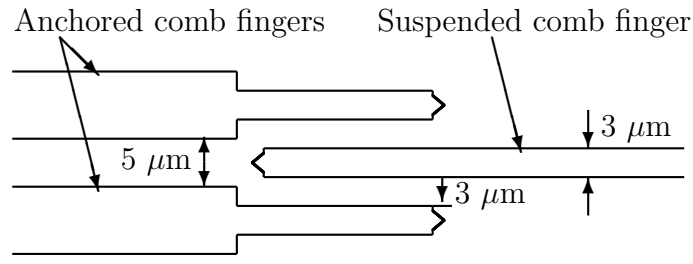


Figure 5.15: Optical image of a released Sidewall Friction Tester (SFT). Notice the ground plane present underneath the entire device. The total footprint of the microinstrument is 2.8 mm^2 .

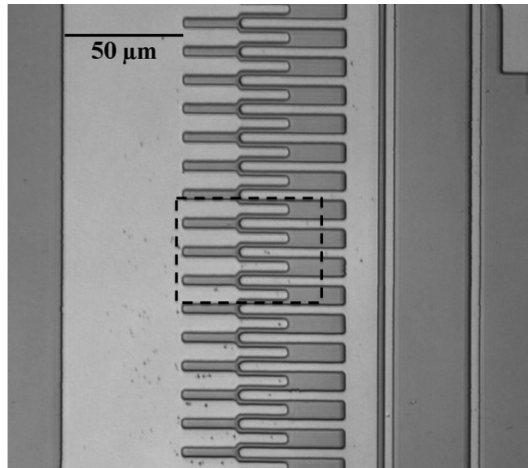
and $3\ \mu\text{m}$ (nominal) wide. Since the minimum feature size that could be resolved in the fabrication process used to fabricate the TP was $3\ \mu\text{m}$ (nominal), the minimum gap between the overlapping lengths of anchored and suspended comb fingers that could be resolved was also $3\ \mu\text{m}$. However, since the electrostatic force generated by a comb-drive actuator is inversely proportional to the gap between its anchored and suspended comb fingers, a smaller gap between the anchored and suspended comb fingers of the comb-drive actuators of the SFT developed in this study was desired so that a larger maximum electrostatic force could be generated using them. Therefore, the anchored comb fingers of the SFT developed in this study are designed to have two segments. The initial segments of adjacent anchored comb fingers, which are $22.8\ \mu\text{m}$ (nominal) long, are $9\ \mu\text{m}$ (nominal) apart from each other, while the final segments, which are $22.2\ \mu\text{m}$ (nominal) long, have a gap of $5\ \mu\text{m}$ (nominal) between them. A schematic diagram illustrating the segmental design of the anchored comb fingers of the SFT developed in this study is shown in Fig. 5.16a. As seen in Fig. 5.16a, in the as-fabricated (unactuated) position, in which they overlap over a length of $20\ \mu\text{m}$ (nominal), the gap between the suspended comb finger and the initial segment of the anchored comb finger is designed to be $3\ \mu\text{m}$ (nominal). However, owing to the segmental design of the anchored comb fingers, during actuation, when the overlap of the suspended and anchored comb fingers will increase beyond $22.8\ \mu\text{m}$ (nominal), the gap between them will decrease to $1\ \mu\text{m}$ (nominal). This will increase the electrostatic force generating capacity of the comb-drive actuators of the SFT developed in this study by a factor of three. In order to ensure that the gap between the tip of a suspended comb finger and the final segment of an anchored comb finger is also $3\ \mu\text{m}$ (nominal) in the as-fabricated position, the suspended comb fingers are designed to have unique pointed tips. Figure 5.16b is an optical image showing one of the sixteen banks of comb fingers of a released Sidewall Friction Tester (SFT). The segmental designs of the anchored comb fingers, which are in their as-fabricated (unactuated)

position, are clearly seen in this image. Figure 5.16c is a magnified optical image of the area enclosed in the box in Fig. 5.16b. The pointed tips of the suspended comb fingers, which are in their as-fabricated (unactuated) positions, are clearly seen in this image.

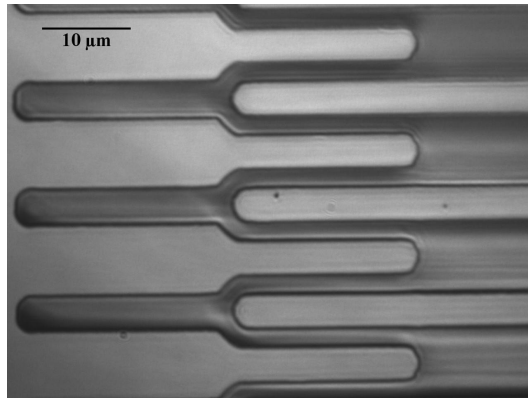
Figure 5.17 is an optical image showing the loading section of a released (unpolished) SFT in its as-fabricated position. Anchored and suspended patterns that are used to track the normal and tangential displacements of the loading beam are clearly labelled in Fig. 5.17. It is clearly visible in Fig. 5.17 that the anchored posts are not aligned with the as-fabricated (unactuated) position of the normal arm (i.e., b is greater than a by $8 \mu\text{m}$). This intentional misalignment is designed to ensure that the overlap of the anchored and suspended comb fingers of the pull drive of the tangential arm is greater than $22.8 \mu\text{m}$ when the normal arm is aligned with the anchored posts during actuation. Also, in the as-fabricated position, both the anchored posts are designed to be $6 \mu\text{m}$ (nominal) apart from the corresponding sidewall surfaces of the loading beam, which ensures that the overlap of the corresponding anchored and suspended comb fingers of the normal arm is also greater than $22.8 \mu\text{m}$ when the loading beam comes in contact with either of the two anchored posts. Since the normal arm and the anchored posts are aligned before the loading beam is brought in contact with a post, application of the normal load at the sidewall interface does not induce an unbalanced moment at it. While the symmetric geometry of the U-beam (see Fig. 5.17), which transfers the electrostatic force generated by the normal arm to the loading beam, ensures that both the ends of the loading beam exert the exact same amount force on the post (i.e., half of the total applied normal load), the alignment of the normal arm with the anchored posts ensures that both the ends of the loading beam are equidistant from the post. As a result, the moments induced at the post by the loads applied at the two ends of the loading beam are exactly equal in magnitude and opposite in direction. Therefore, since no unbalanced moment is



(a)



(b)



(c)

Figure 5.16: (a) A schematic diagram illustrating the segmental design of the anchored comb fingers of the SFT. The diagram is drawn using a scale of 127000:1. In the as-fabricated (unactuated) position, the anchored and suspended comb fingers overlap over a length of $20\ \mu\text{m}$ (nominal). Notice that the gap between them will decrease to $1\ \mu\text{m}$ (nominal) when their overlap increases beyond $22.8\ \mu\text{m}$ (nominal). (b) Optical image showing a bank of interdigitated anchored and suspended comb fingers. The two segments of the anchored comb fingers are clearly visible in this image. (c) Magnified optical image of the area enclosed in the box in image b. The pointed tips of the suspended comb fingers are clearly visible in this image.

induced at the sidewall interface by the applied normal load, no counter-balancing unaccounted additional normal load is applied at it by the tangential arm.

5.6.3 Modeling

Since the geometry of a set of interdigitated anchored and suspended comb fingers is identical to that of a set of parallel plate capacitors, the electrostatic force (F) generated by a comb-drive actuator in the direction parallel to the length of the comb fingers is given by Eq. 5.6.1 [63].

$$F = \alpha\epsilon \frac{nt}{g^\beta} V^2 \quad (5.6.1)$$

Here, α and β , which are influenced by the design of the comb-drive, are parameters that account for the effects of fringing fields and levitation, ϵ is the dielectric constant of the material between the anchored and suspended comb fingers (in the case of our study, it is air), n is the number of suspended comb fingers in the comb-drive actuator, t is the thickness of the comb fingers, g is the gap between the anchored and suspended comb fingers and V is the applied voltage. For simplicity, the constants are lumped into a geometric parameter c . Therefore,

$$c = \alpha\epsilon \frac{nt}{g^\beta} \quad (5.6.2)$$

Accordingly Eq. 5.6.1 becomes,

$$F = cV^2 \quad (5.6.3)$$

The anchored comb fingers of the Sidewall Friction Tester developed in this study have two segments. Therefore, to distinguish between them, subscripts 1 and 2 will be used for the initial and final segments of the anchored comb fingers, respectively. Similarly, subscripts n and t will be used for the normal and tangential arms, respectively.

Accordingly,

$$c_{n1} = \alpha_{n1} \epsilon \frac{nt}{g_{n1}} \quad (5.6.4a)$$

$$c_{n2} = \alpha_{n2} \epsilon \frac{nt}{g_{n2}} \quad (5.6.4b)$$

$$c_{t1} = \alpha_{t1} \epsilon \frac{nt}{g_{t1}} \quad (5.6.4c)$$

$$c_{t2} = \alpha_{t2} \epsilon \frac{nt}{g_{t2}} \quad (5.6.4d)$$

Since the normal and tangential comb-drive actuators of the Sidewall Friction Tester are exactly identical to each other, therefore,

$$c_{n1} = c_{t1} = c_1 \quad (5.6.5a)$$

$$c_{n2} = c_{t2} = c_2 \quad (5.6.5b)$$

Combining Eq. 5.6.3 with Eqs. 5.6.5a and 5.6.5b gives,

$$F_{n1} = c_1 V_n^2 \quad (5.6.6a)$$

$$F_{n2} = c_2 V_n^2 \quad (5.6.6b)$$

$$F_{t1} = c_1 V_t^2 \quad (5.6.6c)$$

$$F_{t2} = c_2 V_t^2 \quad (5.6.6d)$$

Since in both (normal and tangential) arms, the push and pull drives are exactly identical to each other, the electrostatic forces generated by both the (push as well as pull) drives of the normal arm can be determined using the same Eqs. 5.6.6a and 5.6.6b and the electrostatic forces generated by both the (push as well as pull) drives of the tangential arm can be determined using the same Eqs. 5.6.6c and 5.6.6d.

As seen in Fig. 5.17, the design of the loading section is such that the normal arm is not aligned with the anchored posts (i.e., b is greater than a) in its unactuated (as-fabricated) position. However, before bringing the loading beam in contact with a post, the normal arm is aligned with the anchored posts. This is done by pulling the loading section to the left (see Fig. 5.17) using the tangential comb-drive actuator. The force (F_a) needed to align the normal arm with the anchored posts is given by Eq. 5.6.7.

$$F_a = k_t \delta_a \quad (5.6.7)$$

where, k_t is the combined effective spring constant of the thin beam that connects the normal arm to the loading section and all the folded beam flexures of the tangential arm, and δ_a is the distance by which the suspended comb fingers of the pull drive of the tangential arm must be displaced to align the normal arm with the anchored posts. Accordingly, from Fig. 5.17,

$$\delta_a = \frac{b - a}{2} \quad (5.6.8)$$

The stiffness of the thin beam that connects the normal arm to the U-beam is designed to be significantly lesser than the stiffnesses of the U-beam and the shuttle of the normal arm. Therefore, the U-beam and the shuttle of the normal arm are considered as rigid and the bending of the thin beam only is considered in the model of the Sidewall Friction Tester. Also, since δ_a (designed to be $4 \mu\text{m}$) is much smaller than the lengths of the supporting beams, which are $500 \mu\text{m}$ (nominal) long, and the length of the thin beam that connects the normal arm to the U-beam, which is $140 \mu\text{m}$ (nominal) long, the treatment of the folded beam flexures and the thin beam that connects the normal arm to the U-beam as linear elastic (Hookean) springs is valid [35]. The design of the tangential comb-drive actuator is such that a fraction of the length of suspended fingers overlaps with the final segments of the anchored

fingers when the tangential arm is displaced to a distance of δ_a in either direction from its unactuated position. Therefore, the tangential electrostatic force utilized in aligning the normal arm with the anchored posts is given by Eq. 5.6.9.

$$F_a = k_t \delta_a = c_2 V_a^2 \quad (5.6.9)$$

where, V_a is the voltage that is required to be applied to the tangential comb-drive actuator to align the normal arm with the anchored posts. Rearranging Eq. 5.6.9 gives,

$$\delta_a = \frac{c_2}{k_t} V_a^2 = G_{t2} V_a^2 \quad (5.6.10)$$

Accordingly, the transfer function G_{t2} is given by Eq. 5.6.11,

$$G_{t2} = \frac{c_2}{k_t} \quad (5.6.11)$$

Similarly, in the as-fabricated position, the sidewall surfaces of the loading beam and the corresponding anchored posts are separated by a distance of δ_c . Therefore, the force (F_c) required to bring the loading beam in contact with an anchored post is given by Eq. 5.6.12.

$$F_c = k_n \delta_c \quad (5.6.12)$$

where, k_n is the combined effective spring constant of the thin beam that connects the tangential arm to the loading section and all the folded beam flexures of the normal arm. Again, the stiffness of the thin beam that connects the tangential arm to the loading section is designed to be significantly lesser than the stiffnesses of the loading beam and the shuttle of the tangential arm. Therefore, the loading beam and the shuttle of the tangential arm are considered as rigid and the bending of the thin beam only is considered in the model of the Sidewall Friction Tester. Also, δ_c (designed to be 6 μm) is much smaller than the lengths of the supporting beams, which are 500

μm (nominal) long, and the length of the thin beam that connects the tangential arm to the loading section, which is $115 \mu\text{m}$ (nominal) long. Therefore, the treatment of the folded beam flexures and the thin beam that connects the tangential arm to the loading section as linear elastic (Hookean) springs is also valid [35]. Further, the design of the normal comb-drive actuator is also such that a fraction of the length of suspended comb fingers overlaps with the final segments of the anchored comb fingers when the normal arm is displaced to a distance of δ_c in either direction from its unactuated position. Therefore, the normal electrostatic force utilized in bringing the loading beam in contact with an anchored post is given by Eq. 5.6.13.

$$F_c = k_n \delta_c = c_2 V_c^2 \quad (5.6.13)$$

where, V_c is the voltage that is required to be applied to the normal comb-drive actuator to bring the loading beam in contact with an anchored post. Rearranging Eq. 5.6.13 gives,

$$\delta_c = \frac{c_2}{k_n} V_c^2 = G_{n2} V_c^2 \quad (5.6.14)$$

Accordingly, the transfer function G_{n2} is given by Eq. 5.6.15,

$$G_{n2} = \frac{c_2}{k_n} \quad (5.6.15)$$

The coefficient of static friction (μ_s) of the contacting sidewall surfaces can be determined using Eq. 5.6.16,

$$\mu_s = \frac{F_{t2,s} - F_a}{F_{n2,s} - F_c} \quad (5.6.16)$$

where, $F_{n2,s}$ and $F_{t2,s}$ are the total normal and tangential forces generated, at the instant of slip between the loading beam and the anchored post, using the normal and tangential comb-drive actuators, respectively. Substituting Eqs. 5.6.6b, 5.6.6d,

5.6.9 and 5.6.13 in Eq. 5.6.16 gives,

$$\mu_s = \frac{V_{t,s}^2 - V_a^2}{V_{n,s}^2 - V_c^2} \quad (5.6.17)$$

After the initiation of slip at the sidewall interface, the loading beam continues to slide in contact with the anchored post until the sum of the restoring force generated by the folded beam flexures of the tangential arm and the thin beam that connects the normal arm to the U-beam and the kinetic friction force becomes equal to the tangential force generated using the tangential comb-drive actuator. Therefore, the coefficient of kinetic friction (μ_k) of the contacting sidewall surfaces can be determined using Eq. 5.6.18,

$$\mu_k = \frac{F_{t2,s} - F_a - k_t \delta_s}{F_{n2,s} - F_c} \quad (5.6.18)$$

where, δ_s is the distance for which the loading beam slides in contact with the anchored post after the initiation of slip at the sidewall interface. Substituting Eqs. 5.6.6b, 5.6.6d, 5.6.9, 5.6.11 and 5.6.13 in Eq. 5.6.18 gives,

$$\mu_k = \frac{V_{t,s}^2 - V_a^2 - (\delta_s / G_{t2})}{V_{n,s}^2 - V_c^2} \quad (5.6.19)$$

It should be noted that the additional normal load experienced by the sidewall interface due to adhesion between the contacting sidewall surfaces is not considered in Eqs. 5.6.16 and 5.6.18. Therefore, the coefficients of friction determined using Eqs. 5.6.16 and 5.6.18 are engineering coefficients of friction.

5.6.4 Testing Procedure

To actuate the Sidewall Friction Tester (SFT), the electrical contacts are made by touching the actuation pads that are fabricated in the Sidewall Friction Tester with

sharp tungsten probe tips (Signatone SE-20T). The voltages applied to the comb-drive actuators of the Sidewall Friction Tester are generated using a digital-to-analog converter (DAC) and amplified using a high-voltage amplifier (TEGAM, 2350S).

Before actuating each SFT, a and b (see Fig. 5.17) are measured for that SFT, optically with a resolution of $\pm 0.465 \mu\text{m}$, to determine δ_t . The resolution, with which the optical measurements are made, is limited by the size of the pixels in the field of view, which is $0.465 \mu\text{m} \times 0.465 \mu\text{m}$ (objective lens used is Mitutoyo M Plan Apo 10). Next, the restoring forces generated in the normal and tangential arms in response of their displacements are calibrated in order to determine the transfer functions G_{n2} and G_{t2} , respectively. To calibrate the restoring forces generated in the tangential arm, the ground plane (substrate), the suspended movable structure, the anchored posts and the anchored comb fingers of the push drive of the tangential arm are electrically grounded and, a DC voltage is applied to the anchored comb fingers of the pull drive of the tangential arm. The applied voltage is ramped up from 0 V at a rate of 1 V/s to 32 V and the corresponding displacements of the tangential arm are determined using a pattern matching technique. The script used to calibrate the tangential arm of the Sidewall Friction Tester is given in Appendix A.6. To calibrate the restoring forces generated in the normal arm, first, the normal arm is aligned with the anchored posts. This is done by electrically grounding the ground plane (substrate), the suspended movable structure and the anchored post and, applying a DC voltage, which is ramped up from 0 V at a rate of 1 V/s to V_a , to the anchored comb fingers of the pull drive of the tangential arm. Then, the anchored comb fingers of the push drive of the normal arm are electrically grounded and a DC voltage is applied to the anchored comb fingers of the pull drive of the normal arm. The voltage applied to the anchored comb-fingers of the pull drive of the normal arm is ramped up from 0 V at a rate of 1 V/s to 40 V. The position of the loading beam after the normal arm is aligned with the anchored posts is considered as the initial

position and the displacements of the normal arm for each voltage applied to its pull drive are determined using the pattern matching technique. The script used to calibrate the normal arm of the Sidewall Friction Tester is given in Appendix A.7. The patterns that are used to track the positions of the normal and tangential arms during the calibration of the restoring forces generated in them are shown in Fig. 5.14. In addition to determining the G_{t2} , the plot of displacement (of the shuttle of the tangential arm) versus V_t^2 is also used to determine the voltage required to align the normal arm with the anchored posts (i.e., V_a). Similarly, in addition to determining the G_{n2} , the plot of displacement (of the shuttle of the normal arm) versus V_n^2 is also used to determine the voltage required to bring the loading beam in contact with the anchored post (i.e., V_c).

To study the friction characteristics of the contacting sidewall surfaces, the ground plane (substrate), the suspended movable structure and the anchored posts are electrically grounded and a DC voltage is applied to the anchored comb fingers of the pull drives of the tangential and normal arms. First, the voltage applied to the pull drive of the tangential arm is ramped up from 0 V at a rate of 1 V/s to V_a , at which point, the normal arm becomes aligned with the anchored posts. Next, the voltage applied to the pull drive of the normal arm is ramped up from 0 V at a rate of 1 V/s to V_N , which is the voltage that should be applied to the pull drive of the normal arm so that it generates an electrostatic force that corresponds to the external normal load that is desired to be applied at the sidewall interface. The position of the tangential arm (loading beam) at this point is considered as the initial position. After allowing the sidewall interface to equilibrate for 1 min., the voltage applied to the pull drive of the tangential arm is increased beyond V_a at a rate of 0.2 V/s until a slip is initiated at the sidewall interface. The onset of slip between the contacting sidewall surfaces is detected by monitoring the position of the loading beam using the pattern matching technique. The pattern matching technique collects optical images of the

loading section at every increment of the voltage applied to the tangential comb-drive actuator, and uses them to determine the position of the movable pattern relative to its corresponding anchored pattern at every voltage applied to the tangential comb-drive actuator. The pattern matching technique is also used to determine δ_s , which is the distance for which the loading beam slides in contact with the anchored post after the initiation of slip at the sidewall interface. The script used for studying the friction characteristics of the contacting sidewall surfaces, using the SFT, is given in Appendix A.8.

To study the wear characteristics of the contacting sidewall surfaces, the ground plane (substrate), the suspended movable structure and the anchored posts are electrically grounded, an AC voltage with a DC bias is applied to the anchored comb fingers of the pull drive of the tangential arm and a DC voltage is applied to the anchored comb fingers of the pull drive of the normal arm. First, a DC bias, which is ramped up from 0 V at a rate of 1 V/s to V_a , is applied to the pull drive of the tangential arm. At this point, the normal arm becomes aligned with the anchored posts. Next, a DC voltage is applied to the pull drive of the normal arm. The voltage applied to the pull drive of the normal arm is also ramped up from 0 V at a rate of 1 V/s to V_N , which is the voltage that should be applied to the pull drive of the normal arm so that it generates an electrostatic force that corresponds to the external normal load that is desired to be applied at the sidewall interface. After allowing the sidewall interface to equilibrate for 1 min., an AC voltage is superimposed on the DC bias applied to the pull drive of the tangential arm. Wear of the contacting sidewall surfaces can be qualitatively studied by determining the change in their friction coefficients with the accumulation of wear cycles [126, 128, 144].

5.7 Sidewall Friction and Adhesion Tester (SFAT)

The Sidewall Friction and Adhesion Tester can also be used to study the friction and wear characteristics of contacting sidewall surfaces. Additionally, it can be used to determine the adhesion force experienced by contacting sidewall surfaces.

5.7.1 Design

The fundamental design of the Sidewall Friction and Adhesion Tester (SFAT) developed in this study is a modified version of that of the microinstrument designed by Timpe et al. [23]. An optical image of a released SFAT is shown in Fig. 5.18. As seen in Fig. 5.18, the SFAT mainly consists of two comb-drive actuators, which are placed in such a way that their shuttles move in orthogonal directions. One comb-drive actuator (normal arm) is used to form the sidewall interface by bringing the flat sidewall surface of the “loading block” attached to its shuttle in contact with the flat sidewall surface of the “friction block” protruding out of the shuttle of the other comb-drive actuator. The normal arm is also used to apply the normal load at the sidewall interface. The other comb-drive actuator (tangential arm) is used to shear the sidewall interface. Each of the two comb-drive actuators have one push drive and one pull drive (see Fig. 5.19), which allows both the “loading block” as well as the “friction block” to be moved both forward as well as backward from their unactuated positions.

In the normal arm of the SFAT, both the push drive as well as the pull drive have two identical banks of interdigitated anchored and suspended comb fingers. Each of the four banks of comb fingers of the normal have 26 anchored comb fingers and 25 movable comb fingers, all of which are 20 μm (nominal) long and 3 μm (nominal) wide. The shuttle of the normal arm of the SFAT is suspended using two identical folded beam flexures. Each folded beam flexure of the normal arm consists of four identical supporting beams, which are connected to each other by a truss. All the supporting

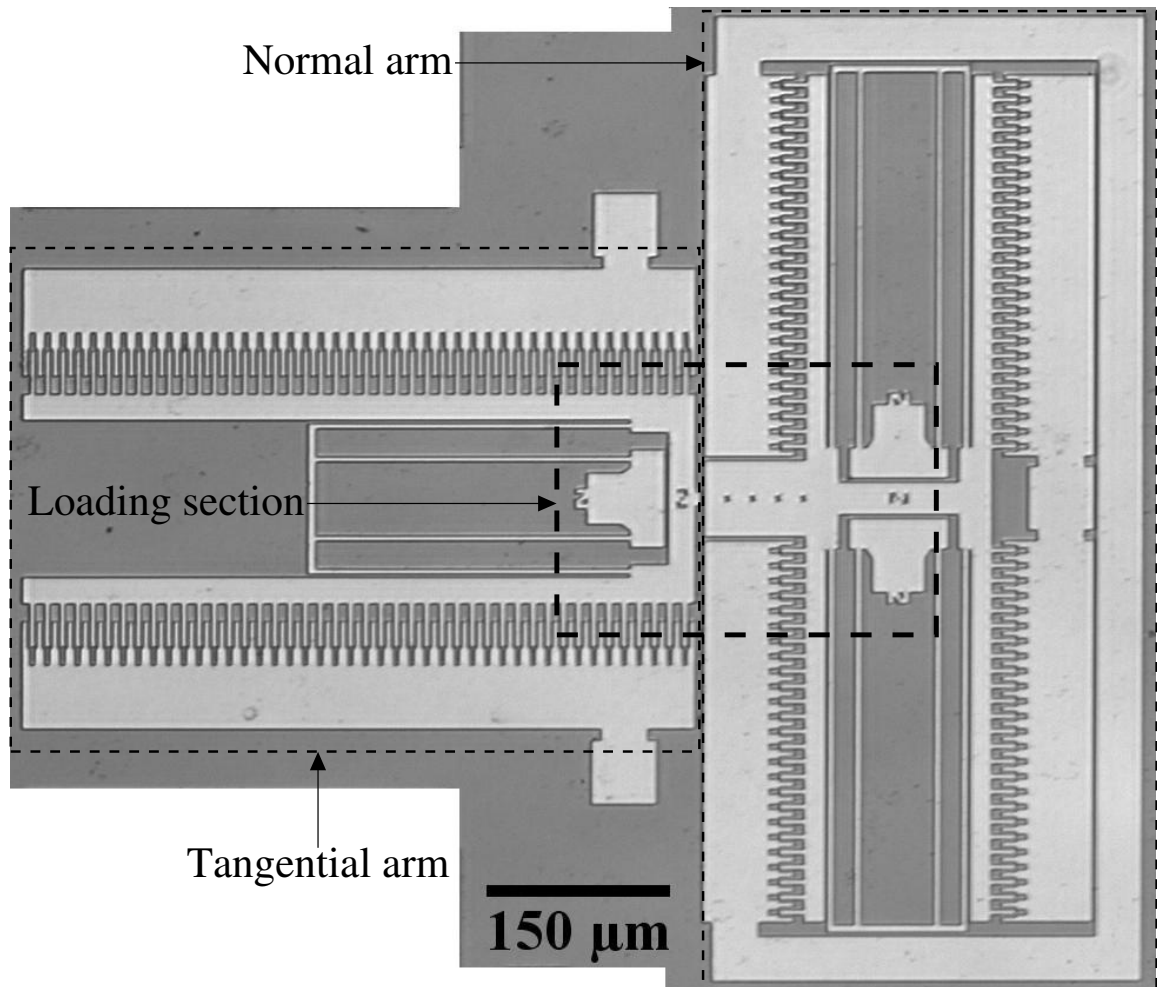
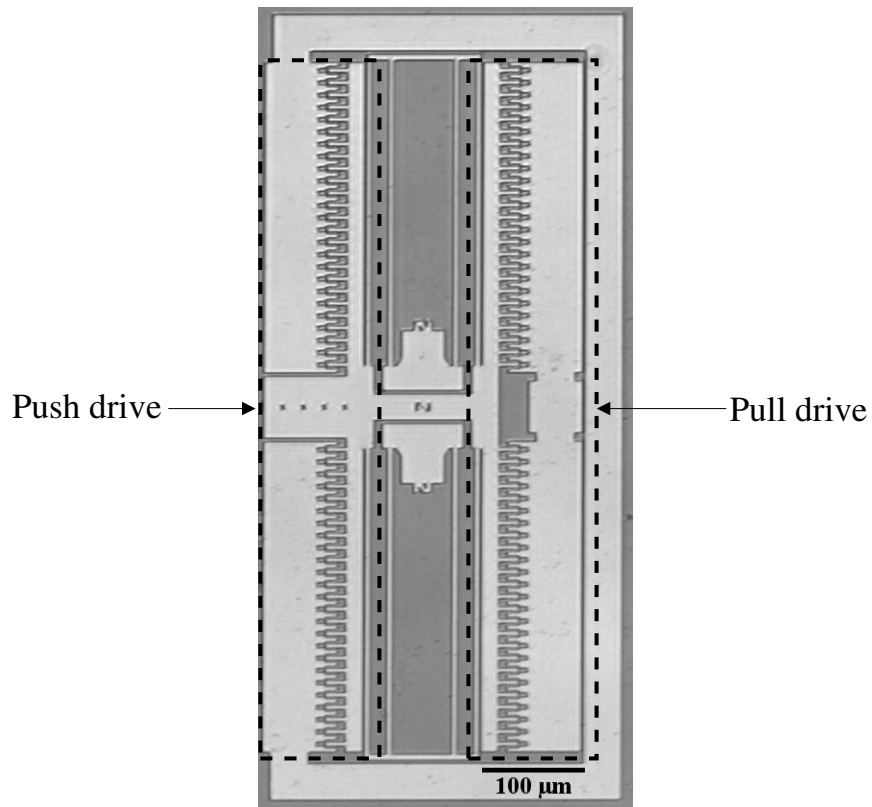


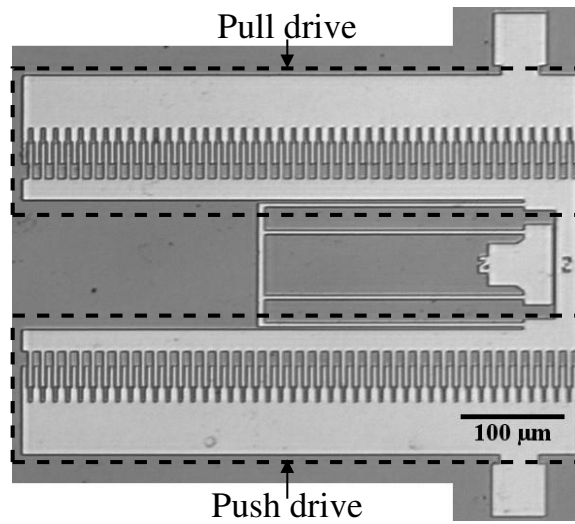
Figure 5.18: Optical image of a released Sidewall Friction and Adhesion Tester (SFAT). Notice the ground plane present underneath the entire device. The total footprint of the microinstrument is 0.47 mm^2 .

beams, which suspend the shuttle of the normal arm, are $300\ \mu\text{m}$ (nominal) long and $3\ \mu\text{m}$ wide (nominal). In the tangential arm of the SFAT, both the push drive as well as the pull drive have only one bank of 45 anchored comb fingers and 44 movable comb fingers. All the comb fingers of the tangential arm are $35\ \mu\text{m}$ (nominal) long and $3\ \mu\text{m}$ (nominal) wide. The shuttle of the tangential arm of the SFAT is suspended using only one folded beam flexure, which consists of four identical supporting beams that are also connected to each other by a truss. All the supporting beams, which suspend the shuttle of the tangential arm, are $250\ \mu\text{m}$ (nominal) long and $3\ \mu\text{m}$ wide (nominal).

The same rationale that was used to explain the segmental design of the anchored comb fingers, and the unique pointed tips of all the comb fingers, of the SFT is also the reason behind the segmental design of the anchored comb fingers, and the unique pointed tips of all the comb fingers, of the SFAT. The initial and final segments of the anchored comb fingers of the normal arm are $12.8\ \mu\text{m}$ (nominal) and $7.2\ \mu\text{m}$ (nominal) long, respectively. The gap between the initial segments of adjacent anchored comb fingers of the normal arm is $9\ \mu\text{m}$ (nominal), which reduces to $5\ \mu\text{m}$ (nominal) between their final segments. The initial and final segments of the anchored comb fingers of the tangential arm are $22.8\ \mu\text{m}$ (nominal) and $12.2\ \mu\text{m}$ (nominal) long, respectively. The gap between the initial segments of adjacent anchored comb fingers of the tangential arm is also $9\ \mu\text{m}$ (nominal) and reduces to $5\ \mu\text{m}$ (nominal) between their final segments. Further, similar to the comb fingers of the SFT (as explained in Fig. 5.16a), in the as-fabricated (unactuated) position, in which, they overlap over a length of $10\ \mu\text{m}$ (nominal), the gap between a suspended comb finger and the initial segment of the corresponding anchored comb finger of the normal arm is designed to be $3\ \mu\text{m}$ (nominal), which reduces to $1\ \mu\text{m}$ (nominal) as the displacement of the shuttle of the normal arm increases beyond $2.8\ \mu\text{m}$ (nominal). In the as-fabricated (unactuated) position, in which, they overlap over a length of $20\ \mu\text{m}$ (nominal), the



(a)

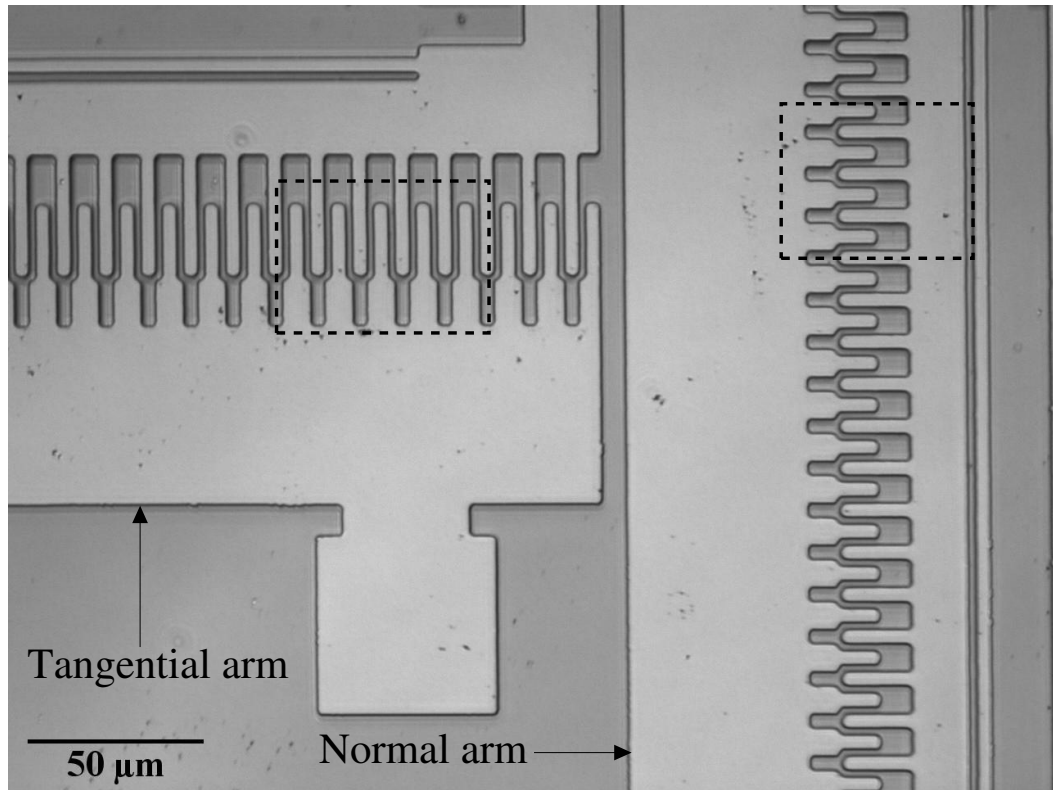


(b)

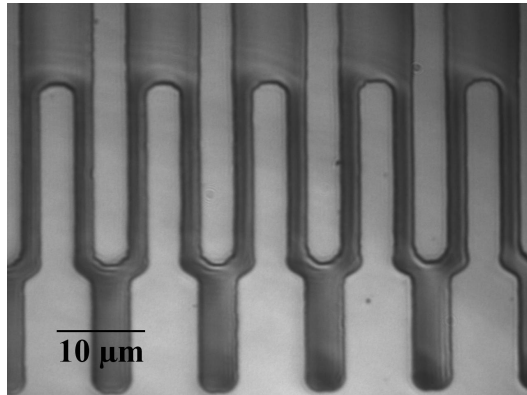
Figure 5.19: (a) Optical image showing the normal arm of a released Sidewall Friction and Adhesion Tester (SFAT). (b) Optical image showing the tangential arm of a released Sidewall Friction and Adhesion Tester (SFAT). Notice that both the normal and the tangential arm have one push drive and one pull drive each.

gap between a suspended comb finger and the initial segment of the corresponding anchored comb finger of the tangential arm is also designed to be $3 \mu\text{m}$ (nominal), and reduces to $1 \mu\text{m}$ (nominal) as the displacement of its shuttle increases beyond $2.8 \mu\text{m}$ (nominal). Accordingly, like the comb-drive actuators of the normal and tangential arms of the SFT, as the displacements of the shuttles of the normal and tangential arms of the SFAT increase beyond $2.8 \mu\text{m}$ (nominal), the electrostatic force generating capacities of their corresponding comb-drive actuators also increase by a factor of three. Figure 5.20a is an optical image showing one bank of comb fingers each of the normal and tangential arms of a released Sidewall Friction and Adhesion Tester (SFAT). The segmental designs of the anchored comb fingers of both the normal as well as tangential arms, which are in their as-fabricated (unactuated) positions, of the SFAT are clearly seen in this image. Figure 5.20b is a magnified optical image showing the comb fingers of the tangential arm of the SFAT, that are enclosed in the box in Fig. 5.20a. Figure 5.20c is a magnified optical image showing the comb fingers of the normal arm of the SFAT, that are enclosed in the box in Fig. 5.20a. The pointed tips of the suspended comb fingers, which are in their as-fabricated (unactuated) positions, of the tangential and normal arms of the SFAT are clearly seen in Fig. 5.20b and Fig. 5.20c, respectively.

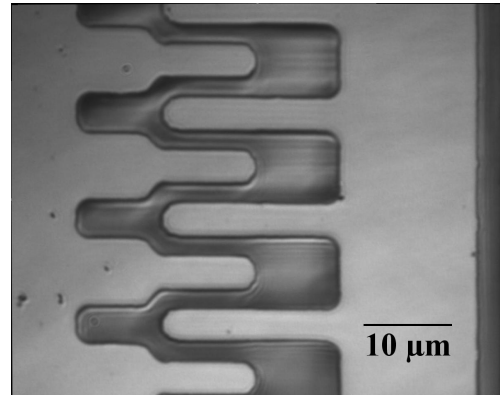
Figure 5.21 is an optical image showing the loading section of a released (unpolished) SFAT in its as-fabricated position. The anchored and suspended patterns that are used to track the displacements of the normal and tangential arms are clearly labelled in Fig. 5.21. Also, it is clearly visible in Fig. 5.21 that in their as-fabricated positions, the “loading block” and the “friction block” are designed to be $4 \mu\text{m}$ (nominal) apart from each other, which ensures that the overlap of the anchored and suspended comb fingers of the push drive of the normal arm of the SFAT becomes greater than $12.8 \mu\text{m}$ when the sidewall interface is formed. The contact area of the



(a)



(b)



(c)

Figure 5.20: (a) Optical image showing one bank of interdigitated comb fingers each of the normal and tangential arms of a released Sidewall Friction and Adhesion Tester (SFAT). The two segments of the anchored comb fingers are clearly visible in this image. (b) Magnified optical image showing the comb fingers of the tangential arm of the SFAT, that are enclosed in the box in Fig. 5.20a. (c) Magnified optical image showing the comb fingers of the normal arm of the SFAT, that are enclosed in the box in Fig. 5.20a. The pointed tips of the suspended comb fingers are clearly visible in both Fig. 5.20b and Fig. 5.20c.

sidewall interface formed by the sidewall surfaces of the “loading block” and the “friction block” is defined by the dimensions of the “friction block”. The friction block is 10 μm (nominal) long, and protrudes 4 μm (nominal) out, from the shuttle of the tangential arm of the SFAT.

5.7.2 Modeling

As explained in section 5.6.3, the electrostatic force (F) generated by a comb-drive actuator in the direction parallel to the length of its comb fingers is given by Eq. 5.7.1.

$$F = cV^2 \quad (5.7.1)$$

where,

$$c = \alpha \epsilon \frac{nt}{g^\beta} \quad (5.7.2)$$

Here, α and β , which are influenced by the design of the comb-drive, are parameters that account for the effects of fringing fields and levitation, ϵ is the dielectric constant of the material between the anchored and suspended comb fingers (in the case of our study, it is air), n is the number of suspended comb fingers in the comb-drive actuator, t is the thickness of the comb fingers, g is the gap between the anchored and suspended comb fingers and V is the applied voltage. Also, since the anchored comb fingers of the Sidewall Friction and Adhesion Tester developed in this study also have two segments, to distinguish between them, subscripts 1 and 2 will be used for their initial and final segments, respectively. Similarly, subscripts n and t will be

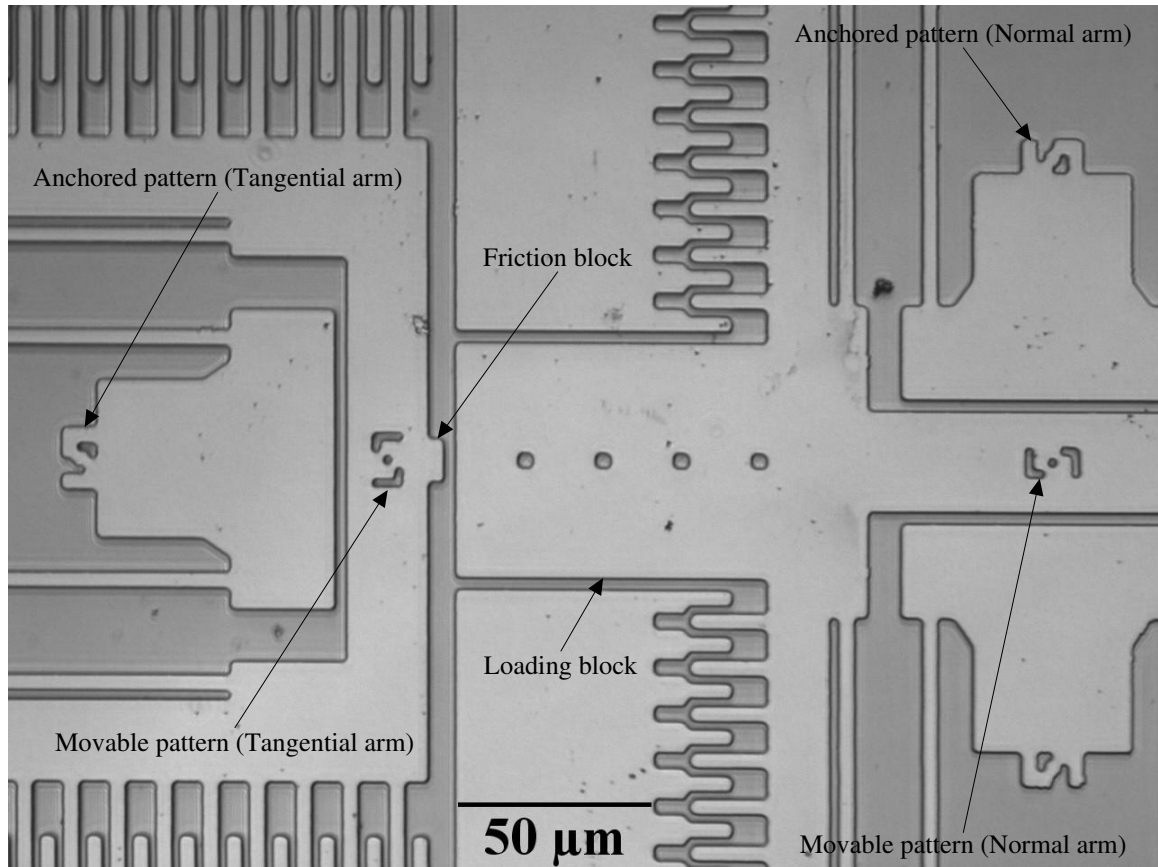


Figure 5.21: Optical image showing the loading section of a released Sidewall Friction and Adhesion Tester. The loading section is in its as-fabricated (unactuated) position. Notice the gap between the loading block and the friction block. It is designed to be $4\mu\text{m}$ (nominal) in their as-fabricated positions. The anchored and suspended patterns that are used to track the displacements of the normal and tangential arms are clearly labelled in the image.

used for the normal and tangential arms, respectively. Accordingly,

$$c_{n1} = \alpha_{n1} \epsilon \frac{nt}{g_{n1}} \quad (5.7.3a)$$

$$c_{n2} = \alpha_{n2} \epsilon \frac{nt}{g_{n2}} \quad (5.7.3b)$$

$$c_{t1} = \alpha_{t1} \epsilon \frac{nt}{g_{t1}} \quad (5.7.3c)$$

$$c_{t2} = \alpha_{t2} \epsilon \frac{nt}{g_{t2}} \quad (5.7.3d)$$

Combining Eq. 5.7.1 with Eqs. 5.7.3a, 5.7.3b, 5.7.3c, and 5.7.3d gives,

$$F_{n1} = c_{n1} V_n^2 \quad (5.7.4a)$$

$$F_{n2} = c_{n2} V_n^2 \quad (5.7.4b)$$

$$F_{t1} = c_{t1} V_t^2 \quad (5.7.4c)$$

$$F_{t2} = c_{t2} V_t^2 \quad (5.7.4d)$$

Since in both (normal and tangential) arms, the push and pull drives are exactly identical to each other, the electrostatic forces generated by both the (push as well as pull) drives of the normal arm can be determined using the same Eqs. 5.7.4a and 5.7.4b and the electrostatic forces generated by both the (push as well as pull) drives of the tangential arm can be determined using the same Eqs. 5.7.4c and 5.7.4d.

As seen in Fig. 5.21, the design of the loading section of the SFAT is such that in the as-fabricated position, the sidewall surfaces of the loading block and the friction block are separated by a distance of δ_c . Therefore, the force (F_c) required to bring the sidewall surface of the loading block in contact with that of the friction block is given by Eq. 5.7.5.

$$F_c = k_n \delta_c \quad (5.7.5)$$

Here, k_n is the combined effective spring constant of the two folded beam flexures of the normal arm. Since δ_c (designed to be $4 \mu\text{m}$) is much smaller than the lengths of the supporting beams, which are $300 \mu\text{m}$ (nominal) long, the treatment of the folded beam flexures of the normal arm as linear elastic (Hookean) springs is valid [35]. Further, the design of the normal comb-drive actuator is such that a fraction of the length of suspended fingers overlaps with the final segments of the anchored fingers when the shuttle of the normal arm is displaced by a distance of δ_c in either direction from its unactuated position. Therefore, the normal electrostatic force utilized in forming the sidewall interface is given by Eq. 5.7.6.

$$F_c = k_n \delta_c = c_{n2} V_c^2 \quad (5.7.6)$$

Here, V_c is the voltage that is required to be applied to the normal comb-drive actuator to bring the sidewall surface of the loading block in contact with that of the friction block. Rearranging Eq. 5.7.6 gives,

$$\delta_c = \frac{c_{n2}}{k_n} V_c^2 = G_{n2} V_c^2 \quad (5.7.7)$$

Accordingly, the transfer function G_{n2} is given by Eq. 5.7.8,

$$G_{n2} = \frac{c_{n2}}{k_n} \quad (5.7.8)$$

Since in the as-fabricated position, the suspended comb fingers of the tangential arm overlap only with the initial segments of the corresponding anchored fingers, the coefficient of static friction (μ_s) of the contacting sidewall surfaces can be determined using Eq. 5.7.9,

$$\mu_s = \frac{F_{t1,s}}{F_{n2,s} - F_c} \quad (5.7.9)$$

Here, $F_{n2,s}$ and $F_{t1,s}$ are the total normal and tangential forces generated, at the instant of slip between the loading block and the friction block, using the normal and tangential comb-drive actuators, respectively. Substituting Eqs. 5.7.4b, 5.7.4c and 5.7.6 in Eq. 5.7.9 gives,

$$\mu_s = \frac{c_{t1}V_{t,s}^2}{c_{n2}(V_{n,s}^2 - V_c^2)} \quad (5.7.10)$$

After the initiation of slip at the sidewall interface, the friction block continues to slide in contact with the loading block until the sum of the restoring force generated by the folded beam flexure of the tangential arm and the kinetic friction force becomes equal to the tangential force generated using the tangential comb-drive actuator. Therefore, the coefficient of kinetic friction (μ_k) of the contacting sidewall surfaces can be determined using Eq. 5.7.11,

$$\mu_k = \frac{F_{t1,s} - k_t\delta_s}{F_{n2,s} - F_c} \quad (5.7.11)$$

Here, δ_s is the distance, for which, the friction block slides in contact with the loading block after the initiation of slip at the sidewall interface. Substituting Eqs. 5.7.4b, 5.7.4c and 5.7.6 in Eq. 5.7.11 gives,

$$\mu_k = \frac{c_{t1}V_{t,s}^2 - k_t\delta_s}{c_{n2}(V_{n,s}^2 - V_c^2)} \quad (5.7.12)$$

The restoring force generated in the folded beam flexure of the tangential arm in response to the displacement of its shuttle to a distance of δ_s is given by Eq. 5.7.13.

$$F_r = k_t\delta_s \quad (5.7.13)$$

Here, k_t is the combined effective spring constant of the folded beam flexure of the tangential arm. Again, since δ_s is usually much smaller (typically a few μm) than the lengths of the supporting beams, which are 250 μm (nominal) long, the treatment

of the folded beam flexure of the tangential arm as linear elastic (Hookean) springs is valid [35]. The equivalent tangential electrostatic force required to displace the shuttle of the tangential arm by a distance of δ_s can be given by Eq. 5.7.14.

$$F_r = k_t \delta_s = c_{t1} V_e^2 \quad (5.7.14)$$

Here, V_e is the voltage that is required to be applied to the tangential comb-drive actuator to displace the shuttle of the tangential arm by a distance of δ_s . Rearranging Eq. 5.7.14 gives,

$$\delta_s = \frac{c_{t1}}{k_t} V_e^2 = G_{t1} V_e^2 \quad (5.7.15)$$

Accordingly, the transfer function G_{t1} is given by Eq. 5.7.16,

$$G_{t1} = \frac{c_{t1}}{k_t} \quad (5.7.16)$$

Substituting Eq. 5.7.8 and Eq. 5.7.16 in Eq. 5.7.10 gives,

$$\mu_s = \left(\frac{k_t}{k_n} \right) \left(\frac{G_{t1}}{G_{n2}} \right) \left(\frac{V_{t,s}^2}{V_{n,s}^2 - V_c^2} \right) \quad (5.7.17)$$

Similarly, substituting Eq. 5.7.8 and Eq. 5.7.16 in Eq. 5.7.12 gives,

$$\mu_k = \left(\frac{k_t}{k_n} \right) \left[\frac{G_{t1} V_{t,s}^2 - \delta_s}{G_{n2} (V_{n,s}^2 - V_c^2)} \right] \quad (5.7.18)$$

Referring to the derivation of Eq. 5.3.4, k_t can be given by Eq. 5.7.19.

$$k_t = E t_t \left(\frac{w_t}{L_t} \right)^3 \quad (5.7.19)$$

Here, E is the elastic modulus of the structural film, t_t is the thickness of the supporting beams of the tangential arm, which in the case of the SFAT developed in this

study, is the thickness of the structural film, w_n and L_n are the width and length of the supporting beams of the tangential arm, respectively. Similarly, k_n can be given by Eq. 5.7.20.

$$k_n = 2Et_n \left(\frac{w_n}{L_n} \right)^3 \quad (5.7.20)$$

where, t_n is the thickness of the supporting beams of the normal arm, which again in the case of the SFAT developed in this study, is the thickness of the structural film, w_n and L_n are the width and length of the supporting beams of the normal arm, respectively. Dividing Eq. 5.7.19 by Eq. 5.7.20 gives,

$$\frac{k_t}{k_n} = \frac{1}{2} \left(\frac{L_n}{L_t} \right)^3 \quad (5.7.21)$$

Substituting Eq. 5.7.21 in Eq. 5.7.17 gives Eq 5.7.22, which can be used to determine the coefficient of static friction of the contacting sidewall surfaces of the SFAT.

$$\mu_s = \frac{1}{2} \left(\frac{L_n}{L_t} \right)^3 \left(\frac{G_{t1}}{G_{n2}} \right) \left(\frac{V_{t,s}^2}{V_{n,s}^2 - V_c^2} \right) \quad (5.7.22)$$

Similarly, substituting Eq. 5.7.21 in Eq. 5.7.18 gives Eq 5.7.23, which can be used to determine the coefficient of kinetic friction of the contacting sidewall surfaces of the SFAT.

$$\mu_k = \frac{1}{2} \left(\frac{L_n}{L_t} \right)^3 \left[\frac{G_{t1} V_{t,s}^2 - \delta_s}{G_{n2} (V_{n,s}^2 - V_c^2)} \right] \quad (5.7.23)$$

The transfer functions G_{t1} and G_{n2} are determined experimentally. It should be noted that the additional normal load experienced by the sidewall interface due to adhesion between the contacting sidewall surfaces is not considered in Eqs. 5.7.9 and 5.7.11. Therefore, the coefficients of friction determined using Eqs. 5.7.22 and 5.7.23 are engineering coefficients of friction.

If the displacement of the shuttle of the tangential arm during the first slip event causes a fraction of the length of its suspended comb fingers to overlap with the final

segments of the corresponding anchored comb fingers, then the coefficient of kinetic friction of the contacting sidewall surfaces of the SFAT is given by Eq.5.7.24 shown below:

$$\mu_k = \frac{1}{2} \left(\frac{L_n}{L_t} \right)^3 \left[\frac{G_{t2} V_{t,s}^2 - \delta_s}{G_{n2} (V_{n,s}^2 - V_c^2)} \right] \quad (5.7.24)$$

The transfer function G_{t2} , which is also determined experimentally, is given by Eq. 5.7.25 shown below:

$$G_{t2} = \frac{c_{t2}}{k_t} \quad (5.7.25)$$

5.7.3 Testing Procedure

To actuate the Sidewall Friction and Adhesion Tester (SFAT), the electrical contacts are made by touching the actuation pads that are fabricated in the Sidewall Friction and Adhesion Tester with sharp tungsten probe tips (Signatone SE-20T). The voltages applied to the comb-drive actuators of the Sidewall Friction and Adhesion Tester are generated using a digital-to-analog converter (DAC) and amplified using a high-voltage amplifier (TEGAM, 2350S).

Before actuating each SFAT, the lengths of the supporting beams of its normal and tangential arms (i.e., L_n and L_t) are measured, optically with a resolution of $\pm 0.465 \mu\text{m}$. The resolution, with which the optical measurements are made, is limited by the size of the pixels in the field of view, which is $0.465 \mu\text{m} \times 0.465 \mu\text{m}$ (objective lens used is Mitutoyo M Plan Apo 10). Next, the restoring forces generated in the normal and tangential arms in response of the displacements of their shuttles are calibrated in order to determine the transfer functions G_{n2} , G_{t1} and G_{t2} , respectively. To calibrate the restoring forces generated in the tangential arm, the ground plane (substrate) and the suspended movable structure as well as the anchored comb fingers of the pull drive of the tangential arm are electrically grounded, and a DC voltage is applied to the anchored comb fingers of the push drive of the tangential arm. The applied voltage is ramped up from 0 V at a rate of 1 V/s to 55 V and the corresponding

displacements of the shuttle of the tangential arm are determined using a pattern matching technique. The script used to calibrate the tangential arm of the Sidewall Friction and Adhesion Tester is given in Appendix A.6. To calibrate the restoring forces generated in the normal arm, the ground plane (substrate) and the suspended movable structure as well as the anchored comb fingers of the pull drive of the normal arm are electrically grounded, and a DC voltage is applied to the anchored comb fingers of the push drive of the normal arm. The voltage applied to the anchored comb-fingers of the push drive of the normal arm is ramped up from 0 V at a rate of 1 V/s to 40 V. The displacements of the shuttle of the normal arm for each voltage applied to its push drive are determined using the pattern matching technique. The script used to calibrate the normal arm of the Sidewall Friction and Adhesion Tester is given in Appendix A.6. The patterns that are used to track the displacements of the normal and tangential arms during the calibration of the restoring forces generated in them are shown in Fig. 5.21. The plot of displacement (of the shuttle of the tangential arm) versus V_t^2 is used to determine the transfer functions G_{t1} and G_{t2} . Similarly, the plot of displacement (of the shuttle of the normal arm) versus V_n^2 is used to determine the transfer function G_{n2} . In addition to determining the G_{n2} , the plot of displacement (of the shuttle of the normal arm) versus V_n^2 is also used to determine the voltage required to bring the loading block in contact with the friction block (i.e., V_c).

To study the friction characteristics of the contacting sidewall surfaces of the SFAT, the ground plane (substrate) and the suspended movable structures of the normal and tangential arms are electrically grounded, and a DC voltage is applied to the anchored comb fingers of the push drives of the normal and tangential arms. First, the voltage applied to the push drive of the normal arm is ramped up from 0 V at a rate of 1 V/s to V_N , which is the voltage that should be applied to the push drive of the normal arm so that it generates an electrostatic force that corresponds

to the external normal load that is desired to be applied at the sidewall interface. The position of the tangential arm (i.e., friction block) at this point is considered as the initial position. After allowing the sidewall interface to equilibrate for 1 min., the voltage applied to the push drive of the tangential arm is increased from 0 V at a rate of 1 V/s until a slip is initiated at the sidewall interface. The onset of slip between the contacting sidewall surfaces of the SFAT is detected by monitoring the position of the friction block using the pattern matching technique. The pattern matching technique is also used to determine δ_s , which is the distance, for which, the friction block slides in contact with the loading block after the initiation of slip at the sidewall interface. The script used for studying the friction characteristics of the contacting sidewall surfaces, using the SFAT, is given in Appendix A.9.

To study the wear characteristics of the contacting sidewall surfaces of the SFAT, the ground plane (substrate) and the suspended movable structures of the normal and tangential arms are electrically grounded, a DC voltage is applied to the anchored comb fingers of the push drive of the normal arm and an AC voltage is applied to the anchored comb fingers of the push drive of the tangential arm. First, a DC voltage is applied to the push drive of the normal arm. The voltage applied to the push drive of the normal arm is ramped up from 0 V at a rate of 1 V/s to V_N , which is the voltage that should be applied to the push drive of the normal arm so that it generates an electrostatic force that corresponds to the external normal load that is desired to be applied at the sidewall interface. After allowing the sidewall interface to equilibrate for 1 min., an AC voltage is applied to the push drive of the tangential arm. Wear of the contacting sidewall surfaces of the SFAT can be qualitatively studied by determining the change in their friction coefficients with the accumulation of wear cycles [126, 128, 144].

To determine the adhesion force experienced by the contacting sidewall surfaces of the SFAT, the ground plane (substrate) and the suspended movable structures of

the normal and tangential arms are electrically grounded, and a DC voltage is applied to the anchored comb fingers of both the push as well as the pull drives of the normal arm. First, the voltage applied to the push drive of the normal arm is ramped up from 0 V at a rate of 1 V/s to V_N , which is the voltage that should be applied to the push drive of the normal arm so that it generates an electrostatic force that corresponds to the external normal load that is desired to be applied at the sidewall interface. Next, after allowing the sidewall interface to equilibrate for 1 min., the DC voltage applied to the pull drive of the normal arm is increased from 0 V at a rate of 0.2 V/s until the two sidewall surfaces that form the sidewall interface are separated from each other. The instant of separation of the contacting sidewall surfaces of the SFAT is detected by monitoring the position of the loading block using the pattern matching technique. The adhesion force experienced by the contacting sidewall surfaces of the SFAT is the difference between the electrostatic forces generated by the push and pull drives of the normal arm at the instant of separation of the contacting sidewall surfaces. The script used to determine the adhesion force experienced by the contacting sidewall surfaces, using the SFAT, is given in Appendix A.10.

Chapter 6

Processes and Techniques Used: Experimental, Analytical, Surface Characterization & Metrology

This chapter briefly discusses all the experimental, analytical, surface characterization and metrology processes/techniques that are used in this study. The processes discussed in this chapter include those that are used for releasing the microinstruments of the Test Platform, coating the surfaces of the microinstruments of the Test Platform with OTS SAM, the synthesis of gold nanoparticles used for tailoring the topography of the test surfaces of the Test Platform and depositing gold nanoparticles on the test surfaces of the Test Platform to tailor their topography. The techniques discussed in this chapter include those that are used for characterizing the gold nanoparticles used to tailor the topography of the test surfaces that are investigated in this study, characterizing the topography of the tailored test surfaces of the Test Platform, characterizing the chemistry of the test surfaces of the Test Platform, characterizing the thickness of the OTS SAM coating investigated in this study and determining the height profile of an actuated cantilever beam.

6.1 Process Used to Release the Microinstruments of the Test Platform

The first step in utilizing the microinstruments of the Test Platform to study the tribology of MEMS interfaces is to “release” them. The microinstruments need to be released before they can be used for testing. The microinstrument release procedure begins with cleaning of the Test Platform chip to strip-off the patterned photoresist layer from it. The microinstruments developed in this study are released by etching the sacrificial layer underlying the device layer in a concentrated solution

of HF (Fischer Scientific, Reagent A.C.S., 49 wt.%) for approximately 11 min., after which, the etchant is completely rinsed away with deionized (DI) water. DI water, with a resistivity of 18 M Ω -cm, is obtained from a Millipak® Millipore system, which has a 0.22 μ m filter installed in-line. The released microinstruments are then placed in hot H₂O₂ (75 - 80 °C) for 10 minutes to oxidize the microstructure surfaces. The H₂O₂ (Fischer Scientific, Certified A.C.S., 30 wt.%) is also finally rinsed away with DI water.

6.2 Process Used to Obtain Oxide-covered Test Surfaces

To obtain test surfaces, which only have a layer of native oxide on them, the DI water is rinsed away with isopropanol (IPA). Following this, the Test Platform chip is supercritically dried in a Tousimis Autosamdri 815-B CPD system. Samples dried using this CPD system have been known to have contaminated surfaces [78]. Therefore, the dried microinstruments are exposed to a low power (25 W), capacitively coupled RF (13.56 MHz) plasma of oxygen (O₂ pressure used is 300 mtorr) to clean the test surfaces before testing. This treatment is similar to that reported by Mayer *et al.*, which resulted in clean, oxidized test surfaces, including the surfaces underneath the microstructures [38]. DI water contact angle measured after this treatment on a simultaneously processed Si(100) monitor chip is found to be <5°, indicating that the cleaned surfaces are hydrophilic. The microinstruments are actuated immediately after the plasma cleaning to minimize contamination from the ambience.

6.3 Preparation of the OTS SAM Coating Solution

All the glasswares that are used for preparing the OTS SAM coating solution are first thoroughly cleaned using an elaborate cleaning procedure. Next, before preparing the coating solution, the crystallizing dish, in which the coating solution is prepared, is conditioned with the OTS precursor molecules. 100 μ l of OTS (Gelest, 97 %+) is

added to 50 ml of anhydrous hexane (Fisher Scientific, Electronic grade, 98.5 %+), in the conditioned crystallizing dish. The resulting 5 mM solution of OTS is thoroughly mixed, after which, the crystallizing dish containing it is covered with a glass dish. The OTS coating solution is kept standing for 45 min. (at room temperature of 22 °C and relative humidity of 46 - 48 %), during which, the trichlorosilane precursor molecules present in the coating solution react with the water vapor present in the ambience, and get hydrolyzed into the corresponding trihydroxy derivatives. Without further delay, the Test Platform chip that is to be coated with OTS-SAM is placed in the coating solution.

6.4 Process Used to Obtain OTS SAM Coated Test Surfaces

To obtain test surfaces coated with OTS SAM, the procedure outlined by Srinivasan *et al.* in [80] is slightly modified and used in this study. The process used in this study begins with completely rinsing away the DI water with IPA (Fischer Scientific, Certified A.C.S.). The IPA is further thoroughly rinsed away with anhydrous hexane (Fischer Scientific, Electronic grade, 98.5 %+). Next, the test platform chip is carefully removed from the anhydrous hexane and transferred into a conditioned OTS (Gelest, 97 %+) coating solution, which is kept in a glass dish that was previously treated with OTS. Care should be taken to ensure that the microinstruments are not exposed to the liquid-vapor interface while transferring the Test Platform chip into the coating solution. The time, for which, the microinstruments are kept in the coating solution depends on the relative humidity of the ambience. The OTS SAM coating investigated in this study is deposited at room temperature (i.e., 22 °C), and a relative humidity of 40 - 45 %, in laboratory air. Therefore, the Test Platform chip is kept in the coating solution for 45 min., after which, it is transferred back to the anhydrous hexane. The anhydrous hexane is subsequently displaced with IPA, and the IPA is similarly displaced with DI water. The coated Test Platform chip is finally

removed, from DI water, in one slow but continuous motion, in such a way that its in-plane surface is perpendicular to the liquid surface. All the solvent displacements are carried out using the fill/drain approach suggested by Ashurst *et al.* [35]. The DI water contact angle measured on a simultaneously coated Si(100) monitor chip is found to be 110° , indicating that the coated surfaces are hydrophobic. Additionally, the thickness of the OTS SAM deposited on the monitor chip, which is determined using an ellipsometer (Rudolph Research, AutoEL-III), is found to be 2.8 ± 0.2 nm, indicating that the studied OTS SAM is a monolayer. The DI water contact angle exhibited by, and the thickness of, the OTS-SAM deposited on the monitor chip, indicate that it is well ordered and densely packed [80, 166]. The crystal-like structure of the OTS-SAM investigated in this study is additionally confirmed by determining the peak frequencies of methylene vibrations exhibited by it, using FTIR spectroscopy. The frequency of the symmetric methylene vibration peak exhibited by the OTS SAM investigated in this study is 2850.52 cm^{-1} and that of the asymmetric methylene vibration peak exhibited by it is 2917.97 cm^{-1} . Further, the OTS-SAM coated monitor chip is also inspected using AFM. The scan shown in Fig. 6.1 indicates that the OTS-SAM coated test surfaces have very few polymerized particulates on them.

6.5 Gold Nanoparticle (AuNP) Synthesis

All the chemicals used to synthesize the dodecanethiol-capped gold nanoparticles, which are used for tailoring the surface topographies of the test surfaces investigated in this study, are purchased from Alfa Aesar (Ward Hill, MA). A two-phase liquid arrested precipitation process similar to that reported by Sigman *et al.* is used to synthesize the dodecanethiol-capped gold nanoparticles [167]. The process begins by adding 36 ml of an aqueous solution containing 0.38 g of hydrogen tetrachloroaurate to an organic solution containing 2.7 g of tetraoctylammonium bromide (phase transfer catalyst) and 24.5 ml toluene. The mixture is stirred for an hour, after which,

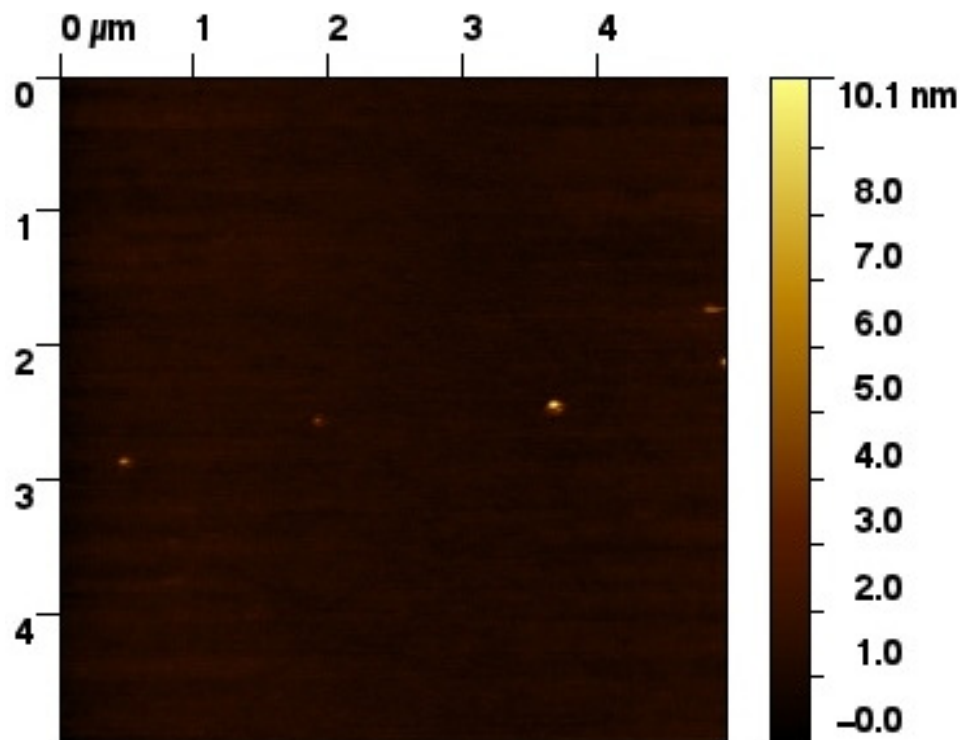


Figure 6.1: AFM image of a $25 \mu\text{m}^2$ area of the OTS SAM coated Si(100) monitor chip, which is processed simultaneously with the OTS SAM coated Test Platform chip. Notice that only four extremely small polymerized particles are present in the $25 \mu\text{m}^2$ area shown in the scan. The rms roughness of the area shown in the image is 0.23 nm.

the aqueous phase is separated and discarded. Next, the gold ions present in the organic phase that is left behind are reduced to ground state by adding 30 ml of an aqueous solution containing 0.5 g of NaBH₄. The resulting mixture is stirred for 8 - 10 h to allow the gold nanoparticles to grow, before removing and discarding the aqueous phase. Next, 240 μ l of 1-dodecanethiol is added to the organic phase that is left behind, and the mixture is stirred for 4 h to cap and stabilize the gold nanoparticles. Finally, the excess 1-dodecanethiol and NaBH₄ are removed by centrifuging the dodecanethiol-capped gold nanoparticle dispersion with equal parts of ethanol, at 4500 rpm for 5 min. After repeating the centrifugation step several times, the dodecanethiol-capped gold nanoparticles are dispersed and stored in hexane. The size of the dodecanethiol-capped gold nanoparticles used to tailor the surface topographies of the test surfaces investigated in this study is characterized using transmission electron microscopy (TEM). A TEM image showing the dodecanethiol-capped gold nanoparticles used in this study is shown in Fig. 6.2. Based on the sizing of 3041 particles, the size of the dodecanethiol-capped gold nanoparticles used in this study is determined to be 5.5 ± 1.2 nm.

6.6 Process Used to Deposit the Dodecanethiol-capped Gold Nanoparticles on the Test Surfaces of the Test Platform

The process reported by Hurst *et al.* in [24] is used for depositing the dodecanethiol-capped gold nanoparticles on the test surfaces of the Test Platform. To coat the test surfaces of the Test Platform with dodecanethiol-capped gold nanoparticles, the Test Platform chip is carefully placed upside-down on top of a stainless steel washer (which is 1.6 mm thick and has an inner diameter of 9.5 mm), inside a glass vial (which is 10 mm deep and has an inner diameter of 14.3 mm), which is kept inside a large beaker filled with hexane (Fischer Scientific, Electronic grade, 98.5 %+), without exposing it to the liquid-vapor interface. Another washer is placed on top

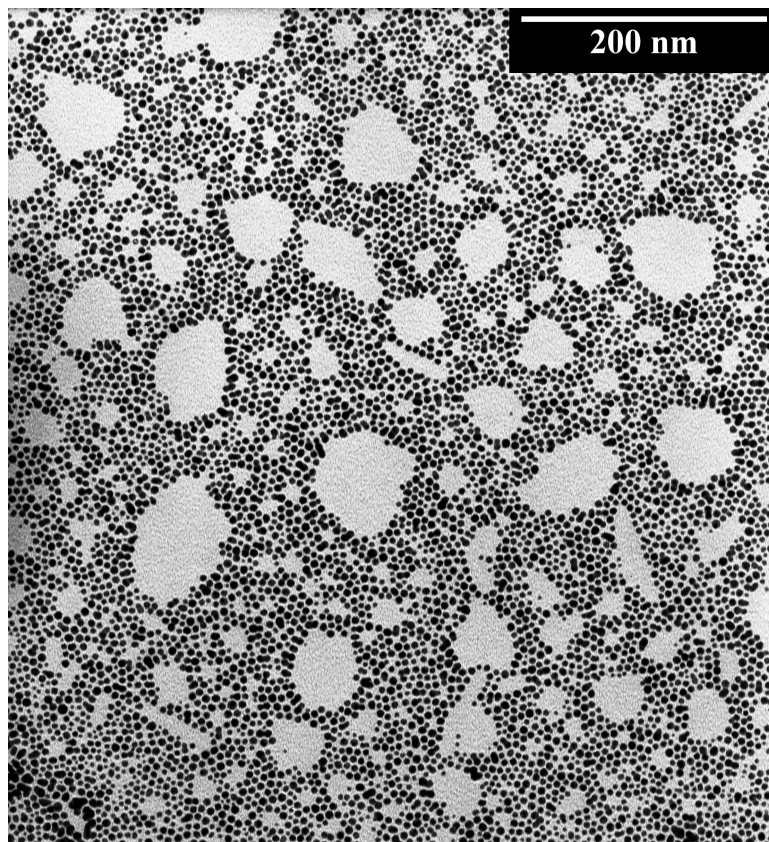


Figure 6.2: A TEM image showing the dodecanethiol-capped gold nanoparticles used to tailor the surface topographies of the test surfaces investigated in this study. The size of the dodecanethiol-capped gold nanoparticles shown in the image is determined to be 5.48 ± 1.16 nm.

of the Test Platform chip to hold it in place. Next, the vial is removed from the hexane-filled beaker, after which, the hexane is carefully removed from the vial up to a level just above the Test platform chip. Next, a known, pre-determined volume of concentrated dodecanethiol-capped gold nanoparticle dispersion (in hexane) is added to the vial and carefully mixed, after which, the vial is placed inside a 30 ml stainless steel high pressure vessel, which is equipped with a quartz viewing window, a resistive temperature detector (RTD), a heating rope and a pressure gauge. Approximately 400 μl of pure hexane is also added alongside the vial, to saturate the vapor-space of the high pressure vessel and prevent evaporation of the organic (hexane-based) nanoparticle dispersion prior to sealing the high pressure vessel. After sealing the high pressure vessel, its chamber is pressurized with CO_2 , first to approximately 23 bar at room temperature (i.e., 22 $^\circ\text{C}$) using a 500 ml Teledyne ISCO piston syringe pump (Lincoln, NE), and then up to the vapor pressure of the gas (i.e., 58 bar at 22 $^\circ\text{C}$) by setting the pump flow rate to 0.4 ml/min. During the pressurization, the CO_2 dissolves in the organic phase, effectively expanding the volume and reducing the solvent strength of the hexane/ CO_2 mixture, which results in the precipitation of the suspended dodecanethiol-capped gold nanoparticles. Specifically, dodecanethiol stabilized AuNPs in the size range of 3 - 7 nm are reported to precipitate in the pressure range of 34.5 - 55.2 bar [129]. Moreover, the precipitating dodecanethiol-capped gold nanoparticles are reported to conformally coat all the surfaces of the microinstruments being coated [24]. Pressurization is continued until the entire chamber of the high pressure vessel is filled with liquid CO_2 , after which, the mixture of liquid CO_2 and the organic solvent (i.e., hexane) is heated isochorically to 40 $^\circ\text{C}$, to transform it into a supercritical fluid. Next, the chamber of the high pressure vessel is flushed with several volumes of pure supercritical CO_2 (at 40 $^\circ\text{C}$ and 90 bar) at a rate of approximately 1.0 ml/min, to ensure the complete removal of the organic solvent (i.e., hexane) from it. Finally, the chamber of the high pressure vessel is slowly

depressurized (at 40 °C) to atmospheric pressure and the dry, dodecanethiol-capped AuNP coated Test Platform chip is removed.

6.7 Contact Angle Goniometry

Contact angle goniometry is used for characterizing the chemistry (i.e., hydrophobicity) of the test surfaces investigated in this study. Specifically, it is used to determine the hydrophobicity of the native oxide covered and the OTS SAM coated test surfaces investigated in this study. Contact angle measurements are made using a Ramé-Hart Standard goniometer (Ramé-Hart, Inc., Model # 200-00-115). The measurement reproducibility of this instrument is $\pm 2^\circ$. To determine the hydrophobicity of a test surface, the contact angle made by a droplet of DI water on it is determined using the sessile drop technique [168]. DI water, with a resistivity of 18 M Ω -cm, is obtained from a Millipak® Millipore system, which has a 0.22 μ m filter installed in-line. The volume of the water droplet used to make the contact angle measurements is 4 μ l.

6.8 Ellipsometry

Ellipsometry is used for characterizing the thicknesses of the surface films that are investigated in this study. Specifically, it is used to determine the thicknesses of the native surface oxide film present on the test surfaces, the oxide film thermally grown on the surfaces of the as-fabricated microinstruments to polish them and the OTS SAM deposited on the microinstruments. The ellipsometer used for this study is a Rudolph Research ellipsometer, which is equipped with a 1 mW (max.) HeNe laser (λ of radiation is 632.8 nm) and AutoEL-III software. This instrument can measure film thicknesses up to 3 μ m and has a measurement reproducibility of $\pm 2\text{\AA}$. A single film model is used to determine the thicknesses of the native surface oxide film present on the test surfaces and the oxide film grown thermally on the surfaces

of the as-fabricated microinstruments [169]. A refractive index of 1.463 is used for the oxide film, in the model. A lumped single film model is used to determine the thickness of the OTS SAM deposited on the test surfaces [169]. A refractive index of 1.45 is used for the organic OTS SAM film, in the model. The lumped single film model determines the combined thickness of the OTS SAM and the underlying native oxide film. Therefore, in order to determine the thickness of the OTS SAM, the thickness of the underlying native oxide film is determined prior to depositing the OTS SAM on it, using the single film model.

6.9 Fourier Transform - Infrared Spectroscopy

Fourier Transform - Infrared (FT-IR) Spectroscopy is used for characterizing the structure (i.e., orderliness and packing density) of the OTS SAM film investigated in this study [170]. Specifically, attenuated total internal reflection FT-IR (i.e., ATR-FTIR) spectroscopy is used in this study. A Si ATR crystal and a Spectrum 2000 FT-IR spectrometer (PerkinElmer) is used for taking the FT-IR scans. The symmetric (observed between 2850 - 2855 cm^{-1}) and asymmetric (observed between 2918 - 2923 cm^{-1}) methylene stretching peaks are used to qualitatively determine the packing and orderliness of the OTS SAM investigated in this study.

6.10 Microscopy

Several microscopy techniques are used either as imaging or as analysis tools in this study. Specifically, optical microscopy is used for characterizing, and during the actuation of, the microinstruments developed in this study, atomic force microscopy is used for characterizing the surface topography of the test surfaces investigated in this study, scanning electron microscopy is used for characterizing the tailored test surfaces investigated in this study and transmission electron microscopy is used for characterizing the dodecanethiol-capped gold nanoparticles that are used to tailor

the surface topography of the test surfaces investigated in this study. The following sections briefly discuss the various microscopy techniques used in this study.

6.10.1 Optical Microscopy

In this study, optical microscopy is used for obtaining the optical images of the microinstruments developed in this study. It is also used for determining the dimensions of the components of the various microinstruments developed in this study. Further, along with a pattern matching technique, it is used to determine the displacements of the various moving components of the microinstruments developed in this study. Additionally, it is used for determining the resonance frequencies of the various Resonators included in the Test Platform. The optical microscope used in this study is custom-built by East Mountain Optomechanical, Inc. The optical microscope is equipped with a green LED (with λ_{max} of 525 nm, Nichia corp.), which is monochromated using a monochromator that transmits 532 nm and used as the illumination source, Mitutoyo M Plan Apo objectives (10X - 100X), which are used as the objective lens, and a charge-coupled device (CCD)-IRIS camera (Sony, XCD-SX910), which is controlled using the MEMScript and used for collecting the optical images.

6.10.2 Atomic Force Microscopy

In this study, atomic force microscopy is specifically used for quantitatively characterizing the topographies of the native oxide covered in-plane as well as sidewall surfaces, and the the test surfaces, whose topographies are tailored using dodecanethiol-capped gold nanoparticles. Additionally, it is used to ascertain the presence /absence of polymerized particulates of precursor molecules on the OTS SAM coated test surfaces. All the AFM images obtained for this study are obtained by operating

the atomic force microscope (Pacific Nanotechnology Nano-R SPM, Model # O-020-0002) in the tapping mode. Details on the working principles and the usage of the atomic force microscope can be found elsewhere [171,172]. The tips that are used for obtaining the AFM images are Si tips (μ masch, Model # NSC35/NoAl), which have a radius of curvature of 10 nm. The parameter that is extracted from an AFM image to quantify the surface topography of the surface being analyzed is the rms roughness of the area of that surface, that is scanned. Additionally, the ASCII data associated with the AFM image of each test surface is processed using the image analysis technique discussed in section 6.12 to determine the surface coverage of the interacting asperities present in the area of that surface, that is scanned.

6.10.3 Scanning Electron Microscopy

In this study, scanning electron microscopy (SEM) is used for qualitatively characterizing the topographies of the test surfaces, whose topographies are tailored by depositing dodecanethiol-capped gold nanoparticles on them. A carbon tape is used as the conducting path while collecting the SEM scans. The qualitative characterization of the topographies of the tailored test surfaces is done in terms of the conformality and uniformity of the dodecanethiol-capped AuNP-based coatings deposited on them as well as the number density of the dodecanethiol-capped gold nanoparticles present on them.

6.10.4 Transmission Electron Microscopy

In this study, transmission electron microscopy (TEM) is used for determining the size of the dodecanethiol-capped gold nanoparticles that are used for tailoring the surface topographies of the test surfaces investigated in this study. In order to determine the size of the dodecanethiol-capped gold nanoparticles, a TEM image of a monolayer of the dodecanethiol-capped gold nanoparticles is obtained. A TEM (carbon) grid

is used for obtaining the TEM image of the monolayer of the dodecanethiol-capped gold nanoparticles. The TEM image is analyzed using an image analysis software called ImageJ. The scale of the processed image obtained from ImageJ is determined using the Eq. 6.10.1, where, δ is the scale of the processed image obtained from ImageJ (in pixels/nm), δ_s is the number of lateral pixels present in the TEM image (in pixels) and M is the magnification used to obtain the TEM image. The size of the dodecanethiol-capped gold nanoparticles is determined from the processed image obtained from ImageJ, using the procedure developed by Kitchens [173].

$$\delta = \frac{M\delta_s}{3.936 \times 10^{-8}} \quad (6.10.1)$$

6.11 Interferometry

Two different interferometric techniques are used in this study. The phase shifting interferometry (PSI) is used for determining the height profiles of all the cantilever beams actuated in this study. The horizontal scanning interferometry (HSI) is used for determining the step edges present at the sidewall interfaces investigated in this study. A custom-built long working distance, incoherent light interference microscope similar to that reported by Sinclair *et al.* in [153] is used to produce the interferograms. The interference microscope is equipped with a green LED (with λ_{max} of 525 nm), which is monochromated using a monochromator that transmits 532 nm and used as the illumination source, a Mitutoyo M Plan Apo 10 objective, which is used as the objective lens, a closed-loop PZT actuator (PI, PZT model # PZ-70E, LVPZT controller model # E-610.SO) with a reference surface mounted on it, which is controlled using the MEMScript and used for taking the phase steps, and a charge-coupled device (CCD)-IRIS camera (Sony, XCD-SX910), which is also controlled using the MEMScript and used for collecting the interferograms.

6.12 Image Analysis Technique Used for Determining the Surface Coverage of the Interacting Asperities

The surface topographies of the test surfaces, whose topographies are tailored using the dodecanethiol-capped gold nanoparticles, are additionally quantified by determining the surface coverage of the interacting asperities present on them. In order to determine the surface coverage of the interacting asperities present on a test surface, the ASCII data associated with the AFM image of a representative area of that surface is processed using a specially-written, elaborate C program, which is written by Dr. W. R. Ashurst (Associate Professor, Department of Chemical Engineering, Auburn University). The C program converts the AFM image into a two-dimensional array of pixels, whose intensities vary on a discrete scale of 0 - 255. The intensity of each pixel is directly proportional to the z-height of the corresponding point in the AFM image. By inputting a threshold intensity in the C program, the pixels, whose intensities are greater than the threshold value can be determined. The fraction of the pixels, whose intensities are greater than the inputted threshold value, is the output of the C program, and the surface coverage of the interacting asperities present on the surface being analyzed.

Chapter 7

Experimental Requirement of the Phase Shifting Interferometry

Digital phase shifting interferometry (PSI), a technique widely used in optical testing, requires interferograms collected at optical phase differences separated by a definite phase step. The five frame interferogram collecting sequence suggested by Hariharan *et al.* is extremely effective in significantly reducing the errors in the height profiles derived using PSI that are caused by phase step errors [176]. In this chapter, I report on a class of five frame sequence which, due to its mathematical equivalence with the one suggested by Hariharan *et al.* and ease of execution, is more commonly used, but is much less effective in reducing the height profile errors caused by phase step errors.

7.1 Introduction

Since its introduction in 1974 by Bruning *et al.*, phase shifting interferometry (PSI) has become a very useful tool and is presently widely used in several applications [174]. In optical testing, PSI is frequently used to determine the flatness of optical surfaces as well as to determine the optical quality of certain optical components [174]. Combined with appropriately designed test structures and analysis routines, it is commonly used by the micro-electromechanical systems (MEMS) community to determine critical material properties such as residual stress, Young's modulus and stress gradient in structural layers used to fabricate useful micromechanisms [153]. Recently, Hurst *et al.* reported a technique, which also employs PSI to study stiction between contacting in-plane MEMS surfaces [175].

In all of its applications, PSI is essentially used to determine the topography of a particular surface by determining the height of every point on that surface. The only experimental step involved in using PSI is the collection of interferograms at different optical phase differences separated by a definite phase step for every point on the surface. Consequently, it is also the only source of experimental errors in PSI derived height profiles. Further, it is widely accepted that the most prominent experimental error is the error in the phase steps taken during the collection of interferograms [174,176]. Because nanometer scale precision is one of the requirements of the MEMS and NEMS based applications, in which, PSI is used, it is essential to ensure that the height profiles derived using PSI are extremely accurate. Therefore, it is necessary to reduce the influence of these phase step errors on the height profiles derived using PSI.

In most of the commonly used interferometers, phase steps are taken using a piezoelectric transducer (PZT), on which, one of the surfaces (i.e., reference or sample) is mounted. Error in the phase steps (i.e., deviation from predetermined nominal value) is usually caused by the non-linearity, and dependence of the PZT on variables such as its age and temperature. Various approaches presently used to reduce the phase step error or its influence on PSI derived height profiles can be broadly classified into two categories: hardware-based and algorithm-based approaches. The additional hardware, and hence expense, associated with the hardware-based approaches, which include actuator calibration schemes, novel shifting hardwares, etc., makes them less attractive than the algorithm based approaches [174]. Algorithm-based approaches focus on using either a specific sequence for collecting the interferograms or a self-correcting computational scheme to address the uncertainty associated with the phase steps. Some strategies involving a combination of the two approaches have also been reported in literature [174]. For example, the equistep algorithm requires additional hardware to ensure that the phase steps are equal but does not require

them to be known accurately [174]. In contrast, a generalized algorithm suggested by Greivenkamp allows unequal phase steps but requires additional hardware to accurately determine them [174].

Examples of prominent algorithm-based approaches include the two algorithms reported by Farrell *et al.*, which do not require the phase steps to be known or equal and hence do not require additional hardware [174]. However, the computational effort involved in them is significantly higher than that involved in the algorithm suggested by Hariharan *et al.* [174, 176]. The algorithm suggested by Hariharan *et al.*, which implicitly evaluates the actual phase steps and uses them to calculate the original optical phase difference between the interfering beams, is one of the most simple, robust and reliable algorithms for PSI [176]. The five frame interferogram collecting sequence used by it significantly reduces the errors in the height profiles derived using PSI, that are caused by phase step errors [176]. In this chapter, I report on a class of five frame sequence, which due to its mathematical equivalence with the one suggested by Hariharan *et al.* and ease of execution, is more commonly used, but is contrastingly much less effective in reducing the height profile errors caused by phase step errors.

7.2 Five Frame Interferogram Collecting Sequence for PSI

The self-calibrating five frame sequence (referred to as H) suggested by Hariharan *et al.* is given by Eqs. (7.2.1a - 7.2.1e) shown below, where I_1 , I_2 , I_3 , I_4 and I_5 are the intensity measurements made at phase steps of $\pm 2\alpha$, $\pm\alpha$, 0 , $\mp\alpha$, $\mp 2\alpha$ respectively

and ϕ is the original optical phase difference between the interfering beams [176].

$$I_1 = A + B + 2\sqrt{AB} \cos(\phi \pm 2\alpha) \quad (7.2.1a)$$

$$I_2 = A + B + 2\sqrt{AB} \cos(\phi \pm \alpha) \quad (7.2.1b)$$

$$I_3 = A + B + 2\sqrt{AB} \cos(\phi) \quad (7.2.1c)$$

$$I_4 = A + B + 2\sqrt{AB} \cos(\phi \mp \alpha) \quad (7.2.1d)$$

$$I_5 = A + B + 2\sqrt{AB} \cos(\phi \mp 2\alpha) \quad (7.2.1e)$$

The class of five frame sequence (referred to as NH), which is mathematically equivalent to sequence H is represented by Eqs. (7.2.2a - 7.2.2e) shown below, where I_1, I_2, I_3, I_4, I_5 are the intensity measurements made at phase steps of $0, \pm\alpha, \pm2\alpha, \pm3\alpha, \pm4\alpha$ respectively.

$$I_1 = A + B + 2\sqrt{AB} \cos(\phi) \quad (7.2.2a)$$

$$I_2 = A + B + 2\sqrt{AB} \cos(\phi \pm \alpha) \quad (7.2.2b)$$

$$I_3 = A + B + 2\sqrt{AB} \cos(\phi \pm 2\alpha) \quad (7.2.2c)$$

$$I_4 = A + B + 2\sqrt{AB} \cos(\phi \pm 3\alpha) \quad (7.2.2d)$$

$$I_5 = A + B + 2\sqrt{AB} \cos(\phi \pm 4\alpha) \quad (7.2.2e)$$

The mathematical equivalence of the two sequences H and NH is evident from the fact that both of them consist of five frames, each separated by a phase step α . Also, for both the sequences, ϕ is given by the same Eq. (7.2.3) when the nominal phase step (i.e., α) is 90° . For completeness, the derivations of Eq. (7.2.3) for sequences H and NH are given in Appendices B.1 and B.2 respectively.

$$\tan \phi = \pm \frac{2(I_2 - I_4)}{2I_3 - I_1 - I_5} \quad (7.2.3)$$

This mathematical equivalence along with only a subtle difference in the experimental execution of the two sequences and the ease of experimental execution of sequence NH are the reasons why sequence NH is more than often used instead of sequence H. However, while sequence H is extremely less sensitive to a small error (ϵ) incurred in each phase step, sequence NH is highly sensitive to it. This is substantiated by Eq. 7.2.4a and Eq. 7.2.4b, which give a first order approximation of the error ($\Delta\phi$) in ϕ due to ϵ , for sequences H and NH respectively. Both Eq. 7.2.4a and Eq. 7.2.4b are derived using an error analysis similar to that reported in [176]. For completeness, the complete error analyses of sequences H and NH are provided in Appendices B.3 and B.4 respectively. It is important to note that Eq. 7.2.4a differs from the analogous equation reported in [176] by a factor of 2. However, it is consistent with the data obtained experimentally. The experiments conducted to substantiate Eq. 7.2.4a and Eq. 7.2.4b are discussed in the following section.

$$\Delta\phi_H = \frac{\epsilon^2}{8} \sin 2\phi \quad (7.2.4a)$$

$$\Delta\phi_{NH} = \pm 2\epsilon \quad (7.2.4b)$$

7.3 Experimental Details

A long working distance, incoherent light interference microscope is used to produce the interferograms. A green LED (with λ_{max} of 525 nm) is monochromated to 532 nm and used as the illumination source. A closed-loop PZT actuator (PI, PZT model # PZ-70E, LVPZT controller model # E-610.SO) with the reference surface mounted on it is used for taking the phase steps. Two 8 mm \times 8 mm Si(100) chips are used as the reflecting surfaces (i.e., reference and sample) for all the experiments.

In order to collect the interferograms using sequence H, initially, a voltage of 1 V is applied to the PZT to move it to a position, from where, it can be moved in both the directions (forward and backward) to collect the interferograms. At this position (starting position), the path lengths of the two arms of the interferometer are precisely matched, in order to obtain the 0th order fringe. Next, the first interferogram is collected by moving the PZT two phase steps forward. The remaining four interferograms are collected by moving the PZT backwards, one phase step for each interferogram. For collecting interferograms using sequence NH, the PZT is initially moved four phase steps forward. This is the starting position for sequence NH, at which, the path lengths of the two arms of the interferometer are precisely matched. The first interferogram for sequence NH is collected at the starting position itself. The remaining four interferograms are again collected by moving the PZT backwards, one phase step for each interferogram.

The nominal phase step used in all the experiments is 90°. In the first experiment, which is conducted to determine the inherent phase step error present in the closed-loop PZT, the displacement of the reference surface in each phase step up to five phase steps is experimentally determined by measuring the displacement of a specific fringe for those phase steps. The inherent phase step error is determined from the difference between the expected and the experimentally measured displacements of the reference surface. Next, before investigating the effectiveness of sequence NH in reducing the height profile errors caused by phase step errors, the error in the determination of ϕ due to the low frequency vibrations present in the experimental setup is determined. For this purpose, the surface height profile of the sample surface is determined five times at intervals of 5 min., using sequence H. No intentional phase step error is added to the nominal phase steps for these experiments. Each of the determined five surface height profiles are then compared with each of the other four surface height profiles and the differences in the corresponding heights of all the points on the sample

surface are used to calculate the rms error ($\Delta\phi$) in ϕ . The effectivenesses of the two sequences H and NH in reducing the height profile errors caused by phase step errors are studied by using them to determine the surface height profile of the sample surface with different amounts of phase step errors intentionally added to the nominal phase step for collecting the interferograms. The first surface height profile is obtained with zero intentional phase step error (ϵ) added to α . For obtaining the next five surface height profiles, ϵ is incremented in steps of 10% (of the nominal phase step) for each subsequent profile. $\Delta\phi$ due to a particular ϵ is determined by comparing the surface height profile obtained with that particular ϵ added to α , with the one obtained with zero phase step error added to α . The effectivenesses of sequences H and NH are studied using both positive as well as negative ϵ .

7.4 Results and Discussion

The measured displacements of the reference surface were 5 nm greater than the expected displacements in all the experiments. This indicates that the closed-loop PZT has an inherent positive ϵ of 7.5% (of α). The maximum $\Delta\phi$ due to the low frequency vibrations present in the interferometer was about 6.77° , which corresponds to a rms error of 5 nm in the surface height profile of the sample surface. $\Delta\phi$, as a function of percentage ϵ (of α), for both the sequences is shown in Fig. 7.1. In Fig. 7.1, H_{exp} and NH_{exp} represent the data obtained experimentally, while H_{th} and NH_{th} represent the $\Delta\phi$ calculated using Eq. 7.2.4a and Eq. 7.2.4b, for sequences H and NH respectively. As seen in Fig. 7.1, the experimentally determined $\Delta\phi$ are in good agreement with those calculated using Eq. 7.2.4a and Eq. 7.2.4b for both the sequences. Also, it is clearly evident from Fig. 7.1 that sequence H makes PSI extremely less sensitive to both positive as well as negative ϵ , and its usage limits $\Delta\phi$ to small values even for ϵ as large as 60% of α . For each of the different ϵ investigated except one, the resulting $\Delta\phi$ in the case of sequence H is less than the maximum $\Delta\phi$

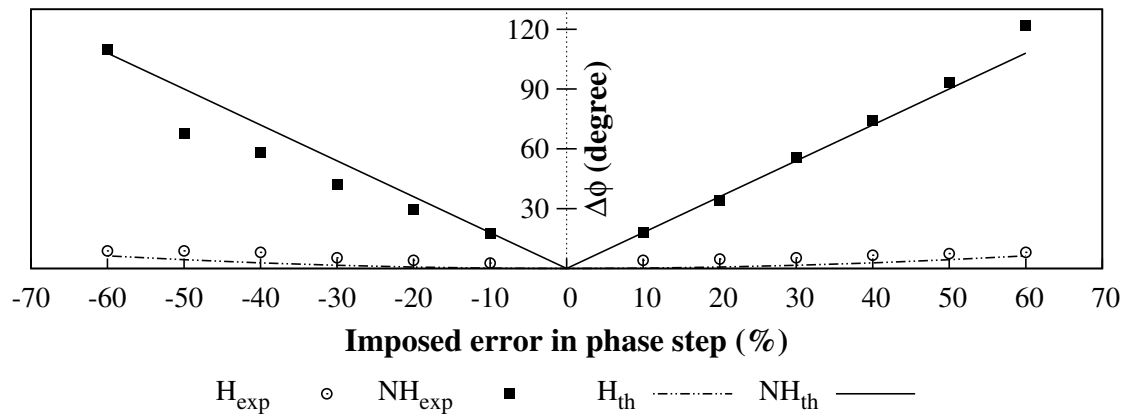


Figure 7.1: Error in ϕ ($\Delta\phi$) for different imposed percentage error ($\% \epsilon$) in α .

due to the low frequency vibrations present in the interferometer. Contrastingly, in the case of sequence NH, PSI is highly sensitive to ϵ and the height profiles derived have significantly larger $\Delta\phi$, which increases linearly with the increase in ϵ . A phase step error of 60% results in $\Delta\phi$ of 8.12° and 121.8° , when sequences H and NH are used, respectively. These correspond to rms errors of 6 nm and 90 nm in the surface height profile of the sample surface, respectively. Further, Fig. 7.1 indicates that positive ϵ result in larger $\Delta\phi$ than the corresponding negative ϵ , for both the sequences. This is attributed to the inherent positive ϵ of the closed-loop PZT, which gets added to the intentionally imposed positive ϵ , thereby increasing them, and gets subtracted from the intentionally imposed negative ϵ , thereby decreasing them.

7.5 Conclusions

I analyzed two distinct classes of the five frame interferogram collecting sequence used in PSI, both mathematically as well as experimentally. The results clearly substantiate the presence of significant errors in the PSI derived height profiles obtained using a mathematically equivalent but experimentally different five frame interferogram collecting sequence than that suggested by Hariharan *et al.*. A significantly high rms error of 90 nm was observed in the height profile derived using sequence NH when ϵ was 60% of α . In contrast, sequence H made PSI extremely less sensitive to ϵ and even for a high ϵ of 60%, a rms error of 6 nm, which is only marginally greater than the maximum rms error due to vibrational disturbances, was observed in the height profile derived using it. Therefore, the five frame interferogram collecting sequence for PSI should be selected cautiously, otherwise, the height profiles derived can have significant errors in them.

Chapter 8

Benchmarking the Microinstruments: Highlighting Key Features & Testing Standard Surfaces

This chapter reports the benchmarking of the microinstruments developed in this study. It illustrates the key features of each of the seven microinstruments developed in this study. Further, in order to substantiate the consistency and reliability of the the results obtained using them, it reports the results of the investigations conducted to study the effects of two standard surface treatments using the microinstruments developed in this study, and compares them with the corresponding results reported in literature. The two types of surfaces studied in this chapter, using the microinstruments developed in this study are surfaces coated with *n*-OTS ($C_{18}H_{37}SiCl_3$) SAM coating (i.e., hydrophobic surfaces) and surfaces having only a layer of native oxide on them (i.e., hydrophilic surfaces). These two surface treatments are considered as standard surface treatments by the MEMS community. All the results reported in this chapter are obtained in laboratory air, at 22 °C and in 45% relative humidity (unless otherwise stated).

8.1 The Pattern Matching Technique

First, in order to determine the uncertainty in the measurements made using the pattern matching technique, the position of a movable pattern is determined thousand times, without moving the pattern, using it. The script used to perform this experiment is given in Appendix A.11. The rms error in the determination of the position of the movable pattern is found to be 7.5 nm. This clearly indicates that the pattern matching technique used in this study determines the displacements of

the movable components of the microinstruments developed in this study extremely accurately. However, it must be noted that the overall resolution of the pattern matching technique used in this study depends on, and is slightly decreased by, the magnification (depth of focus) of the objective lens used in the microscope.

8.2 Residual Stress Tester

Optical images of four Residual Stress Testers of each of the two Test Platform chips investigated in this chapter are collected before and after releasing the Test Platform chips. The magnification of the objective lens used to collect the optical images is 20X. Accordingly, the size of each pixel in the optical images is $0.234 \mu\text{m} \times 0.234 \mu\text{m}$. Careful analysis of all the optical images collected, using the pattern matching technique, indicates that the central beams of all the RSTs investigated in this chapter do not exhibit any rotation. This result implies that the structural films of both the Test Platform chips investigated in this chapter (i.e., the one coated with OTS SAM as well as the one, whose surfaces are covered with only native oxide) do not have any residual stress in them, which is as expected because they are single crystal silicon films. Also, the OTS SAM coating did not induce any stress in the underlying Si(100) structural film. This indicates that either the OTS SAM coating is conformal and uniform or it does not have any significant influence on the stress state of the Si(100) structural film. The former possibility is more likely considering that the characterization of the OTS SAM coating deposited on a monitor Si(100) chip processed simultaneously with the Test Platform chip indicated that the OTS SAM coating investigated in this chapter is a densely-packed, well-ordered monolayer of OTS (see section 6.4). As explained in section 5.2.2, the Mechanical Strength Testers developed in this study are actuated by applying an increasing DC voltage to the open-loop piezo of a specialized micro-manipulator (specifically developed in this study), which pushes the central shuttle of the Mechanical Strength Tester being

actuated in the direction of the arrow shown in Fig. 5.3. The magnification of the objective lens used during the actuation of the Mechanical Strength Testers investigated in this chapter is 10X. Accordingly, the size of each pixel in the field of view is $0.465 \mu\text{m} \times 0.465 \mu\text{m}$. In order to determine the distances, by which, the central shuttle is displaced at the point of fracture of each of the six fracture beams of the Mechanical Strength Tester, the displacements of the central shuttle are determined using the pattern matching technique, at every push, throughout the actuation of the Mechanical Strength Tester. Figure 8.1 is a plot showing the experimentally determined axial and lateral displacements of the central shuttle of one of the MSTs of the OTS SAM coated Test Platform chip versus the corresponding voltage applied to the micro-manipulator that is used to actuate it. The widths of the fracture beams of the OTS SAM coated MST used to obtain the data shown in Fig. 8.1 are measured optically, to be $2.72 \mu\text{m}$ (design width is $3 \mu\text{m}$). The axial displacements of the central shuttle, at which, each of the three pairs of fracture beams of the OTS SAM coated MST got fractured can be clearly seen as discontinuities in the plot representing the axial displacement in Fig. 8.1. The jumps during the axial displacement of the central shuttle, which appear as discontinuities in the plot representing the axial displacement data in Fig. 8.1, are consequences of the decrease in the resistance offered by the OTS SAM coated MST to the extension of the open-loop piezo, at the point of fracture of each pair of fracture beams. This is substantiated by the fact that after each discontinuity, the axial displacement data shown in Fig. 8.1 exhibits an increased slope. In Fig. 8.1, while the discontinuities associated with the fracture of $50 \mu\text{m}$ and $70 \mu\text{m}$ long beams are sharp and significant, that associated with the fracture of $60 \mu\text{m}$ long beams is blunt and relatively less significant. This is because while both the $50 \mu\text{m}$ long as well as $70 \mu\text{m}$ long fracture beams got fractured at the same instant, the two $60 \mu\text{m}$ long fracture beams got fractured individually at axial displacements of $11.45 \mu\text{m}$ and $11.97 \mu\text{m}$, respectively. Also, the plot that represents the lateral

displacements of the central shuttle in Fig. 8.1 indicates that during the entire actuation, the motion of the OTS SAM coated MST is confined to only the axial direction. This confirms that throughout the actuation of the OTS SAM coated MST, the lever arm (i.e., L_c) of each of its actuated fracture beams remained constant.

8.3 Mechanical Strength Tester

On each of the two Test Platform chips (i.e., the one that is coated with OTS SAM as well as the one that has microinstruments, whose surfaces are covered with only native oxide) investigated in this chapter, 16 distinct MSTs are tested. The width of each of the tested fracture beams is measured optically, to be $3.72 \mu\text{m}$ (design width is $4 \mu\text{m}$). The lever arm of each of the tested fracture beams is also measured optically. Table 8.1 reports the measured lever arms as well as the measured displacements of corresponding MSTs at the instant of fracture of the tested fracture beams. It also reports the (calculated) strains that exist in the tested fracture beams at the instant of their fracture. Each value reported in Table 8.1 is an arithmetic mean of 16 measurements, and the corresponding std. dev. is one standard deviation of the sample consisting of those measurements. The mean values of the fracture strain of the structural film reported in Table 8.1 indicate that the results obtained using fracture beams, which have different lengths, are consistent with each other. Even those obtained using MSTs of different Test Platform chips (i.e., OTS SAM coated Test Platform chip and native oxide covered Test Platform chip) are also consistent with each other. This authenticates the reliability of the results obtained using the Test Platform developed in this study. Additionally, the results reported in Table 8.1 indicate that the OTS SAM coating does not alter the fracture strength of the Si(100) structural film, which is as expected, because the thickness of the OTS SAM coating investigated in this chapter, which is 2.8 nm , is significantly lesser than the thickness of the structural film of the Test Platform developed in this study, which is $2 \mu\text{m}$

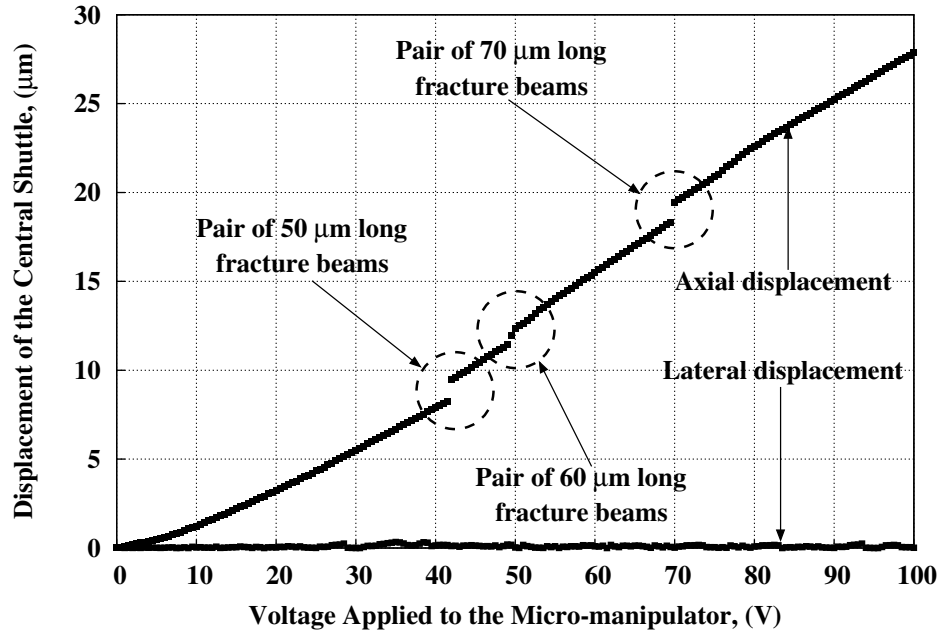


Figure 8.1: A plot showing the experimentally determined axial and lateral displacements of the central shuttle of one of the MSTs of the OTS SAM coated Test Platform chip versus the corresponding voltage applied to the micro-manipulator that is used to actuate it. Notice the discontinuities in the plot that represents the axial displacement data. Also, the lateral displacements of the central shuttle are negligible throughout the actuation of the MST.

Table 8.1: This table reports the measured lever arms as well as the measured displacements of corresponding MSTs at the instant of fracture of the tested fracture beams. It also reports the strains that exist in the tested fracture beams at the instant of their fracture. Each value reported in the table is an arithmetic mean of 16 measurements, and the corresponding std. dev. is one standard deviation of the sample consisting of those measurements.

Beam Length (μm)	L_c (μm)	Displacement at Fracture $\delta_f \pm \text{std. dev. } (\mu\text{m})$		Strain at Fracture $\epsilon_f \pm \text{std. dev. } (\%)$	
		Oxide	OTS	Oxide	OTS
50	41.85	5.99 ± 0.43	6.03 ± 0.35	1.91 ± 0.14	1.92 ± 0.11
60	51.62	9.22 ± 0.62	9.17 ± 0.91	1.93 ± 0.13	1.92 ± 0.19
70	61.38	13.57 ± 0.27	13.57 ± 0.33	2.01 ± 0.04	2.01 ± 0.05

(nominal). Lastly, the fracture strain of the Si(100) structural film determined using the Test Platform developed in this study is in good agreement with that reported in literature for Si(100) films [87, 88, 177, 178]. This authenticates the validity of the results obtained using the Test Platform developed in this study.

8.4 Resonator

As explained in section 5.3, the Resonator developed in this study can be used to determine the elastic modulus (i.e., E) of the structural film used to fabricate the Test Platform. Although the elastic modulus of the structural film of the Test Platform can be determined using a single Resonator and Eq. 5.3.6, in order to eliminate the error induced in the estimate of the elastic modulus by the errors (induced by the resolution of measurement) in the measured dimensions of the Resonator, a set of twenty five different Resonators, which are present at different locations on the Test Platform chip, is used to determine the elastic modulus of its structural film. Five Resonators each are chosen from five of the nine sets of Resonators included in the Test Platform chip.

In this chapter, the elastic modulus of the structural film of the native oxide covered Test Platform chip is determined. The five sets of Resonators that are used for it include Resonators with supporting beam lengths of 200 μm (nominal), 350 μm (nominal), 400 μm (nominal), 450 μm (nominal) and 500 μm (nominal). Table 8.2 reports the drive signals that are used to actuate the five selected sets of Resonators along with their optically observed resonance frequencies. Each resonance frequency reported in Table 8.2 is an arithmetic mean of five measurements, which are made using five distinct Resonators having the same supporting beam length. The square of the observed resonance frequency of each of the five selected sets of Resonators is plotted against their corresponding value of the term that is written in brackets on the right hand side of Eq. 5.3.6. The plot is shown in Fig. 8.2. All the dimensions, which

Table 8.2: This table reports the drive signals used to actuate the Resonators of the native oxide covered Test Platform chip along with their optically observed resonance frequencies. Each resonance frequency reported in the table is an arithmetic mean of five measurements, which are made using five distinct Resonators having the same supporting beam length.

Supporting Beam Length (μm)	DC Bias (V)	AC Drive Signal (Amplitude) (V)	Observed Resonance Frequency (KHz)
200	100	30	13.50 ± 0.005
350	50	20	6.14 ± 0.005
400	40	20	4.72 ± 0.005
450	30	20	3.92 ± 0.005
500	25	20	3.64 ± 0.005

are required to determine the value of the term that is written in brackets on the right hand side of Eq. 5.3.6, of each of the Resonators tested are measured optically, before actuating the Resonator. The experimentally observed resonance frequencies are represented by (\bullet) in the plot. A line fitted to the experimentally obtained data reported in Table 8.2 is also shown in the plot. The high R^2 (i.e., 0.9991) of the linear fit confirms that the resonance behaviour of the Resonators developed in this study can be accurately modeled using the harmonic oscillator equation given by Eq. 5.3.6. According to Eq. 5.3.6, the slope of the fitted line is the elastic modulus (E) of the structural film used to fabricate the Resonators. Therefore, the elastic modulus of the structural film of the native oxide covered Test Platform chip, which is the slope of the fitted line shown in Fig. 8.2, is 130 GPa. This indicates that the elastic modulus (E) of the Si(100) film obtained experimentally using the Test Platform developed in this study is exactly the same as that (i.e., 130 GPa) accepted widely, and published in literature [149]. This again validates the authenticity of the results obtained using the Test Platform developed in this study.

8.5 Cantilever Beam Array

8.5.1 Validating the Authenticity of the Actuation Method Used to Actuate the Cantilever Beams

As explained in section 5.4.2, the cantilever beams (CBs) of the Test Platform developed in this study are actuated (brought in contact with the substrate) manually, by pushing them using a sharp tungsten probe tip (Signatone SE-SMS). The manual force applied on a cantilever beam to bring it in contact with the underlying substrate has the potential of altering the characteristics of the in-plane interface formed between them. Accordingly, it can influence the result obtained using that cantilever beam. Further, if the manual force applied to actuate the cantilever beams

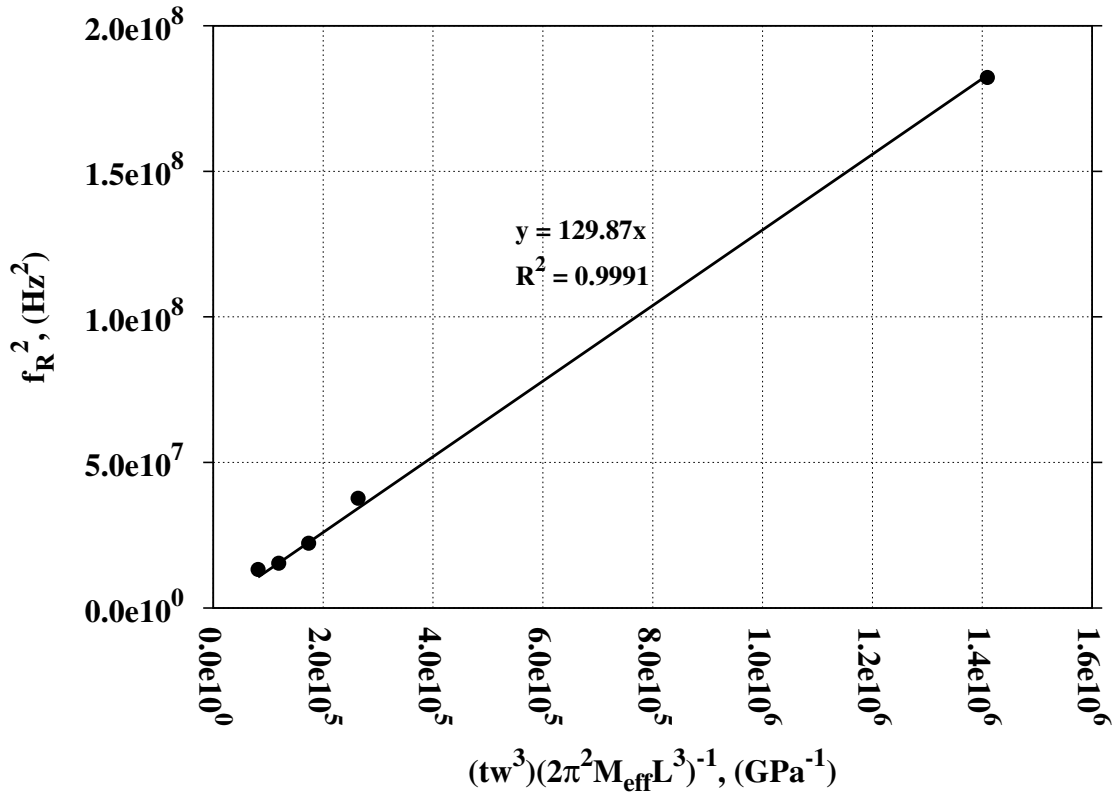
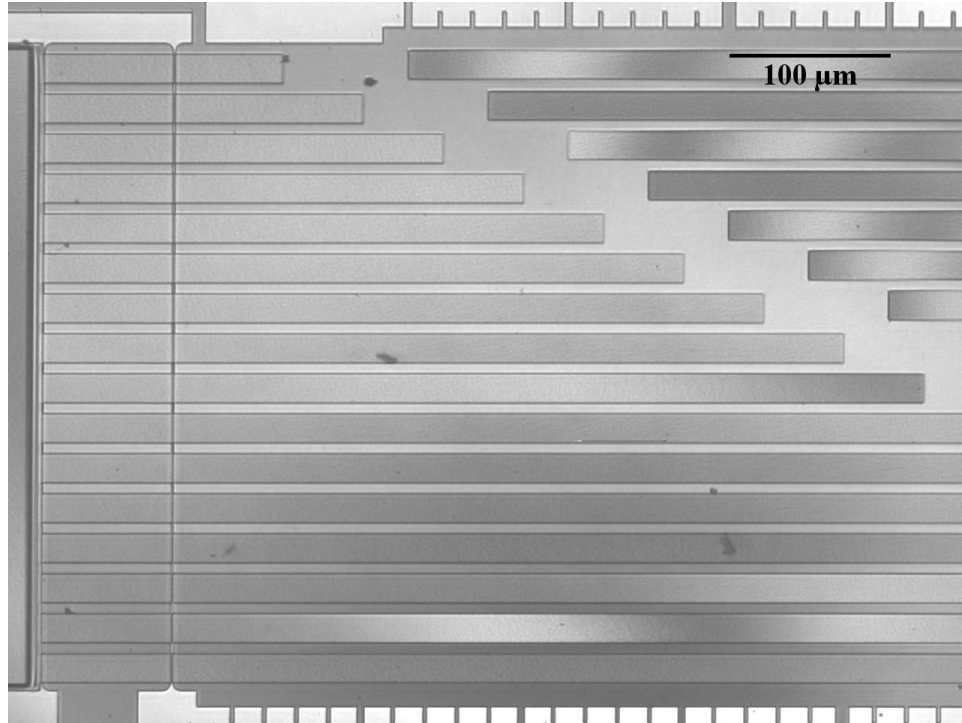
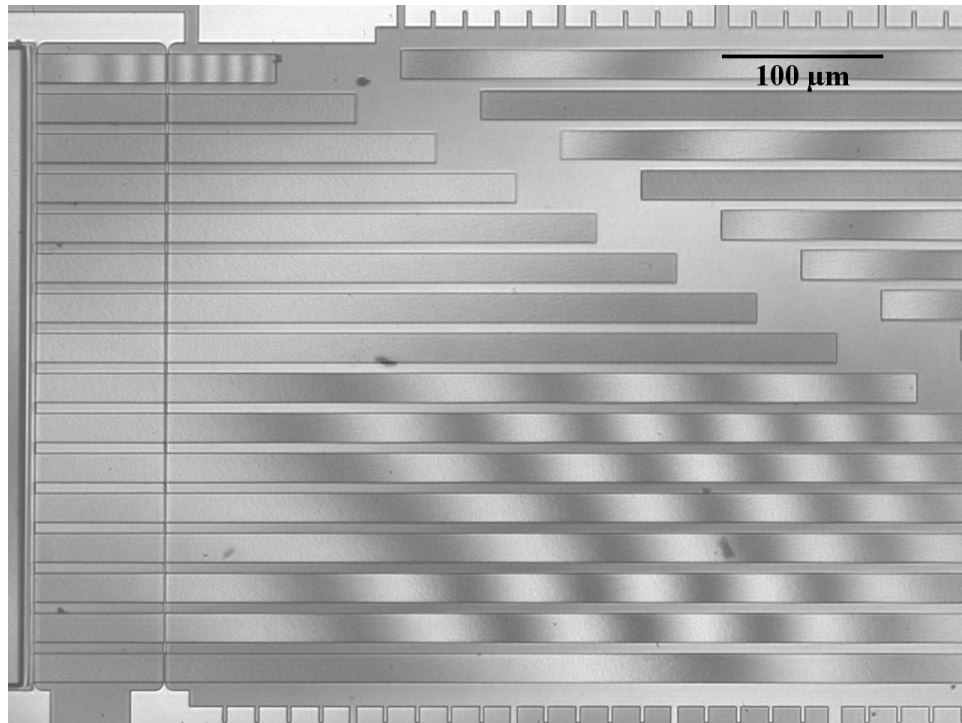


Figure 8.2: A plot of the square of the observed resonance frequency of the Resonators investigated in this chapter versus their corresponding value of the term that is written in brackets on the right hand side of Eq. 5.3.6. The (●) represent the experimentally observed resonance frequencies and (—) is a line fitted to the experimentally obtained data. Notice the high R^2 value of the linear fit. The slope of the fitted line is the experimentally obtained value of E of the structural film of the native oxide covered Test Platform chip.

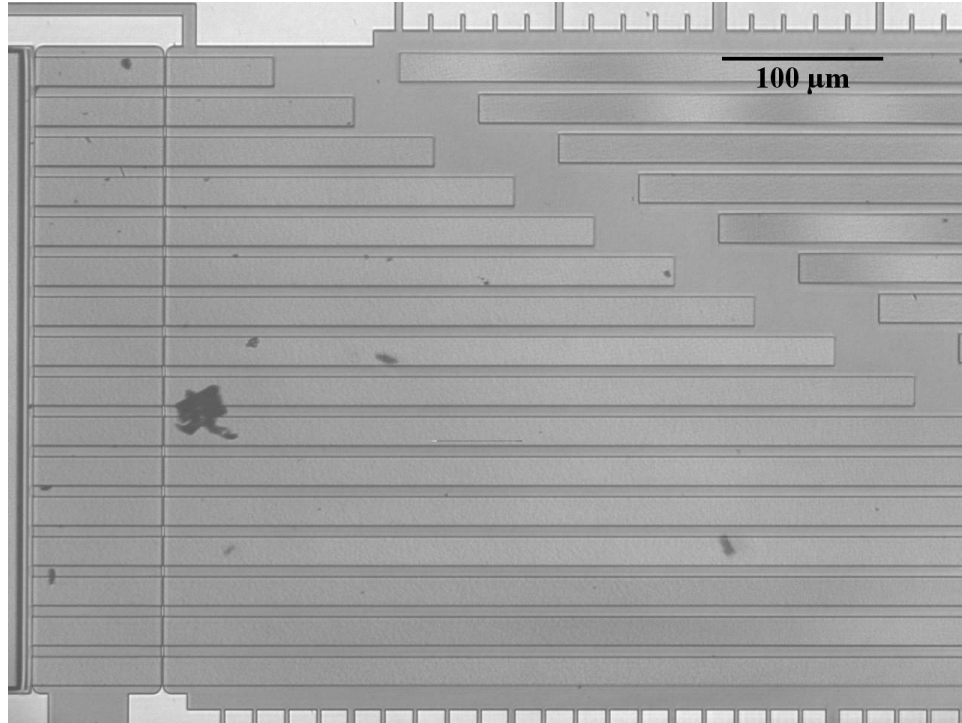


(a)

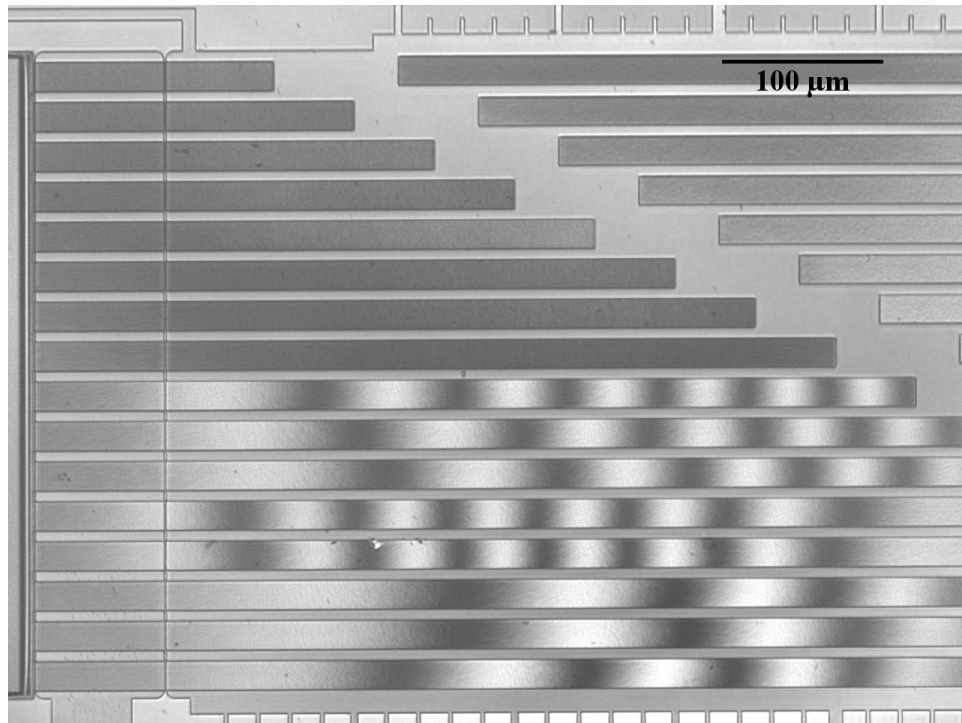


(b)

Figure 8.3: (a) Interferogram of a polysilicon-based CBA, collected before actuation. (b) Interferogram of the CBA shown in Fig. 8.3a, collected after actuation. This CBA was actuated manually.



(a)



(b)

Figure 8.4: (a) Interferogram of a polysilicon-based CBA, collected before actuation. (b) Interferogram of the CBA shown in Fig. 8.4a, collected after actuation. This CBA was actuated electrostatically.

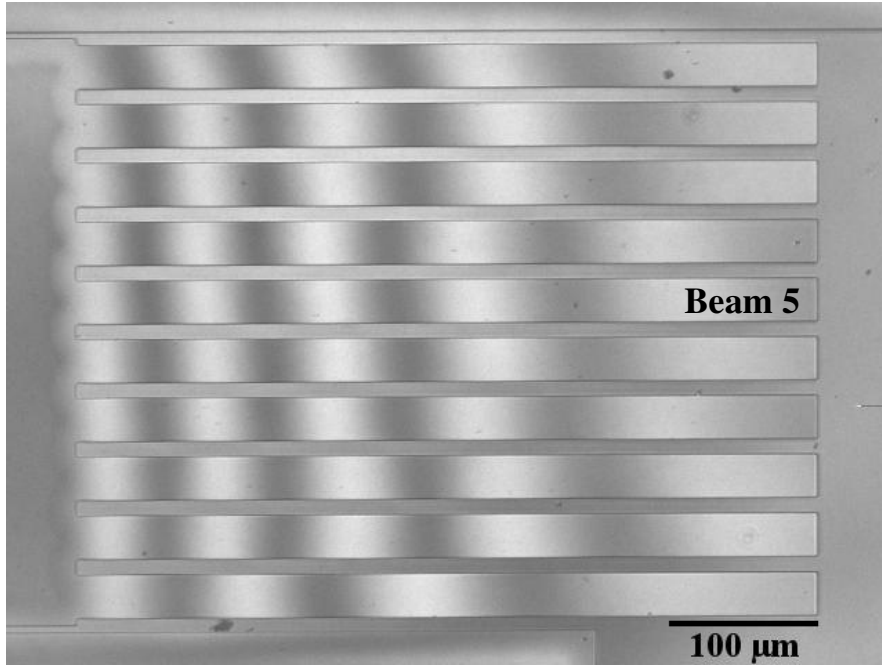
does influence the results obtained using them, then the results obtained using a cantilever beam array will be inconsistent, since the manual force applied to actuate the cantilever beams may vary from beam to beam in the same array. Therefore, in order to ascertain that the manual force exerted on a cantilever beam to actuate it does not have any influence on the result obtained using it, two polysilicon-based cantilever beam arrays fabricated side-by-side on the same chip are actuated, one manually and the other electrostatically. The purpose behind using the polysilicon-based cantilever beam arrays for this analysis is that the cantilever beam arrays of the Test Platform developed in this study cannot be actuated electrostatically. Electrostatic actuation is considered as the standard method for actuating cantilever beam arrays. Figures 8.3a and 8.3b are interferograms showing the polysilicon-based cantilever beam array that is actuated manually, collected before and after the actuation, respectively. Similarly, Figs. 8.4a and 8.4b are interferograms showing the polysilicon-based cantilever beam array that is actuated electrostatically, collected before and after the actuation, respectively. It is clearly evident from Figs. 8.3b and 8.4b that the manual actuation method yields the exact same results as the electrostatic actuation method. The cantilever beams that did not stick in the polysilicon-based CBA, which was actuated electrostatically, also did not stick in the polysilicon-based CBA, which was actuated manually. Further, the same eight longer cantilever beams are stuck, either at their tips or over a fraction of their lengths, in both the CBAs (i.e., the one that is actuated manually as well as the one that is actuated electrostatically). This validates the authenticity of the manual actuation method used to actuate the cantilever beams for this study. The script used for validating the authenticity of the manual actuation method used to actuate the cantilever beams, in this study is given in Appendix A.3.

8.5.2 Stress Gradient at the Sacrificial Oxide-Device Layer Interface

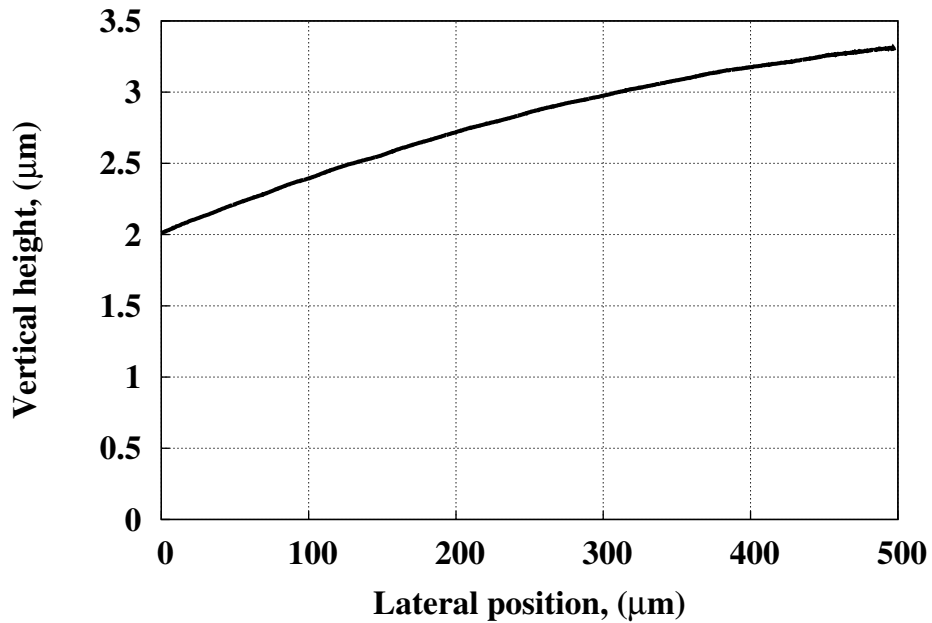
When released, the cantilever beams of the Test Platform developed in this study do not remain horizontal, but are inclined upwards. This is evident in Fig. 8.5a, which is an interferogram showing a released cantilever beam array of the Test Platform chip coated with OTS SAM. The presence of fringes on the cantilever beams shown in Fig. 8.5a clearly indicates that they are not parallel to the substrate. The height profile of beam 5 (labelled in Fig. 8.5a), which is shown in Fig. 8.5b, further substantiates that the cantilever beams shown in Fig. 8.5a are inclined upwards, and have a convex shape. This type of upward-inclined and curved height profile is exhibited by all the cantilever beams of every Test Platform chip, irrespective of the treatments, to which, the Test Platform chips are subjected. The upward inclination of the released cantilever beams of the Test Platform developed in this study is a consequence of the augmentation of the stress-gradient present at the interface of sacrificial oxide and device layer in their anchors. The curvature in their shape is a consequence of the internal moment induced in them by the stress gradient present in their anchors, at the interface of sacrificial oxide and device layer. The stress gradient that exists at the interface of sacrificial oxide and device layer in the anchors of the cantilevers beams of the Test Platform developed in this study is augmented by the high temperature cycling, to which, the Test Platform is exposed during the polishing of its scalloped sidewall test surfaces. This is substantiated by the fact that the released cantilever beams of the Test Platform chip, which is not polished (i.e., exposed to high temperature cycling), are significantly less upward-inclined and curved as compared to those of the Test Platform chip, which is polished. Figure 8.6a is an interferogram showing a released cantilever beam array of a Test Platform chip, which is not polished. The lesser number of fringes present on the cantilever beams shown in Fig. 8.6a as compared to those present on the cantilever beams shown in Fig. 8.5a substantiate their less upward-inclined height profiles as compared to the height profiles of the

cantilever beams shown in Fig. 8.5a. Figure 8.6b, which is the PSI derived height profile of beam 1 labelled in Fig. 8.6a, further provides a quantitative confirmation of the less upward-inclined and less curved height profiles of the cantilever beams, which are not exposed to high temperature cycling, as compared to the height profiles of those, which are exposed to high temperature cycling.

In order to obtain an accurate estimate of the work of adhesion of in-plane surfaces using the cantilever beams of the Test Platform developed in this study, the effects that the stress gradient present at the interface of sacrificial oxide and device layer in their anchors has on their initial (pre-actuated) height profiles must be appropriately accounted for. The stress gradient present at the interface of sacrificial oxide and device layer in the anchors of the cantilever beams of the Test Platform used in this study causes them to have an upward-inclined, convex initial (pre-actuated) height profile. Therefore, the additional work done in bringing the tips of the upward-inclined cantilever beams in contact with the substrate must be included in the estimate of the work of adhesion of in-plane surfaces. The additional work done includes the work done to bend the cantilever beams through an additional height due to their upward inclination, which is stored as an additional bending energy in them, as well as the work done to counter the resistance offered by the stress gradient induced internal moment present in them to their bending. Additionally, the stress gradient present at the interface of sacrificial oxide and device layer in the anchors of the cantilever beams of the Test Platform used in this study causes the adhered (actuated) cantilever beams to have non-zero slopes at their boundary points (i.e., the points, at which, they are connected to their anchors as well as the points, at which, they are adhered to the substrate). The equation used in this study for estimating the apparent work of adhesion of in-plane surfaces (i.e., Eq. 5.4.1) takes into account both the non-zero boundary slopes of the adhered cantilever beams as well as the additional work done to counter the effects of the stress gradient present

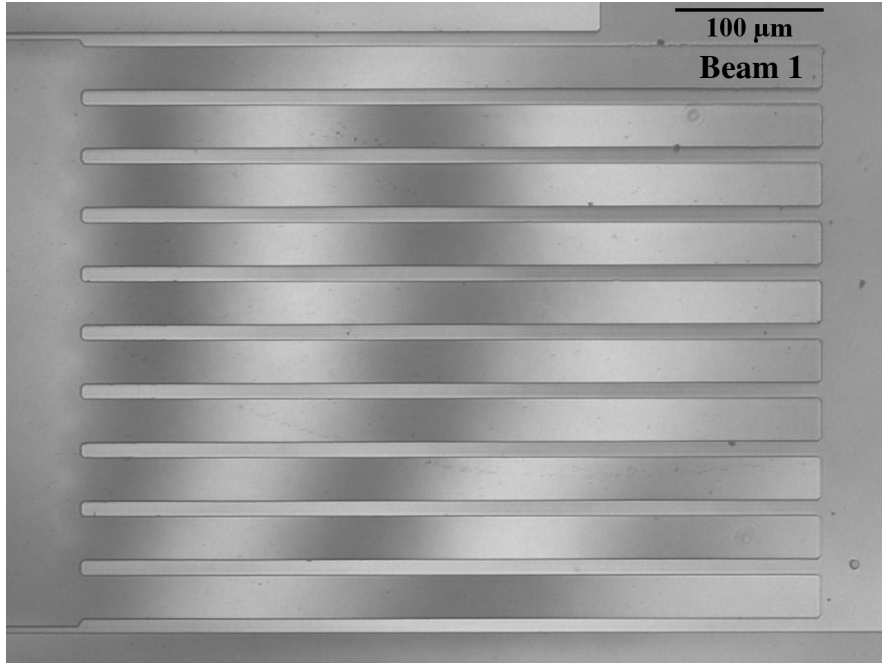


(a)

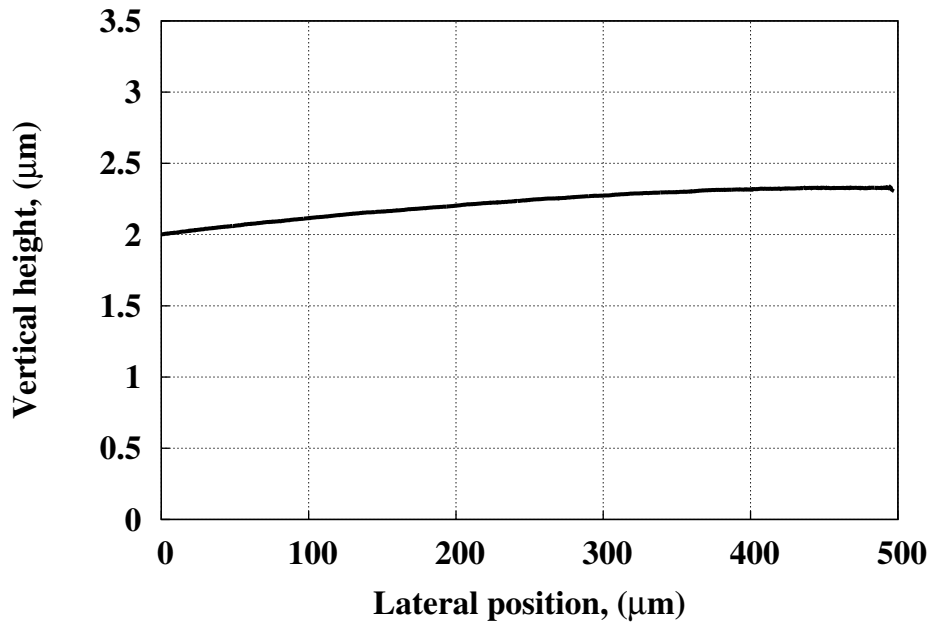


(b)

Figure 8.5: (a) Interferogram showing a released cantilever beam array of the Test Platform chip coated with OTS SAM. Notice the presence of fringes on all the cantilever beams, which indicates that they are not parallel to the substrate. (b) Height profile of beam 5 labelled in Fig. 8.5a. The height profile is obtained experimentally, using phase shifting interferometry. It indicates that beam 5 is inclined upwards, and has a convex shape.



(a)



(b)

Figure 8.6: (a) Interferogram showing a released cantilever beam array of a Test Platform chip, which is not polished. Notice that the number of fringes present on the cantilever beams shown in this image is less, which indicates that they are not parallel to the substrate. (b) Height profile of beam 5 labelled in Fig. 8.5a. The height profile is obtained experimentally, using phase shifting interferometry. It indicates that beam 5 is inclined upwards, and has a convex shape.

at the interface of sacrificial oxide and device layer in their anchors. An analysis to support this claim is provided in Table 8.3, which lists the apparent work of adhesion of OTS SAM coated in-plane surfaces calculated using different methods. Method “S-H” considers that the adhered cantilever beam is S-shaped, and was perfectly parallel to the substrate in its initial (pre-actuated) state. Method “S-I” also considers that the adhered cantilever beam is S-shaped, but uses its PSI derived, experimentally obtained initial (pre-actuated) height profile as the reference. Both the methods “P-H” and “P-I” use the PSI derived, experimentally obtained height profile of the actuated adhered cantilever beam for estimating the apparent work of adhesion of in-plane surfaces. However, while method “P-H” considers that the cantilever beam was perfectly parallel to the substrate in its initial (pre-actuated) state, method “P-I” uses its PSI derived, experimentally obtained initial (pre-actuated) height profile as the reference. The OTS SAM coated cantilever beam used for this analysis exhibited a crack length of $835.3 \mu\text{m}$. It is clearly evident from the data reported in Table 8.3 that the apparent work of adhesion of in-plane surfaces estimated using methods “S-H” and “S-I” is significantly lower than the actual value. This is attributed to the fact that both the methods “S-H” and “S-I” do not consider the non-zero boundary slopes of the adhered cantilever beams. Additionally, method “S-H” neither considers the work done to bend the cantilever beams through an additional height due to their upward inclination nor considers the work done to counter the resistance offered by the stress gradient induced internal moment present in them to their bending. While method “S-I” does consider the work done to bend the cantilever beams through an additional height due to their upward inclination, it still does not consider the work done to counter the resistance offered by the stress gradient induced internal moment present in them to their bending. On the other hand, both the methods “P-H” and “P-I” consider both the work done to bend the cantilever beams through an additional height due to their upward inclination as well as the work done to counter the

resistance offered by the stress gradient induced internal moment present in them to their bending. Therefore, the work of adhesion of OTS SAM coated in-plane surfaces estimated using them appear to be more believable. Table 8.3 additionally indicates that while the work required to counter the resistance offered by the stress gradient induced internal moment present in the cantilever beams to their bending is significantly greater than that required to overcome the restoring forces of the bent (actuated) cantilever beams, and the major fraction of the apparent work of adhesion required by the cantilever beams to remain adhered to the substrate, the work required to bend the cantilever beams through an additional height due to their upward inclination is much lesser than that, and only a minor fraction of it. The method used for determining the apparent work of adhesion of the in-plane surfaces investigated in this study is highlighted in Table 8.3.

8.5.3 Determining the Apparent Work of Adhesion of In-plane Surfaces Coated with Standard Coatings

For each type of surface studied in this chapter (i.e., OTS SAM coated and surfaces with only native oxide on them), four CBAs (consisting of ten cantilever beams each) are used for determining the apparent work of adhesion of in-plane surfaces. The magnification of the objective lens, which is used in the interference microscope that is used to determine the height profile of the actuated cantilever beams, is either 10X or 20X. Accordingly, the size of each pixel in the field of view is either $0.465 \mu\text{m} \times 0.465 \mu\text{m}$ or $0.234 \mu\text{m} \times 0.234 \mu\text{m}$, respectively. Table 8.4 reports the crack lengths and the apparent works of adhesion of in-plane surfaces for both OTS SAM coated surfaces as well as surfaces with only native oxide on them. The results are as expected. OTS SAM coated in-plane surfaces exhibit a much lower apparent work of adhesion than the corresponding surfaces with only native oxide on them. This is expected because the hydrophobic surface chemistry of OTS SAM

Table 8.3: Comparison between the apparent work of adhesion of OTS SAM coated in-plane surfaces calculated using different methods. The OTS SAM coated cantilever beam used for this analysis exhibited a crack length of 835.3 μm . The method used for determining the apparent work of adhesion of the in-plane surfaces investigated in this study is highlighted in the table.

Calculation Method	\mathcal{W}_{ip} ($\mu\text{J}/\text{m}^2$)
S-H	8.848
S-I	8.360
P-H	46.15
P-I	45.12

- S-H: Considers that the adhered cantilever beam is S-shaped.
Considers that it was perfectly parallel to the substrate in its initial state.
- S-I: Considers that the adhered cantilever beam is S-shaped.
Uses its PSI derived initial (pre-actuated) height profile as the reference.
- P-H: Uses the PSI derived height profile of the actuated adhered cantilever beam.
Considers that it was perfectly parallel to the substrate in its initial state.
- P-I:** Uses the PSI derived height profile of the actuated adhered cantilever beam.
Uses its PSI derived initial (pre-actuated) height profile as the reference.

Table 8.4: Comparison between the apparent work of adhesion of in-plane surfaces of OTS SAM coated surfaces and that of surfaces with only native oxide on them. The apparent works of adhesion of in-plane surfaces reported in this table are determined using the CBAs. All the values reported in the table are arithmetic means of 40 measurements and sd is one standard deviation of the sample consisting of those measurements.

Coating	Crack Length $s_{ip} \pm \text{sd}$ (μm)	Apparent Work of Adhesion of In-plane Surfaces $\mathcal{W}_{ip} \pm \text{sd}$ ($\mu\text{J}/\text{m}^2$)
Oxide	99.0 ± 5.5	38700 ± 9300
OTS	833.5 ± 5	45.46 ± 1

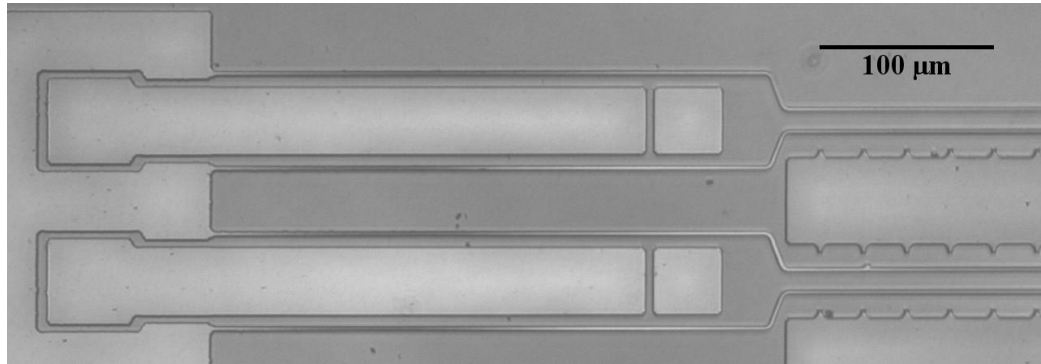
coated surfaces significantly reduces the contribution of capillary forces to stiction between them. Further, for both types of surfaces (OTS SAM coated and surfaces with only native oxide on them), the in-plane surfaces exhibit a higher apparent work of adhesion than the corresponding sidewall surfaces (The apparent works of adhesion of sidewall surfaces are reported in Table 8.5). This is also expected because the sidewall surfaces of the Test Platform have a much higher rms roughness (6.52 nm) than the in-plane surfaces (0.1 nm). In fact, this substantiates the fact that the topographies of contacting MEMS surfaces have a strong influence on the tribological properties of the interface formed by them. Further evidence of the influence of the surface topographies of contacting MEMS surfaces on their tribological properties is provided by the fact that the apparent works of adhesion of in-plane surfaces reported by Ashurst *et al.*, who used microinstruments fabricated using rougher polysilicon surfaces (rms roughness of the in-plane surfaces tested was 5.9 nm and rms roughness of the sidewall surfaces tested was 13.3 nm), is significantly lesser than those obtained using the Test Platform developed in this study, for both the types of surfaces studied in this chapter [6,35,104]. Even though their experiments were conducted at a higher relative humidity (RH) of 50 %, Ashurst *et al.* reported a lower in-plane apparent work of adhesion of 0.012 mJ/m² and 13.1 mJ/m² for OTS coated polysilicon surfaces and polysilicon surfaces with only native oxide on them, respectively.

8.6 Sidewall Beam Array

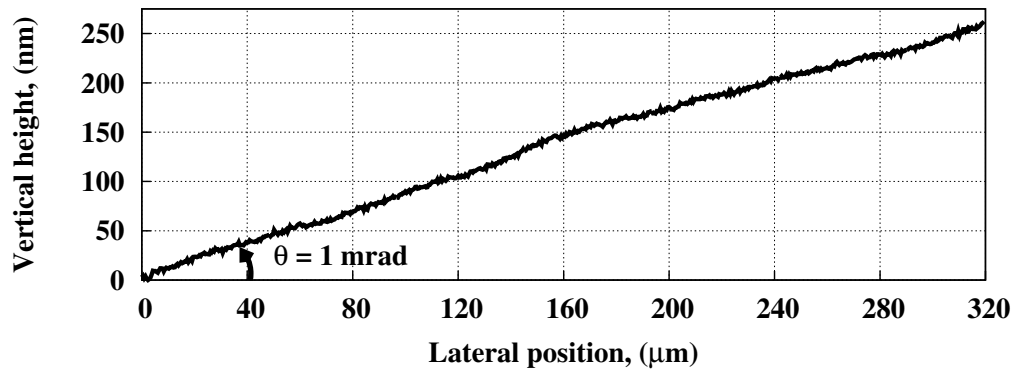
Figure 8.7a is an interferogram showing released sidewall adhesion test microinstruments. The fringes visible on the sidewall beams in Fig. 8.7a reveal two features about the released sidewall beams. First, the released sidewall beams are freestanding. Second, they are not parallel to the substrate. This is also substantiated by Fig. 8.7b, which shows the height profile of the initial segment of the topmost sidewall beam shown in Fig. 8.7a. The height profile shown in Fig. 8.7b clearly indicates

that the sidewall beams are inclined upwards and they exhibit a take-off angle of 1 mrad. This upward inclination of the released sidewall beams is attributed to the stress gradient present at the sacrificial oxide/device layer interface in the anchor. It, unlike the compliance of the sidewall adhesion tester reported in [78], obviates the need to place a constraining clip over the ends of a sidewall beam pair to ensure that the sidewall beams remain in place during the drying process.

Levitation, which is a critical phenomena that ensues in most of the electrostatically actuated microinstruments, needs to be appropriately accounted for to ensure the accuracy of the results obtained using those microinstruments. Historically, researchers have either used an elaborate actuation scheme to account for the effects of levitation or a sophisticated electronic read-out system combined with a theoretical model to subtract the levitation induced contribution from the measured output signal [142, 159]. However, while levitation does ensue during the electrostatic actuation of the sidewall adhesion test microinstrument developed in this study, it has no influence on the results obtained using the microinstrument. This is substantiated by Fig. 8.8, which is an interferogram showing the initial segment of an actuated sidewall adhesion test microinstrument. A voltage of 52 V is applied to the electrode to actuate the sidewall adhesion test microinstrument, in this case. The number of fringes visible on the actuated sidewall beams seen in Fig. 8.8 is much greater than that of the fringes visible on the unactuated sidewall beams seen in Fig. 8.7a. This clearly indicates that levitation ensues and increases the upward inclination of the actuated sidewall beams. However, it has the exact same effect on both the sidewall beams of the microinstrument, which is evident from the presence of the same number of fringes on them. As a result, it has no influence on the apparent interfacial contact area of the two adhered sidewall beams and hence on the apparent work of adhesion of the sidewall surfaces determined using the sidewall adhesion test microinstrument developed in this study. In essence, the design of the sidewall adhesion test



(a)



(b)

Figure 8.7: (a) Interferogram showing released sidewall adhesion test microinstruments. Notice the fringes on the sidewall beams, which clearly indicate that the sidewall beams are freestanding and also not parallel to the substrate (b) Height profile of the initial segment of the topmost sidewall beam shown in Fig. 8.7a. The height profile is obtained using phase shifting interferometry. It clearly indicates that the sidewall beam is inclined upwards and exhibits a take-off angle of 1 mrad.

microinstrument developed in this study obviates the need to account for the effects of levitation on the results obtained using it.

One of the limitations of the sidewall adhesion tester reported by Ashurst *et al.* in [78] was that the sidewall beams that remained stuck to each other after actuation were not perfectly aligned in the z plane, in spite of the measures taken to prevent the misalignment. This effect, which Ashurst *et al.* referred to as “scissoring”, acted to reduce the apparent interfacial contact area of the adhered sidewall beams, and thereby, compromised the accuracy of the apparent work of adhesion determined using the sidewall adhesion tester. Moreover, the amount of scissoring exhibited by different sidewall adhesion testers fabricated on the same chip was random and even that exhibited by the same sidewall adhesion tester was not reproducible [78]. While the scissoring induced error in the determination of apparent work of adhesion of sidewall surfaces is relatively small when stiction between sidewall surfaces is high, it is substantial when the stiction between them is low [78]. Therefore, scissoring makes it difficult to compare the effects of the surface modification strategies used to reduce stiction between MEMS sidewalls. However, the sidewall adhesion test microinstrument developed in this study does not exhibit scissoring at all. This is substantiated by Fig. 8.9a, which is an interferogram showing the final segment of an actuated sidewall adhesion test microinstrument (developed in this study). A voltage of 70 V is applied to the electrode to actuate the sidewall adhesion test microinstrument in this case. Notice that the sidewall beams are adhered over a length of 50 μm at their tips. It is clearly evident in Fig. 8.9a that the adhered sidewall beams are perfectly aligned in the z -plane since the fringes on the two of them exactly match each other in number as well as phase. The small mis-match in the phase of the fringes visible on the two adhered sidewall beams in Fig. 8.9a is due to the torsional twisting of the sidewall interface. The sidewall interface formed by the two adhered sidewall beams experiences a torsional twist because the contacting sidewall beams

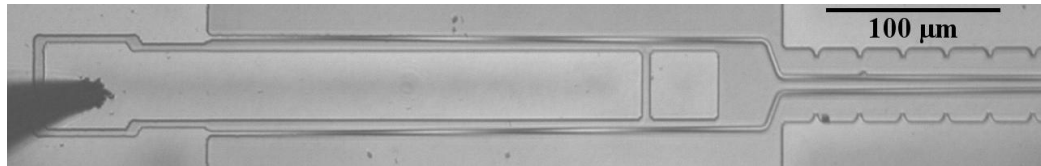


Figure 8.8: Interferogram showing the initial segment of an actuated sidewall adhesion test microinstrument. Voltage applied to the actuation electrode is 52 V. Notice the increased number of fringes visible on the actuated sidewall beams as compared to that of fringes visible on the unactuated sidewall beams shown in Fig. 8.7a, which is a manifestation of levitation. Also notice that the exact same number of fringes are visible on both the actuated sidewall beams.

do not have perfectly vertical sidewall surfaces. The torsional twisting of the sidewall interface was confirmed using phase shifting interferometry. The sidewall angle of the contacting sidewall beams was also determined using phase shifting interferometry and is found to be 89° . However, since the torsional twisting of the sidewall interface does not affect the apparent interfacial contact area of the adhered sidewall beams, it does not induce any error in the determination of the apparent adhesion energy of sidewall surfaces. Figure 8.9b is the interferogram of the same sidewall adhesion test microinstrument that is shown in Fig. 8.9a, collected post-actuation. In the post-actuated state too, the fringes on the two sidewall beams are equal and in-phase, as evident in Fig. 8.9b. In order to determine the reproducibility of the vertical alignment of the adhered sidewall beams of the sidewall adhesion test microinstrument developed in this study, the adhered sidewall beams were carefully pulled apart and re-actuated. Comparing the interferograms of the actuated and re-actuated sidewall adhesion test microinstruments did not reveal any discernible differences in the vertical alignment of the adhered sidewall beams.

For each type of surface studied in this chapter (OTS SAM coated and surfaces with only native oxide on them), eight SBAs are used to determine the apparent work of adhesion of the contacting sidewall surfaces. The magnification of the objective lens of the microscope, which is used to observe the microinstrument during actuation and determine the crack length of each actuated adhered pair of sidewall beams, is 10X. Accordingly, the size of each pixel in the field of view is $0.465 \mu\text{m} \times 0.465 \mu\text{m}$. Table 8.5 reports the crack lengths and the apparent works of adhesion of the contacting sidewall surfaces for both OTS SAM coated surfaces as well as surfaces with only native oxide on them. The results are as expected. OTS SAM coated sidewalls exhibit a much lower apparent work of adhesion than the corresponding surfaces with only native oxide on them. This is expected because the hydrophobic surface chemistry of OTS SAM coated surfaces significantly reduces the contribution

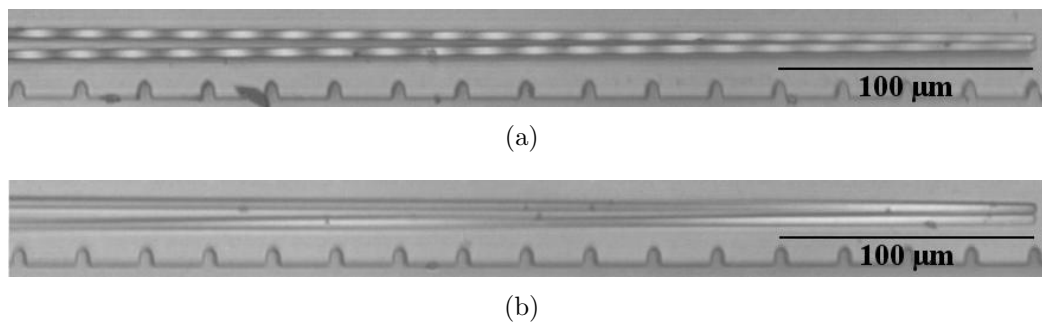


Figure 8.9: (a) Interferogram showing the final segment of an actuated sidewall adhesion test microinstrument. Voltage applied to the actuation electrode is 70 V. The two sidewall beams are stuck to each other over a length of 50 μm at their tips. Notice that while the fringes on the two sidewall beams are equal in number, they are slightly mismatched in phase. (b) Interferogram, showing the final segment of the same sidewall adhesion test microinstrument that is shown in Fig. 8.9a, collected post-actuation. Notice that no “scissoring” is visible on the two sidewall beams, which are stuck over a length of 25 μm at their tips.

Table 8.5: Comparison between the apparent work of adhesion of sidewall surfaces of OTS SAM coated surfaces and that of surfaces with only native oxide on them. The apparent works of adhesion of sidewall surfaces reported in this table are determined using the SBAs. All the values reported in the table are arithmetic means of several measurements and sd is one standard deviation of the sample consisting of those measurements.

Coating	Crack Length $s_s \pm \text{sd}$ (μm)	Apparent Work of Adhesion of Sidewall Surfaces $\mathcal{W}_s \pm \text{sd}$ ($\mu\text{J}/\text{m}^2$)
Oxide	660 ± 10	1070 ± 60
OTS	1550 ± 10	37.65 ± 1

of capillary forces to stiction between them. Further, for both the types of surfaces studied (i.e., OTS SAM coated and surfaces with only native oxide on them), the sidewall surfaces exhibit a lower apparent work of adhesion than that exhibited by the corresponding in-plane surfaces (The apparent works of adhesion of in-plane surfaces are reported in Table 8.4). This is also expected because the sidewall surfaces of the Test Platform developed in this study have a much higher rms roughness (6.52 nm) than its in-plane surfaces (0.1 nm). The difference between the apparent work of adhesion of sidewall surfaces and that of in-plane surfaces is greater in the case of surfaces with only native oxide on them as compared to OTS SAM coated surfaces because the capillary forces present at interfaces between surfaces with only native oxide on them augment the effect of topography on stiction between them.

8.7 Sidewall Friction Tester

As outlined in section 5.6.4, the first step in actuating a Sidewall Friction Tester is to determine the a and b of that Sidewall Friction Tester. The optically measured values of a and b of one of the Sidewall Friction Testers coated with OTS SAM (referred to as test device from now onwards) are $18.135 \mu\text{m}$ and $26.505 \mu\text{m}$, respectively. Therefore, according to Eq. 5.6.8, δ_a for the test device is $4.185 \mu\text{m}$. The magnification of the objective lens that is used in the microscope during the actuation of the Sidewall Friction Testers is 10X. Accordingly, the size of each pixel in the field of view is $0.465 \mu\text{m} \times 0.465 \mu\text{m}$. Figure 8.10 is a plot showing the experimentally determined axial and lateral displacements of the tangential arm of the test device versus the square of the corresponding voltages (V_t^2) applied to its pull drive. As expected, the data representing the axial displacements is clearly divided into two segments, which have significantly different slopes. The segment with the smaller slope corresponds to the initial segment and that with the higher slope corresponds to the final segment of the anchored comb fingers of the tangential comb-drive actuator. Further,

it is evident in Fig. 8.10 that within each segment, the axial displacement of the tangential arm increases linearly with the force generated by the tangential comb-drive actuator. This substantiates the validity of our treatment of the folded beam flexures and the thin beam that connects the tangential arm to the loading section as linear elastic (Hookean) springs. The transfer functions corresponding to the two segments (i.e., G_{t1} and G_{t2} respectively) of the anchored comb fingers of the tangential comb-drive actuator, which are determined by fitting straight lines to the two segments of the axial displacement data shown in Fig. 8.10, are $0.0046 \mu\text{m}/\text{V}^2$ and $0.0128 \mu\text{m}/\text{V}^2$ respectively. Accordingly, the ratio of the experimentally determined G_{t2} to the experimentally determined G_{t1} is 2.78, which confirms that as expected, the electrostatic force generated by the pull drive of the tangential comb-drive actuator increases by close to a factor of 3 when a fraction of the length of suspended comb fingers overlaps with the final segments of the anchored comb fingers. V_a , which is determined by identifying the voltage that corresponds to an axial displacement of δ_a in Fig. 8.10, is 26.1 V. It should be noted that the data point corresponding to δ_a and V_a belongs to the segment of axial displacement data that has a higher slope, which indicates that when the normal arm is aligned with the anchored posts, a fraction of the length of suspended comb fingers overlaps with the final segments of the anchored comb fingers. The data that represents lateral displacements indicates that during the entire calibration, the motion of the tangential arm is confined to only the axial direction.

Figure 8.11 is a plot showing the experimentally determined axial and lateral displacements of the normal arm of the test device versus the square of the corresponding voltages (V_n^2) applied to its pull drive. Again as expected, the data representing the axial displacements is clearly divided into three segments, which have significantly different slopes. The first two segments correspond to the initial and final segments

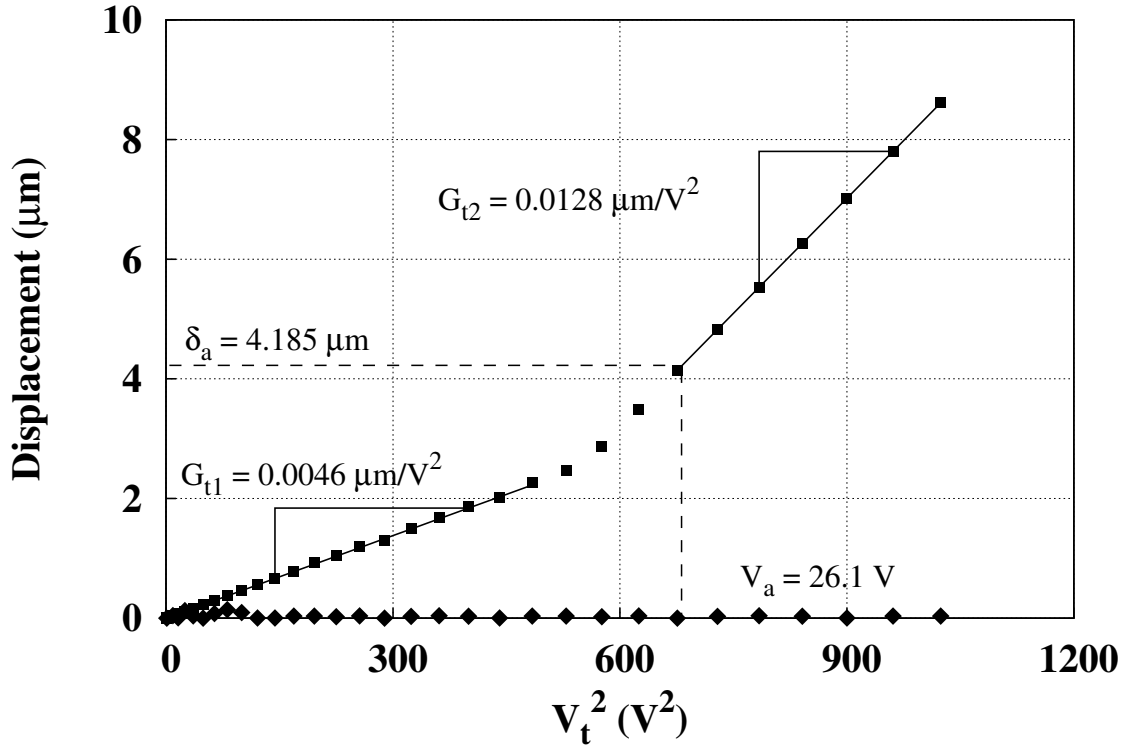


Figure 8.10: A plot showing the experimentally determined axial (■) and lateral (◆) displacements of the tangential arm of the test device versus square of the corresponding voltages (V_t^2) applied to its pull drive. Notice that the data representing the axial displacements is clearly divided into two segments, which have significantly different slopes. The transfer functions G_{t1} and G_{t2} are extracted from the corresponding linear fits (—) of the experimental axial displacement data. δ_a , which is determined optically, is the distance by which the tangential arm should be pulled to its left to align the normal arm with the anchored posts and V_a is the corresponding voltage that should be applied to the pull drive of the tangential arm.

of the anchored comb fingers of the normal comb-drive actuator. Further, it is evident in Fig. 8.11 that within the first two segments, the axial displacement of the normal arm increases linearly with the force generated by the normal comb-drive actuator. This substantiates the validity of our treatment of the folded beam flexures and the thin beam that connects the normal arm to the loading section as linear elastic (Hookean) springs. The transfer functions corresponding to those two segments (i.e., G_{n1} and G_{n2} respectively), which are determined by fitting straight lines to the corresponding data, are $0.0036 \mu\text{m}/V^2$ and $0.0104 \mu\text{m}/V^2$ respectively. The ratio of the experimentally determined G_{n2} to the experimentally determined G_{n1} is 2.88, which again, is close to the design value of 3. The third segment of the axial displacement data indicates that the axial displacement of the normal arm does not increase beyond $6.17 \mu\text{m}$. Therefore, δ_c , which is the distance by which the normal arm should be axially displaced to bring the loading beam in contact with an anchored post, is $6.17 \mu\text{m}$. Accordingly, V_c , which is the voltage that should be applied to a normal comb-drive actuator to bring the loading beam in contact with the corresponding anchored post is 32.6 V. It is determined by identifying the voltage that corresponds to an axial displacement of δ_c in Fig. 8.11. Additionally, it should be noted that even at voltages (applied to the normal comb-drive actuator) greater than V_c , the lateral displacements of the normal arm are negligible. This confirms that no unbalanced moment is induced at the sidewall interface by the normal load applied at it.

Levitation, which is a critical phenomena that ensues in most of the electrostatically actuated microinstruments, has been reported to reduce the apparent contact area of the test sidewall interface of most of the sidewall friction and wear test microinstruments reported to date [23, 85, 143, 159, 179]. The reduction in the apparent contact area of the sidewall interface results in inaccurate determination of the contact pressures applied to it. Therefore, historically, researchers have either used an elaborate actuation scheme or a sophisticated electronic read-out system combined

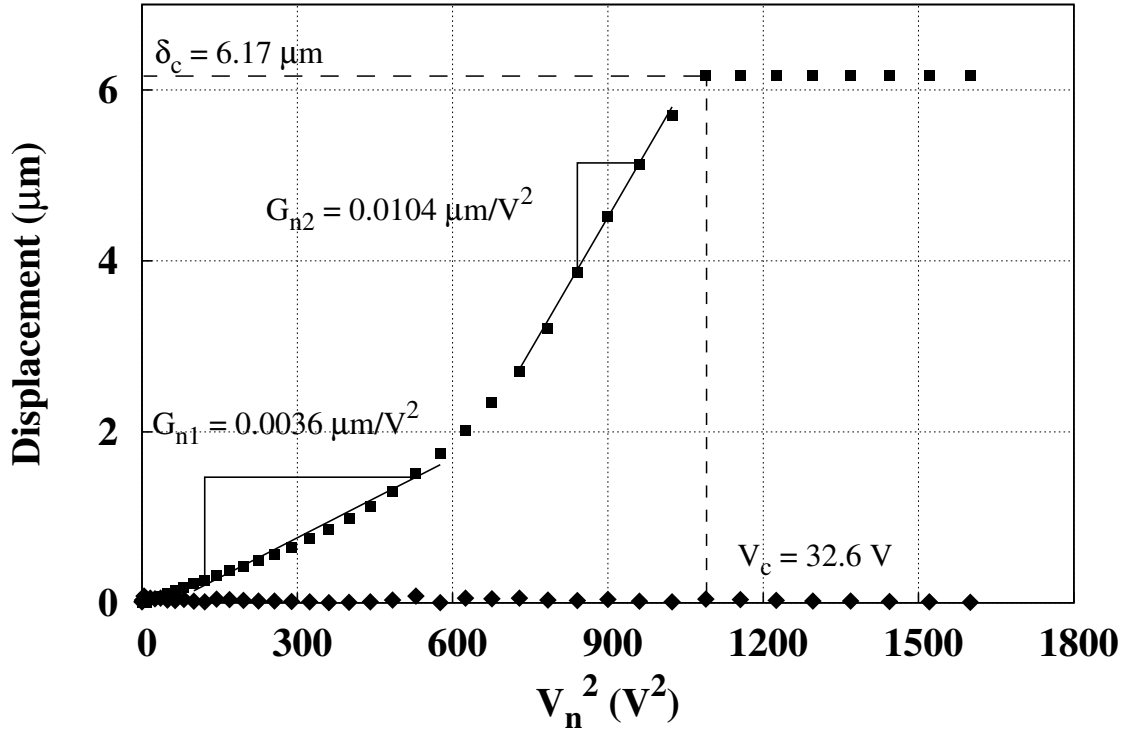


Figure 8.11: A plot showing the experimentally determined axial (■) and lateral (◆) displacements of the normal arm of the test device versus square of the corresponding voltages (V_n^2) applied to its pull drive. Notice that the data representing the axial displacements is clearly divided into three segments, which have significantly different slopes. The transfer functions G_{n1} and G_{n2} are extracted from the corresponding linear fits (—) of the experimental axial displacement data. δ_c is the distance by which the normal arm should be axially displaced in order to bring the loading beam in contact with the anchored post and V_c is the corresponding voltage that should be applied to the normal comb-drive actuator. Notice that even at voltages greater than V_c , the lateral displacements of the normal arm are negligible.

with a theoretical model to account for the effects of levitation [23, 143, 159, 179]. However, no additional measures are required to account for the effects of levitation in the case of the Sidewall Friction Tester developed in this study, since levitation does not ensue in it. This is substantiated by Fig. 8.12, which is an interferogram, showing the loading section of the test device, collected after bringing the loading beam in contact with the anchored post. A voltage of 45 V is applied to the pull drive of the normal comb-drive actuator before collecting this interferogram. The absence of fringes on the normal arm as well as on the loading section in Fig. 8.12 is a reliable evidence of the fact that levitation does not ensue in the Sidewall Friction Tester developed in this study. However, due to the presence of a stress gradient at the sacrificial oxide/device layer interface in the anchored post, the portions of the device layer of the post that are not anchored to the substrate are inclined upwards with a slope of 1 mrad. As a result, a step edge exists at the interface between the sidewall surfaces of the loading beam and the anchored post. This step edge, which is determined using horizontal scanning interferometry (HSI), is found to be 20 nm high. Since the step edge is much smaller than the total height of the sidewall interface, which is 2 μm (nominal), it does not reduce the apparent contact area of the sidewall interface significantly.

To determine the coefficients of static and kinetic friction of the OTS SAM coated sidewall surfaces of the test device, a $V_{n,s}$ of 60 V is applied to the pull drive of its normal comb-drive actuator. The corresponding friction force is determined by ramping up the tangential force applied at the sidewall interface using the tangential comb-drive actuator. A plot showing the onset of slip at the sidewall interface of the test device is shown in Fig. 8.13. In the plot, the displacement of the loading beam, which is determined by considering its position when the normal arm is aligned with the anchored post as the initial position, is plotted against the voltage applied to the tangential comb-drive actuator. As seen in Fig. 8.13, the first slip occurs at

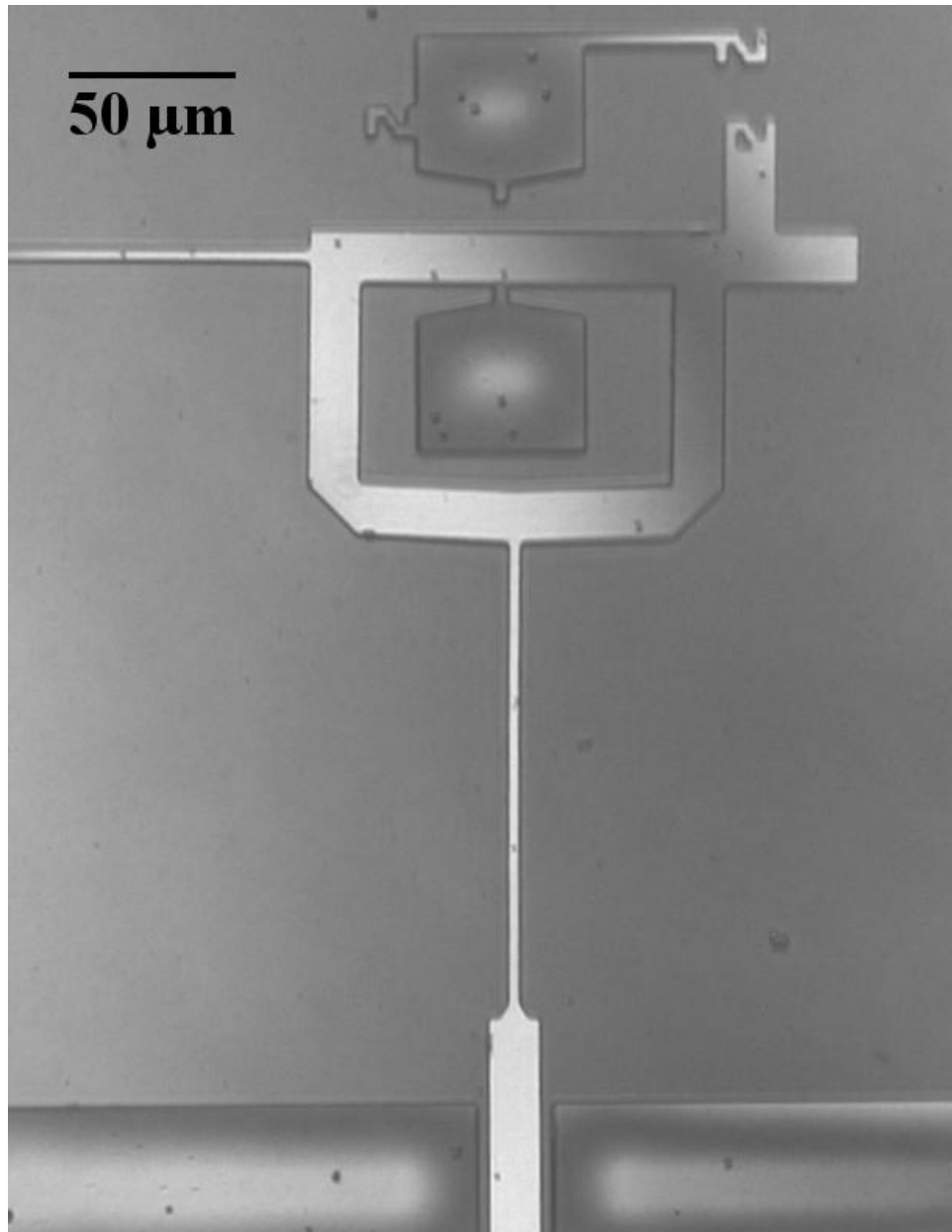


Figure 8.12: An interferogram, showing the loading section of the test device, collected after bringing the loading beam in contact with the anchored post. A voltage of 45 V is applied to the pull drive of the normal comb-drive actuator before collecting this interferogram. Notice the absence of fringes on the normal arm as well as on the loading section. The step edge at the sidewall interface is determined using HSI to be 20 nm.

a voltage of 32.8 V. Accordingly, using $V_{t,s}$ as 32.8 V, $V_{n,s}$ as 60 V, V_a as 26.1 V and V_c as 32.6 V in Eq. 5.6.17 gives a μ_s of 0.16 for the OTS SAM coated sidewall surfaces. Further, the distance for which the loading beam slides in contact with the anchored post after the initiation of the first slip at the sidewall interface (i.e., δ_s) is determined from Fig. 8.13 to be 1.36 μm . Accordingly, Eq. 5.6.19 gives a μ_k of 0.11 for the OTS SAM coated sidewall surfaces. The μ_s and μ_k of the OTS SAM coated sidewall surfaces can also be determined using the second slip that occurs at the $V_{t,s}$ of 34.8 V (see Fig. 8.13).

For each type of surface studied in this chapter (i.e., OTS SAM coated and surface with only native oxide on it), five Sidewall Friction Testers are used to investigate the friction and wear characteristics of contacting sidewalls. Using each Sidewall Friction Tester, the coefficients of static and kinetic friction are determined at normal loads ranging from 2.4 μN - 15.7 μN , which correspond to Hertzian contact pressures (calculated by considering cylinder on flat geometry) of 123 MPa - 312 MPa. This range of normal load is representative of that experienced by most potential and commercialized MEMS during operation. Additionally, in order to obtain statistically significant results, the coefficients of static and kinetic friction are determined five times for each investigated normal load. Table 8.6 reports the engineering coefficients of static and kinetic friction of both OTS SAM coated surfaces as well as surfaces with only native oxide on them. The results are as expected. Again, the coefficients of friction of the oxide covered sidewall test surfaces of the Test Platform developed in this study are greater than those reported in literature, which were obtained using microinstruments that had rougher sidewall test surfaces [23, 79, 85, 126, 128, 141, 143, 147, 150, 151, 159, 162, 164]. The coefficients of both static as well as kinetic friction of surfaces with only native oxide on them are greater than 1. This is attributed to two factors. First, the coefficients of static and kinetic friction reported in Table 8.6 are engineering coefficients of friction and the additional normal load experienced by

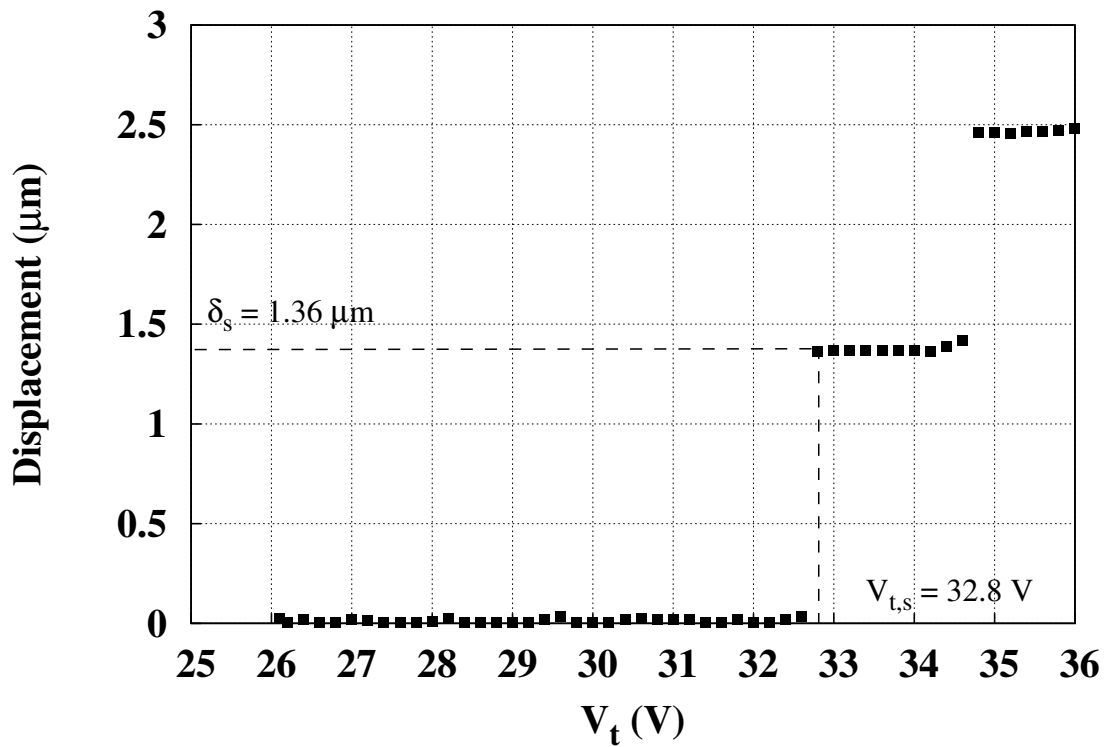


Figure 8.13: A plot showing the onset of slip at an OTS SAM coated sidewall interface. The displacement of the loading beam, which is determined by considering its position when the normal arm is aligned with the anchored post as the initial position, is plotted against the voltage applied to the tangential comb-drive actuator. A normal load of $8.05 \mu\text{N}$, which corresponds to a Hertzian contact pressure of 224 MPa, is applied at the sidewall interface. Notice that the first slip occurred at $V_{t,s}$ of 32.8 V and the second slip occurred at $V_{t,s}$ of 34.8 V.

the sidewall interface due to the adhesion between the contacting sidewall surfaces is not accounted for in their determination. Second, owing to the hydrophilic nature of the surfaces with only native oxide on them, adhesion between contacting sidewall surfaces, which have only native oxide on them, is significantly high and comparable to the externally applied normal loads. Further, the μ_s and μ_k of surfaces with only native oxide on them also vary significantly. This is also attributed to the same two factors as the relative significance of adhesion between contacting sidewall surfaces changes with the externally applied normal load. On the other hand, the μ_s and μ_k of the OTS SAM coated sidewalls are significantly lesser than 1 and they also vary much less as compared to those of surfaces with only native oxide on them. The one factor that is responsible for both of these attributes of the μ_s and μ_k of OTS SAM coated sidewalls is the hydrophobic surface chemistry of the OTS SAM coated sidewalls, due to which, the adhesion between them is significantly lesser than that between the sidewalls with only native oxide on them. The hydrophobic surface chemistry of OTS SAM coated sidewalls is also responsible for the smaller difference between their μ_s and μ_k as compared to that between the μ_s and μ_k of surfaces with only native oxide on them because the relatively higher adhesion between the contacting sidewall surfaces, which have only native on them, augments the effect of sliding on friction.

After determining μ_s and μ_k , each Sidewall Friction Tester is used to study the wear characteristics of its contacting sidewall surfaces. The wear characteristics of the contacting sidewall surfaces are studied by rubbing the loading beam against the anchored post under a normal load of $0.5 \mu\text{N}$, which corresponds to a V_N of 35.5 V and a Hertzian contact pressure of 55.9 MPa (calculated by considering cylinder on flat geometry). The reciprocating motion of the loading beam is achieved by superimposing an AC voltage, which has a frequency of 10 Hz and a peak-to-peak amplitude of 2 V, on V_a , which is the DC bias applied to the pull drive of the tangential arm to align the normal arm with the anchored posts. The change in the μ_s and μ_k

Table 8.6: Comparison between the engineering coefficients of static and kinetic friction of OTS SAM coated surfaces and those of surfaces with only native oxide on them. The engineering coefficients of friction reported in this table are determined using the Sidewall Friction Tester. All the values reported in the table are arithmetic means of 200 measurements and the std. dev. is one standard deviation of the sample consisting of those measurements.

Coating	Coefficient of Static Friction $\mu_s \pm \text{std. dev.}$	Coefficient of Kinetic Friction $\mu_k \pm \text{std. dev.}$
Oxide	1.75 ± 0.40	1.40 ± 0.20
OTS	0.15 ± 0.02	0.11 ± 0.01

of the contacting sidewalls is used as a measure to qualitatively study their wear characteristics. The μ_s and μ_k of OTS SAM coated sidewalls remained unchanged even after 180 min. of operation (i.e., even after accumulating 108000 wear cycles). However, a reliable conclusion about the wear characteristics of the sidewalls with only native on them could not be drawn because, while in some microinstruments with sidewall surfaces having only native oxide on them, the loading beam reciprocated for a few cycles, during which, it exhibited a stick-slip type of motion, in the remaining microinstruments, the loading beam did not reciprocate at all due to the significantly high adhesion between the contacting sidewalls.

8.8 Sidewall Friction and Adhesion Tester

As mentioned in section 4.1.2, the purpose behind including SFAT along with SFT in the Test Platform, for studying the friction and wear characteristics of sidewall surfaces is to determine the influence of the geometries of the surfaces forming the contact interface on the effect of surface topography. While in the SFT, the contact interface is formed between the plane (vertical) surface of a suspended beam and the cylindrical surface of an anchored post, in the SFAT, it is formed between the plane (vertical) surfaces of two suspended shuttles. The magnification of the objective lens that is used in the microscope during the actuation of the Sidewall Friction Testers is 10X. Accordingly, the size of each pixel in the field of view is $0.465 \mu\text{m} \times 0.465 \mu\text{m}$. Figure 8.14 is a plot showing the experimentally determined axial and lateral displacements of the tangential arm of one of the OTS SAM coated Sidewall Friction and Adhesion Testers (referred to as test device from now onwards) versus the square of the corresponding voltages (V_t^2) applied to its push drive. Again, as expected, the data representing the axial displacements is clearly divided into two segments, which have significantly different slopes. The segment with the smaller slope corresponds to the initial segment and that with the higher slope corresponds to the final segment of

the anchored comb fingers of the tangential comb-drive actuator. Also, it is evident in Fig. 8.14 that within each segment, the axial displacement of the tangential arm increases linearly with the force generated by the tangential comb-drive actuator. This substantiates the validity of our treatment of the folded beam flexure of the tangential arm as linear elastic (Hookean) springs. The transfer functions corresponding to the two segments (i.e., G_{t1} and G_{t2} , respectively) of the anchored comb fingers of the tangential comb-drive actuator, which are determined by fitting straight lines to the two segments of the axial displacement data shown in Fig. 8.14, are $0.0011 \mu\text{m}/\text{V}^2$ and $0.0032 \mu\text{m}/\text{V}^2$, respectively. Accordingly, the ratio of the experimentally determined G_{t2} to the experimentally determined G_{t1} is 2.91, which confirms that as expected, the electrostatic force generated by the push drive of the tangential comb-drive actuator increases by close to a factor of 3 when a fraction of the length of suspended comb fingers overlaps with the final segments of the anchored comb fingers. Again, the data that represents lateral displacements indicates that during the entire calibration, the motion of the tangential arm of the test device is confined to only the axial direction.

Figure 8.15 is a plot showing the experimentally determined axial and lateral displacements of the normal arm of the test device versus the square of the corresponding voltages (V_n^2) applied to its push drive. Again as expected, the data representing the axial displacements is clearly divided into three segments, which have significantly different slopes. The first two segments correspond to the initial and final segments of the anchored comb fingers of the normal comb-drive actuator. Further, it is evident in Fig. 8.15 that within the first two segments, the axial displacement of the normal arm increases linearly with the force generated by the normal comb-drive actuator. This substantiates the validity of our treatment of the folded beam flexures of the normal arm as linear elastic (Hookean) springs. The transfer functions corresponding to the two segments of the anchored comb fingers of the normal arm of the test device

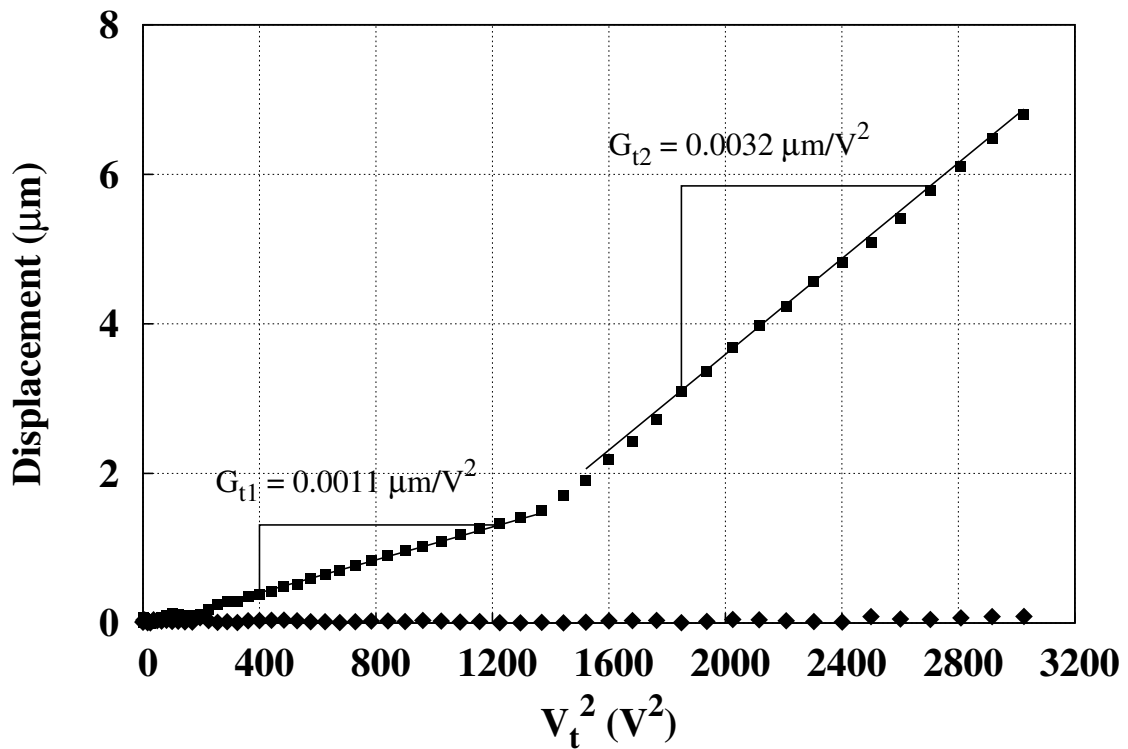


Figure 8.14: A plot showing the experimentally determined axial (■) and lateral (◆) displacements of the tangential arm of one of the OTS SAM coated Sidewall Friction and Adhesion Testers versus square of the corresponding voltages (V_t^2) applied to its push drive. Notice that the data representing the axial displacements is clearly divided into two segments, which have significantly different slopes. The transfer functions G_{t1} and G_{t2} are extracted from the corresponding linear fits (—) of the experimental axial displacement data.

(i.e., G_{n1} and G_{n2} respectively), which are determined by fitting straight lines to the corresponding data, are $0.0020 \mu\text{m}/V^2$ and $0.0059 \mu\text{m}/V^2$, respectively. Accordingly, the ratio of the experimentally determined G_{n2} to the experimentally determined G_{n1} is 2.95, which again, is close to the design value of 3. The third segment of the axial displacement data of the test device indicates that the axial displacement of its normal arm does not increase beyond $3.75 \mu\text{m}$. Therefore, δ_c , which is the distance by which the normal arm should be axially displaced to bring the loading block in contact with the friction block, is $3.75 \mu\text{m}$. Accordingly, V_c , which is the voltage that should be applied to the normal comb-drive actuator of a SFAT to bring its loading block in contact with its friction block, is 33 V. It is determined by identifying the voltage that corresponds to an axial displacement of δ_c in Fig. 8.15. The lateral displacements of the normal arm of the test device are also negligible, indicating that during the entire calibration, the motion of even the normal arm of the test device is confined to only the axial direction.

While levitation does ensue in the Sidewall Friction and Adhesion Testers developed in this study during their electrostatic actuation, it has no influence on the results obtained using them. Although it leads to tilting of both the normal as well as tangential arms of the SFATs, it has a similar effect on both of them. Therefore, it induces only a small step edge at the sidewall interface formed between their loading and friction blocks. Fig. 8.12 is an interferogram showing the sidewall interface formed in the test device. A voltage of 50 V is applied to the push drive of the normal arm to bring the loading block in contact with the friction block, before collecting this interferogram. The absence of fringes on the loading and friction blocks shown in the interferogram substantiates the absence of a significant step edge at the sidewall interface formed by them. The typical step edge that exists at the sidewall interfaces formed in the SFATs developed in this study is determined using horizontal scanning interferometry (HSI) to be about 75 nm high. Since this step edge is much smaller

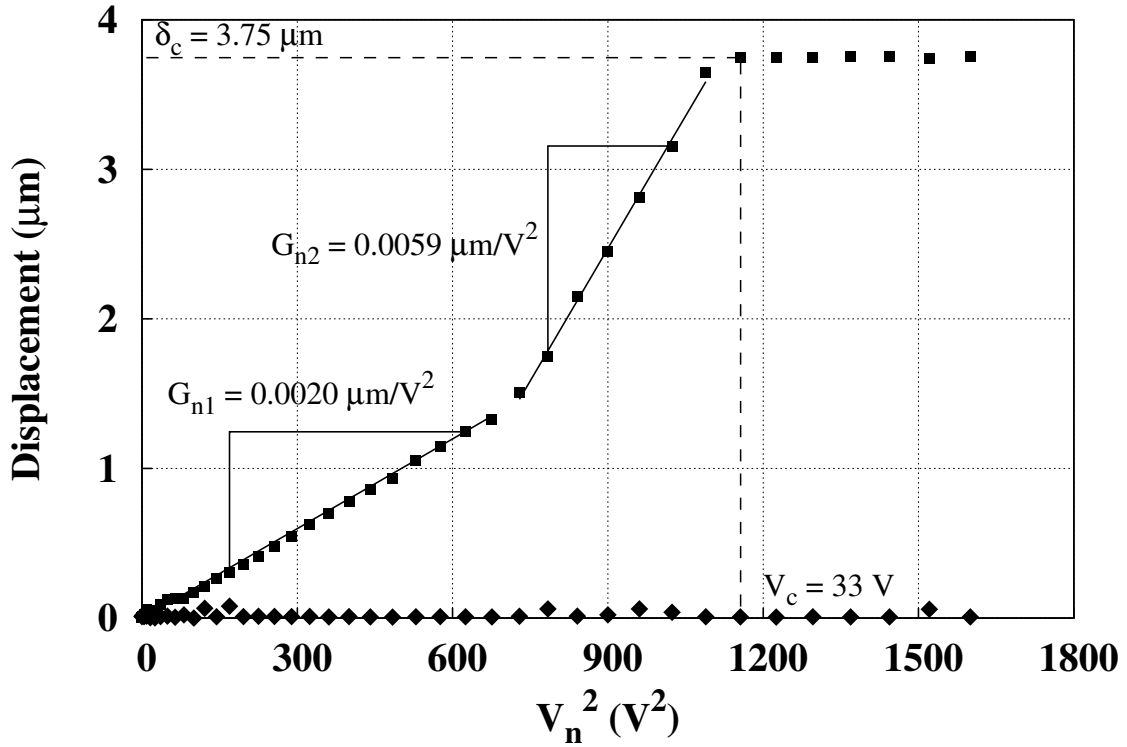


Figure 8.15: A plot showing the experimentally determined axial (■) and lateral (◆) displacements of the normal arm of one of the OTS SAM coated SFAT versus square of the corresponding voltages (V_n^2) applied to its push drive. Notice that the data representing the axial displacements is clearly divided into three segments, which have significantly different slopes. The transfer functions G_{n1} and G_{n2} are extracted from the corresponding linear fits (—) of the experimental axial displacement data. δ_c is the distance by which the normal arm should be axially displaced in order to bring the loading block in contact with the friction block and V_c is the corresponding voltage that should be applied to the normal comb-drive actuator.

than the total (nominal) height of the sidewall interface, which is $2 \mu\text{m}$ (nominal), it does not reduce the apparent contact area of the sidewall interface significantly. Consequently, it does not induce any significant error in the estimation of the contact pressures applied at the sidewall interface. Therefore, no additional measures are required to account for the effects of the levitation induced in the Sidewall Friction and Adhesion Tester developed in this study during their actuation.

To determine the coefficients of static and kinetic friction of the OTS SAM coated sidewall surfaces of the test device, a $V_{n,s}$ of 60 V is applied to the push drive of its normal comb-drive actuator. The corresponding friction force is determined by ramping up the tangential force applied at the sidewall interface using the tangential comb-drive actuator. A plot showing the onset of slip at the sidewall interface of the test device is shown in Fig. 8.17. In the plot, the displacement of the friction block is plotted against the voltage applied to the tangential comb-drive actuator. Two slip events are clearly visible in the plot. One occurs at a voltage of 52 V and the other occurs at a voltage of 57 V. Using the first slip event (i.e., using $V_{t,s}$ as 52 V) and, $V_{n,s}$ as 60 V, V_c as 33 V, G_{t1} as $0.0011 \mu\text{m}/\text{V}^2$, G_{n2} as $0.0059 \mu\text{m}/\text{V}^2$, L_n as $300 \mu\text{m}$ and L_t as $250 \mu\text{m}$ in Eq. 5.7.22 gives a μ_s of 0.17 for the OTS SAM coated sidewall surfaces. Further, the distance, for which, the friction block slides in contact with the loading block during the first slip event (i.e., δ_s) is determined from Fig. 8.13 to be $0.57 \mu\text{m}$, which is less than the distance, by which, the tangential arm should be displaced for the suspended comb fingers of its push drive to overlap with the final segments of the corresponding anchored comb fingers. Therefore, Eq. 5.7.23 can be used to determine the kinetic friction experienced by the sidewall interface of the test device during the first slip event. The μ_k of the OTS SAM coated sidewall surfaces of the test device is determined to be 0.14. The displacement of the shuttle of the tangential arm of the test device during the second slip event does cause a fraction of the length of its suspended comb fingers to overlap with the final segments

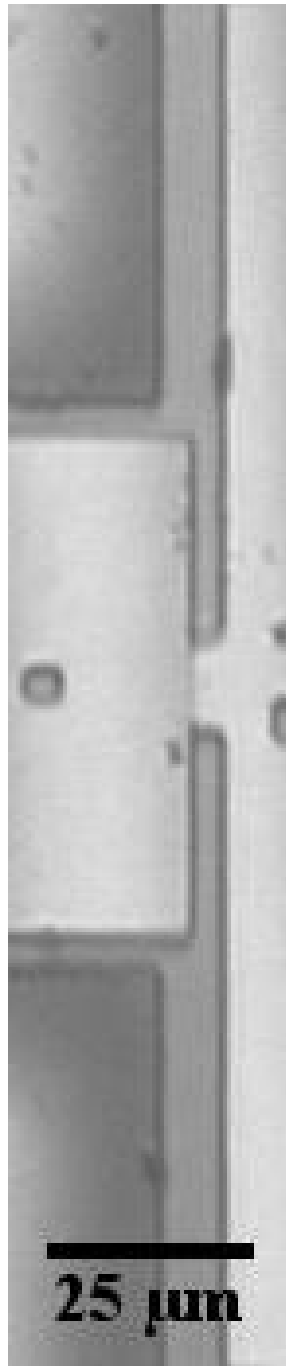


Figure 8.16: An interferogram showing the sidewall interface formed in one of the OTS SAM coated Sidewall Friction and Adhesion Testers. A voltage of 50 V is applied to the push drive of the normal arm to bring the loading block in contact with the friction block, before collecting this interferogram. Notice the absence of fringes on the loading and friction blocks shown in the interferogram. The step edge at the sidewall interface is determined using HSI to be 75 nm.

of the corresponding anchored comb fingers. This is the reason why the distance, for which, the friction block slides in contact with loading block during the second slip event is significantly greater than the distance, for which, it slides during the first slip event. While theoretically, the second slip event exhibited by the SFAT developed in this study can also be used to determine the μ_s and μ_k of the surfaces that form the sidewall interface, the one that is shown in Fig. 8.13 cannot be used because its termination is not caused by the balance between the sum of the restoring force generated by the folded beam flexure of the tangential arm and the kinetic friction force, and the tangential force generated using the tangential comb-drive actuator. It is caused due to the lateral instability encountered by the push drive of the tangential arm during the slip event.

For each type of surface studied in this chapter (i.e., OTS SAM coated and surface with only native oxide on it), five Sidewall Friction and Adhesion Testers are used to investigate the friction and wear characteristics of contacting sidewalls. Using each Sidewall Friction and Adhesion Tester, the coefficients of static and kinetic friction are determined at normal loads ranging from $0.677 \mu\text{N}$ - $7.97 \mu\text{N}$, which correspond to apparent contact pressures (calculated by considering flat on flat geometry) of 0.098 MPa - 1.15 MPa . Additionally, in order to obtain statistically significant results, the coefficients of static and kinetic friction are determined five times for each investigated normal load. Table 8.7 reports the engineering coefficients of static and kinetic friction of both OTS SAM coated surfaces as well as surfaces with only native oxide on them, obtained using the SFATs. The results are as expected. Again, the coefficients of friction of the oxide covered sidewall test surfaces of the Test Platform developed in this study are greater than those reported in literature, which were obtained using microinstruments that had rougher sidewall test surfaces [23, 79, 85, 126, 128, 141, 143, 147, 150, 151, 159, 162, 164]. Further, like in the case of the SFTs investigated in this chapter, the coefficients of both static as well as kinetic friction of surfaces

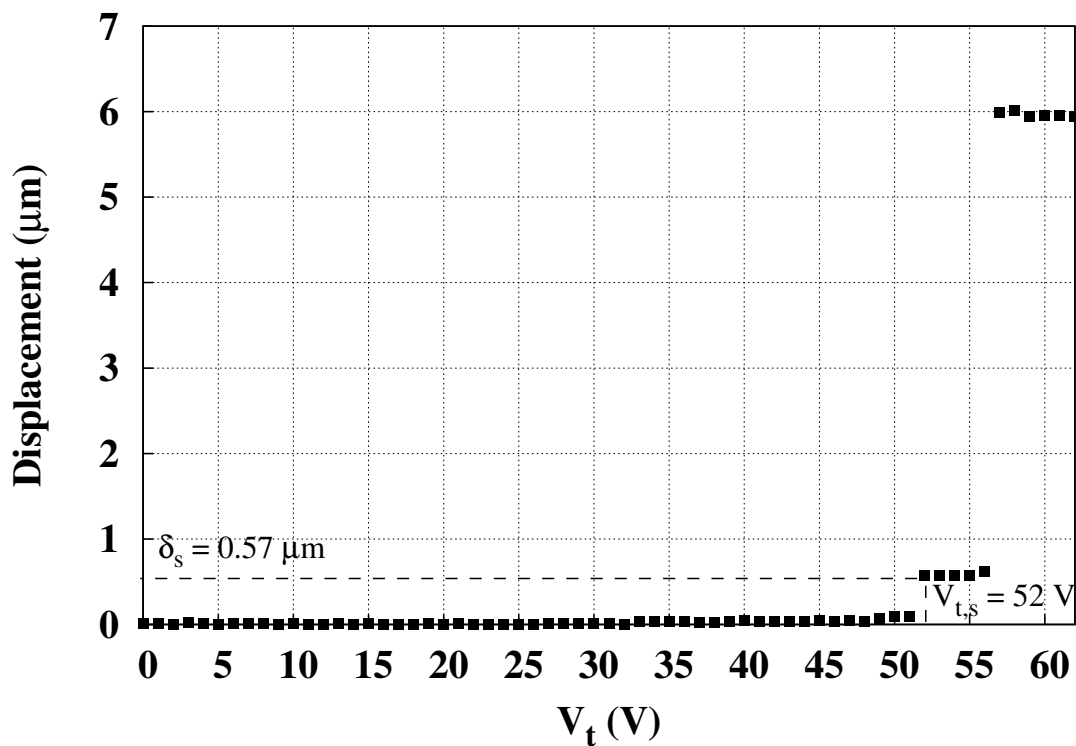


Figure 8.17: A plot showing the onset of slip at an OTS SAM coated sidewall interface investigated using the SFAT developed in this study. The displacement of the friction block is plotted against the voltage applied to the tangential comb-drive actuator. A normal load of $1.82 \mu\text{N}$, which corresponds to an apparent contact pressure of 0.26 MPa , is applied at the sidewall interface. Notice that the first slip occurred at $V_{t,s}$ of 52 V and the second slip occurred at $V_{t,s}$ of 57 V .

with only native oxide on them obtained using the SFATs are also greater than 1, and vary significantly. The fact that owing to the smaller normal loads applied at the sidewall interfaces tested using the SFATs as compared to those applied at the sidewall interfaces tested using the SFTs, the absolute values of, and the variations in, the μ_s and μ_k of the native oxide covered sidewall test surfaces obtained using the SFATs are greater as compared to the μ_s and μ_k of the native oxide covered sidewall test surfaces obtained using the SFTs supports the rationale that the change in the relative significance of the adhesion experienced by contacting sidewall test surfaces with the externally applied normal load is responsible for the greater than 1, and significantly varying, values of the μ_s and μ_k of the native oxide covered sidewall test surfaces obtained using the microinstruments developed in this study. The μ_s and μ_k of OTS SAM coated sidewalls obtained using the SFATs investigated in this chapter are also in good agreement with those obtained using the SFTs investigated in this chapter.

Like the SFTs investigated in this chapter, each Sidewall Friction and Adhesion Tester investigated in this chapter is also used for studying the wear characteristics of OTS SAM coated and native oxide covered sidewall test surfaces. Using SFATs, the wear characteristics of contacting sidewall surfaces are studied by rubbing the friction block against the loading block under a normal load of $0.5 \mu\text{N}$, which corresponds to a V_N of 42.2 V and an apparent contact pressure of 0.072 MPa (calculated by considering flat on flat geometry). The reciprocating motion of the friction block is achieved by superimposing an AC voltage, which has a frequency of 10 Hz and a peak-to-peak amplitude of 6 V, on a DC bias of 43 V applied to the push drive of the tangential arm of the SFAT. Again, the change in the μ_s and μ_k of the contacting sidewalls is used as a measure to qualitatively study their wear characteristics. The μ_s and μ_k of the OTS SAM coated sidewalls investigated using the SFATs remained unchanged even after 300 min. of operation (i.e., even after accumulating 180000 wear

Table 8.7: Comparison between the engineering coefficients of static and kinetic friction of OTS SAM coated surfaces and those of surfaces with only native oxide on them. The engineering coefficients of friction reported in this table are determined using the Sidewall Friction and Adhesion Tester. All the values reported in the table are arithmetic means of 325 measurements and the std. dev. is one standard deviation of the sample consisting of those measurements.

Coating	Coefficient of Static Friction $\mu_s \pm \text{std. dev.}$	Coefficient of Kinetic Friction $\mu_k \pm \text{std. dev.}$
Oxide	1.98 ± 0.45	1.35 ± 0.20
OTS	0.16 ± 0.03	0.13 ± 0.01

cycles). The μ_s and μ_k of the native oxide covered sidewalls investigated using the SFATs remained unchanged only for 8 min. (i.e., 4800 wear cycles), after which, the friction block momentarily exhibited a stick-slip type of motion before its motion ceased completely.

8.9 Conclusions

The details of the key features of all the microinstruments developed in this study are successfully highlighted in this chapter. Additionally, some of the microinstruments developed in this study are convincingly shown to overcome some of the limitations of the previously reported corresponding microinstruments. Further, all the microinstruments developed in this study are successfully used to investigate two standard test surfaces, namely, surfaces coated with *n*-OTS ($C_{18}H_{37}SiCl_3$) SAM coating (i.e., hydrophobic surfaces) and surfaces having only a layer of native oxide on them (i.e., hydrophilic surfaces). The results obtained are compared with the corresponding results reported in literature. The comparisons substantiate the consistency and reliability of the results obtained using the Test Platform developed in this study. Moreover, the apparent work of adhesion of the OTS SAM coated sidewalls, which has never been reported to-date, is obtained in this chapter using the Sidewall Beam Array. The apparent work of adhesion of the OTS SAM coated sidewalls is $37.65 \mu\text{J}/\text{m}^2$. Also, the engineering coefficients of static and kinetic friction of the OTS SAM coated sidewalls, which have also never been reported to-date, are obtained in this chapter using both the Sidewall Friction Tester as well as the Sidewall Friction and Adhesion Tester. The mean engineering coefficients of static and kinetic friction of the OTS SAM coated sidewalls are 0.15 and 0.11, respectively.

Chapter 9

The Effect of Surface Topography

The surfaces (in-plane as well as sidewall) of the Test Platform developed in this study are the smoothest surfaces reported to-date for investigating the tribological characteristics of MEMS interfaces [78,141,164]. Accordingly, their topographies can be considered as baselines, and controllably tailored to enable a systematic study for investigating the effects that the surface topographies of contacting MEMS surfaces have on the stiction and friction characteristics of the interface formed by them. This chapter reports on a technique that is used to tailor the topographies of the surfaces (in-plane as well as sidewall) of the Test Platform developed in this study. It further reports on the methods used to characterize the surface topographies of the tailored test surfaces. Additionally, the stiction and friction characteristics of the tailored test surfaces are also reported in this chapter. This chapter also discusses a dimensionless parameter (i.e., Tribotopography number (τ_{topo})), which can be used to predict the effect that the surface topography of a MEMS surface has on its stiction and friction characteristics. Lastly, this chapter reports on the influence that the contact geometry of an interface has on the effect of surface topography.

9.1 Obtaining Test Surfaces with Distinct Topographies

Both the in-plane as well as sidewall surfaces of the Test Platform developed in this study have fairly smooth topographies to begin with, as indicated by the AFM images shown in Figs. 4.1 and 4.2, respectively. Therefore, their surface topographies can be tailored by texturing them. For this study, the surface topographies of the surfaces of the Test Platform developed in this study are tailored by depositing nanoparticles

on them. The nanoparticles specifically used for this study are dodecanethiol-capped gold nanoparticles. The process used to synthesize the dodecanethiol-capped gold nanoparticles used in this study is described in detail in section 6.5. Accordingly, an untextured Test Platform chip consisting of native oxide covered test surfaces is used as the control sample and five Test Platform chips, whose test surfaces are textured using gold nanoparticles, are used as the test samples. The five test samples are controllably textured in such a way that the surface topographies of the test surfaces of each one of them are distinct and different than those of the test surfaces of each of the others.

As explained in chapter 1, the stiction and friction characteristics of an interface are determined by the various interfacial forces experienced by the two contacting surfaces that form the interface. In the control sample, the examined interface is formed between two native oxide covered silicon surfaces, and characterized by the interactions between pairs of native-oxide covered silicon asperities. In the test samples, the examined interface is formed between gold nanoparticle coated, native oxide covered silicon surfaces. Accordingly, the interfaces formed in the test samples are characterized by the interactions between pairs of a gold asperity and a native-oxide covered silicon asperity as well as between pairs of two gold asperities. The interfacial forces that are reported to prominently exist at the type of interfaces that are formed in the Test Platform chips investigated in this chapter include capillary forces, which are attractive and depend on the contact angle that a droplet of water makes on the surface of the asperities present on the surfaces forming the interface as well as the relative humidity of the testing environment, VDW forces between the non-contacting asperities of the two surfaces forming the interface, which are attractive and depend on the Hamaker constants of the materials of the asperities present on the two surfaces forming the interface, inter-atomic and inter-molecular forces between the asperities that are in contact at the interface, which are attractive and depend

on the surface energies of the materials of the contacting asperities, and the elastic forces exerted by the contacting asperities that are elastically deformed, which are repulsive, depend on the elastic properties of the materials of the contacting asperities and act to push the surfaces forming the interface apart from each other. Owing to the comparable elastic moduli of native oxide and gold (i.e., 70 - 75 GPa and 79 GPa, respectively), the material of the deforming asperities will have a negligible influence on the difference in the elastic forces that will be experienced by the control (i.e., interfaces formed in the control sample) and the test (i.e., interfaces formed in the test samples) interfaces investigated in this study [180–182]. Similarly, owing to the comparable surface energies of native-oxide covered Si(100) and gold surfaces (i.e., 1.36 J/m² and 1.25 J/m², respectively), the material of the contacting asperities will have a negligible influence on the difference in the inter-atomic and inter-molecular forces that will be experienced by the control (i.e., interfaces formed in the control sample) and the test (i.e., interfaces formed in the test samples) interfaces investigated in this study [183,184]. Further, the overall Hamakar constant for the VDW interaction between the native oxide covered silicon and gold (H_{Si-Au}) can be determined using Eq. 9.1.1 shown below [185]:

$$H_{Si-Au} = \sqrt{H_{Si}H_{Au}} \quad (9.1.1)$$

The Hamakar constants of native oxide covered silicon (H_{Si}) and gold (H_{Au}) are 1.7 eV and 1.9 eV, respectively [68, 70, 186]. Accordingly, the H_{Si-Au} determined using Eq. 9.1.1 is 1.8 eV, which is comparable to the overall Hamakar constant for the VDW interaction between two native oxide covered silicon surfaces (i.e., 1.7 eV) [68, 70]. Therefore, the material (or surface chemical composition) of the surfaces forming the interface will have a negligible influence on the difference in the VDW forces that will be experienced by the control (i.e., interfaces formed in the control sample)

and the test (i.e., interfaces formed in the test samples) interfaces investigated in this study. Lastly, at a given relative humidity, the capillary pull experienced by two hydrophilic surfaces forming an interface depends on the contact angle that a droplet of water makes on them. The contact angle that a droplet of water makes on a clean native oxide covered silicon surface is $<5^\circ$ (determined experimentally on a clean native oxide covered Si(100) surface), and that it makes on a clean gold surface is 12° - 18° (determined experimentally on a clean gold-coated Si(100) surface). The experimentally determined values of the contact angles that a droplet of water makes on clean native oxide covered silicon and gold surfaces are in extremely good agreement with those reported in literature [6, 187]. Accordingly, since a droplet of water makes extremely small contact angles on both the native oxide covered silicon as well as the gold surface, and the contact angles made by it on them are comparable, the material (i.e., elemental identity) as well as the surface chemistry of the interacting asperities of the two surfaces forming the interface will have a negligible influence on the difference in the capillary forces that will be experienced by the control (i.e., interfaces formed in the control sample) and the test (i.e., interfaces formed in the test samples) interfaces investigated in this study. Indeed, it has been reported that smooth surfaces coated with gold thin films experience a similar stiction as well as friction as that experienced by the smooth (untextured) in-plane surfaces of the Test Platform developed in this study. Therefore, it can be safely concluded that the effect, which the dodecanethiol-capped gold nanoparticle-based surface texturing will have on the stiction and friction characteristics of the surfaces of the Test Platform developed in this study, will be solely associated with the surface topography change caused by it and will not depend on the chemistry or the material of the nanoparticles used. Therefore, in theory, the results reported in this chapter do not depend on the material of the nanoparticles used to tailor the surface topographies of the test surfaces. For that matter, they also do not depend on the surface texturing technique

used to tailor the surface topographies of the test surfaces. The purpose behind using the dodecanethiol-capped gold nanoparticles for tailoring the surface topographies of the test surfaces investigated in this study is the availability of well established processes for synthesizing gold nanoparticles, and depositing them on MEMS surfaces. The process used for depositing the dodecanethiol-capped gold nanoparticles on the test surfaces investigated in this study is developed by Hurst *et al.*, and described in detail in [24] and section 6.6.

The final surface topography of a surface that is textured using the surface texturing process used in this study depends on the absolute amount of the nanoparticles deposited on it. Therefore, in order to obtain test surfaces (for this study) with distinct surface topographies, the surface texturing process used in this study is tuned to deposit different (distinct) amounts of nanoparticles on each of the Test Platform chips investigated in this chapter. The amount of the nanoparticles that get deposited on the surface being textured can be controlled by controlling the number density of the nanoparticle dispersion used in the surface texturing process used in this study. Specifically, test surfaces with five different (distinct) surface topographies, in addition to the untextured (referred to as control from now onwards) test surfaces, are investigated in this chapter. Therefore, nanoparticle dispersions with five different (distinct) number densities are used in this study. In order to burn-off the dodecanethiol capping ligands present on the gold nanoparticles deposited on the five textured Test Platform chips investigated in this study, each of the five textured Test Platform chips are exposed to an UV-ozone atmosphere for 1 hour before testing.

9.2 Characterization of the Tailored Test Surfaces

In order to understand the effects that the surface topographies of contacting MEMS surfaces have on the stiction and friction characteristics of the interface formed

by them, the test surfaces of all the six (i.e., five tailored and one control) Test Platform chips investigated in this chapter are characterized both topographically as well as tribologically. The topographic characterization of the Test Platform chips investigated in this chapter is accomplished by characterizing the surface topographies of their in-plane surfaces both qualitatively as well as quantitatively. The tribological characterization of the Test Platform chips investigated in this chapter is accomplished by determining the apparent works of adhesion of their in-plane and sidewall surfaces as well as the coefficients of static friction of their sidewall surfaces. The following sections discuss the results of the topographical and tribological characterizations of the Test Platform chips investigated in this study.

9.2.1 Topography

Qualitative Characterization

In order to validate our hypothesis that the amount of the nanoparticles that get deposited on the surface being textured using the surface texturing process used in this study can be controlled by controlling the number density of the nanoparticle dispersion used, the test surfaces, whose topographies are tailored for this study, are characterized to qualitatively determine the relative amounts of the nanoparticles present on them. The qualitative characterization of the textured test surfaces investigated in this chapter is accomplished using SEM. Figure 9.1 shows the SEM images of the substrates of each of the five textured Test Platform chips investigated in this chapter. The numbers indicated on the SEM images are the sample numbers of the corresponding textured Test Platform chips. The nanoparticle dispersion used to texture sample no.1 has the least number density, which is increased monotonously from the nanoparticle dispersion that is used to texture sample no.1 to the nanoparticle dispersion that is used to texture sample no.5. Therefore, it is expected that

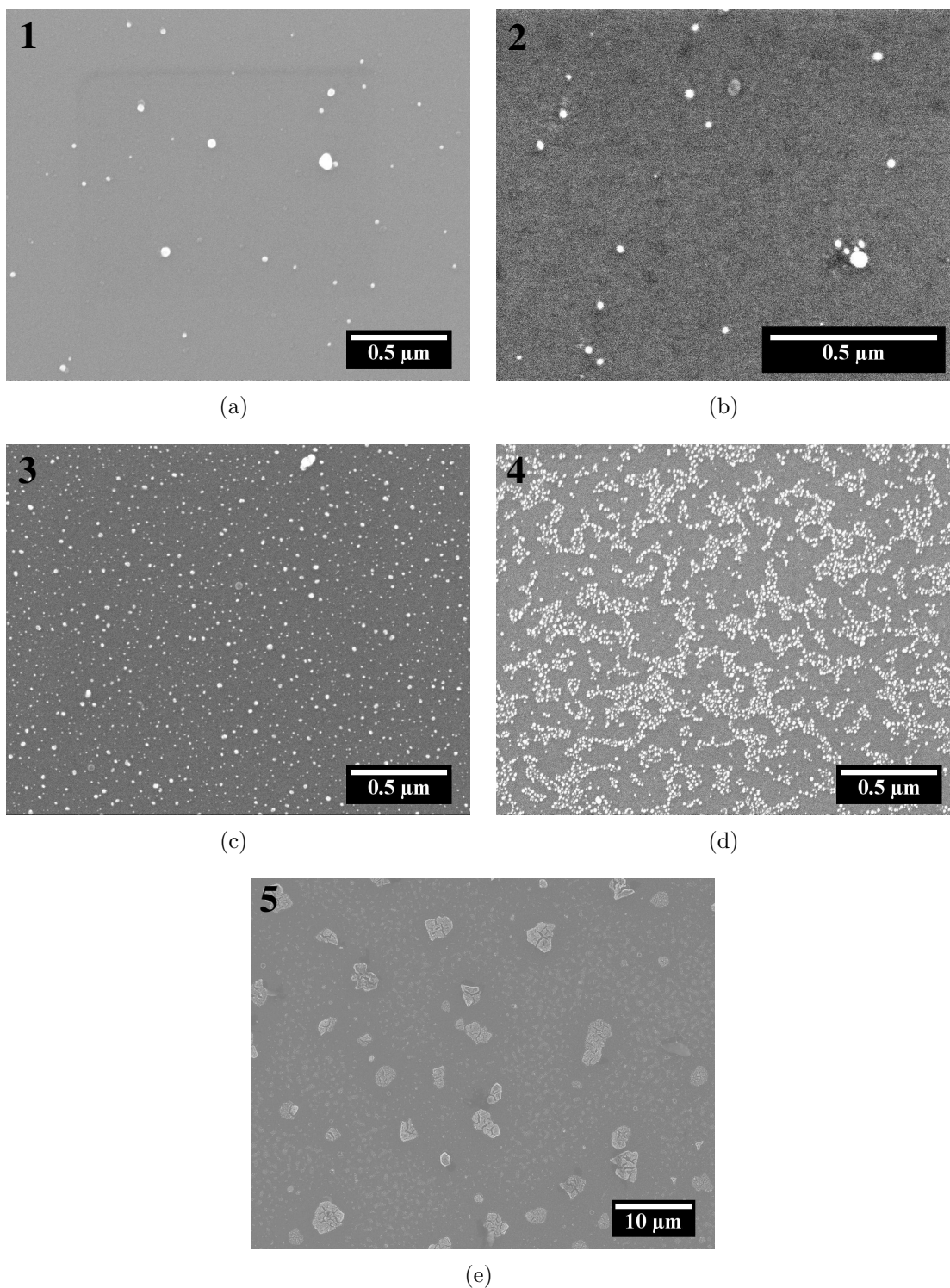


Figure 9.1: SEM images of the substrates of the five textured Test Platform chips investigated in this chapter. The numbers indicated on the SEM images are the sample numbers of the corresponding textured Test Platform chips. Notice the monotonous increase in the amount of the nanoparticles present on the textured surfaces shown in the SEM images from the image a to image e.

the amount of the nanoparticles present on the textured surfaces of the Test Platform chips investigated in this study will monotonously increase from sample no. 1 to sample no. 5. The SEM images shown in Fig. 9.1 clearly indicate that the results of tailoring the surfaces topographies of the Test Platform chips investigated in this study are as expected. It is clearly evident in the SEM images shown in Fig. 9.1 that the amount of the nanoparticles present on the surfaces of the textured Test Platform chips investigated in this study increases monotonously from sample no. 1 to sample no. 5. In order to further validate this observation, a qualitative measure of the amounts of the nanoparticles deposited on each of the five textured Test Platform chips investigated in this chapter is obtained using the Resonators on them. As validated in chapter 8, the resonance frequencies of the Resonators included in the Test Platform are inversely proportional to the effective masses of their suspended resonating structures (i.e., Eq. 5.3.1). Accordingly, the deposition of nanoparticles on the surfaces of a Resonator increases the effective mass of its resonating structure, and consequently decreases its resonance frequency. Therefore, by comparing the resonance frequencies of the nanoparticle coated and uncoated Resonators having the same supporting beam length, the increase in the effective mass of the nanoparticle coated Resonator (i.e., ΔM_{eff}), which is due to the mass of the nanoparticles deposited on it, can be determined. The analysis used for determining the increase in the effective mass of a nanoparticle coated Resonator (i.e., ΔM_{eff}) due to the mass of the nanoparticles deposited on it is elaborated in detail in chapter 10. By comparing the increase in the effective masses of Resonators having the same supporting beam length, fabricated at different locations on a textured Test Platform chip, the uniformity of the nanoparticle coating deposited on that Test Platform chip can be determined. Similarly, by comparing the increase in the effective masses of the Resonators having the same supporting beam length, of each of the five textured

Test Platform chips, a qualitative comparison between the amounts of the nanoparticles deposited on them can be made. Table 9.1 lists the decrease in the resonance frequencies (i.e, Δf_R) and the corresponding increase in the effective masses of the Resonators with 500 μm long supporting beams, of each of the five textured Test Platform chips. Each value reported in table 9.1 is an arithmetic mean of five measurements, which are obtained using five distinct Resonators that are fabricated at different locations on the corresponding Test Platform chip. The results reported in table 9.1 are a quantitative confirmation of the observation that the amount of the nanoparticles present on the surfaces of the textured Test Platform chips investigated in this study increases monotonously from sample no. 1 to sample no. 5. They along with the SEM images shown in Fig. 9.1 indisputably validate my hypothesis that the amount of the nanoparticles that get deposited on the surface being textured can be controlled by controlling the number density of the nanoparticle dispersion used.

Quantitative Characterization

In order to be able to establish a mathematical correlation between the surface topographies of the test surfaces of the Test Platform chips investigated in this chapter and their stiction and friction characteristics, the surface topographies of the test surfaces of the Test Platform chips investigated in this chapter must be quantified in terms of measurable parameters. The quantitative characterization of the textured test surfaces investigated in this chapter is accomplished using AFM. Figure 9.2 shows the AFM images of the substrates of all the Test Platform chips investigated in this chapter. Again, the numbers indicated on the AFM images are the sample numbers of the corresponding textured Test Platform chips. The control sample is a Test Platform chip, whose surfaces are polished, native oxide covered and not textured with the dodecanethiol-capped gold nanoparticles. The AFM images of the substrates of all the textured Test Platform chips investigated in this chapter, which are shown in

Table 9.1: This table lists the decrease in the resonance frequencies (Δf_R) and the corresponding increase in the effective masses (ΔM_{eff}) of the Resonators with 500 μm long supporting beams, of each of the five textured Test Platform chips. Each value reported in the table is an arithmetic mean of five measurements, which are obtained using five distinct Resonators that are fabricated at different locations on the corresponding Test Platform chip.

Sample #	Δf_R (Hz)	$\Delta M_{eff} \times 10^{12}$ (Kg)
1	11.5	0.806
2	15.1	1.06
3	28.7	2.02
4	63.8	4.49
5	126	8.82

Figs. 9.2b - 9.2f, perfectly correlate their SEM images, which are shown in Figs. 9.1a - 9.1f, in terms of the relative amounts of the nanoparticles present on them. The two measurable parameters that are extracted from the AFM images of the substrates of all the Test Platform chips investigated in this chapter are the rms roughnesses of, and the surface coverages of the interacting asperities present on, the surfaces shown in them. The image analysis technique used to process the ASCII data associated with an AFM image, to extract the surface coverage of the interacting asperities present on the surface shown in it, is discussed in detail in section 6.12. Details on the usage of the surface coverage of the interacting asperities present on the in-plane surfaces of the Test Platform chips investigated in this chapter is provided in section 9.3.1.

The rms roughnesses of the in-plane surfaces of each of the six Test Platform chips investigated in this chapter are indicated on their corresponding AFM images, which are shown in Figs. 9.2a - 9.2f. It was expected that the rms roughnesses of the surfaces of the Test Platform chips investigated in this chapter will exhibit a direct correspondence with the amounts of the nanoparticles deposited on them. However, as evident from Figs. 9.2a - 9.2f, the results obtained are counterintuitive. A bar graph showing the rms roughnesses of the in-plane surfaces of the Test Platform chips investigated in this chapter is shown in Fig. 9.3. The direction, in which, the amount of the nanoparticles deposited on the Test Platform chips investigated in this chapter increases is indicated by the arrow in the bar graph. It is clearly evident from the bar graph shown in Fig. 9.3 that the rms roughnesses of the surfaces of the Test Platform chips investigated in this chapter do not exhibit a direct correspondence with the amounts of the nanoparticles present on them. To explain this observation, a schematic is shown in Fig. 9.4. Figure 9.4a shows a schematic diagram of the substrate of the Test Platform developed in this study. The red line, which is covering the top (in-plane) surface of the substrate, shown in Fig. 9.4a represents the surface profile of the substrate. Accordingly, Figs. 9.4b and 9.4c indicate how the rms roughness

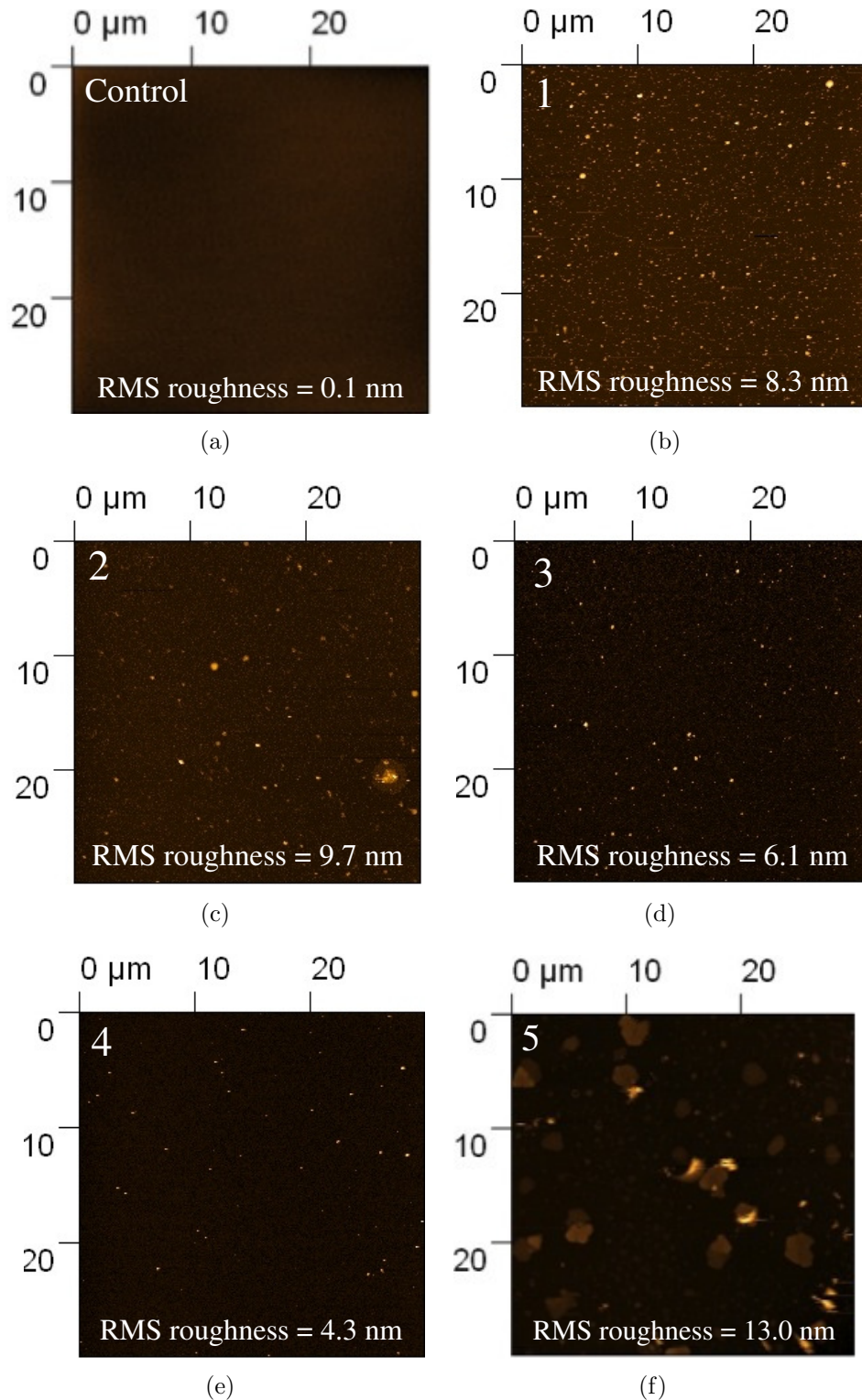


Figure 9.2: AFM images of the substrates of the Test Platform chips investigated in this chapter. The numbers indicated on the AFM images are the sample numbers of the corresponding textured Test Platform chips.

of the top (in-plane) surface of the substrate shown in Fig. 9.4a increases with the deposition of nanoparticles on it. Again, the red lines in Figs. 9.4b and 9.4c represent the surface profiles of the textured substrates shown in them. Further, Fig. 9.4d indicates how, while initially the rms roughness of the top surface of the substrate shown in Fig. 9.4a does increase with the increase in the amount (number) of the nanoparticles deposited on it (i.e., Figs. 9.4b and 9.4c), beyond a certain amount, the nanoparticles getting deposited begin to fill up the surface, thereby decreasing its rms roughness. Additionally, the rms roughness of a textured surface, determined from the AFM image of a representative area on it, is not a function of the amount of the nanoparticles present on it alone but also depends on their positions relative to each other. This is because the resolution, with which the AFM images of the textured surfaces are obtained, is limited by the radius and the tip-angle of the AFM tip used to obtain them.

9.2.2 Stiction and Friction

In order to understand the effects that the surface topography of a MEMS surface has on its stiction and friction characteristics, three important tribological properties of the surfaces of the Test Platform chips investigated are determined in this chapter. The tribological properties that are investigated in this chapter include the apparent work of adhesion of the in-plane surfaces, the apparent work of adhesion of the sidewall surfaces and the coefficient of static friction of the sidewall surfaces. All the experiments that are conducted for this study are performed in laboratory air, at 22 °C and in 45% relative humidity (unless otherwise stated).

The apparent works of adhesion of the in-plane surfaces of the Test Platform chips investigated in this chapter are determined using the Cantilever Beam Array developed in this study. The magnification of the objective lens, which is used in the interference microscope that is used to determine the height profile of the actuated

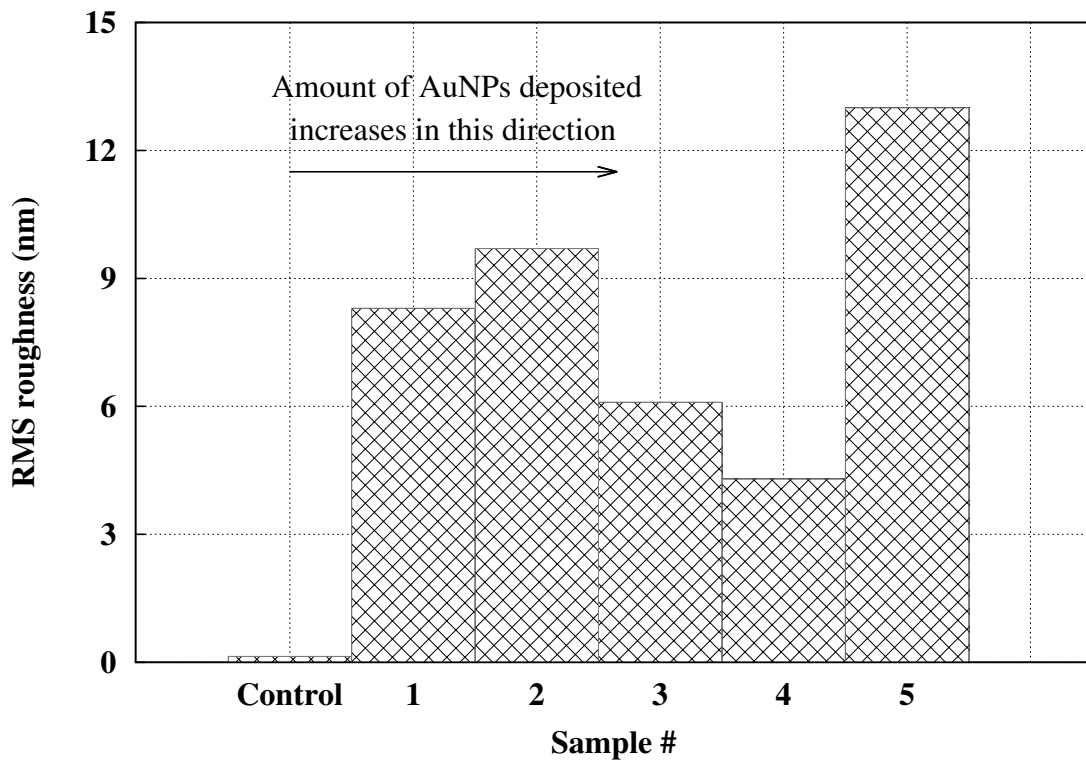
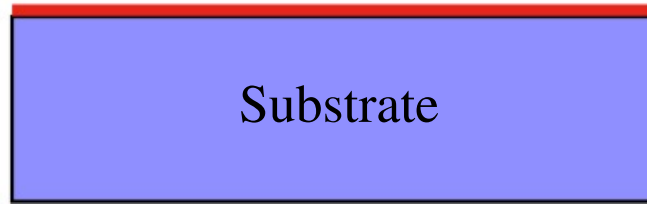
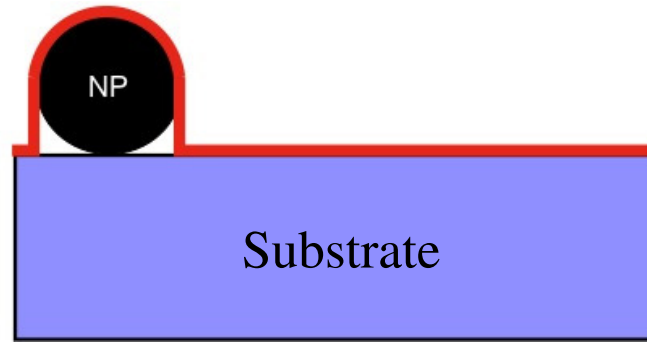


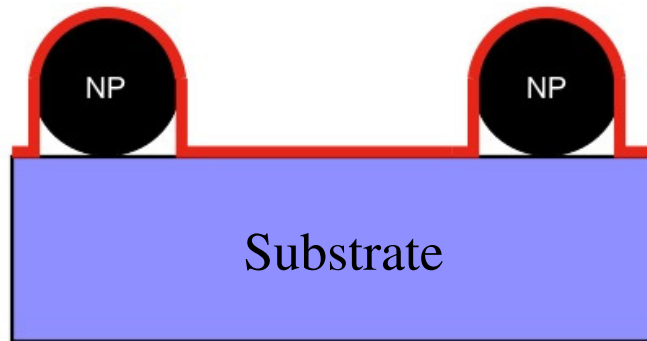
Figure 9.3: Bar graph showing the rms roughnesses of the in-plane surfaces of the Test Platform chips investigated in this chapter.



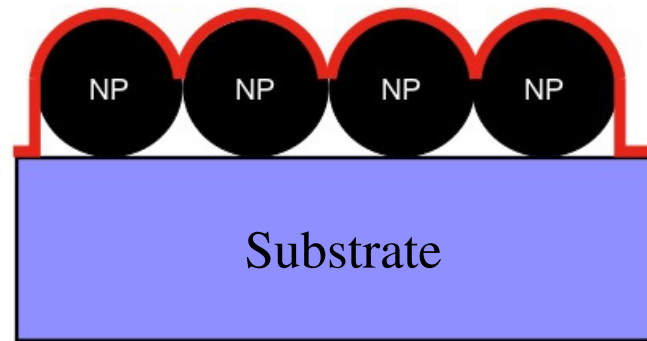
(a)



(b)



(c)



(d)

Figure 9.4: A schematic explaining the observed variations in the roughnesses of the substrates of the Test Platform chips investigated in this chapter. The red lines shown in all the diagrams represent the surface profile of the (untextured or textured) substrates shown in them.

cantilever beams, is either 10X or 20X. Accordingly, the size of each pixel in the field of view is either $0.465 \mu\text{m} \times 0.465 \mu\text{m}$ or $0.234 \mu\text{m} \times 0.234 \mu\text{m}$, respectively. On each of the six Test Platform chips investigated in this chapter, four CBAs consisting of ten cantilever beams each are actuated to obtain a statistically significant data set. Table 9.2 reports the mean observed crack lengths as well as the corresponding mean (calculated) apparent works of adhesion of the in-plane surfaces of all the six Test Platform chips investigated in this chapter.

The apparent works of adhesion of the sidewall surfaces of the Test Platform chips investigated in this chapter are determined using the Sidewall Beam Array developed in this study. The magnification of the objective lens of the microscope, which is used to observe the microinstrument during actuation and determine the crack length of each actuated adhered pair of sidewall beams, is 10X. Accordingly, the size of each pixel in the field of view is $0.465 \mu\text{m} \times 0.465 \mu\text{m}$. On each of the six Test Platform chips investigated in this chapter, eight SBAs are actuated to obtain a statistically significant data set. Table 9.3 reports the mean observed crack lengths and the corresponding mean (calculated) apparent works of adhesion of the contacting sidewall surfaces of all the Test Platform chips investigated in this chapter. Figure 9.5 is a plot showing the variations in the apparent works of adhesion of the in-plane as well as sidewall surfaces with the variations in their surface topographies. The data points plotted in the plot are the mean values of apparent work of adhesion, which are reported in Table 9.2 and Table 9.3. The error bars shown in the plot indicate the maximum and minimum values of the apparent works of adhesion exhibited by the in-plane and sidewall surfaces of that Test Platform chip.

The coefficients of static friction of the contacting sidewall surfaces of the Test Platform chips investigated in this chapter are determined using the Sidewall Friction Tester developed in this study. The magnification of the objective lens that is used in the microscope during the actuation of the Sidewall Friction Testers for this study is

Table 9.2: Comparison between the mean apparent works of adhesion of the in-plane surfaces of the six Test Platform chips investigated in this chapter to study the effect of topography. The apparent works of adhesion of in-plane surfaces reported in this table are determined using the CBAs. All the values reported in the table are arithmetic means of 40 measurements.

Sample #	Crack Length s_{ip} (μm)	Apparent Work of Adhesion of In-plane Surfaces \mathcal{W}_{ip} ($\mu\text{J}/\text{m}^2$)
Control	99.0	38700
1	855.2	32.16
2	266.6	543.6
3	351.5	1209
4	216.1	4780
5	379.5	1058

Table 9.3: Comparison between the mean apparent works of adhesion of the sidewall surfaces of the six Test Platform chips investigated in this chapter to study the effect of topography. The apparent works of adhesion of in-plane surfaces reported in this table are determined using the SBAs. All the values reported in the table are arithmetic means of several measurements.

Sample #	Crack Length s_s (μm)	Apparent Work of Adhesion of In-plane Surfaces \mathcal{W}_s ($\mu\text{J}/\text{m}^2$)
Control	660.1	1070
1	1753	21.50
2	1683	25.33
3	1431	48.52
4	1122	128.2
5	1498	40.38

10X. Accordingly, the size of each pixel in the field of view is $0.465 \mu\text{m} \times 0.465 \mu\text{m}$. On each of the six Test Platform chips investigated, five Sidewall Friction Testers are used to determine the coefficient of static friction of their sidewall surfaces. Using each Sidewall Friction Tester, the coefficient of static friction is determined at normal loads ranging from $2.4 \mu\text{N}$ - $15.7 \mu\text{N}$, which correspond to Hertzian contact pressures (calculated by considering cylinder on flat geometry) of 123 MPa - 312 MPa. This range of normal load is representative of that experienced by most potential and commercialized MEMS during operation. Additionally, in order to obtain statistically significant results, the coefficient of static friction is determined five times for each investigated normal load. Table 9.4 reports the (experimentally determined) mean engineering coefficients of static friction of the contacting sidewall surfaces of all the Test Platform chips investigated in this chapter. Figure 9.6 is a plot showing the variation in the engineering coefficient of static friction of a sidewall surface with the variation in its surface topography. The data points plotted in the plot are the mean values of engineering coefficients of static friction, which are reported in Table 9.3. The error bars shown in the plot indicate the maximum and minimum values of the engineering coefficient of static friction exhibited by the sidewall surfaces of that Test Platform chip.

Like the rms roughnesses of the substrates of the six Test Platform chips investigated in this chapter, the apparent works of adhesion of their in-plane as well as sidewall surfaces and the engineering coefficients of static friction of their contacting sidewall surfaces also do not show a direct correspondence with the amounts of the nanoparticles deposited on them. However, all the three tribological properties investigated in this chapter (i.e., apparent work of adhesion of in-plane surfaces, apparent work of adhesion of sidewall surfaces and the engineering coefficient of static friction of contacting sidewall surfaces) exhibit identical variations with the variation in the surface topographies of the surfaces exhibiting them. In other words, the variation

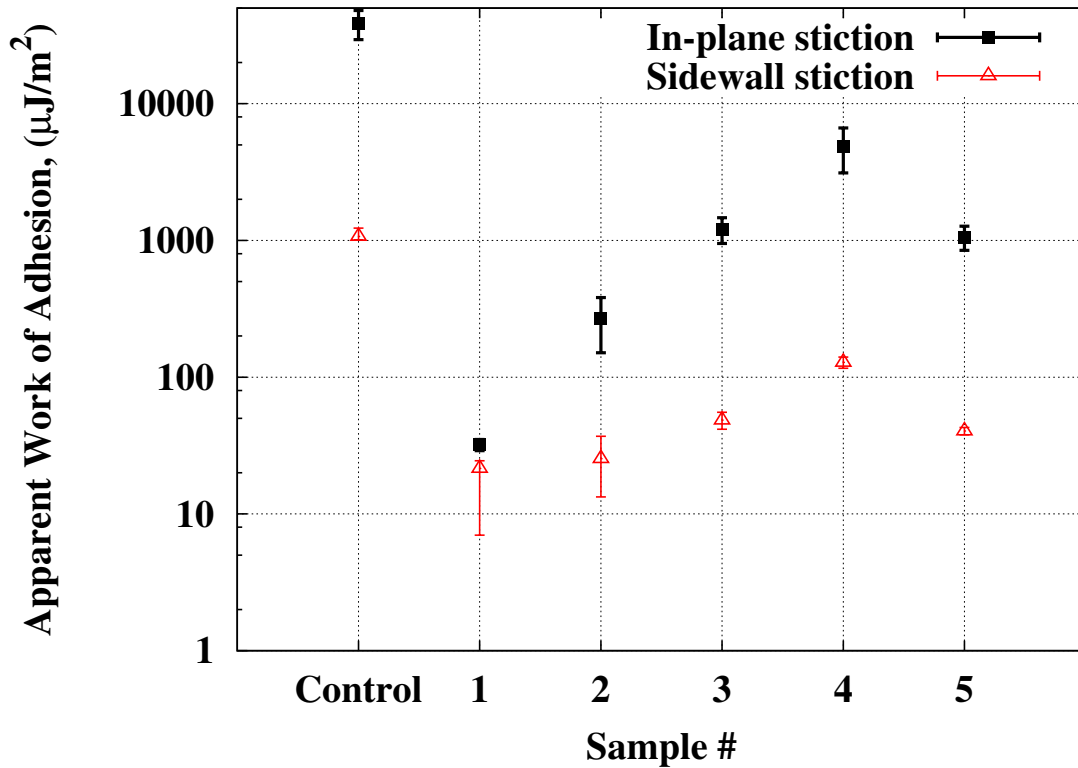


Figure 9.5: A plot showing the variations in the apparent works of adhesion of the in-plane as well as sidewall surfaces with the variations in their surface topographies. The data points plotted in the plot are arithmetic means of several measurements. The error bars shown in the plot indicate the maximum and minimum values of the apparent works of adhesion exhibited by the in-plane and sidewall surfaces of that Test Platform chip.

Table 9.4: Comparison between the mean engineering coefficients of static friction of the sidewall surfaces of the six Test Platform chips investigated in this chapter to study the effect of topography. The engineering coefficients of static friction reported in this table are determined using Sidewall Friction Testers. All the values reported in the table are arithmetic means of 225 measurements.

Sample #	Coefficient of Static Friction μ_s
Control	1.75
1	0.076
2	0.221
3	0.337
4	0.443
5	0.332

in the engineering coefficient of static friction of a sidewall surface with the variation in its surface topography, which is shown in Fig. 9.6, shows a high degree of correspondence with the variation in the apparent work of adhesion of a sidewall surface with the variation in its surface topography, which is shown in Fig. 9.5. This is an experimental confirmation of the already believed theory that the friction experienced by contacting MEMS surfaces shows a strong dependence on the stiction experienced by them. Further, the variations in the apparent works of adhesion of in-plane and sidewall surfaces with the variations in their surface topographies, which are shown in Fig. 9.5, also exhibit a high degree of correspondence with each other. Therefore, I hypothesized that the variations in the apparent works of adhesion of the in-plane and sidewall surfaces investigated in this study are governed by the nano-scale variations in their topographies induced by the nanoparticles deposited on them. However, for my hypothesis to be valid, since the variation in the apparent work of adhesion of an in-plane surface with the variation in its surface topography is identical to the variation in the apparent work of adhesion of a sidewall with the variation in its surface topography, both the in-plane as well as sidewall surfaces of the Test Platform chips investigated in this study should have identical nanoparticle coatings deposited on them. Fig. 9.7a is a SEM image showing the edge of a released cantilever beam of sample no. 4 and Fig. 9.7b is a SEM image of a region of the substrate, which is underneath the cantilever beam shown in Fig. 9.7a. The SEM image shown in Fig. 9.7b is collected after breaking the cantilever beam shown in Fig. 9.7a apart using a probe tip (Signatone 20T). It is clearly evident in Figs. 9.7a and 9.7b that the surfaces shown in them have exactly identical nanoparticle coatings on them, which substantiates that the in-plane and sidewall surfaces of the Test Platform chips investigated in this chapter have exactly identical nanoparticle coatings on them. This supports my hypothesis that the variations in the apparent works of adhesion of the in-plane

and sidewall surfaces investigated in this study are governed by the variations in their nano-scale topographies.

In order to explain the difference between the absolute values of the apparent works of adhesion of the in-plane and sidewall surfaces of the same Test Platform chip, I hypothesized that the lower apparent works of adhesion of the sidewall surfaces of the Test Platform chips investigated in this study as compared to those of the corresponding in-plane surfaces are due to their initial micro-scale surface topographies (i.e., the surface topographies of the underlying untextured sidewall surfaces). The in-plane surfaces investigated in this chapter have extremely smooth initial surface topographies (i.e., their initial (untextured) rms roughness is 0.14 nm), while the sidewall surfaces investigated in this chapter have rougher initial surface topographies (i.e., their initial (untextured) rms roughness is 6.52 nm). In other words, both the micro-scale as well as the nano-scale topographies of a surface have a strong influence on its stiction and friction characteristics. In order to mathematically correlate the surface topography of a surface with its stiction and friction characteristics, the following sections discuss the formulation of a dimensionless parameter, which can be used to predict the effect that the surface topography of a surface will have on its stiction and friction characteristics.

9.3 Tribotopography Number (τ_{topo})

In order to quantitatively understand the effect that the surface topography of a surface has on its tribological (i.e., stiction and friction) properties, the apparent works of adhesion of the in-plane surfaces investigated in this chapter are plotted against their rms roughnesses, which is one of the measurable parameters of their surface topographies. The plot is shown in Fig. 9.8. It was expected that the increase in the rms roughness of the in-plane surfaces investigated in this chapter will either increase their surface area and hence the stiction experienced by them

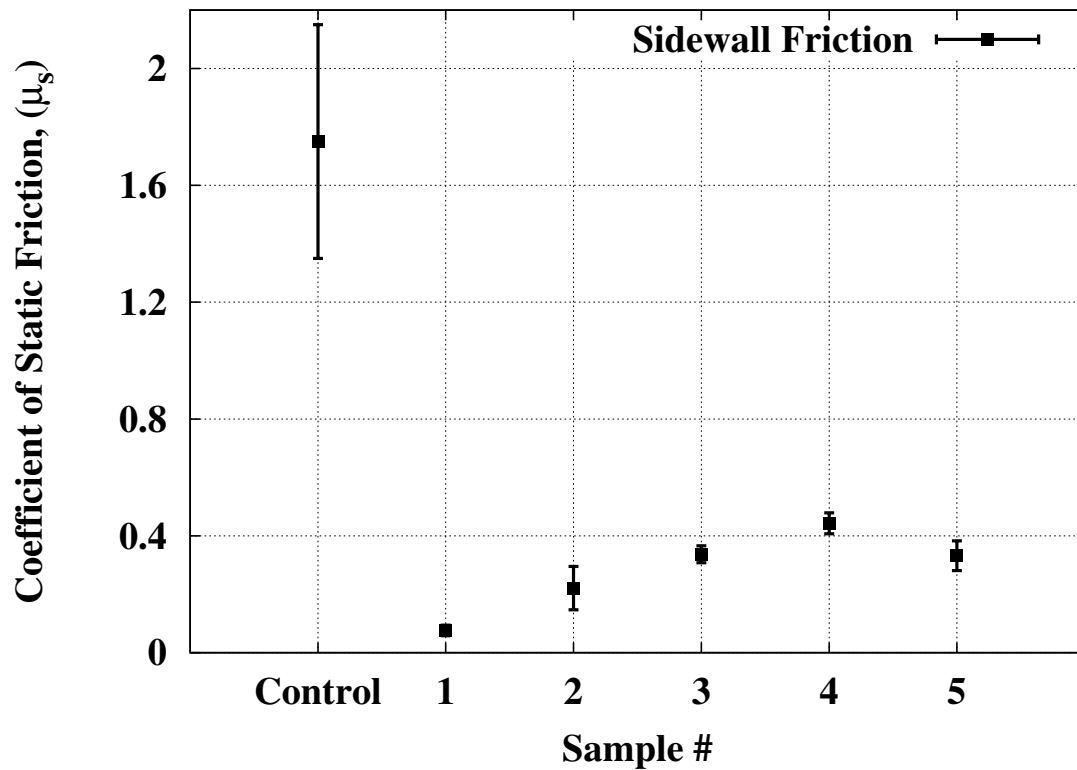
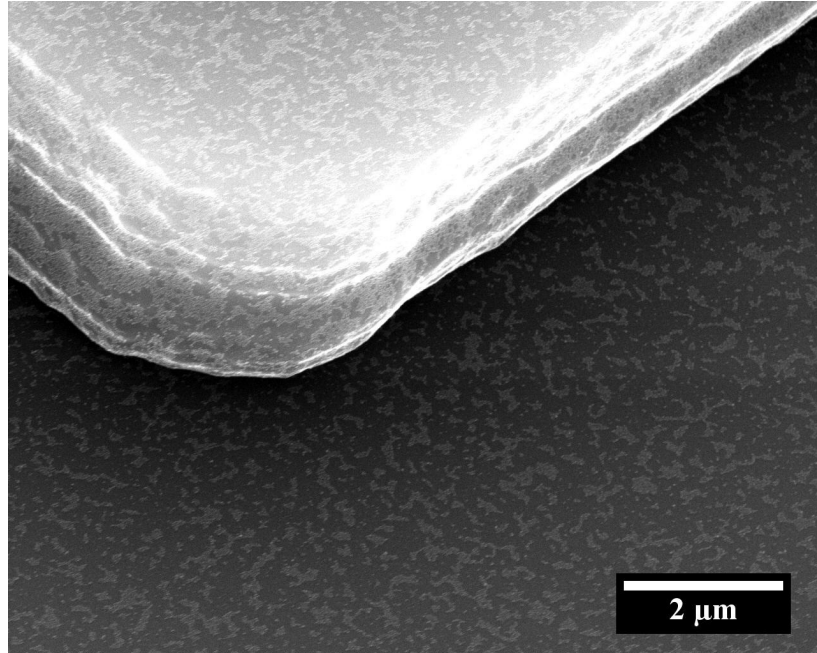
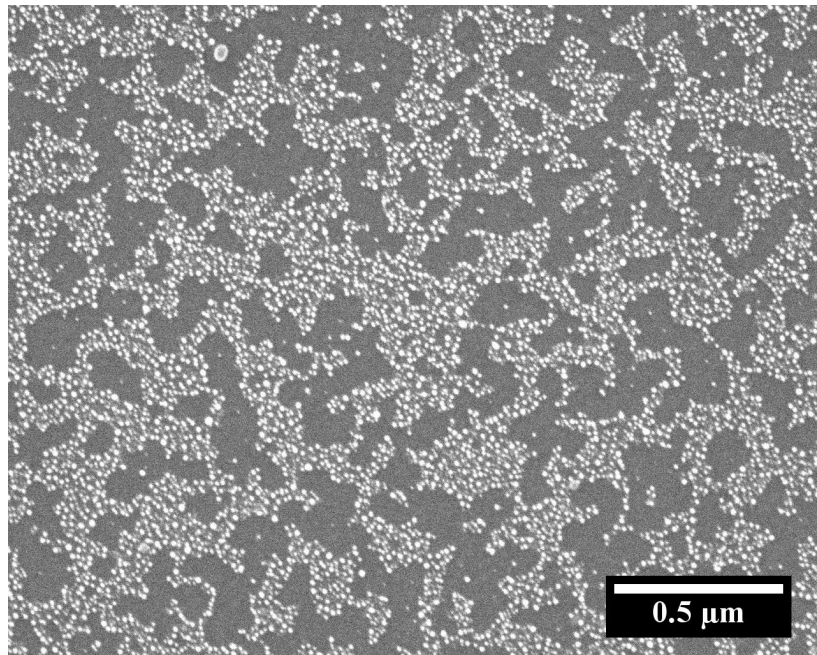


Figure 9.6: A plot showing the variation in the engineering coefficient of static friction of a sidewall surface with the variation in its surface topography. The data points plotted in the plot are arithmetic means of 225 measurements. The error bars shown in the plot indicate the maximum and minimum values of the engineering coefficient of static friction exhibited by the contacting sidewall surfaces of that Test Platform chip.



(a)



(b)

Figure 9.7: (a) A SEM image showing the edge of a released cantilever beam of sample no. 4. (b) A SEM image of a region of the substrate, which is underneath the cantilever beam shown in Fig. 9.7a. The SEM image shown in this image is collected after breaking the cantilever beam shown in Fig. 9.7a apart using a probe tip (Signatone 20T). Notice that the surfaces shown in both the image a as well as the image b have exactly identical nanoparticle coatings on them.

or decrease the contact area of the interface formed by them and hence the stiction experienced by them. In other words, it was expected that the apparent works of adhesion of the in-plane surfaces investigated in this chapter will either increase or decrease monotonously with their rms roughnesses. However, it is clearly evident in the plot shown in Fig. 9.8 that there exists an optimum rms roughness, at which, the in-plane surface exhibits minimum apparent work of adhesion. This observation can be explained by considering the mathematics involved in the calculation of the rms roughness of a surface. The absolute value of the rms roughness of a surface depends on two independent variables, namely, the heights of the asperities present on that surface and their frequencies. While an increase in the heights of the asperities present on a surface, which increases the rms roughness of that surface, decreases the stiction experienced by it, an increase in their frequencies, which also increases the rms roughness of the surface, increases the stiction experienced by it. Therefore, since the two components, which define the rms roughness of a surface, are independent, and change the stiction experienced by it in opposite directions, there exists an optimum roughness, at which, the stiction experienced by the surface is minimum. Accordingly, in order to comprehensively quantify the surface topography of a surface, both the components that define its rms roughness should be quantified individually. The following sections discuss the formulation and validation of the Tribotopography number (τ_{topo}), which is a dimensionless parameter that separately accounts for both the components that define the rms roughness of a surface, and can be used to determine the effect of the surface topography of a surface on its stiction and friction properties.

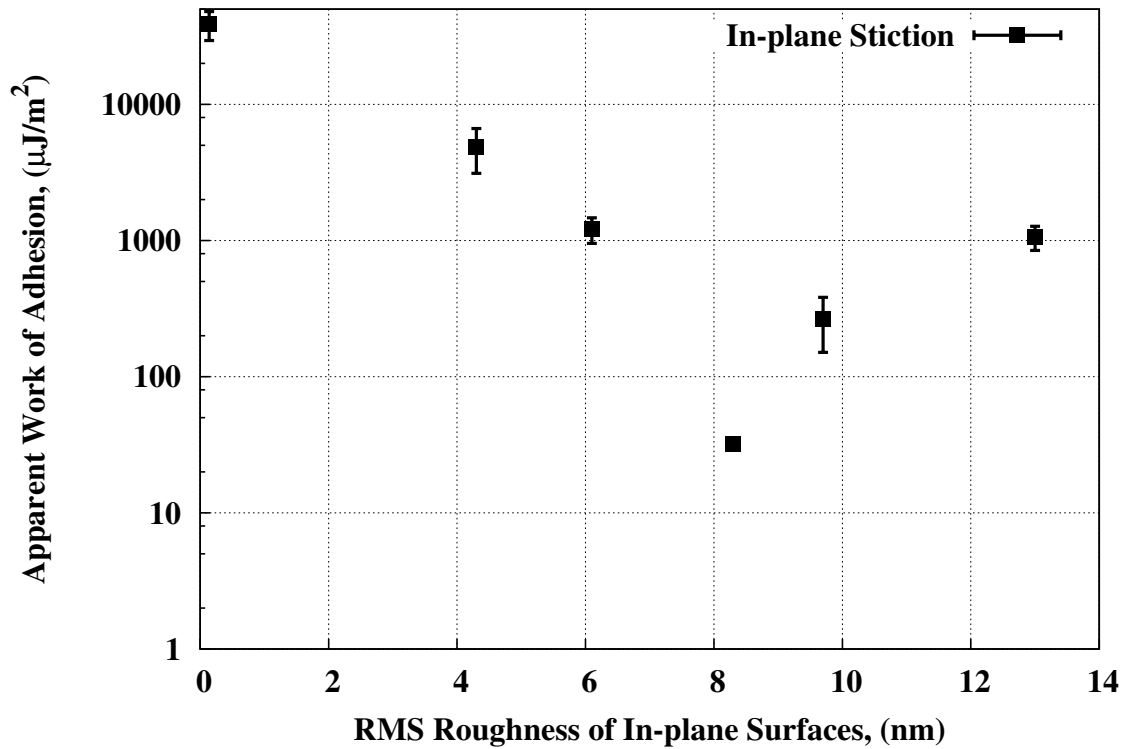


Figure 9.8: A plot of the apparent works of adhesion exhibited by the six in-plane surfaces investigated in this chapter versus their rms roughnesses. The data points plotted in the plot are arithmetic means of 40 measurements. The error bars shown in the plot indicate the maximum and minimum values of the apparent work of adhesion exhibited by the in-plane surface of that Test Platform chip. Notice that the plot indicates that there exists an optimum rms roughness, at which, the in-plane surface experiences minimum stiction.

9.3.1 Formulation

Effect of Surface Topography on Stiction

As mentioned earlier, the two components that define the rms roughness (i.e., surface topography) of a surface change the stiction experienced by it in opposite directions. An increase in the heights of the asperities present on contacting surfaces increases the distance of separation between the contacting surfaces, and hence as explained in section 1.5.1, decreases the attractive forces experienced by them. Accordingly, it also decreases the stiction between them. Therefore, based on the equations reported in section 1.5.1,

$$\mathcal{W} \propto \frac{1}{d^\alpha} \quad (9.3.1)$$

Here, \mathcal{W} is the apparent work of adhesion of the contacting surfaces, d is the distance of separation between the mean planes of the two contacting surfaces and index α is a factor that is determined by the type (see section 1.5.1) of the interfacial force that dominates their stiction behaviour. Further, an increase in the number of the interacting asperities present on the two contacting surfaces increases the area of interaction between them, and hence, the stiction experienced by them. Accordingly,

$$\mathcal{W} \propto n_{asperities} \quad (9.3.2)$$

Here, $n_{asperities}$ is the number of interacting asperities present on one of the two contacting surfaces forming an interface (i.e., a measure of the area of interaction between the two contacting surfaces). Combining Eqs. 9.3.1 and 9.3.2 gives,

$$\mathcal{W} \propto \frac{n_{asperities}}{d^\alpha} \quad (9.3.3)$$

Considering that the elastic moduli of both the native oxide as well as gold are relatively high (i.e., 70 - 75 GPa and 79 GPa, respectively), and the radii of curvature of the asperities present on all the surfaces investigated in this study are extremely small (i.e., mean diameter of the gold nanoparticles used to tailor the topographies of the surfaces of the test samples is 5.5 nm), the asperities that come in contact at the control and test interfaces investigated in this study can be considered as rigid [180–182]. Accordingly, it is safe to conclude that they undergo extremely insignificant elastic deformations. Additionally, the mechanics involved in the methods that are used for determining the apparent works of adhesion of the interfaces investigated in this study ensure that all the attractive forces that exist at an interface are completely balanced by the restoring forces generated by the microinstrument that is used for determining its apparent work of adhesion, instead of by the elastic forces generated by the deformation of the asperities that come in contact at it. This further ensures that the asperities that come in contact at the interfaces investigated in this study do not undergo any elastic and/or plastic deformation. Accordingly, the distances of separation between the mean planes of the two surfaces that form the interfaces that are investigated in this study can be given by the expression shown below [188]:

$$d \propto 2r_{rms} \quad (9.3.4)$$

The above mentioned expression can also be understood by considering that each of the surfaces investigated in this study can be represented by a corresponding equivalent surface such that the rms roughness of the investigated surface is equal to the amplitude of the asperities present on the equivalent surface. The equivalent surfaces are defined by cube-shaped peaks and valleys, have equal number of peaks and valleys and the heights of all the peaks present on each equivalent surface are equal to each other as well as to the depths of all the valleys present on it. Substituting Eq. 9.3.4

in Eq. 9.3.3 gives,

$$\mathcal{W} \propto \frac{n_{asperities}}{(2r_{rms})^\alpha} \quad (9.3.5)$$

Re-writing the generalized Eq. 9.3.5 for a reference surface:

$$\mathcal{W}^o \propto \frac{n_{asperities}^o}{(2r_{rms}^o)^\alpha} \quad (9.3.6)$$

Here, \mathcal{W}^o is the apparent work of adhesion of a reference surface, $n_{asperities}^o$ is the number of interacting asperities present on it and r_{rms}^o is its rms roughness. It should be noted that the reference surface should be a surface, whose tribological (i.e., stiction and friction) behaviour is dominated by the same types (see section 1.5.1) of interfacial forces that dominate the tribological behaviour of the surface being analyzed. Dividing Eq. 9.3.5 by Eq. 9.3.6 gives,

$$\frac{\mathcal{W}}{\mathcal{W}^o} = \left(\frac{n_{asperities}}{n_{asperities}^o} \right) \left(\frac{r_{rms}^o}{r_{rms}} \right)^\alpha \quad (9.3.7)$$

Combining similar terms in Eq. 9.3.7 gives,

$$\frac{\mathcal{W}}{\mathcal{W}^o} = \frac{\Theta}{(\Omega_{rms})^\alpha} \quad (9.3.8)$$

where, Θ , which can be considered as the relative surface coverage of the interacting asperities present on the surface being analyzed, is given by Eq. 9.3.9 shown below:

$$\Theta = \frac{n_{asperities}}{n_{asperities}^o} \quad (9.3.9)$$

and Ω_{rms} , which can be considered as the relative rms roughness of the surface being analyzed, is given by Eq. 9.3.10 shown below:

$$\Omega_{rms} = \frac{r_{rms}}{r_{rms}^o} \quad (9.3.10)$$

The Tribotopography number (i.e., τ_{topo}) of the surface being analyzed is given by Eq. 9.3.11 shown below:

$$\tau_{topo} = \frac{\Theta}{(\Omega_{rms})^\alpha} \quad (9.3.11)$$

Substituting Eq. 9.3.11 in Eq. 9.3.8 gives,

$$\frac{\mathcal{W}}{\mathcal{W}^o} = \tau_{topo} \quad (9.3.12)$$

Rearranging Eq. 9.3.12 gives,

$$\mathcal{W} = \tau_{topo} \mathcal{W}^o \quad (9.3.13)$$

Equation 9.3.13 is a mathematical correlation between the surface topography of a surface and its apparent work of adhesion. It can be used to determine the apparent work of adhesion of a test surface (i.e., a surface, whose apparent work of adhesion is unknown) using its τ_{topo} and the apparent work of adhesion of a reference surface (i.e., a surface, whose tribological behaviour is governed by the same types of interfacial forces that govern the tribological behaviour of the test surface). As indicated by Eqs. 9.3.11, 9.3.9 and 9.3.10, the τ_{topo} of a test surface can be determined using the rms roughnesses of, and the surface coverages of the interacting asperities present on, the test and reference surfaces, all of which, can be obtained from the corresponding representative AFM images of the two surfaces. In essence, Eq. 9.3.13 can be used to determine the effect that the surface topography of a surface has on the stiction experienced by it.

Effect of Surface Topography on Friction

As indicated by the results shown in Figs. 9.5 and 9.6, the static friction experienced by the contacting sidewall surfaces investigated in this chapter shows a strong dependence on the stiction experienced by them. This is attributed to the fact that owing to the hydrophilic nature of the sidewall surfaces investigated in this chapter,

the adhesion force experienced by contacting sidewall surfaces is significantly high and comparable to the external normal loads applied at the interfaces formed by them. Therefore, it acts as additional normal load applied at them. Accordingly, the static friction force experienced by the contacting sidewall surfaces of the Test Platform chips investigated in this chapter should be given by Eq. 9.3.14 shown below:

$$f_s = \mu_{s,t} (N + \mathcal{W}_f) \quad (9.3.14)$$

Here, f_s is the static friction force experienced by the contacting sidewall surfaces, N is the external load applied at the interface formed by them, \mathcal{W}_f is the adhesion force experienced by them and $\mu_{s,t}$ is their true coefficient of static friction, which is a material constant, depends only the materials (i.e., surface energies) of the surfaces forming the interface and shows no dependence on any external factor. Re-writing the generalized Eq. 9.3.14 for a reference surface:

$$f_s^o = \mu_{s,t} (N + \mathcal{W}_f^o) \quad (9.3.15)$$

Here, f_s^o is the static friction force experienced by contacting reference surfaces when an external normal load N is applied at the interface formed by them and \mathcal{W}_o is the adhesion force experienced by them. Again, it should be noted that the reference surface should be a surface, whose tribological (i.e., stiction and friction) behaviour is dominated by the same types (see section 1.5.1) of interfacial forces that dominate the tribological behaviour of the surface being analyzed (i.e., test surface). Subtracting Eq. 9.3.15 from Eq. 9.3.14 gives,

$$f_s - f_s^o = \mu_{s,t} (\mathcal{W}_f - \mathcal{W}_f^o) \quad (9.3.16)$$

Utilizing Eq. 9.3.12, the Tribotopography number (i.e., τ_{topo}) of the test surface can also be given by Eq. 9.3.17 shown below:

$$\tau_{topo} = \frac{\mathcal{W}_f}{\mathcal{W}_f^o} \quad (9.3.17)$$

Applying dividendo to Eq. 9.3.17 gives,

$$\tau_{topo} - 1 = \frac{\mathcal{W}_f - \mathcal{W}_f^o}{\mathcal{W}_f^o} \quad (9.3.18)$$

Rearranging Eq. 9.3.18 gives,

$$\mathcal{W}_f - \mathcal{W}_f^o = \mathcal{W}_f^o (\tau_{topo} - 1) \quad (9.3.19)$$

Substituting Eq. 9.3.19 in Eq. 9.3.16 gives,

$$\mathbf{f}_s - \mathbf{f}_s^o = \mu_{s,t} \mathcal{W}_f^o (\tau_{topo} - 1) \quad (9.3.20)$$

Equation 9.3.20 is a mathematical correlation between the surface topography of a surface and the static friction force experienced by it at a given normal load. It can be used to determine the static friction force experienced by a test surface at a given normal load using its τ_{topo} and the static friction as well as adhesion forces experienced by a reference surface (i.e., a surface, whose tribological behaviour is governed by the same types of interfacial forces that govern the tribological behaviour of the test surface) at the same normal load. In essence, Eq. 9.3.20 can be used to determine the effect that the surface topography of a surface has on the friction experienced by it.

9.3.2 Determination of α for Silicon-type Surfaces

In order to be able to use Eqs. 9.3.13 and 9.3.20 for a particular type of surface, the value of index α for that type of surface must be determined first. Therefore,

this section will discuss the determination of index α for silicon-type surfaces (i.e., surfaces, whose tribological behaviours are governed by the same types of interfacial forces that govern the tribological behaviour of silicon surfaces).

Comparing Eqs. 9.3.11 and 9.3.12 gives,

$$\frac{\mathcal{W}}{\mathcal{W}^o} = \frac{\Theta}{(\Omega_{rms})^\alpha} \quad (9.3.21)$$

Rearranging Eq. 9.3.21 gives,

$$\frac{\Theta}{\mathcal{W}/\mathcal{W}^o} = (\Omega_{rms})^\alpha \quad (9.3.22)$$

Taking natural log of both sides of Eq. 9.3.22 gives,

$$\ln \left(\frac{\Theta}{\mathcal{W}/\mathcal{W}^o} \right) = \alpha \ln (\Omega_{rms}) \quad (9.3.23)$$

Equation 9.3.23 can be used to determine the value of index α . The values of Θ and Ω_{rms} of each of the five textured in-plane surfaces investigated in this chapter are determined using the untextured (control) in-plane surface investigated in this chapter as the reference surface. Accordingly, the values of \mathcal{W}^o and r_{rms}^o used for determining the value of index α for silicon-type surfaces are $38700 \mu\text{J}/\text{m}^2$ and 0.14 nm , respectively. $n_{asperities}$ for each of the five textured in-plane surfaces investigated in this chapter as well as for the reference surface are determined using the image analysis technique explained in section 6.12.

As explained in section 9.3.1, the asperities that come in contact at the interfaces investigated in this chapter do not undergo any elastic and/or plastic deformation. Accordingly, the interfaces investigated in this chapter do not experience any repulsive elastic forces. Further, the insignificant deformation of the asperities that

Table 9.5: This table reports the \mathcal{W} (arithmetic mean), r_{rms} , Ω_{rms} and Θ of all the five textured in-plane surfaces investigated in this study. The values of Θ and Ω_{rms} reported in this table are determined using the untextured (control) in-plane surface as the reference surface. Accordingly, \mathcal{W}^o and r_{rms}^o used are $38700 \mu\text{J}/\text{m}^2$ and 0.14 nm , respectively. The r_{rms} of each of the five textured in-plane surfaces as well as the r_{rms}^o are obtained from their corresponding representative AFM images. $n_{asperities}$ for each of the five textured in-plane surfaces as well as for the reference surface are determined using the image analysis technique explained in section 6.12. The threshold value used in the image analysis technique is the kelvin radius of water at the relative humidity of 45%.

Sample #	\mathcal{W} ($\mu\text{J}/\text{m}^2$)	r_{rms} (nm)	Ω_{rms}	Θ (%)
1	32.16	8.3	59	0.62
2	543.6	9.7	69	6.1
3	1209	6.1	44	22.0
4	4780	4.3	31	75.0
5	1058	13.0	93	23.0

come in contact at the interfaces investigated in this chapter (as explained in section 9.3.1) is also responsible for the significantly small real area of contact of the interfaces investigated in this chapter as compared to their area of interaction. The contacting asperities (determined using the image analysis technique explained in section 6.12) present at the interfaces investigated in this chapter are small fractions of the interacting asperities (determined using the image analysis technique explained in section 6.12) present on them. Therefore, the inter-atomic and inter-molecular forces experienced by the interfaces investigated in this chapter are only a small fraction of the apparent works of adhesion exhibited by them. Accordingly, the interfacial forces that contribute significantly to the apparent works of adhesion of the interfaces investigated in this chapter are the capillary pull experienced by the interacting asperities and the VDW forces between the non-interacting asperities, of the two surfaces forming the interface. However, it has been reported that the tribological behaviour of silicon-type surfaces is dominated by the capillary forces experienced by them [71, 189]. Accordingly, the threshold value, which needs to be inputted in the image analysis technique to obtain the $n_{asperities}$ present on the surface being analyzed, used for each surface investigated in this chapter is the height value obtained after subtracting the $z_{interaction}$ (of that surface) from the z-scale of the AFM image of a representative area of that surface. The $z_{interaction}$ of a surface is the depth from the highest point on it, up to which, the asperities present on it experience a capillary pull at the relative humidity, at which, the experiments are performed. It depends on the kelvin radius of water (r_k) at the relative humidity, at which, the experiments are performed and the contact angles that a droplet of water makes on the two contacting surfaces that form the interface. It can be determined using Eq. 9.3.24, which is shown below:

$$z_{interaction} = r_k \frac{\cos \theta_1 + \cos \theta_2}{2} \quad (9.3.24)$$

Here, θ_1 and θ_2 are the contact angles that a droplet of water makes on the two contacting surfaces that form the interface. In the control sample, the examined interface is formed between two native oxide covered silicon surfaces, and characterized by the interactions between pairs of native-oxide covered silicon asperities. Therefore, the $z_{interaction}$ of the surfaces of the control sample (i.e, $z_{interaction}^c$) is determined using Eq. 9.3.25 shown below:

$$z_{interaction}^c = r_k \cos \theta_1 \quad (9.3.25)$$

Here, θ_1 is the contact angle that a droplet of water makes on a clean native oxide covered silicon surface. The value of θ_1 used for determining the number of interacting asperities present on the surfaces of the control sample is 0° (mean of the experimentally determined values). In the test samples, the examined interface is formed between gold nanoparticle coated, native oxide covered silicon surfaces. Accordingly, the interfaces formed in the test samples are characterized by the interactions between pairs of a gold asperity and a native-oxide covered silicon asperity as well as between pairs of two gold asperities. Therefore, the $z_{interaction}$ of the surfaces of the test samples (i.e, $z_{interaction}^t$) is determined using Eq. 9.3.26 shown below:

$$z_{interaction}^t = r_k \frac{\cos \theta_1 + 3 \cos \theta_2}{4} \quad (9.3.26)$$

Here, θ_1 and θ_2 are the contact angles that a droplet of water makes on clean native oxide covered silicon and clean gold surfaces, respectively. The values of θ_1 and θ_2 used for determining the number of interacting asperities present on the surfaces of the test samples are 0° (mean of the experimentally determined values) and 15° (mean of the experimentally determined values), respectively. All the experiments reported in this chapter are performed at a relative humidity of 45%. The kelvin radius of water (calculated using Eq. 1.5.6) at a relative humidity of 45% is 0.66 nm [189]. In order to convert the threshold value (from length units) to its corresponding value on a scale

of 0 - 255, the z-scale of the AFM image being analyzed is converted to an intensity scale ranging from 0 - 255. The r_{rms} of each of the five textured in-plane surfaces investigated in this chapter as well as the r_{rms}^o are obtained from their corresponding representative AFM images. Table 9.5 reports the \mathcal{W} (arithmetic mean), r_{rms} , Ω_{rms} and Θ of all the five textured in-plane surfaces investigated in this study. Figure 9.9 shows a plot, in which, the ordinates of Eq. 9.3.23 are plotted against its abscissae. The data points plotted in Fig. 9.9 are obtained using the mean values of \mathcal{W} reported in Table 9.5. The error bars shown in the plot indicate one standard deviation of the sample of 40 measurements used to determine that data point. A line fitted to the mean values of the ordinates of Eq. 9.3.23, plotted in Fig. 9.9, is also plotted in Fig. 9.9. The high R^2 value of the linear fit indicates that the mathematical correlation (i.e., Eq. 9.3.13) between the surface topography of a surface and its apparent work of adhesion developed in section 9.3.1 is in good agreement with the data obtained experimentally. According to Eq. 9.3.23, the slope of the linear fit represents the value of index α . Therefore, the experimentally obtained value of the index α for silicon-type surfaces, which is extracted from the slope of the linear fit shown in Fig. 9.9, is 0.5.

9.3.3 Validation

In order to substantiate the validities of the mathematical correlation between the surface topography of a surface and its apparent work of adhesion (i.e., Eq. 9.3.13) developed in section 9.3.1 and the value of index α for silicon-type surfaces obtained experimentally, it is essential to determine the apparent work of adhesion of a surface, which is not used to determine the value of index α for silicon-type surfaces, using its Tribotopography number and compare it with the corresponding value obtained experimentally. For this purpose, the apparent work of adhesion of the sidewall surface of the control (untextured) sample is determined, using its Tribotopography number.

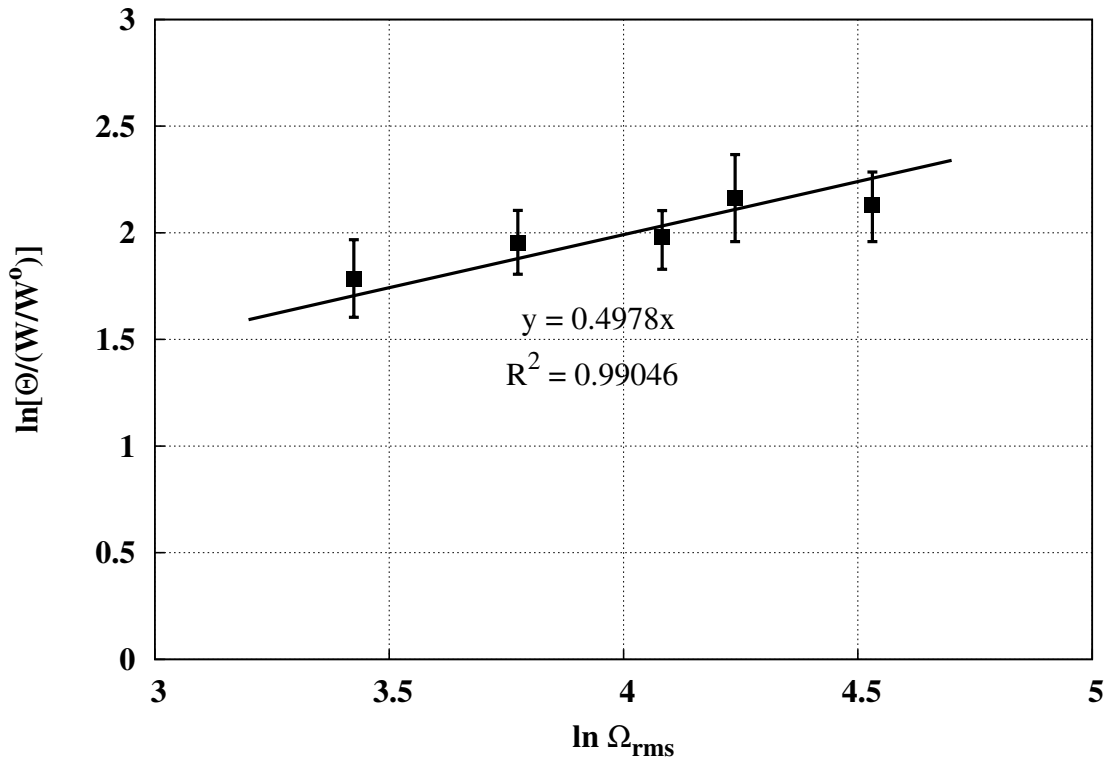


Figure 9.9: A plot, in which, the ordinates of Eq. 9.3.23 are plotted against its abscissae. The data points (■) plotted in Fig. 9.9 are obtained using the mean values of \mathcal{W} reported in Table 9.5. The error bars shown in the plot indicate one standard deviation of the sample of 40 measurements used to determine that data point. A line (—) fitted to the data points (■) is also shown in the plot. Notice the high R^2 value of the linear fit.

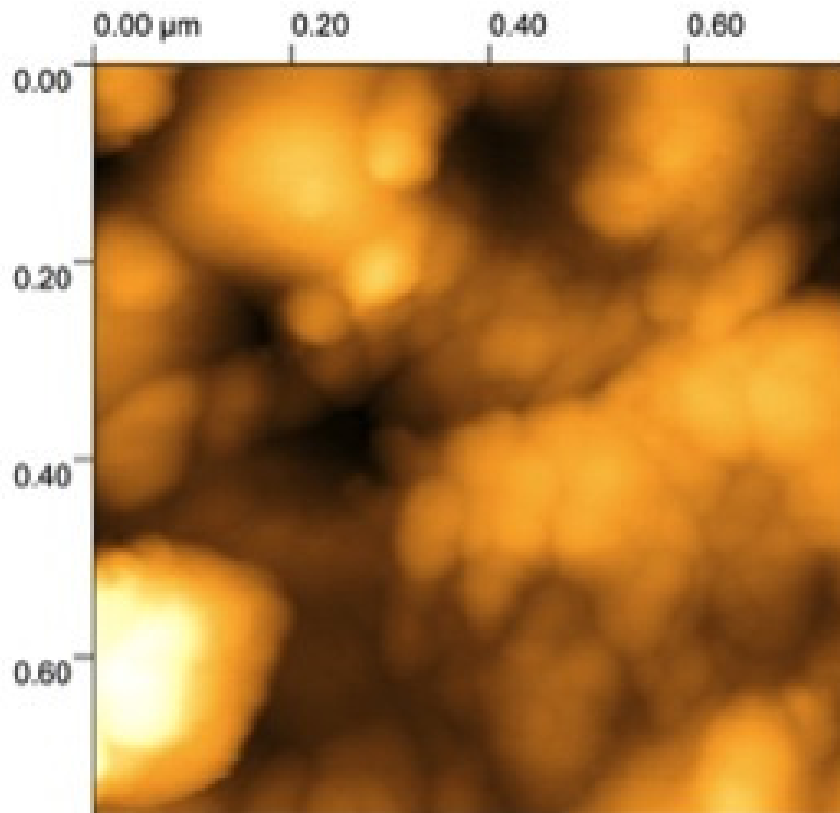


Figure 9.10: A representative AFM image of the sidewall surface of the control (untextured) sample. The rms roughness of the surface shown in the image is 6.52 nm. The z-scale of the image is 41.8 nm.

Figure 9.10 shows a representative AFM image of the sidewall surface of the control (untextured) sample. The r_{rms} and the $n_{asperities}$ of the sidewall surface of the control sample are obtained using this AFM image. The Ω_{rms} and the Θ of the sidewall surface of the control (untextured) sample are obtained using the in-plane surface of the control (untextured) sample as the reference surface and Eq. 9.3.25. Table 9.6 reports the r_{rms} , Ω_{rms} , Θ and τ_{topo} of the sidewall surface of the control (untextured) sample. It also reports the apparent works of adhesion of the sidewall surface of the control sample, determined using its τ_{topo} and obtained experimentally. The close agreement between the apparent work of adhesion of the sidewall surface of the control sample determined using its τ_{topo} and that obtained experimentally substantiates the validities of the mathematical correlation between the surface topography of a surface and its apparent work of adhesion (i.e., Eq. 9.3.13) developed in section 9.3.1 and the value of index α for silicon-type surfaces obtained experimentally. Since the mathematical correlation between the surface topography of a surface and the friction force experienced by it, which is represented by Eq. 9.3.20, is based on the mathematical correlation between the surface topography of a surface and its apparent work of adhesion (i.e., Eq. 9.3.13), the analysis reported in this section also substantiates the validity of the former.

Like most mathematical correlations, the two mathematical correlations developed in this study (i.e., one between the surface topography of a surface and its apparent work of adhesion (Eq. 9.3.13) and the other between the surface topography of a surface and the friction experienced by it (Eq. 9.3.20)), also have some constraints. While the generalized form of the Tribotopography number (i.e., Eq. 9.3.11) can be used for any surface, the value of index α (i.e., 0.5) determined experimentally in this study can be used only for silicon-type surfaces (i.e., surfaces, whose tribological behaviours are governed by the same types of interfacial forces that govern the tribological behaviour of silicon surfaces). Additionally, for hydrophobic silicon-type

Table 9.6: This table reports the r_{rms} , Ω_{rms} , Θ and τ_{topo} of the sidewall surface of the control (untextured) sample. The r_{rms} reported in this table is obtained using the AFM image shown in Fig. 9.10. The Ω_{rms} and the Θ reported in the table are obtained using the in-plane surface of the control (untextured) sample as the reference surface. The table also reports the apparent works of adhesion of the sidewall surface of the control sample, determined using its τ_{topo} and obtained experimentally.

Parameter	Unit	Value
r_{rms}	nm	6.52
Ω_{rms}	-	46.6
Θ	%	18.1
τ_{topo}	-	0.027
\mathcal{W}_{topo}	$\mu\text{J}/\text{m}^2$	1040
\mathcal{W}_{exp}	$\mu\text{J}/\text{m}^2$	1070

surfaces, the value of index α (i.e., 0.5) that is determined experimentally in this study can be used only for $d \geq 20$ nm. For $d < 20$ nm, the value of index α for hydrophobic silicon-type surfaces increases to a value between 2.5 - 3.0. Further, for hydrophilic silicon-type surfaces, the two mathematical correlations developed in this study (i.e., Eq. 9.3.13 and Eq. 9.3.20) are valid for $d \geq r_k(\cos \theta_1 + \cos \theta_2)$. For all $d \leq r_k(\cos \theta_1 + \cos \theta_2)$, the value of Θ of the contacting hydrophilic silicon-type surfaces is 1, and their topographies do not exhibit any influence on their stiction and friction characteristics.

9.3.4 Significance of the Tribotopography Number (τ_{topo})

Historically, several mathematical models have been developed to correlate the surface topography of a surface with its stiction characteristics [188,190]. However, each of those models were developed using a statistical surface profile model, which was required to represent the surface topographies of the surfaces being studied, and an appropriate contact mechanics model (i.e., JKR, DMT, MD, etc.), which was required to represent the interfacial forces experienced by the two contacting surfaces forming the interface [188,190]. The statistical surface profile models used assume that the height distribution of the asperities present on the surfaces being investigated can be comprehensively represented by the statistical probability distribution functions such the Gaussian distribution (used in most of the previously reported models) or the exponential distribution, and that all of them have spherical tips having the exact same radius of curvature [188–190]. Both of these assumptions compromise the accuracy of the typical statistical surface profile models used, in representing the surface topographies of MEMS surfaces. Further, the contact mechanics model that were used for representing the interfacial forces existing at the interface being investigated were determined by determining the Tabor adhesion parameter of the two surfaces

forming the interface [189]. The Tabor adhesion parameter of an interface is a dimensionless parameter, which represents the statistical average of a competition between the repulsive elastic forces exerted by the deformed taller asperities of the two surfaces forming the interface that try to prize them apart, and the attractive adhesive forces between their contacting asperities that try to hold them together [190]. The original Tabor adhesion parameter, which was formulated by Fuller and Tabor, is calculated using the standard deviation of the heights of the asperities present on a surface as the characteristic length, and therefore, can be used only for those interfaces, at which, the short-range solid-solid interactions (i.e., inter-atomic and inter-molecular forces) are the dominant contribution of the total interfacial forces [189]. However, in the case of interfaces that are formed between hydrophilic surfaces in humid environments, the interfacial interactions are dominated by the long-range capillary forces. Therefore, Fogden *et al.*, Maugis *et al.* and Xu *et al.* separately formulated a modified Tabor adhesion parameter, which is calculated using the kelvin radius at the relative vapor pressure, at which, the experiment is performed as the characteristic length, and therefore, can be used for those interfaces, at which, the capillary forces are the dominant interfacial force [189, 191, 192]. While both the original Tabor adhesion parameter as well as the modified Tabor adhesion parameter are extremely useful in understanding the interfacial interactions of single asperity contacts, for interfaces that consist of multiple point contacts, they can be used only as a qualitative measure of the effect of surface topography, and require the use of an appropriate statistical surface profile model and an appropriate contact mechanics model for quantitatively determining the effect that the surface topography of a surface has on its stiction characteristics. On the other hand, the Tribotopography number (i.e., τ_{topo}) formulated in this chapter eliminates the need of a statistical surface profile model for quantifying the effect that the surface topography of a surface has on its stiction and

friction characteristics. Additionally, it, and hence, the two mathematical correlations formulated using it, can be used for interfaces represented by the entire spectra of the two Tabor adhesion parameters.

9.4 Influence of the Geometry of the Contact Interface on the Effect of Surface Topography

In order to determine the influence of the geometry of the contact interface on the effect that the surface topographies of the surfaces forming the interface have on its tribological characteristics, the engineering coefficients of static friction of the sidewall surfaces of all the six Test Platform chips investigated in this study are determined using both the Sidewall Friction Testers (SFTs) as well as the Sidewall Friction and Adhesion Testers (SFATs). In the SFT, the contact interface is formed between the plane (vertical) surface of a suspended beam and the cylindrical surface of an anchored post, and in the SFAT, it is formed between the plane (vertical) surfaces of two suspended shuttles. On each of the six Test Platform chips investigated, five Sidewall Friction Testers as well as five Sidewall Friction and Adhesion Testers are used to determine the engineering coefficient of static friction of their sidewall surfaces. While using each Sidewall Friction Tester, the engineering coefficient of static friction is determined at normal loads ranging from $2.4 \mu\text{N}$ - $15.7 \mu\text{N}$, which correspond to Hertzian contact pressures (calculated by considering cylinder on flat geometry) of 123 MPa - 312 MPa, using each Sidewall Friction and Adhesion Tester, the engineering coefficient of static friction is determined at normal loads ranging from $0.677 \mu\text{N}$ - $7.97 \mu\text{N}$, which correspond to apparent contact pressures (calculated by considering flat on flat geometry) of 0.098 MPa - 1.15 MPa. In order to obtain statistically significant results, the coefficient of static friction is determined five times at each investigated normal load, using both the SFTs as well as the SFATs. All the experiments that are conducted for this study are performed in laboratory air, at $22 \text{ }^\circ\text{C}$ and in 45% relative

humidity. The magnification of the objective lens used in the microscope during the actuation of SFTs and SFATs for this study is 10X. Accordingly, the size of each pixel in the field of view is $0.465 \mu\text{m} \times 0.465 \mu\text{m}$. Figure 9.11 is a plot showing the μ_s of the sidewall surfaces of all the six Test Platform chips, determined using both the SFTs as well as the SFATs. The data points plotted in the plot are arithmetic means of several measurements. The error bars shown in the plot indicate the maximum and minimum values of the engineering coefficient of static friction exhibited by the sidewall surfaces of that Test Platform chip. The close agreements between each of the μ_s determined using the SFTs and the corresponding μ_s determined using the SFATs indicates that the geometry of the contact interface does not have any influence on the effect that the surface topographies of the surfaces forming the interface have on its tribological characteristics.

9.5 Conclusions

In this study, I have successfully used a dodecanethiol-capped gold nanoparticle-based surface texturing technique to tailor the topographies of the surfaces (in-plane as well as sidewall) of five Test Platform chips. Additionally, I have successfully investigated six Test Platform chips (five textured using the dodecanethiol-capped gold nanoparticle-based surface texturing technique and one untextured (control)) to understand the effect that the surface topography of a surface has on its tribological (i.e., stiction and friction) characteristics. The surface topographies of the surfaces of each of the six Test Platform chips investigated in this study are characterized qualitatively using SEM and quantitatively using AFM. The qualitative characterization of the surface topographies of the surfaces of the six Test Platform chips investigated in this study confirmed that while on the same Test Platform chip, both the in-plane as well as sidewall surfaces have identical nanoparticle coatings on them, the surfaces of different Test Platform chips have distinct surface topographies. Additionally, it

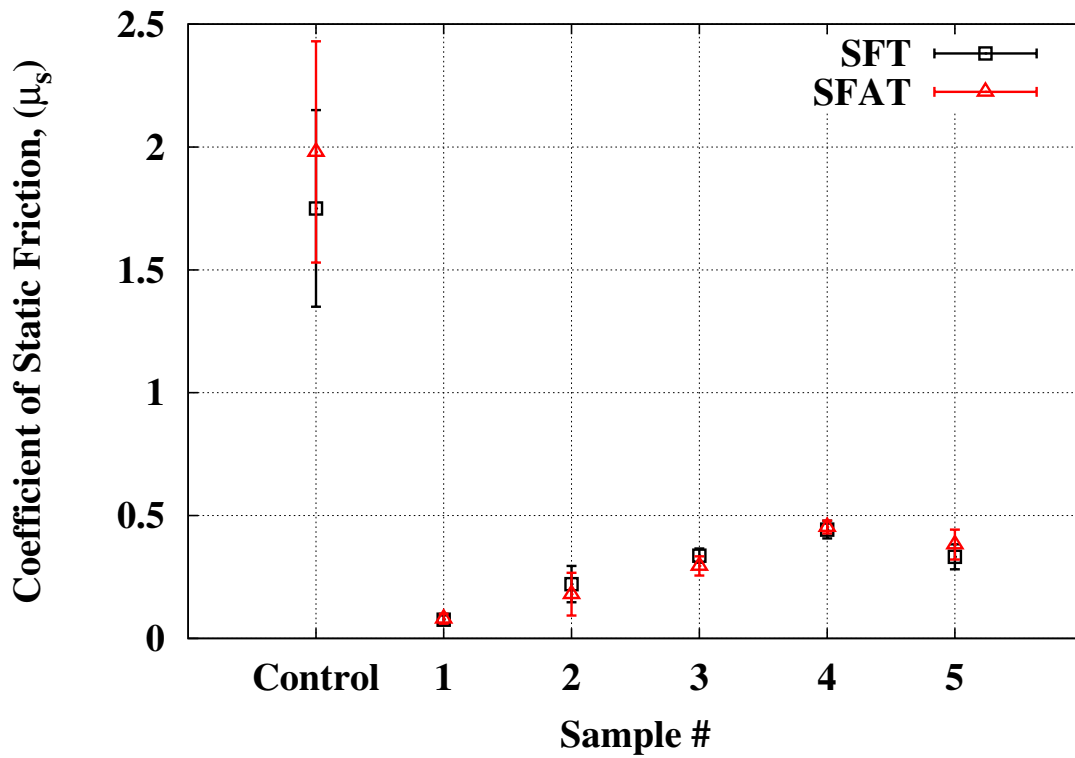


Figure 9.11: A plot showing the μ_s of the sidewall surfaces of all the six Test Platform chips, determined using both the SFTs as well as the SFATs. The data points plotted in the plot are arithmetic means of several measurements. The error bars shown in the plot indicate the maximum and minimum values of the engineering coefficient of static friction exhibited by the sidewall surfaces of that Test Platform chip. Notice the close agreements between the μ_s determined using the SFTs and those determined using the SFATs.

validated my hypothesis that the amount of the nanoparticles that get deposited on the surface being textured can be controlled by controlling the number density of the nanoparticle dispersion used. The quantitative characterization of the surface topographies of the surfaces of the six Test Platform chips investigated in this study is successfully used to quantify them in terms of two measurable parameters, namely, the rms roughness and the surface coverage of the interacting asperities present on the surface. Further, in order to understand the effects that the surface topography of a MEMS surface has on its stiction and friction characteristics, three important tribological properties of the surfaces of each of the six Test Platform chips investigated in this study, which are the apparent work of adhesion of the in-plane surfaces, the apparent work of adhesion of the sidewall surfaces and the coefficient of static friction of the sidewall surfaces, are determined. The tribological characterization of the surfaces of the six Test Platform chips investigated in this study provided an experimental confirmation of the already believed theory that the friction experienced by contacting MEMS surfaces shows a strong dependence on the stiction experienced by them. Additionally, it indicated that both the micro-scale as well as the nano-scale topographies of a surface have a strong influence on its stiction and friction characteristics.

In order to mathematically correlate the surface topography of a surface with its stiction and friction characteristics, a dimensionless parameter called Tribotopography number (i.e., τ_{topo}), which separately accounts for both the components that define the rms roughness of a surface, and can be used to predict the effect that the surface topography of a surface will have on its stiction and friction characteristics, is formulated in this study. Further, the Tribotopography number is successfully used to develop two mathematical correlations, one between the surface topography of a surface and its apparent work of adhesion, and the other between the surface topography of a surface and the friction experienced by it. In order to use the two

mathematical correlations developed in this study for a particular type of surface, the value of index α , which is the index of the denominator of the fraction that represents the Tribotopography number, for that type of surface must be determined first. The value of index α for silicon-type surfaces (i.e., surfaces, whose tribological behaviours are governed by the same types of interfacial forces that govern the tribological behaviour of silicon surfaces) is determined in this study. This study also reports an analysis (i.e., experimental validation), which substantiates the validities of the two mathematical correlations developed to correlate the surface topography of a surface with its stiction and friction characteristics, respectively. Additionally, it also discusses the constraints, under which, the two mathematical correlations are valid. The two mathematical correlations developed in this study can be used to quantitatively determine the effect that the surface topography of a surface will have on its stiction and friction characteristics. Lastly, in order to determine the influence of the geometry of the contact interface on the effect that the surface topographies of the surfaces forming the interface have on its tribological characteristics, the engineering coefficients of static friction of the sidewall surfaces of all the six Test Platform chips investigated in this study are determined using both the Sidewall Friction Testers (SFTs) as well as the Sidewall Friction and Adhesion Testers (SFATs). The results indicate that the geometry of the contact interface does not have any influence on the effect that the surface topographies of the surfaces forming the interface have on its tribological characteristics.

Chapter 10

A Simple Experimental Technique to Estimate the Surface Coverage of the Nanoparticle-based Monolayer Coatings Used to Texture MEMS Surfaces

10.1 Introduction

As explained in section 1.3, commercialization of an extremely large number of useful MEMS prototypes is hindered by their poor reliabilities, which are consequences of the dominance of surface phenomena such as stiction, friction and wear, at the micron scale. Therefore, a significant fraction of the research conducted by the MEMS community is focussed on devising strategies that can be used to improve the tribological characteristics of MEMS surfaces. One strategy that is being considered by the MEMS community for addressing the tribological issues that plague most MEMS devices consists of altering the surface topographies of MEMS surfaces by depositing nanoparticles on them [24, 27, 130]. Indeed, it has been demonstrated that the gold nanoparticle-based coatings significantly reduce the stiction experienced by in-plane polysilicon as well as silicon surfaces [24, 27, 130]. However, the reduction in stiction achieved by the different studies reported in literature are significantly different [24, 130, 156]. Based on the results obtained in the previous chapter, this can be attributed to the difference in the τ_{topo} of the test surfaces investigated in those studies. Accordingly, the effectiveness of a nanoparticle-based coating strongly depends on the τ_{topo} of the coated surface. Therefore, the surface coverage of the coating can serve as an effective parameter in the comparison between the effectivenesses of various nanoparticle-based (sub-)monolayer coatings. This study reports a simple experimental technique to determine the surface coverage of the nanoparticle-based monolayer coatings used to texture MEMS surfaces.

10.2 Estimation of Surface Coverage

The surface coverage of a nanoparticle-based (sub-)monolayer coating can be determined using the Resonator developed in this study. Details on the designs and actuation procedures of the Resonators included in the Test Platform developed in this study are given in section 5.3. Also derived in section 5.3.3, is the equation that can be used to determine the resonance frequencies of the Resonators included in the Test Platform developed in this study. The equation is reproduced here as Eq. 10.2.1 for completeness.

$$f_R = \frac{1}{2\pi} \sqrt{2E \frac{tw^3}{M_{eff}L^3}} \quad (10.2.1)$$

Here, f_R is the resonance frequency of the Resonator being tested, E is the elastic modulus of the structural film, t is the thickness of the structural film and w and L are the width and length of the supporting beams of the Resonator being tested, respectively and M_{eff} is the effective mass of the resonating structure. By differentiating both sides of Eq. 10.2.1 with respect to M_{eff} we get,

$$\Delta f_R = - \left[\frac{1}{4\pi} \sqrt{2Et \left(\frac{w}{L}\right)^3} \right] M_{eff}^{-3/2} \Delta M_{eff} \quad (10.2.2)$$

Rearranging Eq. 10.2.2 gives,

$$\Delta M_{eff} = -4\pi M_{eff}^{3/2} \left[2Et \left(\frac{w}{L}\right)^3 \right]^{-1/2} \Delta f_R \quad (10.2.3)$$

Here, Δf_R is the amount, by which, the resonance frequency of a Resonator developed in this study changes when the effective mass of its resonating structure changes by ΔM_{eff} and M_{eff} is the original effective mass of its resonating structure.

The deposition of nanoparticles on the surfaces of the Resonator increases the effective mass of its resonating structure, and as indicated by Eq. 10.2.1, decreases its resonance frequency. Therefore, by comparing the resonance frequencies of the

nanoparticle coated and uncoated Resonators having the same supporting beam length, the increase in the effective mass of the Resonator, which is due to the mass of the nanoparticles deposited on it, can be determined using Eq. 10.2.3. The t , w and L , which are the thickness, width and length of the supporting beams of the Resonator, respectively, are measured optically and Δf_R is given by Eq. 10.2.4 shown below:

$$\Delta f_R = f_R^{coated} - f_R^{uncoated} \quad (10.2.4)$$

Here, f_R^{coated} , which is the resonance frequency of the Resonator coated with nanoparticles is determined experimentally. The original effective mass of the resonating structure (i.e., M_{eff}) of the Resonator being tested can be given by the Rayleigh equation shown below:

$$M_{eff} = M_s + \frac{1}{4}M_t + \frac{12}{35}M_b \quad (10.2.5)$$

Here, M_s , M_t and M_b are the masses of the shuttle, the two trusses and the eight supporting beams of the Resonator being tested, respectively. M_s , M_t and M_b are determined using the dimensions of the corresponding components of the Resonator, which are measured optically. ΔM_{eff} , which represents the increase in the effective mass of a Resonator caused by the deposition of nanoparticles on it can be further decomposed into two components, as shown in Eq. 10.2.6 below:

$$\Delta M_{eff} = M_{eff}^{coated} - M_{eff}^{uncoated} \quad (10.2.6)$$

Here, $M_{eff}^{uncoated}$ is the effective mass of the resonating structure of the uncoated Resonator, which is the same as M_{eff} . M_{eff}^{coated} , which is the effective mass of the resonating structure of the coated Resonator, can be given by Eq. 10.2.7 shown below:

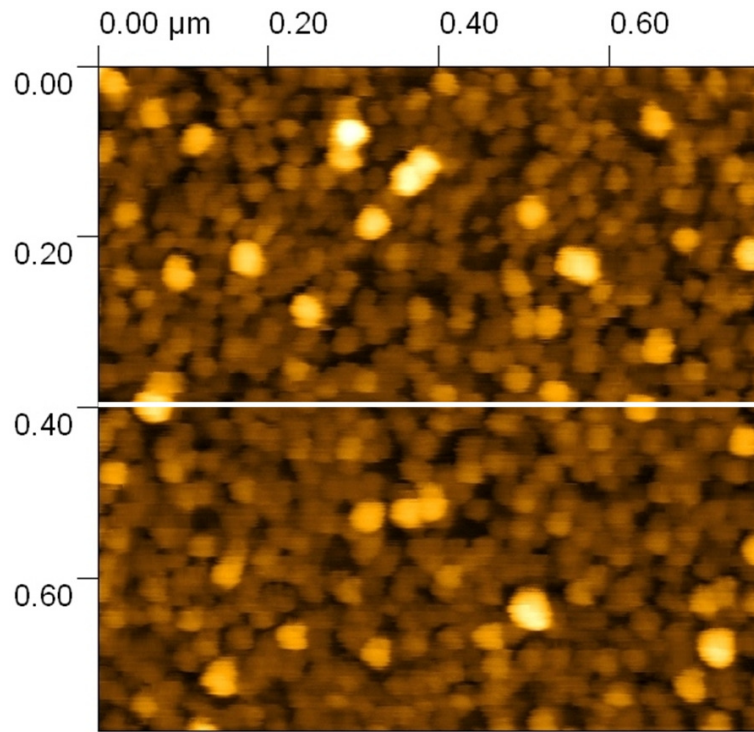
$$M_{eff}^{coated} = M_{eff}^{uncoated} + \eta \frac{2d_{np}\rho_{np}}{3} \left(A_s + \frac{1}{4}A_t + \frac{12}{35}A_b \right) \quad (10.2.7)$$

Here, A_s , A_t and A_b are the total surface areas of the shuttle, the two trusses and the eight supporting beams of the Resonator being tested, respectively, are determined using the dimensions of the corresponding components, which are measured optically. d_{np} and ρ_{np} are the mean diameter and density of the nanoparticles deposited on the Resonator being tested, and η is the surface coverage of the coating consisting of them. Substituting Eqs. 10.2.7 and 10.2.6 in Eq. 10.2.3 gives Eq. 10.2.8, which can be used to determine the surface coverage of a nanoparticle-based (sub-)monolayer coating.

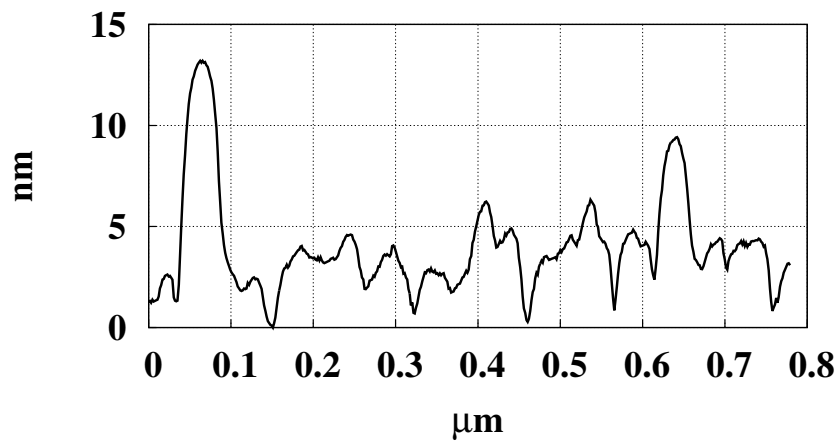
$$\eta \frac{2d_{np}\rho_{np}}{3} \left(A_s + \frac{1}{4}A_t + \frac{12}{35}A_b \right) = -4\pi M_{eff}^{3/2} \left[2Et \left(\frac{w}{L} \right)^3 \right]^{-1/2} \Delta f_R \quad (10.2.8)$$

10.3 Results

In order to experimentally test the technique discussed in the previous section, one Test Platform chip is released and coated with nanoparticles using the processes reported in sections 6.1 and 6.6, respectively. Again, the nanoparticles specifically used for this study are dodecanethiol-capped gold nanoparticles. The process used to synthesize the dodecanethiol-capped gold nanoparticles used in this study is described in detail in section 6.5. In order to burn-off the dodecanethiol capping ligands present on the gold nanoparticles deposited on the Test Platform chip before testing the Resonators on it, the Test Platform chip is exposed to an UV-ozone atmosphere for 1 hour before testing. The coated Test Platform chip is first characterized, using AFM. Figure 10.1a shows a high resolution AFM image of the top surface of one of the Resonators of the coated Test Platform chip. A linescan taken across the AFM image shown in Fig. 10.1a, which is shown in Fig. 10.1b, clearly confirms that the nanoparticle coating deposited on the Test Platform chip being investigated in this study is a sub-monolayer coating.



(a)



(b)

Figure 10.1: (a) A high resolution AFM image of the top surface of one of the Resonators of the coated Test Platform chip. The rms roughness of the surface shown in image a is 2.06 nm. The z-scale of image a is 13.8 nm. (b) Linescan along the white line drawn across image a.

In order to eliminate the error that is induced in the estimate of the surface coverage of a nanoparticle coating, by the errors (induced by the resolution of measurement) in the measured dimensions of the Resonator, two sets of five Resonators each are used in this study. All the Resonators belonging to the same set have supporting beams of the same length, and those belonging to different sets have supporting beams of different lengths. The two sets of Resonators that are used in this study include Resonators with supporting beam lengths of 200 μm (nominal) and 350 μm (nominal). Further, the five Resonators belonging to each of the two sets of Resonators tested in this study are selected from different locations on the coated Test Platform chip. All the Resonators are actuated in laboratory air, at 22 °C and in 45% relative humidity. The magnification of the objective lens used in the microscope for this study is 10X. Accordingly, the size of each pixel in the field of view is 0.465 $\mu\text{m} \times 0.465 \mu\text{m}$. The resonance frequencies of the Resonators tested in this study are determined optically, with an accuracy of ± 5 Hz. Table 10.1 reports the optically observed resonance frequencies of the two sets of Resonators tested in this study. Each resonance frequency reported in Table 10.1 is an arithmetic mean of five measurements, which are made using five distinct Resonators having the same supporting beam length. In order to obtain the surface coverage of the nanoparticle coating deposited on the Test Platform chip that is investigated in this study, Eq. 10.2.8 is fitted to the two experimentally obtained resonance frequencies reported in Table 10.1 using the elastic modulus (E) of the structural film and the surface coverage of the nanoparticle coating (i.e., η) as the fitting parameters. The values of ρ_{np} and d_{np} used for obtaining the surface coverage of the nanoparticle coating deposited on the Test Platform chip investigated in this study are 19300 Kg/m³ and 5.48 nm, respectively. The surface coverage of the nanoparticle coating represented by the AFM image shown in Fig. 10.1a is determined to be 89 %, which appears to be consistent with its appearance in the AFM image. The elastic modulus of the

AuNP coated structural film is determined to be 130 GPa, which is expected since the AuNP coating is discontinuous and so is not expected to alter the elastic modulus of the structural film of the Resonators used to determine its surface coverage.

The resolution, with which, the experimental technique presented in this study can determine the surface coverage of nanoparticle coatings is fixed by the resolution, with which, the resonance frequencies of the Resonators used to determine the surface coverage of nanoparticle coatings are determined. The resonance frequencies of the Resonators used in this study are determined by visually monitoring the amplitudes of their oscillations. Therefore, the resolution, with which, the resonance frequencies are determined in this study is ± 5 Hz. However, the use of a capacitance-measurement based technique for detecting the resonance of the Resonators can enable the determination of surface coverage of nanoparticle coatings with significantly high resolution. Further, it should be noted that the technique presented in this study can be used to determine the surface coverage of only sub-monolayer nanoparticle coatings because the derivation of Eq. 10.2.7 assumes that the entire change in the effective mass of the Resonator is caused by only a single layer of coating.

10.4 Conclusions

In this study, I have successfully demonstrated a simple technique based on optically determined resonance for determining the surface coverage of sub-monolayer nanoparticle coatings, which can be used to texture MEMS surfaces. The modeling as well as the experimental validation of the technique are presented in the study. The factor that defines the resolution of the technique is also discussed in the study. The surface coverage of the coating can serve as an effective parameter in the comparison between the effectivenesses of various nanoparticle-based (sub-)monolayer coatings. Unfortunately, the technique presented in this study can be used to determine the surface coverage of only sub-monolayer nanoparticle coatings.

Table 10.1: This table reports the optically observed resonance frequencies of the two sets of Resonators tested in this study. Each resonance frequency reported in the table is an arithmetic mean of five measurements, which are made using five distinct Resonators having the same supporting beam length.

Supporting Beam Length (μm)	Observed Resonance Frequency (KHz)
200	17.01 ± 0.005
350	8.276 ± 0.005

Chapter 11

Surface Texturing: A Potent Alternative to Reduce Stiction and Friction Experienced by MEMS Surfaces

This chapter reports on a novel gold nanoparticle (AuNP) coating, which is deposited on micro-electromechanical systems (MEMS) surfaces using the gas-expanded liquid technique, and has the potential to be used as an alternative of OTS SAM for reducing the stiction and friction experienced by them. A complete characterization of the AuNP coating is presented in this chapter. The AuNP coating is characterized using atomic force microscopy (AFM) and several microinstruments developed in this study. Surface coverage of the AuNP coating, which is determined using the Resonator developed in this study; and the tribological properties including the work of adhesion, the coefficients of static and kinetic friction and the apparent rupture strength of the AuNP coating, which are determined using the Cantilever Beam Array, the Sidewall Beam Array and the Sidewall Friction and Adhesion Tester developed in this study, respectively, are reported in this chapter.

11.1 Introduction

Despite years of research, the MEMS community is yet to find a solution that sufficiently addresses the reliability issues that limit the commercial success of a wide spectrum of useful MEMS prototypes. Further, the continuously increasing number of smaller, more complex and more useful new MEMS is making the already dire need of improving the tribological behaviour of MEMS interfaces even more pressing. To-date, while several approaches that alter the chemical composition of MEMS surfaces have been significantly investigated, very little attention has been paid to approaches

that alter the topography of MEMS surfaces. This chapter reports a novel gold nanoparticle (AuNP) coating that significantly reduces stiction and friction between MEMS surfaces by texturing them.

Initial investigations that probed the potential of surface texturing to improve MEMS reliability altered the topography of MEMS surfaces by etching them in wet anisotropic etchants. These investigations, which only studied the effect of surface texturing on stiction between in-plane MEMS surfaces, reported that surface texturing reduced the stiction experienced by in-plane surfaces by a moderate factor of 20 [127]. In 2006, when DelRio *et al.* studied the effect of the presence of silicon carbide (SiC) particles (diameter ranging between 20-50 nm) on polysilicon-based contacting MEMS surfaces on the (in-use, in-plane) stiction experienced by them, and reported that the deposition of nanoparticles (NPs) on contacting MEMS surfaces can significantly reduce the stiction between them, NPs emerged as a new tool that can be used to texture MEMS surfaces [27]. However, the nanoparticles that textured the MEMS test surfaces that were used in the investigations conducted by DelRio *et al.* were adventitiously formed on them (i.e., the particles were not deposited intentionally) by a side reaction during the sacrificial layer growth, and a process to controllably deposit NPs on MEMS surfaces was not available at that time [24, 27]. A process to controllably deposit AuNPs on MEMS was only recently reported by Hurst *et al.*, who studied the effect of dodecanethiol-capped AuNP-based surface texturing on the stiction experienced by the in-plane polysilicon surfaces and reported about 100X reduction in in-plane stiction [24].

Due to the fact that each of the past studies, which investigated the effect of nanoparticle (NP) based surface texturing, reported only moderate reduction in stiction between textured in-plane surfaces, I postulated that the effectivenesses of the nanoparticle-based coatings investigated in them were reduced by the grain-boundary induced inherent roughness of the polysilicon test surfaces used in them. Therefore,

I investigated the effect of AuNP-based surface texturing on the stiction experienced by relatively smooth single crystal silicon in-plane surfaces [130]. My investigations revealed that the effectiveness of AuNP-based surface texturing not only depends on the inherent roughness of the test surfaces but also depends strongly on the surface coverage of the coating (refer to results reported in Chapter 9). In this chapter, I report the reduced stiction experienced by the relatively smooth single crystal silicon in-plane MEMS surfaces textured using the AuNP coating with the most effective surface coverage. Further, the effect of the same AuNP coating on the stiction as well as friction experienced sidewall surfaces is reported. Surface coverage and apparent rupture strength of the studied AuNP coating are also reported in the chapter.

11.2 Experimental Details

11.2.1 Coatings

The test chip (i.e., the Test Platform chip coated with the AuNP coating that is investigated in this study) used in this study is released and coated with AuNPs using the processes reported in sections 6.1 and 6.6, respectively. The amount of concentrated dodecanethiol-capped AuNP dispersion (in hexane) added to the vial, in which, the test chip is placed for coating, to obtain the AuNP coating investigated in this study is $2.5 \mu\text{l}$. The dodecanethiol-capped gold nanoparticles used in this study are also synthesized using the process described in detail in section 6.5. In order to burn-off the dodecanethiol capping ligands present on the gold nanoparticles deposited on the Test Platform chip, the Test Platform chip is exposed to an UV-ozone atmosphere for 1 hour before testing.

Two different control chips are used in this study. While both of them are released using the same process, which is reported in section 6.1, one of them (control chip I) is further subjected to the process reported in section 6.2 while the other (control chip II) is further subjected to the process reported in section 6.4. Accordingly, the

test surfaces of one control chip are covered with only native oxide, while those of the other are coated with OTS SAM.

11.2.2 Microinstruments Used

The surface coverage of the AuNP coating investigated in this chapter is determined using the technique reported in chapter 10. The two sets of Resonators that are used for determining the surface coverage of the AuNP coating investigated in this chapter include Resonators with supporting beam lengths of 200 μm (nominal) and 350 μm (nominal). Both the sets of Resonators used in this study consist of five Resonators each, which are selected from different locations on the test chip. The magnification of the objective lens used in the microscope during the actuation of the Resonators used in this study is 10X. Accordingly, the size of each pixel in the field of view is 0.465 $\mu\text{m} \times 0.465 \mu\text{m}$. The resonance frequencies of the Resonators tested in this study are determined optically, with an accuracy of ± 10 Hz.

The reduction in the stiction experienced by the in-plane surfaces of the Test Platform due to the AuNP coating investigated in this chapter is determined by determining the apparent works of adhesion of the in-plane surfaces of the test as well as control chips. The apparent works of adhesion of the in-plane surfaces of the Test Platform chips (i.e, the test chip and the two control chips) investigated in this chapter are determined using the Cantilever Beam Array developed in this study. Details on the design and actuation procedure of the Cantilever Beam Arrays included in the Test Platform developed in this study are given in section 5.4. The magnification of the objective lens, which is used in the interference microscope that is used to determine the height profile of the actuated cantilever beams, is either 10X or 20X. Accordingly, the size of each pixel in the field of view is either 0.465 $\mu\text{m} \times 0.465 \mu\text{m}$ or 0.234 $\mu\text{m} \times 0.234 \mu\text{m}$, respectively. On each Test Platform chip

investigated in this chapter, four CBAs consisting of ten cantilever beams each are actuated to obtain a statistically significant data set.

The reduction in the stiction experienced by the sidewall surfaces of the Test Platform due to the AuNP coating investigated in this chapter is determined by determining the apparent works of adhesion of the sidewall surfaces of the test as well as control chips. The apparent works of adhesion of the sidewall surfaces of the Test Platform chips (i.e, the test chip and the two control chips) investigated in this chapter are determined using the Sidewall Beam Array developed in this study. Details on the design and actuation procedure of the Sidewall Beam Arrays included in the Test Platform developed in this study are given in section 5.5. The magnification of the objective lens of the microscope, which is used to observe the microinstrument during actuation and determine the crack length of each actuated adhered pair of sidewall beams, is 10X. Accordingly, the size of each pixel in the field of view is $0.465 \mu\text{m} \times 0.465 \mu\text{m}$. On each Test Platform chip investigated in this chapter, eight SBAs are actuated to obtain a statistically significant data set.

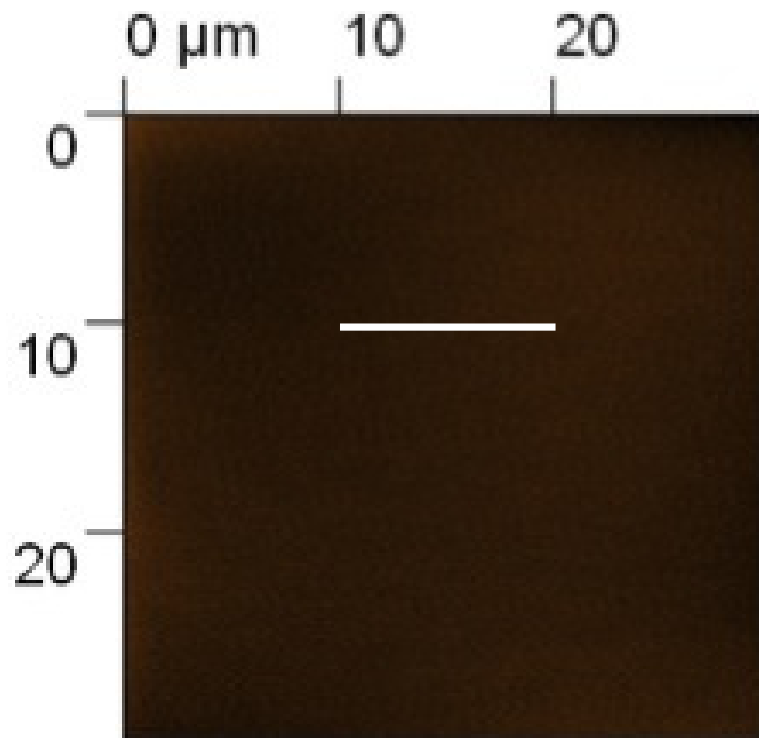
The reduction in the friction experienced by the surfaces of the Test Platform due to the AuNP coating investigated in this chapter is determined by determining the engineering coefficients of static and kinetic friction of the sidewall surfaces of the test as well as control chips. The engineering coefficients of static and kinetic friction of the contacting sidewall surfaces of the Test Platform chips (i.e, the test chip and the two control chips) investigated in this chapter are determined using the Sidewall Friction and Adhesion Tester developed in this study. Details on the design and actuation procedure of the Sidewall Friction and Adhesion Tester developed in this study are given in section 5.7. The magnification of the objective lens used in the microscope during the actuation of the Sidewall Friction and Adhesion Testers for this study is 10X. Accordingly, the size of each pixel in the field of view is $0.465 \mu\text{m} \times 0.465 \mu\text{m}$. On each Test Platform chip investigated, five Sidewall Friction and Adhesion Testers

are used to determine the engineering coefficients of static and kinetic friction of its sidewall surfaces. Using each Sidewall Friction and Adhesion Tester, the engineering coefficients of static and kinetic friction are determined at normal loads ranging from $0.677 \mu\text{N}$ - $3.28 \mu\text{N}$, which correspond to apparent contact pressures (calculated by considering flat on flat geometry) of 0.098 MPa - 0.473 MPa . Additionally, in order to obtain statistically significant results, the coefficients of friction are determined five times at each investigated normal load.

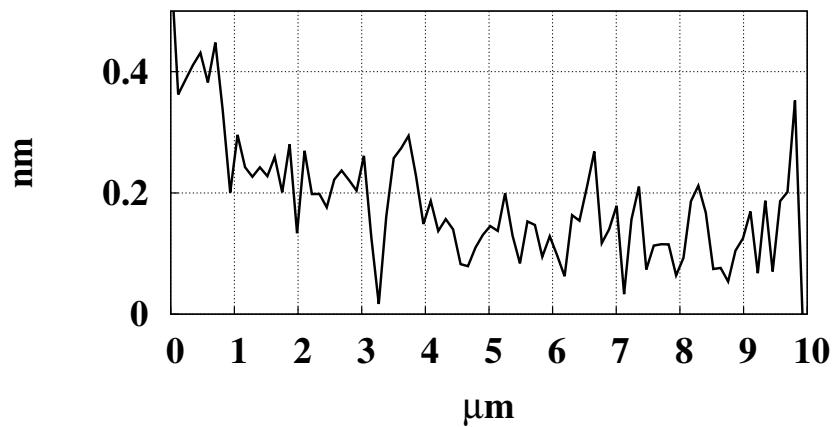
11.3 Results and Discussion

11.3.1 Topographical Properties of the AuNP Coating

The topography of the AuNP coated surfaces of the test chip is characterized using an atomic force microscope (AFM). Figures 11.1a and 11.2a are AFM images of the native oxide covered (uncoated) substrate of the control chip I and the AuNP coated substrate of the test chip, respectively. It is clearly evident from Figs. 11.1a and 11.2a that the AuNP coating significantly increases the roughness of the surfaces coated with it. While the substrate of the control chip I is extremely smooth (rms roughness is 0.097 nm), the AuNP coated substrate shown in Fig. 11.2a has a significant rms roughness of 8.3 nm . The mean peak/valley ratio (obtained from the linescan shown in Figure 11.2b) of the topography of the AuNP coated substrate, which is shown in Fig. 11.2a, is about 5 nm , which compares well with the mean diameter of the AuNPs used to coat the test chip. This indicates that the topmost layer of AuNPs deposited on the surfaces of the test chip has a sub-monolayer coverage. The surface coverage, which is determined using the Resonators, of the AuNP coating deposited on the test chip is determined to be 16% , which appears to be consistent with its appearance in the AFM image (i.e., Fig. 11.2)a.

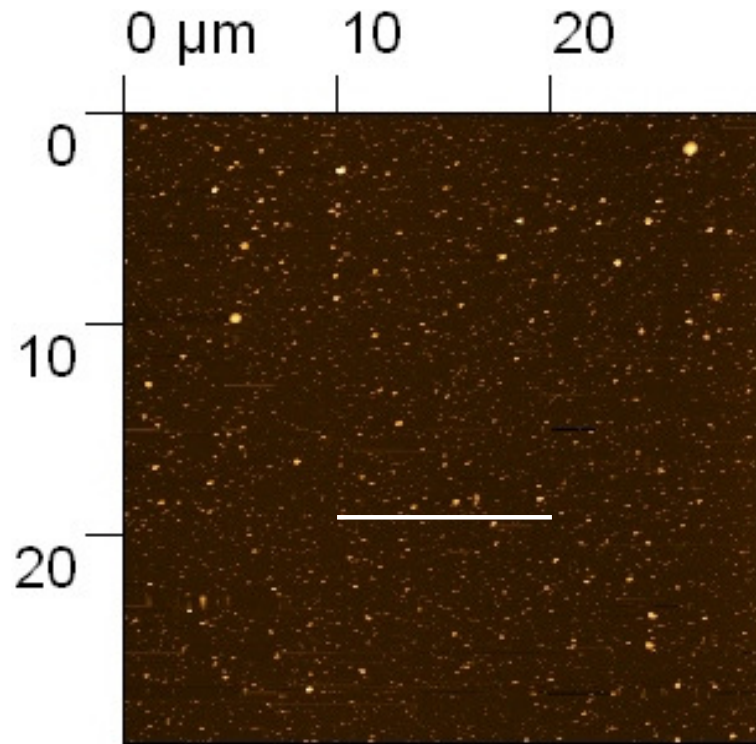


(a)

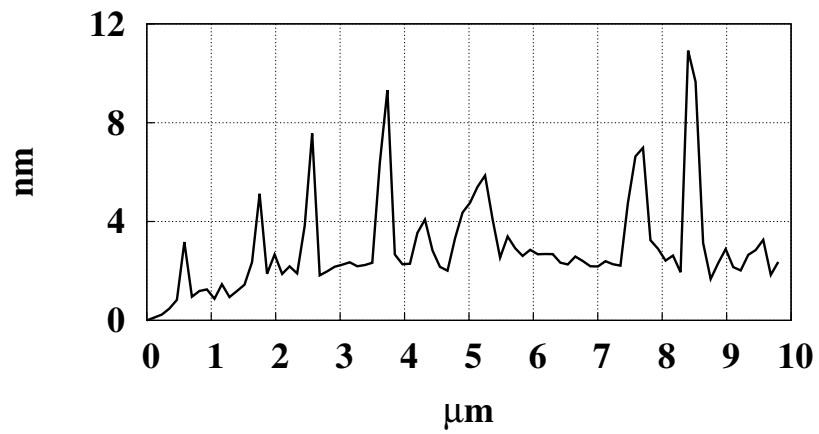


(b)

Figure 11.1: (a) AFM image of the native oxide covered uncoated substrate of the control chip I. The rms roughness of the surface shown in image a is 0.097 nm. (b) Linescan along the white line drawn across image a.



(a)



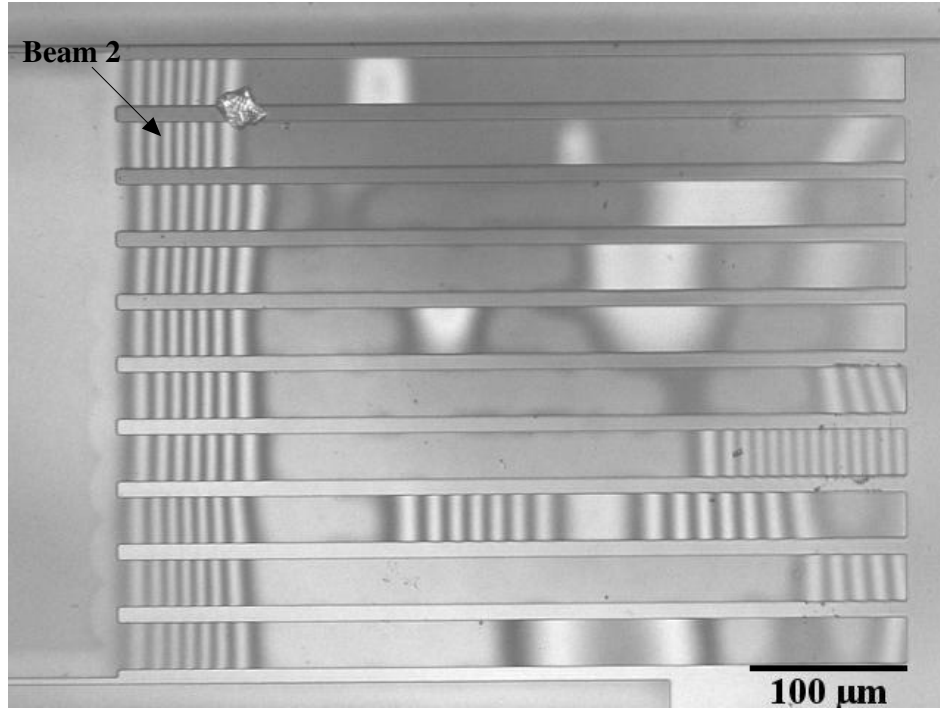
(b)

Figure 11.2: (a) AFM image of the AuNP coated substrate of the test chip. The rms roughness of the surface shown in image a is 8.3 nm. (b) Linescan along the white line drawn across image a.

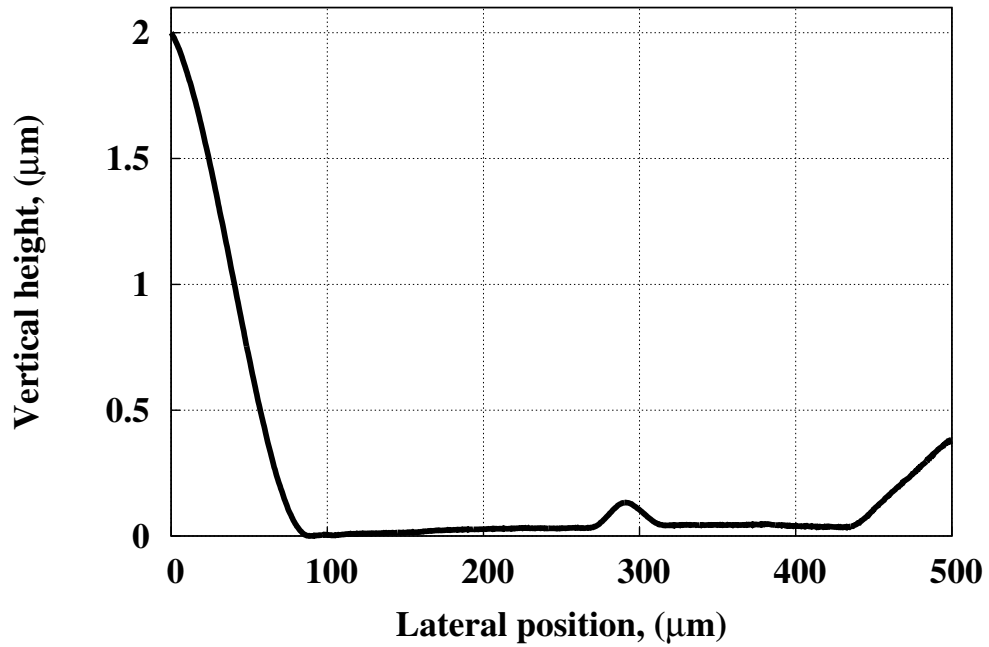
11.3.2 Tribological Properties of the AuNP Coating

The tribological properties of the AuNP coating deposited on the test chip that are characterized in this study include the apparent work of adhesion of coated in-plane surfaces, the apparent work of adhesion of coated sidewall surfaces, the engineering coefficients of static and kinetic friction of coated sidewall surfaces and its apparent rupture strength. All the results reported in this study are obtained in laboratory air, at 22 °C and in 45% relative humidity. Figures 11.3a and 11.4a are interferograms showing one tested Cantilever Beam Array of the control chip I and the test chip, respectively. It is clearly evident from Figs. 11.3a and 11.4a that the AuNP coating significantly increases the crack length exhibited by the in-plane surfaces. The increased crack length exhibited by the AuNP coated in-plane surfaces is further substantiated by the experimentally obtained (PSI derived) height profiles shown in Figs. 11.3b and 11.4b, which indicate that the uncoated in-plane surfaces of the control chip I exhibit a crack length of less than 100 μm , while the AuNP coated in-plane surfaces of the test chip exhibit a crack length of close to 850 micron. The apparent works of adhesion of the sidewall surfaces investigated in this study are determined using the Sidewall Beam Array. Figures 11.5a and 11.5b are optical images showing the five longest sidewall beam pairs of a released Sidewall Beam Array of the test chip, collected before and after actuating the Sidewall Beam Array, respectively. It is clearly evident from Figs. 11.5a and 11.5b that the crack length exhibited by the AuNP coated sidewalls is also significantly large.

Table 11.1 lists the critical tribological properties of the native oxide covered hydrophilic surfaces of the control chip I, the OTS SAM coated hydrophobic surfaces of the control chip II and the AuNP coated surfaces of the test chip. All the values reported in Table 11.1 are arithmetic means of several measurements and sd is one standard deviation of the sample consisting of those measurements. It is clearly evident from the \mathcal{W}_{ip} reported in Table 11.1 that the AuNP coated in-plane surfaces

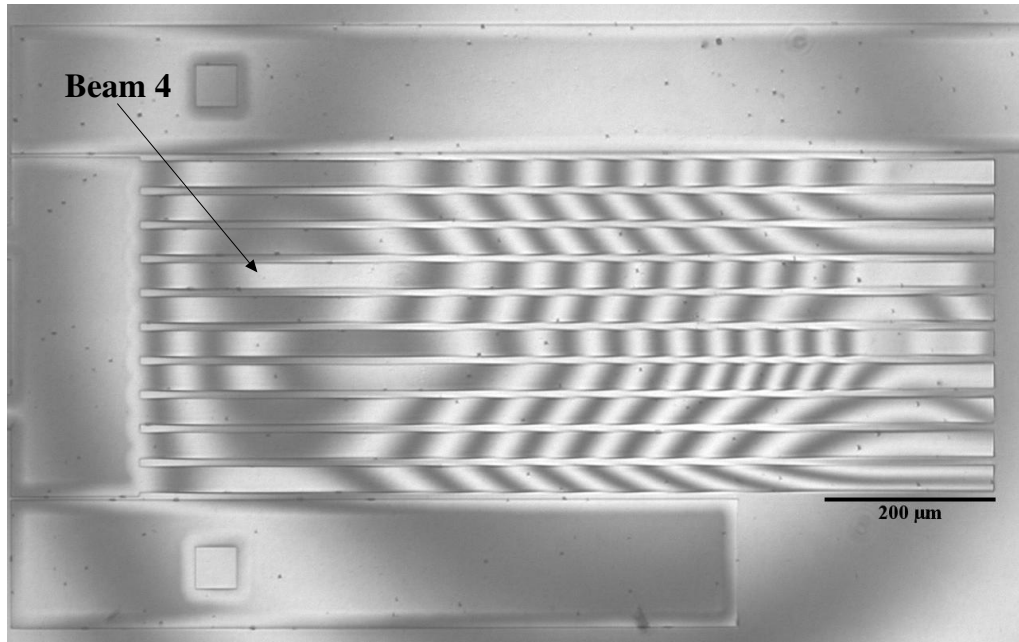


(a)

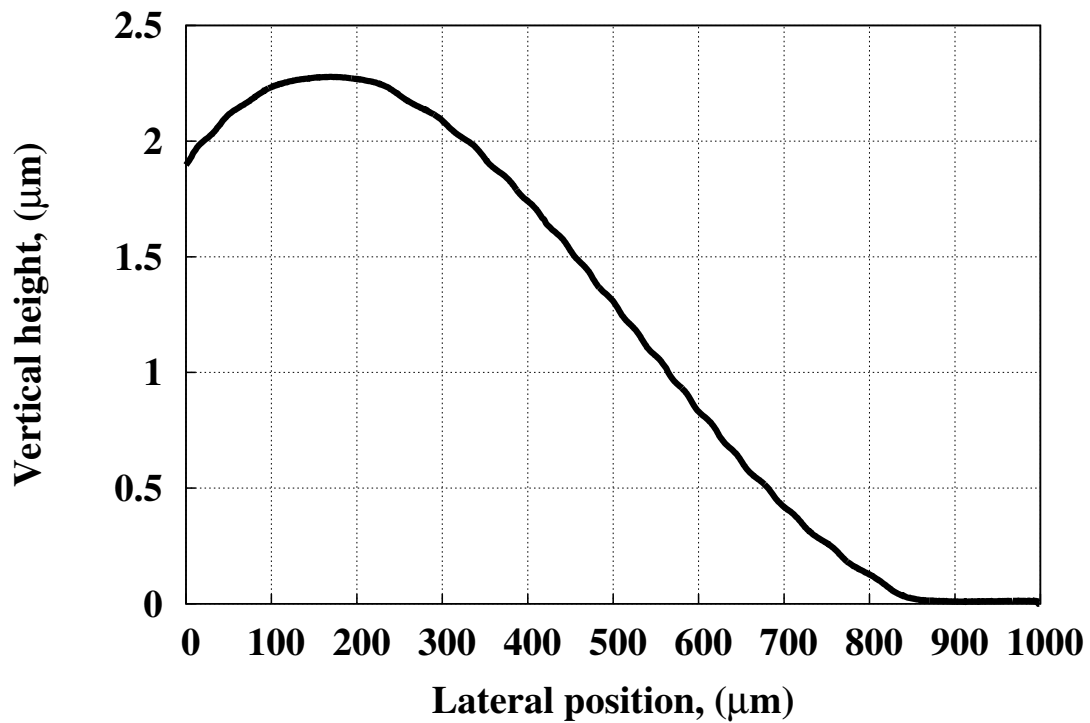


(b)

Figure 11.3: (a) An interferogram showing a tested Cantilever Beam Array of the control chip I. (b) Experimentally determined height profile of beam 2 labelled in image a. The height profile is determined using phase shifting interferometry. Notice that the crack of beam 2 labelled in image a is less than $100 \mu\text{m}$.

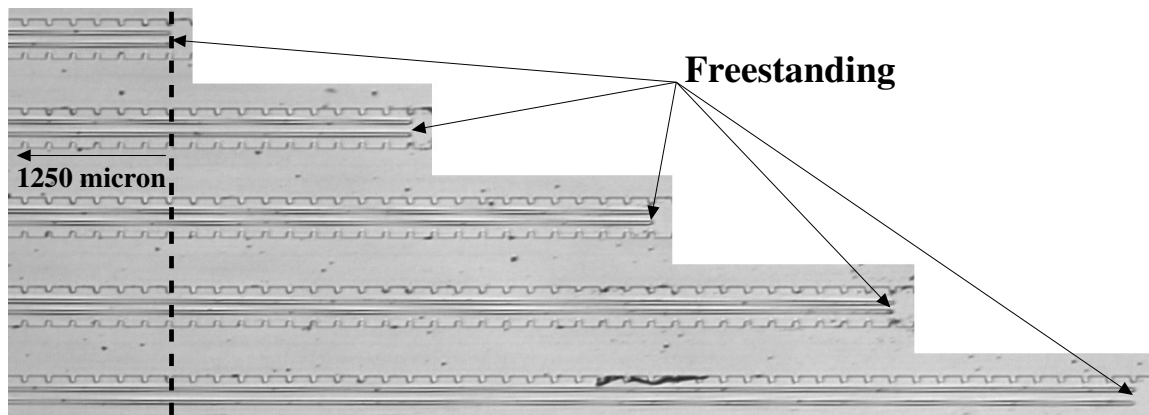


(a)

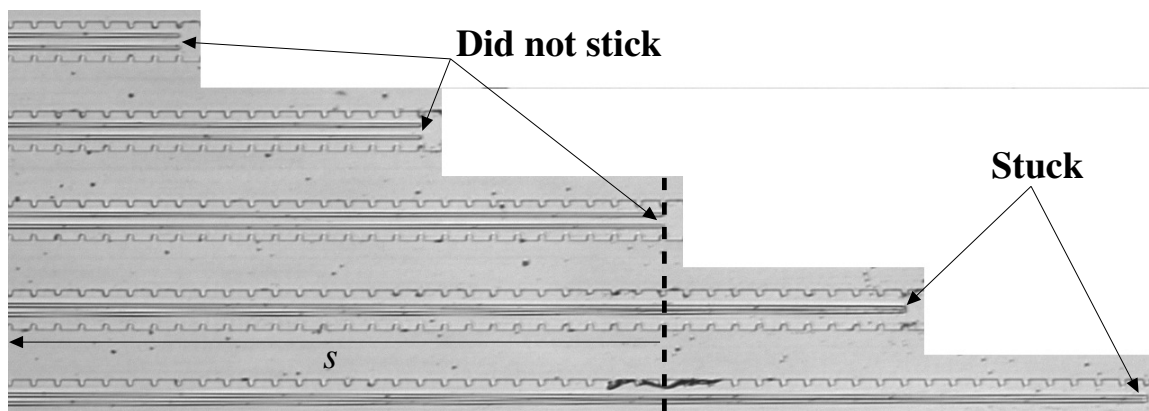


(b)

Figure 11.4: (a) An interferogram showing a tested Cantilever Beam Array of the test chip. (b) Experimentally determined height profile of beam 4 labelled in image a. The height profile is determined using phase shifting interferometry. Notice that the crack of beam 4 labelled in image a is close to $850 \mu\text{m}$.



(a)



(b)

Figure 11.5: (a) Optical image showing the five longest sidewall beam pairs of a released Sidewall Beam Array of the test chip, collected before actuating the Sidewall Beam Array. Notice that the sidewall beams of each of the five sidewall beam pairs shown in this image are apart from each other. (b) Optical image of the Sidewall Beam Array shown in image a, collected after actuating it. Notice that the sidewall beams of the three shorter sidewall beam pairs shown in this image peeled apart completely, while those of the two longer sidewall beam pairs remained stuck, after actuation.

exhibit a factor of 1000 reduction in the stiction experienced by the uncoated native oxide covered in-plane surfaces of the control chip I. Further, the AuNP coated sidewalls also exhibit a factor of 50 reduction in the stiction experienced by the uncoated native oxide covered sidewall surfaces of the control chip I. It should be noted that although the reduction in \mathcal{W}_s is less than that in \mathcal{W}_{ip} , the absolute value of the \mathcal{W}_s of the AuNP coated sidewalls is significantly low, and marginally lower than the \mathcal{W}_{ip} of the corresponding AuNP coated in-plane surfaces. The engineering coefficients of both static as well as kinetic friction of the AuNP coated sidewalls, which are 0.08 (mean) and 0.07 (mean), respectively, are also significantly smaller than those of the native oxide covered sidewalls of the control chip I, which are 1.98 (mean) and 1.35 (mean), respectively. Additionally, the results reported in Table 11.1 indicate that the stiction and friction properties of the AuNP coated surfaces are marginally better than those of the corresponding OTS SAM coated surfaces too.

In order to determine the rupture strength of the AuNP coating investigated in this study, a SFAT is used to determine μ_s of the AuNP coated sidewalls at different normal loads. The normal loads tested for this study range from $0.677 \mu\text{N}$ - $4.43 \mu\text{N}$, which correspond to apparent contact pressures (calculated by considering flat on flat geometry) of 0.098 MPa - 0.64 MPa . The normal applied at the sidewall interface is first increased from $0.677 \mu\text{N}$ to $4.43 \mu\text{N}$ and then decreased back to $0.677 \mu\text{N}$. At each investigated normal load, the μ_s of the AuNP coated contacting sidewalls is determined five times. The normal load, at which, the μ_s of the AuNP coated sidewalls increases irreversibly is considered as the rupture strength of the AuNP coating. Figure 11.6 shows a plot of the (mean) μ_s of the AuNP coated contacting sidewalls versus the corresponding voltage applied to the comb-drive actuator of the normal arm. The arrows shown in the plot indicate the direction, in which, the normal load applied at the sidewall interface of the SFAT used for this study is changed. It is clearly evident in the plot that the (mean) μ_s of the AuNP coated contacting

Table 11.1: Comparison between the critical tribological properties of the native oxide covered hydrophilic surfaces of the control chip I, the OTS SAM coated hydrophobic surfaces of the control chip II and the AuNP coated surfaces of the test chip. All the values reported in the table are arithmetic means of several measurements and sd is one standard deviation of the sample consisting of those measurements.

Coating	$\mathcal{W}_{ip} \pm \text{sd}$ ($\mu\text{J}/\text{m}^2$)	$\mathcal{W}_s \pm \text{sd}$ ($\mu\text{J}/\text{m}^2$)	$\mu_s \pm \text{sd}$	$\mu_k \pm \text{sd}$
Oxide	38700 ± 9300	1070 ± 60	1.98 ± 0.45	1.35 ± 0.2
OTS	45.46 ± 1	37.65 ± 1	0.155 ± 0.03	0.13 ± 0.01
AuNP	32.16 ± 3	21.50 ± 3	0.081 ± 0.02	0.072 ± 0.01

sidewalls changed irreversibly when a voltage of 77 V (i.e., V_r) is applied to the comb-drive actuator of the normal arm. The normal load applied at the sidewall interface when the voltage V_r is applied to the normal comb-drive actuator is $3.5 \mu\text{N}$, which corresponds to an apparent contact pressure (calculated by considering flat on flat geometry) of 500 kPa. Therefore, the apparent rupture strength of the AuNP coating investigated in this chapter is 500 kPa.

11.4 Conclusions

In this study, I have successfully characterized the topography and the critical tribological properties of a AuNP coating that is extremely effective in reducing the stiction and friction experienced by MEMS surfaces. The AuNP coating investigated in this study significantly increased the roughnesses of the surfaces coated with it. It has a surface coverage of 16 % and an apparent rupture strength of 500 kPa. The in-plane surfaces coated with the AuNP coating investigated in this study exhibit a reduced apparent work of adhesion of $32.16 \pm 3 \mu\text{J}/\text{m}^2$, and the sidewall surfaces coated with it exhibit a reduced apparent work of adhesion of $21.50 \pm 3 \mu\text{J}/\text{m}^2$ and reduced engineering coefficients of static and kinetic friction of 0.081 ± 0.02 and 0.072 ± 0.01 , respectively. The AuNP coating reduces the stiction experienced by the native oxide covered hydrophilic in-plane surfaces by a factor of 1000, and that experienced by the native oxide covered hydrophilic sidewall surfaces by a factor of 50.

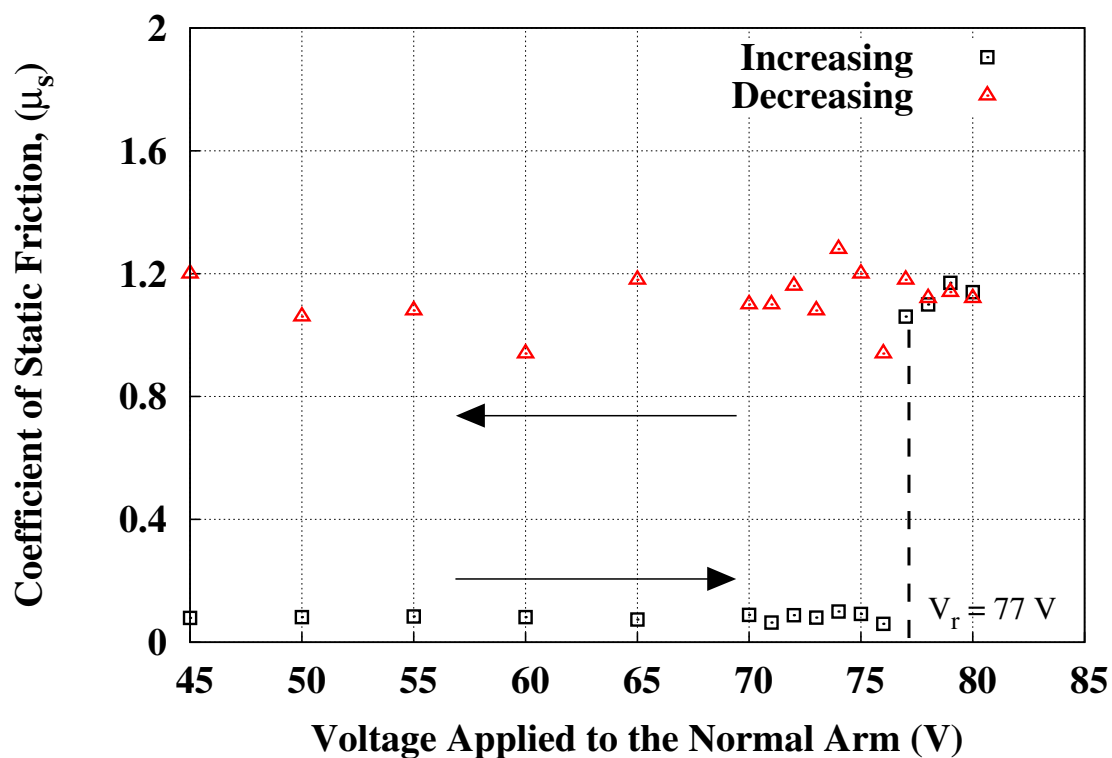


Figure 11.6: A plot of the (mean) μ_s of the AuNP coated contacting sidewalls versus the corresponding voltage applied to the comb-drive actuator of the normal arm. The arrows shown in the plot indicate the direction, in which, the normal load applied at the sidewall interface of the SFAT used for this study is changed. Notice that the (mean) μ_s of the AuNP coated contacting sidewalls changed irreversibly when a voltage of 77 V is applied to the normal comb-drive actuator.

Chapter 12

Summary

12.1 The Test Platform

This study reports on the successful development of a test platform (TP), which not only overcomes the limitations of the previously reported test platforms but is also a versatile tool that can be used to systematically study the tribology of MEMS surfaces. The details of the design and fabrication of the Test Platform are discussed in the study. The Test Platform is fabricated using a SOI (silicon-on-insulator) wafer, due to which, the material properties of its structural film do not vary at all. The use of a single crystal structural film (i.e., Si(100)) for fabricating the Test Platform also ensures that the topographies of the surfaces (in-pane as well as sidewall) of the microinstruments included in it also do not vary from chip to chip. Further, in order to be able to fabricate the TP using a facile, inexpensive and less time consuming fabrication process, a single mask scheme is devised in this study for fabricating the Test Platform. All the microinstruments of the Test Platform are fabricated on a 1 cm \times 1 cm SOI chip. Additionally, in order to ensure that the sidewall surfaces of the microinstruments included in the Test Platform are relatively smooth so that a systematic investigation of the effects that the surface topographies of MEMS surfaces have on their stiction and friction characteristics can be conducted, a polishing technique to smoothen the scalloped as-fabricated sidewalls of the Test Platform is developed in this study. The polishing technique developed in this study yields relatively much smoother sidewall surfaces.

In order to be able to systematically investigate, and establish a meaningful and reliable correlation between, the effects that a particular factor has on the different tribological properties (i.e., stiction, friction and wear) of MEMS surfaces, seven different types of microinstruments are included in the Test Platform. Their dimensions are determined keeping in mind that fabricating all of them on the same chip should not cause any issues during the release of the Test Platform. The test platform (TP) has microinstruments that can be used to determine several different material properties of the structural film. The Residual Stress Tester (RST) can be used to determine the residual stress present in a released device layer (structural film). The Mechanical Strength Tester (MST) can be used to determine the fracture strength of the device layer. The “Resonator” can be used to determine the elastic modulus of the device layer. Additionally, the Test Platform has a microinstrument (i.e., Cantilever Beam Array (CBA)) that can be used to study the stiction characteristics of the in-plane surfaces. Although, most of the tribological studies reported to-date have been conducted using in-plane surfaces, in devices belonging to several of the emerging classes of MEMS such as microgears and microsliders, more vertical (sidewall) surfaces come into contact during operation than horizontal (in-plane) surfaces, and findings of investigations carried out using in-plane interfaces are not applicable to sidewall interfaces [78,79,126,142]. Therefore, microinstruments in which sidewalls form the test interface are needed to study the tribological behaviour of sidewall interfaces. The Test Platform developed in this study conveniently addresses this need. It has different microinstruments for studying the stiction characteristics of in-plane and sidewall surfaces. While, as mentioned before, the CBA can be used to study the stiction characteristics of the in-plane surfaces, the stiction characteristics of the sidewall surfaces can be studied using the Sidewall Beam Array (SBA). Lastly, the Test Platform has two different microinstruments (i.e., the Sidewall Friction Tester (SFT) and the Sidewall Friction and Adhesion Tester (SFAT)) that can be used to

study the friction as well as wear characteristics of the sidewall surfaces. The purpose behind including two different microinstruments for studying the friction and wear characteristics of sidewall surfaces is to determine the influence of the geometries of the surfaces forming the contact interface on the effect of surface topography.

12.2 Microinstruments

The designs, actuation procedures and modeling of each of the seven types of microinstruments included in the Test Platform are explained in detail in this study. The details of the key features of all the (seven types of) microinstruments are successfully highlighted in this study. Additionally, some of the microinstruments developed in this study are convincingly shown to overcome some of the limitations of the previously reported corresponding microinstruments. Further, all the (seven types of) microinstruments developed in this study are successfully used to investigate two standard test surfaces, namely, surfaces coated with *n*-OTS ($C_{18}H_{37}SiCl_3$) SAM coating (i.e., hydrophobic surfaces) and surfaces having only a layer of native oxide on them (i.e., hydrophilic surfaces). The results obtained are compared with the corresponding results reported in literature. The comparisons substantiate the consistency and reliability of the results obtained using the Test Platform developed in this study. Additionally, the apparent work of adhesion of the OTS SAM coated sidewalls, which has never been reported to-date, is obtained in this study using the Sidewall Beam Array. The apparent work of adhesion of the OTS SAM coated sidewalls is $37.65 \mu J/m^2$. Also, the engineering coefficients of static and kinetic friction of the OTS SAM coated sidewalls, which have also never been reported to-date, are obtained in this study using both the Sidewall Friction Tester as well as the Sidewall Friction and Adhesion Tester. The mean engineering coefficients of static and kinetic friction of the OTS SAM coated sidewalls are 0.15 and 0.11, respectively.

12.3 Effect of Surface Topography

The investigation conducted to study the effect of surface topography reports the successful use of a dodecanethiol-capped gold nanoparticle-based surface texturing technique for tailoring the topographies of the surfaces (in-plane as well as sidewall) of five Test Platform chips. Additionally, it reports the successful investigation of six Test Platform chips (five textured using the dodecanethiol-capped gold nanoparticle-based surface texturing technique and one untextured (control)) conducted to understand the effect that the surface topography of a surface has on its tribological (i.e., stiction and friction) characteristics. The surface topographies of the surfaces of each of the six Test Platform chips investigated in this study are characterized qualitatively using SEM and quantitatively using AFM. The qualitative characterization of the surface topographies of the surfaces of the six Test Platform chips investigated in this study confirmed that while on the same Test Platform chip, both the in-plane as well as sidewall surfaces have identical nanoparticle coatings on them, the surfaces of different Test Platform chips have distinct surface topographies. Additionally, it validated the hypothesis proposed in this study that the amount of the nanoparticles that get deposited on the surface being textured can be controlled by controlling the number density of the nanoparticle dispersion used. The quantitative characterization of the surface topographies of the surfaces of the six Test Platform chips investigated in this study is successfully used to quantify them in terms of two measurable parameters, namely, the rms roughness and the surface coverage of the interacting asperities present on the surface. Further, in order to understand the effects that the surface topography of a MEMS surface has on its stiction and friction characteristics, three important tribological properties of the surfaces of each of the six Test Platform chips investigated in this study, which are the apparent work of adhesion of the in-plane surfaces, the apparent work of adhesion of the sidewall surfaces and the engineering coefficient of static friction of the sidewall surfaces, are

determined. The tribological characterization of the surfaces of the six Test Platform chips investigated in this study provided an experimental confirmation of the already believed theory that the friction experienced by contacting MEMS surfaces shows a strong dependence on the stiction experienced by them. Additionally, it indicated that both the micro-scale as well as the nano-scale topographies of a surface have a strong influence on its stiction and friction characteristics.

In order to mathematically correlate the surface topography of a surface with its stiction and friction characteristics, a dimensionless parameter called Tribotopography number (i.e., τ_{topo}), which separately accounts for both the components that define the rms roughness of a surface, and can be used to predict the effect that the surface topography of a surface will have on its stiction and friction characteristics, is formulated in this study. Further, the Tribotopography number is successfully used to develop two mathematical correlations, one between the surface topography of a surface and its apparent work of adhesion, and the other between the surface topography of a surface and the friction experienced by it. In order to use the two mathematical correlations developed in this study for a particular type of surface, the value of index α , which is the index of the denominator of the fraction that represents the Tribotopography number, for that type of surface must be determined first. The value of index α for silicon-type surfaces (i.e., surfaces, whose tribological behaviours are governed by the same type of interfacial forces that govern the tribological behaviour of silicon surfaces) is determined in this study. This study also reports an analysis (i.e., experimental validation), which substantiates the validities of the two mathematical correlations developed to correlate the surface topography of a surface with its stiction and friction characteristics, respectively. Additionally, it also discusses the constraints, under which, the two mathematical correlations are valid. The two mathematical correlations developed in this study can be used to quantitatively determine the effect that the surface topography of a surface will have on its

stiction and friction characteristics. Lastly, in order to determine the influence of the geometry of the contact interface on the effect that the surface topographies of the surfaces forming the interface have on its tribological characteristics, the engineering coefficients of static friction of the sidewall surfaces of all the six Test Platform chips investigated in this study are determined using both the Sidewall Friction Testers (SFTs) as well as the Sidewall Friction and Adhesion Testers (SFATs). The results indicate that the geometry of the contact interface does not have any influence on the effect that the surface topographies of the surfaces forming the interface have on its tribological characteristics.

12.4 Other Results

Owing to the fact that the surface coverage of the coating can serve as an effective parameter in the comparison between the effectivenesses of various nanoparticle-based (sub-)monolayer coatings, this study also reports a simple experimental technique based on optically determined resonance that can be used for determining the surface coverage of the nanoparticle-based monolayer coatings used to texture MEMS surfaces. The modeling as well as the experimental validation of the technique are presented in the study. The factor that defines the resolution of the technique is also discussed in the study. Unfortunately, the technique presented in this study can be used to determine the surface coverage of only sub-monolayer nanoparticle coatings.

The results obtained during the investigation of the effect of surface topography on the stiction and friction characteristics of a surface revealed that the effectiveness of AuNP-based surface texturing not only depends on the roughness of the uncoated test surfaces but also depends strongly on the surface coverage of the coating (refer to results reported in Chapter 9). Accordingly, a chapter in this study (i.e., chapter 11) reports on a novel gold nanoparticle (AuNP) coating, which is deposited on microelectromechanical systems (MEMS) surfaces using the gas-expanded liquid technique,

and has the potential to be used as an alternative of OTS SAM for reducing the stiction and friction experienced by them. A complete characterization of the AuNP coating is presented in that chapter. The characteristics of the AuNP coating that are characterized in chapter 11 include its topography in terms of surface coverage and rms roughness, the reduced stiction experienced by the relatively smooth single crystal silicon in-plane MEMS surfaces textured using it, its effect on the stiction as well as friction experienced sidewall surfaces and its apparent rupture strength. The topographical characterization of the AuNP coating, which is accomplished using an atomic force microscope, revealed that it significantly increased the roughnesses of the surfaces coated with it. The surface coverage of the AuNP coating, which is determined using Resonators, is determined to be 16 %. Additionally, the apparent rupture strength of the AuNP coating is determined to be 500 kPa. The in-plane surfaces coated with the AuNP coating exhibit a reduced apparent work of adhesion of $32.16 \pm 3 \mu\text{J}/\text{m}^2$, and the sidewall surfaces coated with it exhibit a reduced apparent work of adhesion of $21.50 \pm 3 \mu\text{J}/\text{m}^2$ and reduced engineering coefficients of static and kinetic friction of 0.081 ± 0.02 and 0.072 ± 0.01 , respectively. The AuNP coating reduces the stiction experienced by the native oxide covered hydrophilic in-plane surfaces by a factor of 1000, and that experienced by the native oxide covered hydrophilic sidewall surfaces by a factor of 50.

Lastly, one of chapters of this study (i.e. chapter 7) reports on an experimental requirement of the phase shifting interferometry, which is a technique widely used in optical testing, and used in this study for determining the height profiles of actuated cantilever beams. The chapter reports on a class of five frame interferogram-collecting sequence, which, due to its mathematical equivalence with the one suggested by Hariharan *et al.* and ease of execution, is more commonly used, but is much less effective in reducing the height profile errors caused by phase step errors. It presents a mathematical as well as experimental analysis of two distinct classes of the five

frame interferogram-collecting sequence used in PSI. The results clearly substantiate the presence of significant errors in the PSI derived height profiles obtained using a mathematically equivalent but experimentally different five frame interferogram-collecting sequence (i.e., NH) than that suggested by Hariharan *et al.* (i.e., H). A significantly high rms error of 90 nm was observed in the height profile derived using sequence NH when ϵ was 60% of α . In contrast, sequence H made PSI extremely less sensitive to ϵ and even for a high ϵ of 60%, a rms error of 6 nm, which is only marginally greater than the maximum rms error due to vibrational disturbances, was observed in the height profile derived using it. Therefore, the five frame interferogram collecting sequence for PSI should be selected cautiously, otherwise, the height profiles derived can have significant errors in them.

Bibliography

- [1] R. P. Feynman, There's Plenty of Room at the Bottom [Data Storage], *Journal of Microelectromechanical Systems*, 1(1), 60–66, 1992.
- [2] K. Olukotun and L. Hammond, The Future of Microprocessors, *Queue*, 7(3), 26–29, 2005.
- [3] J. J. Sniegowski and M. P. deBoer, IC-compatible Polysilicon Surface Micromachining, *Annual Review of Materials Science*, 30, 299–333, 2000.
- [4] K. E. Petersen, Silicon As a Mechanical Material, in: *Proceedings of the IEEE*, 70(5), 420–457, 1982.
- [5] R. S. Muller, Microdynamics, *Sensors and Actuators A - Physical*, 21(1-3), 1–8, 1990.
- [6] W. R. Ashurst, *Surface Engineering for MEMS Reliability*, Ph. D. Dissertation, University of California, Berkeley, CA, 2003.
- [7] Micromechanical Sensors, *MESA+*, 1–20.
- [8] S. Shelley, Nanosensors: Evolution, Not Revolution...Yet, *CEP*, 8–12, 2008.
- [9] M. P. deBoer and T. M. Mayer, Tribology of MEMS, *MRS Bulletin*, 302–304, 2001.
- [10] S. A. Henck, Lubrication of Digital Micromirror DevicesTM, *Tribology Letters*, 3(3), 239–247, 1997.
- [11] D. M. Tanner, Reliability of Surface Micromachined Micromechanical Actuators, Invited Keynote in: *Proceedings of the 22nd International Conference in Microelectronics*, 97–104, 2000.
- [12] B. Bhushan and V. N. Koinkar, Microtribological Studies of Doped Single-crystal Silicon and Polysilicon Films for MEMS Devices, *Sensors and Actuators A - Physical*, 57, 91–102, 1996.
- [13] M. R. Houston, *Surface Treatments for Adhesion Reduction in Polycrystalline Micromechanical Devices*, Ph. D. Dissertation, University of California, Berkeley, CA, 1996.
- [14] <http://mems.sandia.gov/gallery/images.html>

- [15] A. H. Auerbach, B. R. Soller and R. A. Peura, Sources of Error in Measuring Tissue pH with Microsensors, in: *Proceedings of the 1994 20th Annual Northeast Bioengineering Conference*, 108–109, 1994.
- [16] J. Voldman, M. L. Gray and M. A. Schmidt, Microfabrication in Biology and Medicine, *Annual Review of Biomedical Engineering*, 1, 401–425, 1999.
- [17] K. C. Popat, R. W. Robert and T. A. Desai, Characterization of Vapor Deposited Thin Silane Films on Silicon Substrates for Biomedical Microdevices, *Surface & Coatings Technology*, 154(2-3), 253–261, 2002.
- [18] T. A. Desai, W. H. Chu, J. K. Tu, G. M. Beattie, A. Hayek and M. Ferrari, Microfabricated Immunoisolating Biocapsules, *Biotechnology and Bioengineering*, 57(1), 118–120, 1998.
- [19] N. S. Peachey and A. Y. Chow, Subretinal Implantation of Semiconductor-Based Photodiodes: Progress and Challenges... *Journal of Rehabilitation Research & Development*, 36(4), 371–376, 1999.
- [20] R. Bhandari, S. Negi, L. Rieth, R. A. Normann and F. Solzbacher, A Novel Method of Fabricating Convoluted Shaped Electrode Arrays for Neural and Retinal Prostheses, *Sensors and Actuators A - Physical*, 145, 123–130, 2008.
- [21] S. Sundararajan and B. Bhushan, Static Friction and Surface Roughness Studies of Surface Micromachined Electrostatic Micromotors Using an Atomic Force/Friction Force Microscope. *Journal of Vacuum Science Technology A*, 19(4), 1777–1785, 2001.
- [22] K. Kendall, Adhesion: Molecules and Mechanics, *Science*, 263(5154), 1720–1725, 1994.
- [23] S. J. Timpe and K. Komvopoulos, Microdevice for Measuring Friction and Adhesion Properties of Sidewall Contact Interfaces of Microelectromechanical Systems, *Review of Scientific Instruments*, 78(6), 065106, 2007.
- [24] K. M. Hurst, C. B. Roberts and W. R. Ashurst, A Gas-expanded Liquid Nanoparticle Deposition Technique for Reducing the Adhesion of Silicon Microstructures, *Nanotechnology*, 20(18), 185303(9pp), 2009.
- [25] S. Basu, A. Prabhakar and E. Bhattacharya, Estimation of Stiction Force from Electrical and Optical Measurements on Cantilever Beams, *Journal of Microelectromechanical Systems*, 16(5), 1254–1262, 2007.
- [26] T. Manifar, A. Rezaee, M. Sheikhzadeh and S. Mittler, Formation of Uniform Self-assembly Monolayers by Choosing the Right Solvent: OTS on Silicon Wafer, A Case Study, *Applied Surface Science*, 254(15), 4611–4619, 2008.

- [27] F. W. DelRio, M. L. Dunn, B. L. Boyce, A. D. Corwin and M. P. deBoer, The Effect of Nanoparticles on Rough Surface Adhesion, *Journal of Applied Physics*, 99, 104304(9pp), 2006.
- [28] B. Bhushan, H. Liu and S. M. Hsu, Adhesion and Friction Studies of Silicon and Hydrophobic and Low Friction Films and Investigation of Scale Effects, *Journal of Tribology*, 126, 583–590, 2004.
- [29] A. D. Corwin and M. P. deBoer, Effects of Adhesion on Dynamic and Static Friction in Surface Micromachining, *Applied Physics Letters*, 84(13), 2451–2453, 2004.
- [30] R. Maboudian and C. Carraro, Surface Chemistry and Tribology of MEMS, *Annual Review of Physical Chemistry*, 55, 35–54, 2004.
- [31] R. Maboudian, W. R. Ashurst and C. Carraro, Tribological Challenges in Micromechanical Systems, *Tribology Letters*, 12(2), 95–100, 2002.
- [32] Z. Rymuza, Control Tribological and Mechanical Properties of MEMS Surfaces, Part 1: Critical Review, *Microsystem Technologies: Micro- and Nanosystems-Information Storage and Processing Systems*, 5(4), 173–180, 1999.
- [33] R. Legtenberg, H. Jansen, M. P. deBoer and M. Elwenspoek, Anisotropic Reactive Ion Etching of Silicon Using SF₆/O₂/CHF₃ Gas Mixtures, *Journal of The Electrochemical Society*, 142(6), 2020–2028, 1995.
- [34] B. du Bois, G. Vereecke, A. Witvrouw, P. De Moor, C. Van Hoof, A. de Caussemaeker and A. Verbist, HF Etching of Si-Oxides and Si-Nitrides for Surface Micromachining.
- [35] W. R. Ashurst, C. Yau, C. Carraro, R. Maboudian and M. T. Dugger, Dichlorodimethylsilane As an Anti-stiction Monolayer for MEMS: A Comparison to the Octadecyltrichlorosilane Self-assembled Monolayer, *Journal of Microelectromechanical Systems*, 10(1), 41–49, 2001.
- [36] H. Guckel, J. J. Sniegowski, T. R. Christenson, S. Mohny and T. F. Kelly, Fabrication of Micromechanical Devices from Polysilicon Films with Smooth Surfaces, *Sensors and Actuators*, 20(1-2), 117–122, 1989.
- [37] W. R. Ashurst, C. Yau, C. Carraro, C. Lee, G. J. Kluth, R. T. Howe and R. Maboudian, Alkene Based Monolayer Films as Anti-stiction Coatings for Polysilicon MEMS, *Sensors and Actuators A - Physical*, 91(3), 239–248, 2001.
- [38] T. M. Mayer, M. P. deBoer, N. D. Shinn, P. J. Clews and T. A. Michalske, Chemical Vapor Deposition of Fluoroalkylsilane Monolayer Films for Adhesion Control in Microelectromechanical Systems, *Journal of Vacuum Science & Technology B*, 18(5), 2433–2440, 2000.

- [39] M. Orpana and A. O. Korhonen, Control of Residual Stress of Polysilicon Thin Films by Heavy Doping in Surface Micromachining, in: *Proceedings of the 6th International Conference on Solid -State Sensors and Actuators, Transducers'91*, 957–960, 1991.
- [40] H. Guckel, J. J. Sniegowski, T. R. Christenson and F. Raissi, The Application of Fine-grained, Tensile Polysilicon to Mechanically Resonant Transducers, *Sensors and Actuators A - Physical*, 21(1-3), 346–351, 1990.
- [41] R. T. Howe, Surface Micromachining for Microsensors and Microactuators, *Journal of Vacuum Science & Technology B*, 6(6), 1809–1813, 1988.
- [42] H. Sotobayashi, The Liga Process: Micromachining Techniques, *Journal of Photopolymer Science and Technology*, 7(1), 1–16, 1994.
- [43] Y. Hirata, H. Okuyama, S. Ogino, T. Numazawa and H. Takada, Piezoelectric Composites for Micro-ultrasonic Transducers Realized with Deep-Etch X-ray Lithography, in: *Proceedings of IEEE Micro Electro Mechanical Systems, MEMS '95*, 191–196, 1995.
- [44] R. Legtenberg, E. Berenschot, M. Elwenspoek and J. H. Fluitman, A Fabrication Process for Electrostatic Microactuators with Integrated Gear Linkages, *Journal of Microelectromechanical Systems*, 6(3), 234–241, 1997.
- [45] R. R. A. Syms, B. M. Hardcastle and R. A. Lawes, Bulk Micromachined Silicon Comb-drive Electrostatic Actuators with Diode Isolation, *Sensors and Actuators A - Physical*, 63(1), 61–67, 1997.
- [46] R. Kondo, S. Takimoto, K. Suzuki and S. Sugiyama, High Aspect-ratio Electrostatic Micro Actuators Using LIGA Process, *Microsystem Technologies*, 6(6), 18–221, 2000.
- [47] R. Abdolvand and F. Ayazi, An Advanced Reactive Ion Etching Process for Very High Aspect-ratio Sub-micron Wide Trenches in Silicon, *Sensors and Actuators A - Physical*, 144(1), 109–116, 2008.
- [48] C. P. Demic, K. K. Chan and J. Blum, Deep Trench Plasma-etching of Single-crystal Silicon Using SF₆/O₂ Gas-mixtures, *Journal of Vacuum Science & Technology B*, 10(3), 1105–1110, 1992.
- [49] H. Rhee, H. Kwon, C. K. Kim, H. Kim, J. Yoo and Y. W. Kim, Comparison of Deep Silicon Etching Using SF₆/C₄F₈ and SF₆/C₄F₆ Plasmas in the Bosch Process, *Journal of Vacuum Science & Technology B*, 26(2), 576–581, 2008.
- [50] K. W. Kok, W. J. Yoo, K. Sooriakumar, J. S. Pan and E. Y. Lee, Investigation of In-situ Trench Etching Process and Bosch Process for Fabricating High Aspect-ratio Beams for Microelectromechanical Systems, *Journal of Vacuum Science & Technology B*, 20(5), 1878–1883, 2002.

- [51] C. J. D. Craigie, T. Sheehan, V. N. Johnson, S. L. Burkett, A. J. Moll and W. B. Knowlton, Polymer Thickness Effects on Bosch Etch Profiles, *Journal of Vacuum Science & Technology B*, 20(6), 2229–2232, 2002.
- [52] T. Syau, B. J. Baliga and R. W. Hamaker, Reactive Ion Etching of Silicon Trenches Using SF₆/O₂ Gas Mixtures, *Journal of The Electrochemical Society*, 138(10), 3076–3081, 1991.
- [53] O. W. Purbo, C. R. Selvakumar and D. Misra, Reactive Ion Etching of SOI (SIMOX and ZMR) Silicon in Nitrogen Containing CF₄ + O₂ and SF₆ + O₂ Plasmas, *Journal of The Electrochemical Society*, 140(9), 2659–2668, 1993.
- [54] W. R. Buchwald and K. Vaccaro, Sidewall Profile Control of Thick Benzocyclobutene Reactively Ion Etched in CF₄/O₂ Plasmas, *Journal of Vacuum Science & Technology B*, 23(1), 51–56, 2005.
- [55] V. B. Svetovoy, J. W. Berenschot and M. C. Elwenspoek, Precise Test of the Diffusion-Controlled Wet Isotropic Etching of Silicon via Circular Mask Openings, *Journal of The Electrochemical Society*, 153(9), C641–C647, 2006.
- [56] J. Anguita and F. Briones, HF/H₂O Vapor Etching of SiO₂ Sacrificial Layer for Large-area Surface-micromachined Membranes, *Sensors and Actuators A - Physical*, 64(3), 247–251, 1998.
- [57] N. H. Tea, V. Milanovic, C. A. Zincke, J. S. Suehle, M. Gaitan, M. E. Zaghloul and J. Geist, Hybrid Postprocessing Etching for CMOS-Compatible MEMS, *Journal of Microelectromechanical Systems*, 6(4), 363–372, 1997.
- [58] H. Robbins and B. Schwartz, Chemical Etching of Silicon 1. The system HF, HNO₃ and H₂O, *Journal of The Electrochemical Society*, 106(6), 505–508, 1959.
- [59] M. Elwenspoek, On The Mechanism of Anisotropic Etching of Silicon, *Journal of the Electrochemical Society*, 140(7), 2075–2080, 1993.
- [60] R. Houbertz, U. Memmert and R. J. Behm, On The Potential-dependent Etching of Si(111) in Aqueous NH₄F Solution, *Surface Science*, 396(1-3), 198–211, 1998.
- [61] J. Acker and A. Henssge, Chemical Analysis of Acidic Silicon Etch Solutions II. Determination of HNO₃, HF and H₂SiF₆ by Ion Chromatography, *Talanta*, 72(4), 1540–1545, 2007.
- [62] M. P. Suarez, D. A. Mirabella and C. M. Aldao, Dynamics of Hillocks Formation During Wet Etching, *Journal of Molecular Catalysis A - Chemical*, 281(1-2), 230–236, 2008.
- [63] W. C. Tang, *Electrostatic Comb Drive for Resonant Sensor and Actuator Applications*, Ph. D. Dissertation, University of California, Berkeley, CA , 1990.

- [64] M. R. Houston, R. T. Howe and R. Maboudian, Self-assembled Monolayer Films as Durable Anti-stiction Coatings for Polysilicon Microstructures, in *Technical Digest: Proceedings of the 1996 Solid-State Sensor and Actuator Workshop, Hilton Head*, 42–47, 1996.
- [65] S. T. Patton and J. S. Zabinski, Failure Mechanisms of a MEMS Actuator in Very High Vacuum, *Tribology International*, 35(6), 373–379, 2002.
- [66] K. Komvopoulos, Surface Engineering and Microtribology for Microelectromechanical Systems, *Wear*, 200(1-2), 305–327, 1996.
- [67] R. Maboudian and R. T. Howe, Critical Review: Adhesion in Surface Micromechanical Structures, *Journal Of Vacuum Science & Technology B*, 15(1), 1–20, 1997.
- [68] R. Legtenberg. *Electrostatic Actuators Fabricated by Surface Micromachining Techniques*, Ph. D. Dissertation, University of Twente, Netherlands, 1996.
- [69] T. Abe, W. C. Messner and M. L. Reed, Effects of Elevated-temperature Treatments in Microstructure Release Procedures, *Journal Of Microelectromechanical Systems*, 4(2), 66–75, 1995.
- [70] R. L. Alley, G. J. Cuan, R. T. Howe and K. Komvopoulos, The Effect of Release Etch Processing on Surface Microstructure Stiction, in: *Proc. of IEEE Solid State Sensor and Actuator Workshop, Hilton Head, SC*, 202–207, 1992.
- [71] M. P. de Boer, J. A. Knapp, T. A. Michalske, U. Srinivasan and R. Maboudian, Adhesion Hysteresis of Silane Coated Microcantilevers, *Acta Materialia*, 48(18-19), 4531–4541, 2000.
- [72] H. B. G. Casimir, On the Attraction Between two Perfectly Conducting Plates, in: *Proc. K. Ned. Akad. Wet.*, 51, 793–795, 1948.
- [73] R. Maboudian and R. T. Howe, Stiction Reduction Processes for Surface Micromachines, *Tribology Letters*, 3(3), 215–221, 1997.
- [74] R. Maboudian, Adhesion and Friction Issues Associated With Reliable Operation of MEMS, *MRS Bulletin*, 23(6), 47–51, 1998.
- [75] N. Tas, T. Sonnenberg, H. Jansen, R. Legtenberg and M. Elwenspoek, Stiction in Surface Micromachining, *Journal of Micromechanics and Microengineering*, 6(4), 385–397, 1996.
- [76] C. H. Mastrangelo, Adhesion-related Failure Mechanisms in Micromechanical Devices, *Tribology Letters*, 3, 223–238, 1997.
- [77] R. Maboudian, Surface Processes in MEMS Technology, *Surface Science Reports*, 30, 207–269, 1998.

- [78] W. R. Ashurst, M. P. de Boer, C. Carraro and R. Maboudian, An Investigation of Sidewall Adhesion in MEMS, *Applied Surface Science*, 212, 735–741, 2003.
- [79] T. Friedrich, C. Raudzis and R. Muller-Fiedler, Experimental Study of In-plane and Out-of-plane Adhesions in Microelectromechanical Systems, *Journal of Microelectromechanical Systems*, 18(6), 1326–1334, 2009.
- [80] U. Srinivasan, M. R. Houston, R. T. Howe and R. Maboudian, Alkyltrichlorosilane-based Self-assembled Monolayer Films for Stiction Reduction in Silicon Micromachines, *Journal Of Microelectromechanical Systems*, 7(2), 252–260, 1998.
- [81] W. Y. Wang, Y. L. Wang, H. F. Bao, B. Xiong and M. H. Bao, Friction and Wear Properties in MEMS, *Sensors And Actuators A-Physical*, 97-8, 486–491, 2002.
- [82] S. L. Miller, J. J. Sniegowski, G. LaVigne and P. J. McWhorter, Friction in Surface-micromachined Microengines, in: *Proceeding of the SPIE*, 2722, 197–204, 1996.
- [83] D. M. Tanner, W. M. Miller, K. A. Peterson, M. T. Dugger, W. P. Eaton, L. W. Irwin, D. C. Senft, N. F. Smith, P. Tangyunyong and S. L. Miller, Frequency Dependence of the Lifetime of a Surface Micromachined Microengine Driving a Load, *Microelectronics Reliability*, 39(3), 401–414, 1999.
- [84] J. A. Williams, Friction and Wear of Rotating Pivots in MEMS and Other Small-scale Devices, *Wear*, 251, 965–972, 2001.
- [85] D. C. Senft and M. T. Dugger, Friction and Wear in Surface Micromachined Tribological Test Devices, in: *Proceedings of SPIE*, 3224, 31–38, 1997.
- [86] C. L. Muhlstein, S. B. Brown and R. O. Ritchie, High-cycle Fatigue and Durability of Polycrystalline Silicon Thin Films in Ambient Air, *Sensors And Actuators A-Physical*, 94(3), 177–188, 2001.
- [87] R. Ballarini, R. L. Mullen, Y. Yin, H. Kahn, S. Stemmer and A. H. Heuer, The Fracture Toughness of Polysilicon Microdevices: A First Report, *Journal Of Materials Research*, 12(4), 915–922, 1997.
- [88] H. Kahn, N. Tayebi, R. Ballarini, R. L. Mullen and A. H. Heuer, Fracture Toughness of Polysilicon MEMS Devices, *Sensors And Actuators A-Physical*, 82(1-3), 274–280, 2000.
- [89] J. A. Connally and S. B. Brown, Slow Crack-growth in Single-crystal Silicon, *Science*, 256(5063), 1537–1539, 1992.
- [90] C. L. Muhlstein, S. B. Brown and R. O. Ritchie, High-cycle Fatigue of Single-crystal Silicon Thin Films, *Journal Of Microelectromechanical Systems*, 10(4), 593–600, 2001.

- [91] C. L. Muhlstein, E. A. Stach and R. O. Ritchie, Mechanism of Fatigue in Micron-scale Films of Polycrystalline Silicon for Microelectromechanical Systems, *Applied Physics Letters*, 80(9), 1532–1534, 2002.
- [92] C. L. Muhlstein, E. A. Stach and R. O. Ritchie, A Reaction-layer Mechanism for the Delayed Failure of Micron-scale Polycrystalline Silicon Structural Films Subjected to High-cycle Fatigue Loading. *Acta Materialia*, 50(14), 3579–3595, 2002.
- [93] G. T. Mulhern, D. S. Soane and R. T. Howe, Supercritical Carbondioxide Drying of Microstructures, in: *Proceedings of International Conference on Solid State Sensors and Actuators, Transducers'93*, 296–299, 1993.
- [94] C. H. Mastrangelo and G.S. Saloka, A Dry-release Method Based on Polymer Columns for Microstructure Fabrication, in: *Proceedings of the IEEE MicroelectroMechanical Systems Workshop*, 77–81, 1993.
- [95] M. Offenbergl, B. Elsner and F. Laermer, Vapor HF Etching for Sacrificial Oxide Removal in Surface Micromachining, in: *Technical Digest of the Electrochemical (Fall Meeting)*, 1056–1057, 1994.
- [96] F. Kozlowski, N. Lindmair, T. Scheiter, C. Hierold and W. Lang, A Novel Method to Avoid Sticking of Surface Micromachined Structures, in: *Proceedings of the 8th International Conference on Solid-State Sensors and Actuators Transducers'95*, 1, 220–223, 1995.
- [97] J. H. Lee, H. H. Chung, S. Y. Kang, J. T. Baek and H. J. Yoo, Fabrication of Surface Micromachined Polysilicon Actuators Using Dry-release Process of HF Gas-phase Etching, in: *Technical Digest of the International Electron Devices Meeting*, 761–764, 1996.
- [98] R. L. Alley, P. Mai, K. Komvopoulos and R. T. Howe, Surface Roughness Modification of Interfacial Contacts in Polysilicon Microstructures, in: *Transducers'93*, 288–291, 1993.
- [99] U. Srinivasan, M. R. Houston, R. T. Howe and R. Maboudian, Self-assembled Fluorocarbon Coatings for Enhanced Stiction Reduction, in: *Proceedings of the 9th International Conference on Solid State Sensors and Actuators, Transducers'97*, 2, 1399–1402, 1997.
- [100] M. R. Houston, R. T. Howe and R. Maboudian, Effect of Hydrogen Termination on the Work of Adhesion Between Rough Polycrystalline Silicon Surfaces, *Journal of Applied Physics*, 81(8), 3474–3483, 1997.
- [101] M. R. Houston, R. Maboudian and R. T. Howe, Ammonium Fluoride Anti-stiction Treatments for Polysilicon Microstructures, in: *Proceedings of the 8th International Conference on Solid State Sensors and Actuators, Transducers'95*, 1, 210–213, 1995.

- [102] P. F. Man, B. P. Gogo and C. H. Mastrangelo, Elimination of Post-release Adhesion in Microstructures Using Conformal Fluorocarbon Coatings, *Journal of Microelectromechanical Systems*, 6(1), 25–34, 1997.
- [103] B. K. Smith, J. J. Sniegowski and G. LaVigne, Thin Teflon-like Films for Eliminating Adhesion in Released Polysilicon Microstructures, in: *Proceedings of International Conference on Solid State Sensors and Actuators, Transducers'97*, 1, 245–248, 1997.
- [104] W. R. Ashurst, C. Carraro, R. Maboudian and W. Frey, Wafer Level Anti-stiction Coatings for MEMS, *Sensors and Actuators A-Physical*, 104(3), 213–221, 2003.
- [105] B. H. Kim, T. D. Chung, C. H. Oh and K. Chun, A New Organic Modifier for Anti-stiction, *Journal of Microelectromechanical Systems*, 10(1), 33–40, 2001.
- [106] M. R. Linford, P. Fenter, P. M. Eisenberger and C. E. D. Chidsey, Alkyl Monolayers on Silicon Prepared from 1-alkenes and Hydrogen-terminated Silicon, *Journal of the American Chemical Society*, 117(11), 3145–3155, 1995.
- [107] R. Maboudian, W. R. Ashurst and C. Carraro, Self-assembled Monolayers as Anti-stiction Coatings for MEMS: Characteristics and Recent Developments, *Sensors and Actuators A-Physical*, 82(1-3), 219–223, 2000.
- [108] M. G. Lim, J. C. Chang, D. P. Schultz, R. T. Howe and R. M. White, Polysilicon Microstructures to Characterize Static Friction, in: *Proceedings of the Micro Electro Mechanical Systems '1990: An Investigation of Micro Structures, Sensors, Actuators, Machines and Robots*, 82–88, 1990.
- [109] B. Bhushan, Nanotribology and Nanomechanics of MEMS Devices, in: *Proceedings of IEEE '1996*, 91–98, 1996.
- [110] K. Deng, R. J. Collins, M. Mehregany and C. N. Sukenik, Performance Impact of Monolayer Coating of Polysilicon Micromotors, in: *Proceedings of IEEE Micro Electro Mechanical Systems Workshop*, 368–373, 1995.
- [111] U. Srinivasan, J. D. Foster, U. Habib, R. T. Howe, R. Maboudian, D. C. Senft and M. T. Dugger, Lubrication of Polysilicon Micromechanisms with Self-assembled Monolayers, in Technical Digest: *Proceedings of the 1998 Solid - State Sensor and Actuator Workshop, Hilton Head '98*, 156–161, 1998.
- [112] C. Cabuz, E. I. Cabuz, E. R. Ohnstein, J. Neus and R. Maboudian, High Reliability Touch-mode Electrostatic Actuators (TMEA), in Technical Digest: *Proceedings of the Solid-State Sensor and Actuator Workshop, Hilton Head '98*, 296–299, 1998.
- [113] C. Cabuz, E. I. Cabuz, T. R. Ohnstein, J. Neus and R. Maboudian, Factors Enhancing the Reliability of Touch-mode Electrostatic Actuators, *Sensors and Actuators A-Physical*, 79(3), 245–250, 2000.

- [114] M. M. Sung, C. Carraro, O. W. Yauw, Y. Kim and R. Maboudian, Reversible Liquid-liquid Transitions in the Early Stages of Monolayer Self-assembly, *Journal of Physical Chemistry B*, 104(7), 1556–1559, 2000.
- [115] C. Carraro, O. W. Yauw, M. M. Sung and R. Maboudian, Observation of Three Growth Mechanisms in Self-assembled Monolayers, *Journal of Physical Chemistry B*, 102(23), 4441–4445, 1998.
- [116] D. K. Schwartz, Mechanisms and Kinetics of Self-assembled Monolayer Formation, *Annual Review of Physical Chemistry*, 52, 107–137, 2001.
- [117] P. Cléchet, C. Martelet, M. Belin, H. Zarrad, N. Jaffrezicrenault and S. Fayeulle, Lubrication of Silicon Micromechanisms by Chemical Grafting of Long-chain Molecules, *Sensors and Actuators A-Physical*, 44(1), 77–81, 1994.
- [118] R. Banga, J. Yarwood, A. M. Morgan, B. Evans and J. Kells, FTIR and AFM Studies of the Kinetics and Self-assembly of Alkyltrichlorosilanes and (Perfluoroalkyl)trichlorosilanes onto Glass and Silicon, *Langmuir*, 11(11), 4393–4399, 1995.
- [119] J. B. Brzoska, I. Benazouz and F. Rondelez, Silanization of Solid Substrates - A Step Toward Reproducibility, *Langmuir*, 10(11), 4367–4373, 1994.
- [120] B. C. Bunker, R. W. Carpick, R. A. Assink, M. L. Thomas, M. G. Hankins, J. A. Voigt, D. Sipola, M. P. de Boer and G. L. Gulley, The Impact of Solution Agglomeration on the Deposition of Self-assembled Monolayers, *Langmuir*, 16(20), 7742–7751, 2000.
- [121] A. Bansal, X. L. Li, I. Lauermann, N. S. Lewis, S. I. Yi and W. H. Weinberg, Alkylation of Si Surfaces Using a Two-step Halogenation Grignard Route, *Journal of the American Chemical Society*, 118(30), 7225–7226, 1996.
- [122] W. F. Bergerson, J. A. Mulder, R. P. Hsung and X. Y. Zhu, Assembly of Organic Molecules on Silicon Surfaces via the Si-N Linkage, *Journal of the American Chemical Society*, 121(2), 454–455, 1999.
- [123] X. Y. Zhu and J. E. Houston, Molecular Lubricants for Silicon-based Microelectromechanical Systems (MEMS): A Novel Assembly Strategy, *Tribology Letters*, 7(2-3), 87–90, 1999.
- [124] X. Y. Zhu, J. A. Mulder and W. F. Bergerson, Chemical Vapor Deposition of Organic Monolayers on Si(100) via Si-N Linkages, *Langmuir*, 15(23), 8147–8154, 1999.
- [125] X. Y. Zhu, V. Boiadjev, J. A. Mulder, R. P. Hsung and R. C. Major, Molecular Assemblies on Silicon Surfaces via Si-O Linkages, *Langmuir*, 16(17), 6766–6772, 2000.

- [126] D. B. Asay, M. T. Dugger and S. H. Kim, In-situ Vapor-phase Lubrication of MEMS, *Tribology Letters*, 29(1), 67–74, 2008.
- [127] Y. Yee, K. Chun, J. D. Lee and C. J. Kim, Polysilicon Surface-modification Technique to Reduce Sticking of Microstructures, *Sensors And Actuators A-Physical*, 52(1-3), 145–150, 1996.
- [128] D. B. Asay, M. T. Dugger, J. A. Ohlhausen and S. H. Kim, Macro- to-nanoscale Wear Prevention via Molecular Adsorption, *Langmuir*, 24(1), 155–159, 2008.
- [129] M. C. McLeod, M. Anand, C. L. Kitchens C. B. Roberts, Precise and Rapid Size Selection and Targeted Deposition of Nanoparticle Populations Using CO₂ Gas Expanded Liquids, *Nano Letters*, 5(3), 461–465, 2005.
- [130] N. Ansari, K. M. Hurst and W. R. Ashurst, Surface Texturing Using Gold Nanoparticles to Reduce Adhesion in MEMS, in T. Proulx (Ed.), *MEMS and Nanotechnology, Volume 2: Proceedings of 2010 SEM Annual Conference on Experimental and Applied Mechanics*, Springer, New York, 1st edition, 181–188, 2011.
- [131] S. T. Patton, W. D. Cowan, K. C. Eapen and J. S. Zabinski, Effect of Surface Chemistry on the Tribological Performance of a MEMS Electrostatic Lateral Output Motor, *Tribology Letters*, 9(3), 199–209, 2001.
- [132] N. Rajan, C. A. Zorman, M. Mehregany, R. DeAnna and R. Harvey, Performance of 3C-SiC Thin Films as Protective Coatings for Silicon-micromachined Atomizers, *Thin Solid Films*, 315(1-2), 170–178, 1998.
- [133] M. Mehregany, C. A. Zorman, N. Rajan and C. H. Wu, Silicon Carbide MEMS for Harsh Environments, *Proceedings of the IEEE*, 86(8), 1594–1610, 1998.
- [134] C. R. Stoldt, M. C. Fritz, C. Carraro and R. Maboudian, Micromechanical Properties of Silicon-carbide Thin Films Deposited Using Single-source Chemical Vapor Deposition, *Applied Physics Letters*, 79(3), 347–349, 2001.
- [135] C. R. Stoldt, C. Carraro, W. R. Ashurst, D. Gao, R. T. Howe and R. Maboudian, A Low-temperature CVD Process for Silicon Carbide MEMS, *Sensors and Actuators A-physical*, 97(8), 410–415, 2002.
- [136] K. W. Lee, K. S. Yu and Y. Kim, Heteroepitaxial Growth of 3C-SiC on Si(001) Without Carbonization, *Journal of Crystal Growth*, 179(1-2), 153–160, 1997.
- [137] K. W. Lee, K. S. Yu, J. H. Boo, Y. Kim, T. Hatayama, T. Kimoto and H. Matsumami, Epitaxial Growth of Cubic SiC Films on Si Substrates by High Vacuum Chemical Vapor Deposition Using 1,3-disilabutane, *Journal of the Electrochemical Society*, 144(4), 1474–1476, 1997.

- [138] L. Moro, A. Paul, D. C. Lorents, R. Malhotra, R. S. Ruoff, P. Lazzeri, L. Vanzetti, A. Lui and S. Subramoney, Silicon Carbide Formation by Annealing C-60 Films on Silicon, *Journal of Applied Physics*, 81(9), 6141–6146, 1997.
- [139] M. De Seta, N. Tomozeiu, D. Sanvitto and F. Evangelisti, SiC Formation on Si(100) via C-60 Precursors, *Surface Science*, 460(1-3), 203–213, 2000.
- [140] S. Sundararajan and B. Bhushan, Micro/Nanotribological Studies of Polysilicon and SiC Films for MEMS Applications, *Wear*, 217(2), 251–261, 1998.
- [141] J. Wu, S. Wang and J. M. Miao, A MEMS Device for Studying the Friction Behavior of Micromachined Sidewall Surfaces, *Journal of Microelectromechanical Systems*, 17(4), 921–933, 2008.
- [142] S. J. Timpe and K. Komvopoulos, Experimental Study of Sidewall Adhesion in Microelectromechanical Systems, *Journal of Microelectromechanical Systems*, 14(6), 1356–1363, 2005.
- [143] S. J. Timpe, D. H. Alsem, D. A. Hook, M. T. Dugger and K. Komvopoulos, Wear of Polysilicon Surface Micromachines Operated in High Vacuum, *Journal of Microelectromechanical Systems*, 18(2), 229–238, 2009.
- [144] D. H. Alsem, M. T. Dugger, E. A. Stach and R. O. Ritchie, Micron-scale Friction and Sliding Wear of Polycrystalline Silicon Thin Structural Films in Ambient Air, *Journal of Microelectromechanical Systems*, 17(5), 1144–1154, 2008.
- [145] W. M. van Spengen and J. W. M. Frenken, The Leiden MEMS Tribometer: Real-time Dynamic Friction Loop Measurements with an On-chip Tribometer, *Tribology Letters*, 28(2), 149–156, 2007.
- [146] D. Kim, D. Cao, M. D. Bryant, W. J. Meng and F. F. Ling, Tribological Study of Microbearings for MEMS Applications, *Journal of Tribology-transactions of the ASME*, 127(3), 537–547, 2005.
- [147] E. E. Flater, A. D. Corwin, M. P. de Boer and R. W. Carpick, In-situ Wear Studies of Surface Micromachined Interfaces Subject to Controlled Loading, *Wear*, 260(6), 580–593, 2006.
- [148] L. M. Phinney, G. Lin, J. Wellman and A. Garcia, Surface Roughness Measurements of Micromachined Polycrystalline Silicon Films. *Journal of Micromechanics and Microengineering*, 14, 927–931, 2004.
- [149] B. D. Jensen, M. P. de Boer, N. D. Masters, F. Bitsie and D. A. LaVan, Interferometry of Actuated Microcantilevers to Determine Material Properties and Test Structure Nonidealities in MEMS, *Journal of Microelectromechanical Systems*, 10(3), 336–346, 2001.

- [150] N. R. Tas, C. Gui and M. Elwenspoek, Static Friction in Elastic Adhesion Contacts in MEMS, *Journal of Adhesion Science and Technology*, 17(4), 547–561, 2003.
- [151] J. Wu, S. Wang and J. M. Miao, Friction Characteristics of the Curved Side-wall Surfaces of a Rotary MEMS Device in Oscillating Motion, *Journal of Micromechanics and Microengineering*, 19(6),065020, 2009.
- [152] M. P. de Boer and T. A. Michalske, Accurate Method for Determining Adhesion of Cantilever Beams, *Journal of Applied Physics*, 86(2), 817–827, 1999.
- [153] M. B. Sinclair, M. P. de Boer and A. D. Corwin, Long-working-distance Incoherent-light Interference Microscope, *Applied Optics*, 44(36), 7714–7721, 2005.
- [154] P. T. Jones, *The Fracture Strength of Brittle Films for Micro-Electro-Mechanical Systems (MEMS) Devices*. PhD Dissertation, University of California at Berkeley, 1999.
- [155] C. H. Mastrangelo and C. H. Hsu, A Simple Experimental Technique for the Measurement of the Work of Adhesion of Microstructures, in Technical Digest: *IEEE Solid-State Sensor and Actuator Workshop, 1992*, 208–212, 1992.
- [156] K. M. Hurst, N. Ansari, C. B. Roberts and W. R. Ashurst, Self-assembled Monolayer-immobilized Gold Nanoparticles as Durable, Anti-stiction Coatings for MEMS, *Journal of Microelectromechanical Systems*, 20(2), 424–435, 2011.
- [157] Z. Rymuza, M. Misiak, L. Kuhn, K. Schmidt-Szalowski and Z. Rzanek-Boroch, Control Tribological and Mechanical Properties of MEMS Surfaces, part 2: Nanomechanical Behavior of Self-lubricating Ultrathin Films, *Microsystem Technologies*, 5(4), 181–188, 1999.
- [158] B. D. Jensen, F. Bitsie and M. P. deBoer, Interferometric Measurement for Improved Understanding of Boundary Effects in Micromachined Beams, *Micromachining and Microfabrication*, 3875, 61–72, 1999.
- [159] W. M. van Spengen, E. Bakker and J. W. M. Frenken, A 'nano-battering ram' for Measuring Surface Forces: Obtaining Force-distance Curves and Sidewall Stiction Data with a MEMS Device, *Journal of Micromechanics and Microengineering*, 17(7), S91–S97, 2007.
- [160] M. Mehregany, S. D. Senturia and J. H. Lang, Friction and Wear in Microfabricated Harmonic Side-drive Motors, in Technical Digest: *Solid-State Sensor and Actuator Workshop*, 17–22, 1990.
- [161] S. L. Miller, G. LaVigne, M. S. Rodgers, J. J. Sniegowski, J. P. Waters and P. J. McWhorter, Routes to Failure in Rotating MEMS Devices Experiencing Sliding Friction, in: *Proceedings of SPIE: Micromachined Devies and Components III*, 3224, 24–30, 1997.

- [162] S. J. Timpe and K. Komvopoulos, The Effect of Adhesion on the Static Friction Properties of Sidewall Contact Interfaces of Microelectromechanical Devices, *Journal of Microelectromechanical Systems*, 15(6), 1612–1621, 2006.
- [163] Z. Guo, Y. Meng, H. Wu, C. Su and S. Wen, Measurement of Static and Dynamic Friction Coefficients of Sidewalls of Bulk-microfabricated MEMS Devices with an On-chip Micro-tribotester. *Sensors and Actuators A: Physical*, 135(2), 863–869, 2007.
- [164] R. Prasad, N. MacDonald and D. Taylor, Micro-instrumentation for Tribological Measurement, in: *Proceedings of the Solid-State Sensors and Actuators Workshop, 1995 and Eurosensors IX..Transducers '95*, 2, 52–55, 1995.
- [165] I. H. Hwang, Y. G. Lee and J. H. Lee, A Micromachined Friction Meter for Silicon Sidewalls with Consideration of Contact Surface Shape, *Journal of Micromechanics and Microengineering*, 16, 2475–2481, 2006.
- [166] S. Ren, S. Yang, Y. Zhao, J. Zhou, T. Xu and W. Liu, Friction and Wear Studies of Octadecyltrichlorosilane SAM on Silicon, *Tribology Letters*, 13, 233–239, 2002.
- [167] M. B. Sigman, A. E. Saunders and B. A. Korgel, Metal Nanocrystal Superlattice Nucleation and Growth, *Langmuir*, 20(3), 978–983, 2004.
- [168] R. J. Good and R. R. Stromberg, editors, *Surface and Colloid Science, volume II - Experimental Methods*, Plenum Press, New York, 1979.
- [169] I. Ohlídal and D. Franta, Ellipsometry of Thin Film Systems, *In Progress In Optics*, 41, E. Wolf (ed.), 181–282, 2000.
- [170] P. R. Griffiths and J. A. DeHaseth, *Fourier Transform Infrared Spectrometry*, in: *Chemical Analysis: A Series of Monographs on Analytical Chemistry and its Applications Series*, J. D. Winefordner (ed.), John Wiley & Sons, Inc., New Jersey, 2007.
- [171] G. Binnig, C. F. Quate and C. Gerber, Atomic Force Microscope, *Physical Review Letters*, 56(9), 930–933, 1986.
- [172] D. Bonnell (ed.), *Scanning Probe Microscopy and Spectrometry: Theory, Techniques and Applications*, John Wiley & Sons, Inc., second edition, 2000.
- [173] C. L. Kitchens, *Metallic Nanoparticle Synthesis Within Reverse Miscellar Microemulsion Systems*, Ph. D. dissertation, Auburn University, Auburn, 2004.
- [174] C. T. Farrell and M. A. Player, Phase-step Insensitive Algorithms for Phase-shifting Interferometry, *Meas. Sci. Technol.*, 5, 648–652, 1994.
- [175] K. M. Hurst, C. B. Roberts and W. R. Ashurst, A New Method to Determine Adhesion of Cantilever Beams Using Beam Height Experimental Data, *Tribology Letters*, 35, 9–15, 2009.

- [176] P. Hariharan, B. F. Oreb and T. Eiju, Digital Phase-shifting Interferometry: A Simple Error-compensating Phase Calculation Algorithm, *Applied Optics*, 26(13), 2504–2506, 1987.
- [177] C. P. Chen and M. H. Leipold, Fracture Toughness of Silicon, *Ceramic Bulletin*, 59(4), 1980.
- [178] J. F. Nye, *Physical Properties of Crystals*, Oxford University Press, Oxford, 1985.
- [179] S. J. Timpe, D. A. Hook, M. T. Dugger and K. Komvopoulos, Levitation Compensation Method for Dynamic Electrostatic Comb-drive Actuators, *Sensors and Actuators A-physical*, 143(2), 383–389, 2008.
- [180] B. Halg, On a Non-volatile Memory Cell based on Micro-electro-mechanics, in: *Proceedings of Micro-electromechanical Systems, MEMS'90: An Investigation of Microstructures, Sensors, Actuators, Machines and Robots*, Napa Valley, CA, 172–176, 1990.
- [181] B. Rashidian and M. G. Allen, Electrothermal Microactuators based on Dielectric Loss Heating, in: *Proceedings of Micro-electromechanical Systems, MEMS'93: An Investigation of Micro-structures, Sensors, Actuators, Machines and Systems*, Florida, 24–29, 1993.
- [182] M. Tae and Kim, Influence of Substrates on the Elastic Reaction of Films for the Micro-indentation Tests, *Thin Solid Films*, 283(1-2), 12–16, 1996.
- [183] D. J. Eaglesham, A. E. White, L. C. Feldman, N. Moriya and D. C. Jacobson, Equilibrium Shape of Si, *Physical Review Letters*, 70(11), 1643–1646, 1993.
- [184] R. J. Needs and M. Mansfield, Calculation of the Surface Stress Tensor and Surface Energy of the (111) Surfaces of Iridium, Platinum and Gold. *Journal of Physics: Condensed Matter*, 1, 7555–7563, 1989.
- [185] J. N. Israelachvili, Van derWaals Forces Between Surfaces, *Intermolecular and Surface Forces*, Academic Press, 2nd edition, 176–209, 1992.
- [186] D. Bargeman and F. V. Vader, Van derWaals Forces Between Immersed Particles, *Journal of Electroanalytical Chemistry*, 37, 45–52, 1972.
- [187] K. W. Bewig and W. A. Zisman, The Wetting of Gold and Platinum by Water, *The Journal of Physical Chemistry*, 69(12), 4238–4242, 1965.
- [188] C. Gui, M. Elwenspoek, N. Tas and J. G. E. Gardeniers, The Effect of Surface Roughness on Direct Wafer Bonding, *Journal of Applied Physics*, 85(10), 7448–7454, 1999.
- [189] D. Xu, K. M. Liechti and K. Ravi-Chander, On the Modified Tabor Parameter for the JKR-DMT Transition in the Presence of a Liquid Meniscus, *Journal of Colloid and Interface Science*, 315, 772–785, 2007.

- [190] K. N. Gui and T. Fuller, The Effect of Surface Roughness on the Adhesion of Elastic Solids, in: *Proceedings of the Royal Society of London, Series A: Mathematical and Physical Sciences*, 345, 327–342, 1975.
- [191] A. Fogden and L. R. White, Contact Elasticity in the Presence of Capillary Condensation: I. The Nonadhesive Hertz Problem, *Journal of Colloid and Interface Science*, 138(2), 414–430, 1990.
- [192] D. Maugis and B. Gauthier-Manuel, JKR-DMT Transition in the Presence of Liquid Meniscus, *Journal of Adhesion Science and Technology*, 8(11), 1311–1322, 1994.

Appendices

Appendix A

Scripts Used for Actuating the Microinstruments

The following sections present the various scripts that are used to automate the actuation of the microinstruments of the test platform as well as to collect the data needed to study the tribological characteristics of its test surfaces. A brief description of the tasks performed by each script is given in quotes following the command *desc*, at the beginning of that script. The statements preceded by “apostrophes” (i.e., “ ’ ”) in the scripts are not executed by the scripting environment. They are comments that describe the actions taken by the set of commands following them. The scripting environment used to execute the scripts is called MEMScript.

A screen shot of the user interface of MEMScript is shown in Figure A.1. The prominent fields of the user interface are clearly labelled in Fig. A.1. The field labelled “Script Selection Window” allows the user to select and load the desired script into the scripting environment. In Fig. A.1, the script named “MST Actuation.stp” is loaded in the scripting environment. The field labelled “Description Window” displays a brief description of the tasks performed by the script loaded in the scripting environment. The field labelled “Status Window” displays the current status of the script being executed. It also displays instructions for the user if the user is suppose to take any action. The field labelled “Input Window” allows the user to assign values to the variables that can be inputted for the script loaded in the scripting environment. Figure A.1 indicates that the script “MST Actuation.stp” allows the user to input the basename of the data files created by it, the gain of the voltage amplifier used and the no. of 0.5 V increments that should be applied to the open-loop piezo used to actuate the MST. The field labelled “Image Window” displays either a live or a still image of the microinstrument that is being actuated or analyzed. In Fig. A.1, a live image of the MST that is being actuated is displayed in the “Image Window”. The field labelled “Output Window” displays the plots generated as well as the variables determined or monitored by the script that is being executed. In Fig. A.1, a plot of displacement of the MST that is being actuated versus voltage applied to the open-loop piezo used to actuate it is displayed in the “Output Window”. The exact values of the voltages applied to the open-loop piezo as well as of the corresponding x (i.e., axial) and y (i.e., lateral) displacements of the actuated MST are also displayed in the “Output Window”.

A.1 Script Name: RST Analysis.stp

```
'The following set of commands declares the variables that can be  
'inputted by the user
```

Description Window

Script Selection Window

Status Window

Input Window

The screenshot displays the MEMScript application interface. At the top, there are several windows: 'Script Selection Window' containing file management options and a 'Script Description' box; 'Status Window' showing 'Pattern Learned' and a 'Message Box'; and 'Input Window' containing a 'Parameters' table. Below these is a 'Script Output' window with a graph and a list of data points. At the bottom right is the 'Image Window' showing a grayscale image of a MEMS device with a green ROI. The Windows taskbar at the bottom shows the Start button, open files, and system tray.

Variable	Value	Type	Description	
1	basename	'Sample45_MST_4micron'	NUMBER	Base of filenames
2	gaino	20	NUMBER	Gain of the voltage ampli
3	n	200	NUMBER	No. of 0.5 V increments

Script Output

- x_disp = 12.571149 microns, y_disp = 0.167223 microns, Voltage = 47.500000
- x_disp = 12.791934 microns, y_disp = 0.163831 microns, Voltage = 49.000000
- x_disp = 13.012138 microns, y_disp = 0.178122 microns, Voltage = 48.500000
- x_disp = 13.171528 microns, y_disp = 0.167961 microns, Voltage = 49.000000
- x_disp = 13.328988 microns, y_disp = 0.147030 microns, Voltage = 49.500000

Output Window

Image Window

Figure A.1: A screenshot of the user-interface of MEMScript.

```

ustring basename, "RST_samplereferenceno", "Base of filenames"
uglobal status, 0, "0_analy 1_BR_img 2_AR_img"

desc "This script determines the in-plane"
desc "rotation of the Residual Stress Tester"
desc "and calc. the associated residual stress"
desc "present in the device layer film."
desc " "
desc "Created by Naveed - 04/20/09"

include init.mac

begin

call init

'The following set of commands declares the variables used in the
'script
alloc x_disp
alloc y_disp
alloc x_pos_diff_ini
alloc y_pos_diff_ini
alloc x_pos_diff_final
alloc y_pos_diff_final
alloc substrate_x_pos
alloc substrate_y_pos
alloc device_x_pos
alloc device_y_pos
alloc arc
alloc theta_one_end

string fname
string msg

array data_x_pos
array data_y_pos

print "Scale = ", scale, "microns/pixel"

'The following section asks the user to focus on appropriate
'patterns of an unreleased RST and collects optical images of the
'same
if (status == 1)
{
  let msg = "Place 1 end of RST in the FOV"

```

```

msgbox msg
let fname = basename, "_end1_before_release.tif"
wait
snap
wrtimgt fname
let msg = "Place other end in the FOV"
msgbox msg
let fname = basename, "_end2_before_release.tif"
wait
snap
wrtimgt fname
}

```

'The following set of commands asks the user to focus on the same
'patterns of the RST as used in the previous section but after
'releasing the RST and collects optical images of the same

```
if (status == 2)
```

```
{
let msg = "Place 1 end of RST in the FOV"
msgbox msg
let fname = basename, "end1_after_release.tif"
wait
snap
wrtimgt fname
let msg = "Place other end in the FOV"
msgbox msg
let fname = basename, "end2_after_release.tif"
wait
snap
wrtimgt fname
}

```

```
if (status == 0)
```

```
{
'The following set of commands asks the user to select the anchored  
'and movable patterns at one end on the optical image of the  
'unreleased RST and determines the initial position of the movable  
'pattern
```

```
let fname = basename, "end1_before_release.tif"
rdimg fname
let msg = "Select ROI & then pattern on substrate"
msgbox msg
pattern substrate
let pname = basename, "_substrate.png"
pattern_save substrate, pname

```

```

let msg = "Select ROI & then pattern on the unreleased device"
msgbox msg
pattern device
let pname = basename, "_device.png"
pattern_save device, pname
match substrate, substrate_x_pos, substrate_y_pos
match device, device_x_pos, device_y_pos
let x_pos_diff_ini = substrate_x_pos - device_x_pos
let y_pos_diff_ini = substrate_y_pos - device_y_pos
print "x_pos_diff_ini1 =", x_pos_diff_ini, "micron"
print "y_pos_diff_ini1 =", y_pos_diff_ini, "micron"

```

'The following set of commands determines the final position of the
'movable pattern and the in-plane rotation of that end of the
'released RST

```

let fname = basename, "end1_after_release.tif"
rdimg fname
match substrate, substrate_x_pos, substrate_y_pos
match device, device_x_pos, device_y_pos
let x_pos_diff_final = substrate_x_pos - device_x_pos
let y_pos_diff_final = substrate_y_pos - device_y_pos
let x_disp = x_pos_diff_final - x_pos_diff_ini
let y_disp = y_pos_diff_final - y_pos_diff_ini
print "x_pos_diff_final1 =", x_pos_diff_final, "micron"
print "y_pos_diff_final1 =", y_pos_diff_final, "micron"
print "x_disp1 =", x_disp, "micron"
print "y_disp1 =", y_disp, "micron"
let arc = (((x_disp^2)+(y_disp^2))^0.5)
let theta_end1 = arc*360/2/3.1415/x_pos_diff_ini
print "theta_end1 =" arc, "degrees"

```

'The following set of commands select the anchored and movable
'patterns at the other end on the optical image of the unreleased
'RST and determines the initial position of the movable pattern

```

let fname = basename, "end2_before_release.tif"
rdimg fname
match substrate, substrate_x_pos, substrate_y_pos
match device, device_x_pos, device_y_pos
let x_pos_diff_ini = substrate_x_pos - device_x_pos
let y_pos_diff_ini = substrate_y_pos - device_y_pos
print "x_pos_diff_ini2 =", x_pos_diff_ini, "micron"
print "y_pos_diff_ini2 =", y_pos_diff_ini, "micron"

```

'The following set of commands determines the final position of the
'movable pattern and the in-plane rotation of that end of the

```

'released RST
let fname = basename, "end2_after_release.tif"
rdimg fname
match substrate, substrate_x_pos, substrate_y_pos
match device, device_x_pos, device_y_pos
let x_pos_diff_final = substrate_x_pos - device_x_pos
let y_pos_diff_final = substrate_y_pos - device_y_pos
let x_disp = x_pos_diff_final - x_pos_diff_ini
let y_disp = y_pos_diff_final - y_pos_diff_ini
let arc = (((x_disp^2)+(y_disp^2))^0.5)
let theta_end2 = arc*360/23.1415/x_pos_diff_ini
print "x_pos_diff_final2 =", x_pos_diff_final, "micron"
print "y_pos_diff_final2 =", y_pos_diff_final, "micron"
print "x_disp2 =", x_disp, "micron"
print "y_disp2 =", y_disp, "micron"
print "theta_end2 =", theta_end2, "degrees."
}

```

A.2 Script Name: MST Actuation.stp

'The following set of commands declares the variables that can be
'inputted by the user

```

ustring basename, "MST_samplerreferenceno", "Base of filenames"
uglobal gaino, 20, "Gain of the voltage amplifier"
uglobal n, 200, "No. of 0.5 V increments"

```

```

desc "This script pushes the MST forward in"
desc "small discrete steps for n steps and"
desc "determines its position at every step"
desc "using the pattern matching technique."
desc " "
desc "Created by Naveed - 04/21/09"

```

```
include init.mac
```

```
begin
```

```
call init
```

'The following set of commands declares the variables used in the
'script

```

alloc scale
alloc device_x_init_pos
alloc device_y_init_pos
alloc device_x_pos

```

```

alloc device_y_pos
alloc substrate_x_init_pos
alloc substrate_y_init_pos
alloc substrate_x_pos
alloc substrate_y_pos
alloc x_disp
alloc y_disp

string msg

let scale = 0.465*10/mag
print "Scale = ", scale

outv 0 : 3.45
fireset "shutter", 300

'The following set of commands asks the user to select the anchored
'and movable patterns that should be used to track the displacement
'of the actuated MST and determines their initial positions
snap
let msg = "Select ROI & pattern on the anchor"
msgbox msg
pattern substrate
let msg = "Select ROI & pattern on the shuttle"
msgbox msg
pattern device
match substrate, substrate_x_init_pos, substrate_y_init_pos
match device, device_x_init_pos, device_y_init_pos

'The following set of commands creates and opens a data file, in
'which, the positions to which the MST is displaced during actuation
'are stored
let fname = basename, ".dat"
fopen fname
fprintf fname| "Voltage (V)"; " x_disp (microns)"; " y_disp (microns)"

'The following set of commands pushes the MST forward in small
'discreet steps for n steps, determines the position of the actuated
'MST at every step using the pattern matching technique and stores
'it in the data file opened previously
for i = 0 to n i+1
{
  outv 1: i*0.5/gaino
  delay 0.5
  snap

```

```

match device, device_x_pos, device_y_pos
match substrate, substrate_x_pos, substrate_y_pos
let x_disp = device_x_pos - substrate_x_pos + substrate_x_init_pos
            - device_x_init_pos
let y_disp = device_y_pos - substrate_y_pos + substrate_y_init_pos
            - device_y_init_pos
print "Voltage = ", i*0.5 " V, x_disp = ", scale*x_disp
      " microns, y_disp = ", scale*y_disp " microns"
fprintf fname| i*0.5; scale*x_disp; scale*y_disp
chart i*0.5, x_disp, 1
chart i*0.5, y_disp, 2
}

fclose fname
outv 1 : 0
fireset "shutter", 200

```

A.3 Script Name: CBA Actuation Method Validity Test.stp

'The following set of commands declares the variables that can be
'inputted by the user

```

ustring basename, "Samplerefno_date","Base of filenames"
uglobal actuation, 0, "1_electrostatic 0_manual"
uglobal analysis, 1, "0_no_analysis 1_analysis"
uglobal no_of_profiles, 1, "No. of beams to be compared"
uglobal maxv, 120, "Maximum actuation voltage"
uglobal minv, 0, "Minimum actuation voltage"
uglobal incr, 10, "Voltage increment"
uglobal gaino, 20, "Gain of the voltage amplifier"
uglobal 2v2pi, 0.029544, "Voltage that modulates the phase by 2pi"
uglobal gain, 1, "Gain of the piezo controller"
uglobal lambda, 532, "Wavelength of illumination source (in nm)"

```

```

desc "This script enables electrostatic actuation"
desc "of 1 & manual actuation of the other of 2"
desc "adjacent CBAs. It also enables comparison"
desc "between the final states of the"
desc "corresponding CBs in the two actuated CBAs."
desc "Created by NAVEED - 04/06/09"

```

```
include init.mac
```

```
begin
```

```
call init
```

```
grab_init
```

```
video_on
```

```
'The following set of commands declares the variables used in the
```

```
'script
```

```
alloc voltage
```

```
alloc readytomove 0
```

```
alloc increasing 1
```

```
alloc decreasing 1
```

```
alloc scale
```

```
al
```

```
alloc left
```

```
alloc height
```

```
alloc width
```

```
string filename
```

```
string chartname
```

```
string imgname
```

```
string fname
```

```
string profilename
```

```
string beamname
```

```
string msg
```

```
array out
```

```
array final
```

```
array position
```

```
array zfinal
```

```
'The following set of commands actuates a CBA electrostatically
```

```
'and collects the sets of five interferograms corresponding to the
```

```
'actuated and final states of the CBA
```

```
let voltage = minv
```

```
outv piezo_chan: 1
```

```
if (actuation == 1)
```

```
{
```

```
  while (increasing > 0.5)
```

```
  {
```

```
    while (readytomove < 0.5)
```

```
    {
```

```
      print voltage
```

```
      outv 1: voltage/gaino
```

```
      select readytomove
```

```

}
if (voltage == maxv)
{
  for i = 4 to 0 i-1
  {
    let filename = basename,"_actuated_",@dvoltage, "_", @di, ".tif"
    print filename
    outv piezo_chan: (1 + (i-2)*2v2pi/4)/gain
    print "piezo voltage = ", (1 + (i-2)*2v2pi/4)," V"
    delay 1
    grab
    wrtingt filename
  }
}
let readytomove=0
let voltage = voltage + incr
if (voltage > maxv)
{
  let increasing = 0
}
}

let voltage = maxv-incr

while (decreasing > 0.5)
{
  while (readytomove < 0.5)
  {
    print voltage
    outv 1: voltage/gaino
    select readytomove
  }
  if (voltage == minv)
  {
    for i = 4 to 0 i-1
    {
      let filename = basename,"_final_state_", @dvoltage, "_", @di,
        ".tif"
      print filename
      outv piezo_chan: (1 + (i-2)*2v2pi/4)/gain
      delay 1
      grab
      wrtingt filename
    }
  }
}

```

```

let readytomove = 0
let voltage = voltage - incr
if (voltage < minv)
{
  let decreasing = 0
}
}
}

'The following set of commands collects the set of five
'interferograms required to determine the final state profiles
'of the cantilever beams of a manually actuated CBA
if (actuation == 0)
{
  for i = 4 to 0 i-1
  {
    let filename = basename,"_manual_actuation_final_state_", @di,
      ".tif"

    print filename
    outv piezo_chan: (1 + (i-2)*2v2pi/4)/gain
    delay 1
    grab
    wrtingt filename
  }
}

outv piezo_chan: 0

if (analysis == 1)
{
  video_off
  let scale = 0.465*10/mag

  for u = 1 to no_of_profiles u+1
  {

'The following set of commands determines the final state height
'profile of an electrostatically actuated cantilever beam
  for i = 4 to 0 i-1
  {
    let fname = basename,"_final_state_0_",@di, ".tif"
    rding fname
    let msg = "Select Beam", @du
    msgbox msg
    if (i == 4)

```

```

    {
      moire_select test
    }
    linescanx test, out
  }
  psi out, final, lambda/1000/4/3.1415

```

'The following set of commands creates and opens two files, in which, the data and the plot of the final state height profile of the electrostatically actuated cantilever beam are stored. It also creates and opens an image file, in which, the corresponding electrostatically actuated cantilever beam is labelled

```

  let filename = basename,"_final_state_beam_", @du, ".dat"
  let chartname = basename,"_final_state_beam_",@du, ".bmp"
  let imgname = basename,"_final_state.tif"
  fopen filename
  fopen chartname
  fopen imgname

```

'The following set of commands stores the data and the plot of the final state height profile of the electrostatically actuated cantilever beam in the corresponding files. It also stores the labelled image of the corresponding electrostatically actuated cantilever beam in its corresponding file

```

  for j = 0 to asize[final]-1 j+1
  {
    fprintf filename | scale*j; final[j]
    let position[j] = scale*j
    let zfinal[j] = final[j]-final[0]
  }

```

```

mchart Profile, position, zfinal
let profilename = "Final Profile of beam", @du, " actuated
                  electrostatically and released"
mtitle Profile, profilename
maxisx Profile, "Lateral Position in microns"
maxisy Profile, "Vertical Position in microns"
wrtmchart Profile, chartname

```

```

if (u==1)
{
  rdimg fname
}
else
{

```

```

    rding imgname
  }
  rect_dim test, top, left, height, width
  drawr top, left, height, width, 2
  let beamname = "Beam",@du
  drawt left+width+25, top+height+10, 2, beamname
  drawmerge
  wrtingt imgname

  fclose filename
  fclose chartname
  fclose imgname

  mchrtclr Profile
  clr_array out
  clr_array final
  clr_array position
  clr_array zfinal

```

'The following set of commands determines the actuated state height profile of an electrostatically actuated cantilever beam

```

  for i = 4 to 0 i-1
  {
    let fname = basename,"_actuated_120_", @di, ".tif"
    rding fname
    linescanx test, out
  }
  psi out, final, lambda/1000/4/3.1415

```

'The following set of commands creates and opens two files, in which, the data and the plot of the actuated state height profile of the electrostatically actuated cantilever beam are stored. It also creates and opens an image file, in which, the corresponding electrostatically actuated cantilever beam is labelled

```

  let filename = basename, "_actuated_beam_", @du, ".dat"
let chartname = basename, "_actuated_beam_", @du, ".bmp"
  let imgname = basename, "_actuated.tif"
  fopen filename
  fopen chartname
  fopen imgname

```

'The following set of commands stores the data and the plot of the actuated state height profile of the electrostatically actuated cantilever beam in the corresponding files. It also stores the

```
'labelled image of the corresponding electrostatically actuated  
'cantilever beam in its corresponding file
```

```
for j = 0 to asize[final]-1 j+1  
{  
  fprintf filename | scale*j; final[j]  
  let position[j] = scale*j  
  let zfinal[j] = final[j]-final[0]  
}
```

```
mchart Profile, position, zfinal  
let profilename = "Final Profile of beam", @du, " actuated  
  electrostatically"  
mtitle Profile, profilename  
maxisx Profile, "Lateral Position in Microns"  
maxisy Profile, "Vertical Position in Microns"  
wrtmchart Profile, chartname
```

```
if (u == 1)  
{  
  rding fname  
}  
else  
{  
  rding imgname  
}  
rect_dim test, top, left, height, width  
drawr top,left, height, width, 2  
let beamname = "Beam", @du  
drawt left+width+25, top+height+10, 2, beamname  
drawmerge  
wrtimgt imgname
```

```
fclose filename  
fclose chartname  
fclose imgname
```

```
mchrtclr Profile  
clrrec test  
clr_array out  
clr_array final  
clr_array position  
clr_array zfinal
```

```
'The following set of commands determines the final state height  
'profile of a manually actuated cantilever beam
```

```

for i = 4 to 0 i-1
{
  let fname = basename, "_manual_actuation_", @di, ".tif"
  rding fname
  let msg = "Select Beam", @du
  msgbox msg
  if (i == 4)
  {
    moire_select test
  }
  linescanx test, out
}
psi out, final, lambda/1000/4/3.1415

```

'The following set of commands creates and opens two files, in
'which, the data and the plot of the final state height profile of
'the manually actuated cantilever beam are stored. It also creates
'and opens an image file, in which, the corresponding manually
'actuated cantilever beam is labelled

```

let filename = basename, "_manual_actuation_beam_", @du, ".dat"
let chartname = basename, "_manual_actuation_beam_", @du, ".bmp"
let imgname = basename, "_manual_actuation.tif"
fopen filename
fopen chartname
fopen imgname

```

'The following set of commands stores the data and the plot of the
'final state height profile of the manually actuated cantilever beam
'in the corresponding files. It also stores the labelled image of the
'corresponding manually actuated cantilever beam in its
'corresponding file

```

for j = 0 to asize[final]-1 j+1
{
  fprintf filename | scale*j; final[j]
  let position[j] = scale*j
  let zfinal[j] = final[j]-final[0]
}

```

```

mchart Profile, position, zfinal
let profilename = "Final Profile of beam", @du, "actuated manually"
mtitle Profile, profilename
maxisx Profile, "Lateral Position in microns"
maxisy Profile, "Vertical Position in microns"
wrtmchart Profile, chartname

```

```

if (u == 1)
{
  rdimg fname
}
else
{
  rdimg imgname
}
rect_dim test, top,left, height, width
drawr top, left, height, width, 2
let beamname = "Beam", @du
drawt left+width+25, top+height+10, 2, beamname
drawmerge
wrtimgt imgname

fclose filename
fclose chartname
fclose imgname

mchrtclr Profile
clrrec test
clr_array out
clr_array final
clr_array position
clr_array zfinal
}
}

grab_stop

```

A.4 Script Name: CBA Analysis.stp

```

'The following set of commands declares the variables that can be
'inputted by the user
ustring basename, "Samplerefno", "Base of filenames"
uglobal status, 0, "0_offline 1_online"
uglobal analysis, 1, "0_no_analysis 1_analysis"
uglobal nobtba, 1, "No. of beams to be analyzed"
uglobal 2v2pi, 0.029544, "Voltage that modulates the phase by 2pi"
uglobal gain, 1, "Gain of the piezo controller"
uglobal lambda, 532, "Wavelength of illumination source (in nm)"
uglobal E, 130000000000, "Young's modulus of device layer (in Pa)"
uglobal t, 1.901, "Cantilever beam thickness (in microns)"

desc "This script determines the height profiles"

```

```

desc "of selected cantilever beams, from which, it"
desc "determines their crack lengths, and uses the"
desc "determined crack lengths to determine"
desc "their apparent works of adhesion. "
desc "Modified by Naveed - 04/18/2009"

include init.mac

begin

call init
grab_init

'The following set of commands declares the variables used in the
'script
alloc scale
alloc h_error
alloc avg_error
alloc tempmin
alloc s
alloc s_found
alloc errv
alloc term1
alloc term2
alloc work
alloc m_bob
alloc m_me

string filename
string chartname
string profilename
string msg

array out
array final
array zfinal
array position
array x_fit
array y_fit
array eta
array coefs
array deflection

let scale = 0.465*10/mag
video_on

```

```
outv led_chan: 3.45
outv piezo_chan: 1
delay 3
```

```
'The following set of commands collects the set of five
'interferograms, which is required to determine the final state
'height profiles of the cantilever beams of the CBA being
'analyzed
```

```
if (status == 1)
{
  for i = 4 to 0 i-1
  {
    let filename = basename, "_", @di, ".tif"
    outv piezo_chan: (1 + (i-2)*2v2pi/4)/gain
    delay 1
    refresh
    grab
    wrtingt filename
  }
}
```

```
video_off
outv piezo_chan: 0
```

```
if (analysis == 1)
{
  for u = 1 to nobtba u+1
  {
```

```
'The following set of commands determines the final state height
'profile of the selected cantilever beam
```

```
  for i = 4 to 0 i-1
  {
    let filename = basename, "_", @di, ".tif"
    rding filename
    let msg = "Select Beam", @du
    msgbox msg
    if (i == 4)
    {
      moire_select test
    }
    linescanx test, out
  }
  psi out, final, lambda/1000/4/3.1415
```

'The following set of commands creates and opens two files, in
'which, the data and the plot of the final state height profile of
'the selected cantilever beam are stored

```
let filename = basename, "_beam_", @du, ".dat"  
let chartname = basename, "_beam_", @du, ".bmp"  
fopen filename  
fopen chartname
```

'The following set of commands stores the data and the plot of the
'final state height profile of the selected cantilever beam in the
'corresponding files

```
for j = 0 to asize[final]-1 j+1  
{  
  let position[j] = scale*j  
  let zfinal[j] = final[j] + abs[final[asize[final]-1]]  
  fprintf filename | position[j]; zfinal[j]  
}
```

```
mchart Profile, position, zfinal  
let profilename = "Profile of beam", @du  
mtitle Profile, profilename  
maxisx Profile, "Lateral Position in microns"  
maxisy Profile, "Vertical Position in microns"  
wrtmchart Profile, chartname
```

```
fclose chartname
```

'The following set of commands determines the crack length of the
'selected cantilever beam

```
print "Analysis of Beam", @du  
let tempmin = 100  
  
for i = 0 to asize[position]-1 i+1  
{  
  let s = position[i]  
  let h_error = 0  
  clr_array x_fit  
  clr_array y_fit  
  
  for j = 0 to asize[position]-1 j+1  
  {  
    let x_fit[j] = position[j]  
    if (x_fit[j] < s)  
    {  
      let y_fit[j] = zfinal[0]*(2*position[j]^3/s^3
```

```

        - 3*position[j]^2/s^2 + 1)
    }
    else
    {
        let y_fit[j] = zfinal[0]*(2*s^3/s^3 - 3*s^2/s^2 + 1)
    }
    let h_error = h_error + ((zfinal[j] - y_fit[j])^2)
}

let avg_error = h_error/asize[x_fit]
print "When s = ", position[i], " microns"
print "The error is ", avg_error
if (avg_error <= tempmin)
{
    let tempmin = avg_error
    let s_found = s
}
refresh
}
print "Crack length of Beam", @du, " = ", s_found, " microns"

```

'The following set of commands fits the final state height profile of
'the selected cantilever beam to a third order polynomial of eta

```

for i = 0 to s_found/scale i+1
{
    let eta[i] = position[i]/s_found
    let deflection[i] = zfinal[i]
}

poly_fit eta, deflection, coefs, errv, 3
print "The coefficients are: ", coefs[3], " ,", coefs[2], " ,",
      coefs[1], " ,", coefs[0]
print "The polyfit error is: ", errv

clr_array x_fit
clr_array y_fit

for i = 0 to asize[eta]-1 i+1
{
    let x_fit[i] = eta[i]
    let y_fit[i] = coefs[3]*eta[i]^3 + coefs[2]*eta[i]^2
                  + coefs[1]*eta[i] + coefs[0]
    chart x_fit[i], y_fit[i], 2
    chart x_fit[i], zfinal[i], 1
}

```

```

'The following set of commands determines the apparent work of
'adhesion of the selected cantilever beam and stores it and the
'corresponding crack length in the data file opened previously
  let term1 = E*3*(t^3)/2/(s_found^4)
  let term2 = (coefs[3]^2) + (coefs[3]*coefs[2]) + (1/3)*(coefs[2]^2)
  let work = term1*term2/1000
  let m_bob = 2 - coefs[3]/coefs[0]
  let m_me = -coefs[2]/coefs[3]
  print "m_bob = ", m_bob
  print "m_me = ", m_me
  print " "
  print " "
  print " "
  print "The crack length of Beam", @du, " is ", s_found, " microns"
  fprintf filename| "The crack length of Beam", @du, " is ", s_found,
    " microns"
  if (s_found == position[asize[position]-1])
  {
    print "Beam", @du," is arc-shaped with m_bob = ", m_bob, ", m_me =
      = ", m_me, "."
    fprintf filename| "Beam", @du, " is arc-shaped with m_bob = ",
      m_bob, ", m_me = ",m_me, "."
  }
  else
  {
    print "Beam", @du," is S-shaped with m_bob = ", m_bob, ", m_me =
      ", m_me"."
    fprintf filename|"Beam", @du," is S-shaped with m_bob = ", m_bob,
      ", m_me = ", m_me"."
  }
  print "The apparent work of adhesion of Beam", @du, " is: ", work,
    " mJ/m^2."
  fprintf filename|"The apparent work of adhesion of Beam", @du, "is:
    ", work, " mJ/m^2."

fclose filename
mchrtclr Profile
clrrec test
clr_array out
clr_array final
clr_array position
clr_array zfinal
clr_array eta
clr_array coefs

```

```

    clr_array deflection
  }
}

```

```
grab_stop
```

A.5 Script Name: SB Actuation and Analysis.stp

'The following set of commands declares the variables that can be
'inputted by the user

```

ustring basename, "Samplerefno", "Base of filenames"
uglobal status, 1, "1_online 0_offline"
uglobal analysis, 0, "1_analysis 0_no_analysis"
uglobal nobtba, 1, "No. of beams to be analyzed"
uglobal maxv, 65, "Maximum actuation voltage"
uglobal minv, 0, "Minimum actuation voltage"
uglobal incr, 1, "Voltage increment"
uglobal gaino, 20, "gain of the TEGAM"
uglobal s_found, 1965, "Observed crack length (in microns)"
uglobal E, 130000000000, "Young's modulus of device layer (in Pa)"
uglobal t, 3.255, "Sidewall beam thickness (in microns)"
uglobal h, 9.77, "As-fabricated distance between Sidewall beams"

```

```

desc "This script electrostatically actuates"
desc "a pair of sidewall beams as well as"
desc "determines the apparent of work of"
desc "adhesion between them."
desc " "
desc "Created by NAVEED - 04/21/09"

```

```
include init.mac
```

```
begin
```

```

call init
grab_init

```

```
video_on
```

'The following set of commands declares the variables used in the
'script

```

alloc voltage
alloc readytomove 0
alloc increasing 1
alloc decreasing 1

```

```

alloc scale
alloc xp1
alloc yp1
alloc xp2
alloc yp2
alloc work

string fname
string msg

let scale = 0.465*10/mag
outv 0 : 3.45
fireset "shutter", 300

if (status == 1)
{
'The following set of commands actuates a pair of sidewall beams
'electrostatically
  let voltage = minv
  while (increasing > 0.5)
  {
    while (readytomove < 0.5)
    {
      print voltage
      outv 1: voltage/gaino
      select readytomove
    }
    if (voltage == maxv)
    {
      let fname = basename, "_actuated_", @dvoltage, "V.tif"
      fopen fname
      grab
      wrtingt fname
      fclose fname
    }
    let readytomove = 0
    let voltage = voltage + incr
    if (voltage > maxv)
    {
      let increasing = 0
    }
  }
}

let voltage = maxv-incr
while (decreasing > 0.5)

```

```

{
while (readytomove < 0.5)
{
print voltage
outv 1: voltage/gaino
select readytomove
}
if (voltage == minv)
{
let fname = basename, "_released_", @dvoltage, "V.tif"
fopen fname
grab
wrtimgt fname
fclose fname
}
let readytomove = 0
let voltage = voltage - incr
if (voltage < minv)
{
let decreasing = 0
}
}
}

if (a == 1)
{
'The following set of commands determines the apparent work of
'adhesion of an electrostatically actuated pair of sidewall beams
if (s_found == 0)
{
for u = 1 to nobtba u+1
{
let fname = basename, "_released_0V.tif"
rdimg fname
let msg = "Select starting pt. on Beam", @du
msgbox msg
point xp1, yp1
let msg = "Select end of crack length on Beam", @du
msgbox msg
point xp2, yp2
let s_found = scale*(xp2-xp1)
print "The crack length of Beam", @du,"is ", @ds_found,
" microns."
let work = E*3*(t^3)/(s_found^4)/1000*(h^2)/4
print "The work of adhesion of Beam", @du,"is: ", work,

```

```

        " mJ/m^2."
    }
}
if (s_found != 0)
{
    print "The crack length of Beam", @d1, "is ", s_found, " microns."
    let work = E*3*(t^3)/(s_found^4)/1000*(h^2)/4
    print "The work of adhesion of Beam is: ", work, " mJ/m^2."
}
}

```

grab_stop

A.6 Script Name: Comb - drive Actuator Calibration.stp

'The following set of commands declares the variables that can be
'inputted by the user

```

ustring basename, "Samplerefno", "Base of filenames"
uglobal num, 50, "Number of 1V increments"
uglobal gaino, 20, "Gain of the voltage amplifier"
uglobal p, 1, "1_pull_cycle 0_no_pull_cycle"
uglobal pb, 0, "1_pullback_cycle 0_no_pullback_cycle"
uglobal E, 130000000000, "Young's modulus of device layer (in Pa)"
uglobal t, 1.884632, "Thickness of restoring springs (in microns)"
uglobal w, 2.79, "Width of restoring springs (in microns)"
uglobal L, 300, "Length of restoring springs (in microns)"
uglobal n, 25, "No. of suspended comb fingers"
uglobal xo, 8.835, "Initial overlap (in microns)"
uglobal g, 2.79, "Initial gap (in microns)"

```

```

desc "This script applies an increasing DC voltage"
desc "to the comb-drive actuator and determines the"
desc "corresponding displacement of the suspended"
desc "shuttle using a pattern matching technique. It"
desc "can be used to calibrate a comb drive actuator."
desc "Created by Naveed - 05/27/2009"

```

include init.mac

begin

call init

'The following set of commands declares the variables used in the
'script

```
alloc scale
alloc voltage
alloc voltage_pb
alloc device_x_init_pos
alloc device_y_init_pos
alloc device_x_pos
alloc device_y_pos
alloc substrate_x_init_pos
alloc substrate_y_init_pos
alloc substrate_x_pos
alloc substrate_y_pos
alloc x_disp
alloc y_disp
alloc kx
alloc ky
alloc ky_pb
alloc ke
alloc ke_pb
```

```
string fname
string msg
```

```
array voltage
array voltage_pb
array x_pos
array x_pos_pb
array y_pos
array y_pos_pb
```

```
let scale = 0.465*10/mag
print "Scale = ", scale
outv 0 : 3.45
fireset "shutter", 300
```

'The following set of commands asks the user to select the anchored
'and movable patterns that should be used to track the displacement
'of the suspended shuttle and determines their initial positions

```
snap
```

```
let msg = "Select ROI & pattern on the anchor"
```

```
msgbox msg
```

```
pattern substrate
```

```
let msg = "Select ROI & pattern on the shuttle"
```

```
msgbox msg
```

```
pattern device
```

```
match substrate, substrate_x_init_pos, substrate_y_init_pos
```

```

match device, device_x_init_pos, device_y_init_pos

if (p == 1)
{
'The following set of commands creates and opens a data file, in
'which, the voltages applied to one of the two comb-drive actuators
'and the corresponding displacements of the suspended shuttle are
'stored
  let fname = basename, "_inc_disp.dat"
  fopen fname
  fprintf fname| "Voltage (V)"; "sq. Voltage (sq. V)"; "x_disp
                (microns)"; "y_disp (microns)"; "ky (N/m)"; "ke (N/m)"

'The following set of commands applies an increasing voltage to
'one of the two comb-drive actuators, determines the
'corresponding displacements of the suspended shuttle using the
'pattern matching technique and stores the applied voltage and
'shuttle displacements in the data file opened previously. It also
'determines the theoretical lateral mechanical and the theoretical
'lateral electrostatic stiffnesses of the suspension springs of the
'suspended structure, which change with the displacement of the
'shuttle, and stores them in the data file opened previously
  for i = 0 to num i+1
  {
    outv 1: i/gaino
    let voltage[i] = i
    print "Voltage = ", i
    delay 1
    snap
    match substrate, substrate_x_pos, substrate_y_pos
    match device, device_x_pos, device_y_pos,
    let x_disp = device_x_pos - substrate_x_pos + substrate_x_init_pos
                - device_x_init_pos
    let y_disp = device_y_pos - substrate_y_pos + substrate_y_init_pos
                - device_y_init_pos
    print "x_disp = ", x_disp*scale, " microns, y_disp = ",
          y_disp*scale, " microns"
    let x_pos[i] = x_disp*scale
    let y_pos[i] = y_disp*scale
    'For the tangential arm of SFAT
    'let ky = E*w*t/L/1000000*((8*(t^2))/((3*(y_pos[i]^2)) +
    (8*(t^2))))
    'For the normal arm of SFAT and the comb-drive actuator of
    'Resonator
    let ky = 50/9*E*w/L/(x_pos[i]^2)*(t^3)/1000000

```

```

'For the tangential arm of SFAT
let ke = n*8.85/1000000000000*t*(y_pos[i] + xo)*(voltage[i]^2
      *1000000*((1/((g - x_pos[i])^3)) + (1/((g - x_pos[i])^3)))
'For the normal arm of SFAT and the comb-drive actuator of
'Resonator
let ke = n*8.85/1000000000000*t*(x_pos[i] + xo)*(voltage[i]^2
      *1000000*((1/((g - y_pos[i])^3)) + (1/((g - y_pos[i])^3)))
print "ky = ", ky, "N/m"
print "ke = ", ke, "N/m"
fprintf fname| voltage[i]; voltage[i]^2; x_pos[i]; y_pos[i]; ky; ke
}
fclose fname
}

if (pb == 1)
{
'The following set of commands creates and opens a data file, in
'which, the voltages applied to the other of the two comb-drive
'actuators and the corresponding displacements of the suspended
'shuttle are stored
  let fname = basename, "_dec_disp.dat"
  fopen fname
  fprintf fname| "Voltage (V)"; "sq. Voltage (sq. V)"; "x_disp
      (microns)"; "y_disp (microns)"; "ky (N/m)"; "ke (N/m)"
  let msg = "Hit select to start the pull back cycle"
  msgbox msg
  wait

'The following set of commands applies an increasing voltage to the
'other of the two comb-drive actuators, determines the corresponding
'displacements of the suspended shuttle using the pattern matching
'technique and stores the applied voltage and shuttle displacements
'in the data file opened previously. It also determines the
'theoretical lateral mechanical and the theoretical lateral
'electrostatic stiffnesses of the suspension springs of the suspended
'structure, which change with the displacement of the shuttle, and
'stores them in the data file opened previously
  for i = 0 to num i+1
  {
    outv 2: i/gaino
    let voltage_pb[i] = i
    print "Voltage_pb = ", i
    delay 1
    snap
    match substrate, substrate_x_pos, substrate_y_pos

```

```

match device, device_x_pos, device_y_pos
let x_disp = device_x_pos - substrate_x_pos + substrate_x_init_pos
            - device_x_init_pos
let y_disp = device_y_pos - substrate_y_pos + substrate_y_init_pos
            - device_y_init_pos
print "x_disp = ", x_disp*scale, " microns, y_disp = ",
      y_disp*scale, " microns"
let x_pos_pb[i] = x_disp*scale
let y_pos_pb[i] = y_disp*scale
'For the tangential arm of SFAT
'let ky_pb = E*w*t/L/1000000*((8*(t^2))/((3*(y_pos_pb[i]^2)
            + (8*(t^2))))
'For the normal arm of SFAT and the comb-drive actuator of
'Resonator
let ky_pb = 50/9*E*w/L/(x_pos_pb[i]^2)*(t^3)/1000000
'For the tangential arm of SFAT
let ke_pb = n*8.85/1000000000000*t*(y_pos_pb[i] + xo)
            *(voltage_pb[i]^2)*1000000*((1/((g - x_pos_pb[i])^3))
            + (1/((g - x_pos_pb[i])^3)))
'For the normal arm of SFAT and the comb-drive actuator of
'Resonator
let ke_pb = n*8.85/1000000000000*t*(x_pos_pb[i] + xo)
            *(voltage_pb[i]^2)*1000000*((1/((g - y_pos_pb[i])^3))
            + (1/((g - y_pos_pb[i])^3)))
print "ky_pb = ", ky_pb, "N/m"
print "ke_pb = ", ke_pb, "N/m"
fprintf fname| voltage_pb[i]; voltage_pb[i]; x_pos_pb[i];
            y_pos_pb[i]; ky_pb; ke_pb
}
fclose fname
}

outv 1: 0
outv 2: 0

for i = 0 to asize[voltage]-1 i+1
{
  if (p == 1)
  {
'The following set of commands plots the voltages applied to one of
'the two comb-drive actuators versus the corresponding x and y
'displacements of the suspended shuttle
  chart voltage[i], x_pos[i], 1
  chart voltage[i], y_pos[i], 2
  }
}

```

```

    if (pb == 1)
    {
    'The following set of commands plots the voltages applied to the
    'other of the two comb-drive actuators versus the corresponding x
    'and y displacements of the suspended shuttle
        chart voltage_pb[i], x_pos_pb[i], 3
        chart voltage_pb[i], y_pos_pb[i], 4
    }
}

let msg = "Hit select to see the next chart"
msgbox msg
wait
chrtclr

for j = 0 to asize[voltage]-1 j+1
{
    if (p == 1)
    {
    'The following set of commands plots the square of the voltages
    'applied to one of the two comb-drive actuators versus the
    'corresponding x and y displacements of the suspended shuttle
        chart ((voltage[j])^2), x_pos[j], 1
        chart ((voltage[j])^2), y_pos[j], 2
    }
    if (pb == 1)
    {
    'The following set of commands plots the square of the voltages
    'applied to the other of the two comb-drive actuators versus the
    'corresponding x and y displacements of the suspended shuttle
        chart ((voltage_pb[j])^2), x_pos_pb[j], 3
        chart ((voltage_pb[j])^2), y_pos_pb[j], 4
    }
}

}

'The following set of commands determines the theoretical axial
'stiffness of the suspension springs of the suspended structure and
'stores it in the data file opened previously
'For the tangential arm of SFAT
'let kx = E*t/1000000*((w/L)^3)
'For the normal arm of SFAT and the comb-drive actuator of Resonator
let kx = 2*E*t/1000000*((w/L)^3)
print "kx_theoretical = ", kx, " N/m"
fprintf fname| "kx_theoretical = ", kx, " N/m"

```

A.7 Script Name: SFT Normal Arm Comb - drive Actuator Calibration.stp

```
'The following set of commands declares the variables that can be
'inputted by the user
ustring basename, "Samplerefno", "Base of filenames"
uglobal Va, 40, "V req. to align the normal arm with the anch. post"
uglobal num, 50, "Number of 1V increments"
uglobal gaino, 20, "Gain of the voltage amplifier"
uglobal p, 1, "1_pull_cycle 0_no_pull_cycle"
uglobal pb, 0, "1_pullback_cycle 0_no_pullback_cycle"
uglobal E, 130000000000, "Young's modulus of device layer (in Pa)"
uglobal t, 1.884632, "Thickness of restoring springs (in microns)"
uglobal w, 2.79, "Width of restoring springs (in microns)"
uglobal L, 300, "Length of restoring springs (in microns)"
uglobal n, 25, "No. of suspended comb fingers"
uglobal xo, 8.835, "Initial overlap (in microns)"
uglobal g, 2.79, "Initial gap (in microns)"

desc "This script 1st aligns the normal arm with"
desc " the anchored post, then applies an increasing "
desc "DC V to the normal arm and determines the"
desc "corresponding displacement of the suspended"
desc "shuttle using a pattern matching technique."
desc "Created by Naveed - 05/27/2009"

include init.mac

begin

call init

'The following set of commands declares the variables used in the
'script
alloc scale
alloc voltage
alloc voltage_pb
alloc device_x_init_pos
alloc device_y_init_pos
alloc device_x_pos
alloc device_y_pos
alloc substrate_x_init_pos
alloc substrate_y_init_pos
alloc substrate_x_pos
alloc subsrate_y_pos
```

```

alloc x_disp
alloc y_disp
alloc kx
alloc ky
alloc ky_pb
alloc ke
alloc ke_pb

string fname
string msg

array voltage_t
array voltage
array voltage_pb
array x_pos
array x_pos_pb
array y_pos
array y_pos_pb

let scale = 0.465*10/mag
print "Scale = ", scale
outv 0 : 3.45
fireset "shutter", 300

'The following set of commands asks the user to select the anchored
'and movable patterns that should be used to track the displacement
'of the suspended shuttle and determines their initial positions
snap
let msg = "Select ROI & pattern on the anchor"
msgbox msg
pattern substrate
let msg = "Select ROI & pattern on the shuttle"
msgbox msg
pattern device
match substrate, substrate_x_init_pos, substrate_y_init_pos
match device, device_x_init_pos, device_y_init_pos

'The following set of commands creates and opens a data file, in
'which, the voltages applied to the tangential comb-drive actuator
'to align the normal arm with the anchored posts and the corresponding
'displacements of the suspended shuttle are
'stored
let fname = basename,"_align.dat"
fopen fname
fprintf fname| "Voltage (V)"; "sq. Voltage (sq. V)"; "x_disp

```

```

(microns)"; "y_disp (microns)"

'The following set of commands applies a voltage of Va to the
'tangential comb-drive actuator in order to align the normal arm with
'the anchored posts. It determines the corresponding displacement of
'the loading beam using the pattern matching technique and stores it
'in the data file opened previously
for i = 0 to Va i+1
{
  outv 3: i/gaino
  print "Vt = ", i
  delay 0.5
  snap
  match substrate, substrate_x_pos, substrate_y_pos
  match device, device_x_pos, device_y_pos
  let x_disp = device_x_pos - substrate_x_pos + substrate_x_init_pos
    - device_x_init_pos
  let y_disp = device_y_pos - substrate_y_pos + substrate_y_init_pos
    - device_y_init_pos
  print "x_disp = ", scale*x_disp, " microns, y_disp = ",
    scale*y_disp, " microns"
  let voltage_t[i] = i
  fprintf fname| voltage_t[i]; voltage_t[i]^2; x_disp*scale; y_disp*scale
}
fclose fname
wait

fireset "shutter", 200
delay 0.5

'The following set of commands collects an interferogram showing the
'SFT after the normal arm is aligned with the anchored posts
snap
wrtimgt basename,"_normal_arm_aligned_fringes.tif"
wait

fireset "shutter",300
delay 0.5

'The following set of commands collects an optical image showing the
'SFT after the normal arm is aligned with the anchored posts
snap
wrtimgt basename,"_normal_arm_aligned.tif"

wait

```

```

fireset "shutter",200
delay 0.5
video_on

if (p == 1)
{
'The following set of commands creates and opens a data file, in
'which, the voltages applied to one of the two comb-drive actuators
'and the corresponding displacements of the suspended shuttle are
'stored
  let fname = basename,"_inc_disp.dat"
  fopen fname
  fprintf fname| "Voltage (V)"; "sq. Voltage (sq. V)"; "x_disp
                (microns)"; "y_disp (microns)"; "ky (N/m)"; "ke (N/m)"

'The following set of commands applies an increasing voltage to
'one of the two comb-drive actuators, determines the
'corresponding displacements of the suspended shuttle using the
'pattern matching technique and stores the applied voltage and
'shuttle displacements in the data file opened previously. It also
'determines the theoretical lateral mechanical and the theoretical
'lateral electrostatic stiffnesses of the suspension springs of the
'suspended structure, which change with the displacement of the
'shuttle, and stores them in the data file opened previously
  for i = 0 to num i+1
  {
    outv 1: i/gaino
    let voltage[i] = i
    print "Voltage = ", i
    delay 1
    snap
    match substrate, substrate_x_pos, substrate_y_pos
    match device, device_x_pos, device_y_pos,
    let x_disp = device_x_pos - substrate_x_pos + substrate_x_init_pos
                - device_x_init_pos
    let y_disp = device_y_pos - substrate_y_pos + substrate_y_init_pos
                - device_y_init_pos
    print "x_disp = ", x_disp*scale, " microns, y_disp = ",
          y_disp*scale, " microns"
    let x_pos[i] = x_disp*scale
    let y_pos[i] = y_disp*scale
    'For the tangential arm of SFAT
    'let ky = E*w*t/L/1000000*((8*(t^2))/((3*(y_pos[i]^2)) +
                (8*(t^2))))

```

```

'For the normal arm of SFAT and the comb-drive actuator of
'Resonator
let ky = 50/9*E*w/L/(x_pos[i]^2)*(t^3)/1000000
'For the tangential arm of SFAT
let ke = n*8.85/1000000000000*t*(y_pos[i] + xo)*(voltage[i]^2
      *1000000*((1/((g - x_pos[i])^3)) + (1/((g - x_pos[i])^3)))
'For the normal arm of SFAT and the comb-drive actuator of
'Resonator
let ke = n*8.85/1000000000000*t*(x_pos[i] + xo)*(voltage[i]^2
      *1000000*((1/((g - y_pos[i])^3)) + (1/((g - y_pos[i])^3)))
print "ky = ", ky, "N/m"
print "ke = ", ke, "N/m"
fprintf fname| voltage[i]; voltage[i]^2; x_pos[i]; y_pos[i]; ky; ke
}
fclose fname
}

if (pb == 1)
{
'The following set of commands creates and opens a data file, in
'which, the voltages applied to the other of the two comb-drive
'actuators and the corresponding displacements of the suspended
'shuttle are stored
  let fname = basename, "_dec_disp.dat"
  fopen fname
  fprintf fname| "Voltage (V)"; "sq. Voltage (sq. V)"; "x_disp
                (microns)"; "y_disp (microns)"; "ky (N/m)"; "ke (N/m)"
  let msg = "Hit select to start the pull back cycle"
  msgbox msg
  wait

'The following set of commands applies an increasing voltage to the
'other of the two comb-drive actuators, determines the corresponding
'displacements of the suspended shuttle using the pattern matching
'technique and stores the applied voltage and shuttle displacements
'in the data file opened previously. It also determines the
'theoretical lateral mechanical and the theoretical lateral
'electrostatic stiffnesses of the suspension springs of the suspended
'structure, which change with the displacement of the shuttle, and
'stores them in the data file opened previously
  for i = 0 to num i+1
  {
    outv 2: i/gaino
    let voltage_pb[i] = i
    print "Voltage_pb = ", i
  }
}

```

```

delay 1
snap
match substrate, substrate_x_pos, substrate_y_pos
match device, device_x_pos, device_y_pos
let x_disp = device_x_pos - substrate_x_pos + substrate_x_init_pos
            - device_x_init_pos
let y_disp = device_y_pos - substrate_y_pos + substrate_y_init_pos
            - device_y_init_pos
print "x_disp = ", x_disp*scale, " microns, y_disp = ",
      y_disp*scale, " microns"
let x_pos_pb[i] = x_disp*scale
let y_pos_pb[i] = y_disp*scale
'For the tangential arm of SFAT
'let ky_pb = E*w*t/L/1000000*((8*(t^2))/((3*(y_pos_pb[i]^2)
            + (8*(t^2))))
'For the normal arm of SFAT and the comb-drive actuator of
'Resonator
let ky_pb = 50/9*E*w/L/(x_pos_pb[i]^2)*(t^3)/1000000
'For the tangential arm of SFAT
let ke_pb = n*8.85/10000000000000*t*(y_pos_pb[i] + xo)
            *(voltage_pb[i]^2)*1000000*((1/((g - x_pos_pb[i])^3))
            + (1/((g - x_pos_pb[i])^3)))
'For the normal arm of SFAT and the comb-drive actuator of
'Resonator
let ke_pb = n*8.85/10000000000000*t*(x_pos_pb[i] + xo)
            *(voltage_pb[i]^2)*1000000*((1/((g - y_pos_pb[i])^3))
            + (1/((g - y_pos_pb[i])^3)))
print "ky_pb = ", ky_pb, "N/m"
print "ke_pb = ", ke_pb, "N/m"
fprintf fname| voltage_pb[i]; voltage_pb[i]; x_pos_pb[i];
            y_pos_pb[i]; ky_pb; ke_pb
}
fclose fname
}

outv 1: 0
outv 2: 0
outv 3: 0

for i = 0 to asize[voltage]-1 i+1
{
  if (p == 1)
  {
'The following set of commands plots the voltages applied to one of
'the two comb-drive actuators versus the corresponding x and y

```

```

'displacements of the suspended shuttle
  chart voltage[i], x_pos[i], 1
  chart voltage[i], y_pos[i], 2
}
if (pb == 1)
{
'The following set of commands plots the voltages applied to the
'other of the two comb-drive actuators versus the corresponding x
'and y displacements of the suspended shuttle
  chart voltage_pb[i], x_pos_pb[i], 3
  chart voltage_pb[i], y_pos_pb[i], 4
}
}

let msg = "Hit select to see the next chart"
msgbox msg
wait
chrtclr

for j = 0 to asize[voltage]-1 j+1
{
  if (p == 1)
  {
'The following set of commands plots the square of the voltages
'applied to one of the two comb-drive actuators versus the
'corresponding x and y displacements of the suspended shuttle
    chart ((voltage[j])^2), x_pos[j], 1
    chart ((voltage[j])^2), y_pos[j], 2
  }
  if (pb == 1)
  {
'The following set of commands plots the square of the voltages
'applied to the other of the two comb-drive actuators versus the
'corresponding x and y displacements of the suspended shuttle
    chart ((voltage_pb[j])^2), x_pos_pb[j], 3
    chart ((voltage_pb[j])^2), y_pos_pb[j], 4
  }
}

'The following set of commands determines the theoretical axial
'stiffness of the suspension springs of the suspended structure and
'stores it in the data file opened previously
'For the tangential arm of SFAT
'let kx = E*t/1000000*((w/L)^3)

```

```

'For the normal arm of SFAT and the comb-drive actuator of Resonator
let kx = 2*E*t/1000000*((w/L)^3)
print "kx_theoretical = ", kx, " N/m"
fprintf fname| "kx_theoretical = ", kx, " N/m"

```

A.8 Script Name: SFT Friction Test.stp

```

'The following set of commands declares the variables that can be
'inputted by the user
ustring basename, "Samplerefno, "Base of filenames"
uglobal Va, 40, "V req. to align the normal arm with the anch. post"
uglobal Vn, 60, "Max. V appl. to the norm. comb-drive actuator"
uglobal Vt, 200, "No. of 0.2V incr. appl. to the tang. comb-drive act."
uglobal gaino, 20, "Gain of the voltage amplifier"

```

```

desc "This script 1st aligns the normal arm with the"
desc "anchored post, then applies a normal load of Vn"
desc " at the sidewall interf., then applies an incr. tang."
desc "load to shear the interf. It detects the onset of"
desc "slip using the pattern matching tech. to study fric."
desc "Created by Naveed - 06/24/09"

```

```
include init.mac
```

```
begin
```

```
call init
```

```

'The following set of commands declares the variables used in the
'script

```

```

alloc scale
alloc device_x_init_pos
alloc device_y_init_pos
alloc device_x_pos
alloc device_y_pos
alloc substrate_x_init_pos
alloc substrate_y_init_pos
alloc substrate_x_pos
alloc subsrate_y_pos
alloc x_disp
alloc y_disp

```

```
string fname
```

```
string msg
```

```

array voltage
array x_pos
array y_pos

let scale2 = 0.465*10/mag
print "Scale = ", scale
outv 0 : 3.45

fireset "shutter",300
delay 0.5

'The following set of commands asks the user to select the anchored
'and movable patterns that should be used to track the tangential
'displacements of the loading beam and determines their initial
'positions
snap
let msg = "Select ROI & pattern on the anchor"
msgbox msg
pattern substrate
let msg = "Select ROI & pattern on the shuttle"
msgbox msg
pattern device
match substrate, substrate_x_init_pos, substrate_y_init_pos
match device, device_x_init_pos, device_y_init_pos

'The following set of commands creates and opens a data file, in
'which, the voltages applied to the tangential comb-drive actuator
'and the corresponding tangential displacements of the loading beam
'are stored
let fname = basename,"_fric_test.dat"
fopen fname
fprintf fname| "Voltage (V)"; "x_disp (microns)"; "y_disp (microns)"

'The following set of commands applies a voltage of Va to the
'tangential comb-drive actuator in order to align the normal arm with
'the anchored posts. It determines the corresponding displacement of
'the loading beam using the pattern matching technique and stores it
'in the data file opened previously
for i = 0 to Va i+1
{
  outv 2: i/gaino
  print "Vt = ", i
  delay 0.5
  snap
  match substrate, substrate_x_pos, substrate_y_pos

```

```

match device, device_x_pos, device_y_pos
let x_disp = device_x_pos - substrate_x_pos + substrate_x_init_pos
            - device_x_init_pos
let y_disp = device_y_pos - substrate_y_pos + substrate_y_init_pos
            - device_y_init_pos
print "x_disp = ", scale*x_disp, " microns, y_disp = ",
      scale*y_disp, " microns"
let voltage[i] = i
let x_pos[i] = x_disp*scale
let y_pos[i] = y_disp*scale
fprintf fname| voltage[i]; x_pos[i]; y_pos[i]
}

wait

fireset "shutter", 200
delay 0.5

'The following set of commands collects an interferogram showing the
'SFT after the normal arm is aligned with the anchored posts
snap
wrtimgt basename,"_normal_arm_aligned_fringes.tif"
wait

fireset "shutter",300
delay 0.5

'The following set of commands collects an optical image showing the
'SFT after the normal arm is aligned with the anchored posts
snap
wrtimgt basename,"_normal_arm_aligned.tif"

wait

fireset "shutter",200
delay 0.5
video_on

'The following set of commands applies an increasing DC voltage to
'the push drive of the normal comb-drive actuator in order to bring
'the loading beam in contact with the anchored post and apply the
'desired normal load Vn at the sidewall interface
for i = 0 to Vn i+1
{
  outv 1: i/gaino

```

```

    print "Vn= ",i
    delay 1
    refresh
}

video_off

'The following set of commands collects an interferogram showing the
'SFT after the loading beam is brought in contact with the anchored
'post and a normal load of Vn is applied at the sidewall interface
snap
wrtimgt basename, "_beam_post_contact_fringes.tif"

wait

fireset "shutter",300
delay 0.5

'The following set of commands collects an optical image showing the
'SFT after the loading beam is brought in contact with the anchored
'post and a normal load of Vn is applied at the sidewall interface
snap
wrtimgt basename, "_beam_post_contact.tif"

'The following set of commands applies an increasing voltage to the
'tangential comb-drive actuator, determines the corresponding
'tangential displacements of the loading beam using the pattern
'matching technique and stores the applied voltage and tangential
'displacements of the loading beam in the data file opened previously.
for i = 0 to Vt i+1
{
    outv 2: Va + i/gaino/5
    print "Vt = ", i
    delay 0.5
    snap
    match substrate, substrate_x_pos, substrate_y_pos
    match device, device_x_pos, device_y_pos
    let x_disp = device_x_pos - substrate_x_pos + substrate_x_init_pos
                - device_x_init_pos
    let y_disp = device_y_pos - substrate_y_pos + substrate_y_init_pos
                - device_y_init_pos
    print "x_disp = ", scale*x_disp, " microns, y_disp = ",
          scale*y_disp, " microns"
    let voltage[Va + i] = Va + i/5
    let x_pos[Va+i] = x_disp*scale

```

```

    let y_pos[Va + i] = y_disp*scale
    fprintf fname| voltage[Va + i]; x_pos[Va + i]; y_pos[Va + i]
}

'The following command collects an optical image of the SFT showing
'the sidewall interface after the completion of the friction test
wrtimgt basename,"_final_state.tif"
fclose fname

outv 2: 0
delay 1
outv 1: 0

'The following set of commands plots the voltages applied to pull
'drive of the tangential comb-drive actuator versus the corresponding
'x and y displacements of the loading beam
for i = 0 to asize[voltage]-1 i+1
{
    chart voltage[i], x_pos[i], 1
    chart voltage[i], y_pos[i], 2
}

```

A.9 Script Name: SFAT Friction Test.stp

```

'The following set of commands declares the variables that can be
'inputted by the user
uststring basename, "Samplerefno", "Base of filenames"
uglobal Vn, 75, "Max. V appl. to the norm. comb-drive actuator"
uglobal Vt, 200, "No. of 1V incr. appl. to the tang. comb-drive act."
uglobal gaino, 20, "Gain of the voltage amplifier"

desc "This script applies a normal load of Vn at the "
desc "sidewall interf. using the norm. comb-drive act."
desc "& then applies an incr. tang. load at it using"
desc "the tang. comb-drive act. It detects the onset of"
desc "slip using the pattern matching tech. to study fric."
desc "Created by Naveed - 06/24/09"

include init.mac

begin

call init

'The following set of commands declares the variables used in the

```

```

'script
alloc scale
alloc device_x_init_pos
alloc device_y_init_pos
alloc device_x_pos
alloc device_y_pos
alloc substrate_x_init_pos
alloc substrate_y_init_pos
alloc substrate_x_pos
alloc substrate_y_pos
alloc x_disp
alloc y_disp

string fname
string msg

array voltage
array x_pos
array y_pos

video_on
let scale2 = 0.465*10/mag
print "Scale = ", scale
outv 0 : 3.45

'The following set of commands applies an increasing DC voltage to
'the push drive of the normal comb-drive actuator in order to bring
'the normal arm in contact with the tangential arm and apply the
'desired normal load Vn at the sidewall interface
for i = 0 to Vn i+1
{
  outv 1: i/gaino
  print "Vn = ", i
  delay 1
  refresh
}
video_off

'The following set of commands collects an interferogram showing the
'SFAT after the normal arm is brought in contact with the tangential
'arm and a normal load of Vn is applied at the sidewall interface
snap
wrtimgt basename,"_normal_tangential_arm_contact_fringes.tif"
wait

```

```
fireset "shutter",300
delay 0.5
```

```
'The following set of commands collects an optical image showing the
'SFAT after the normal arm is brought in contact with the tangential
'arm and a normal load of Vn is applied at the sidewall interface
snap
wrtimgt basename,"_normal_tangential_arm_contact.tif"
```

```
'The following set of commands asks the user to select the anchored
'and movable patterns that should be used to track the displacement
'of the tangential arm and determines their initial positions
let msg = "Select ROI & pattern on the anchor"
msgbox msg
pattern substrate
let msg = "Select ROI & pattern on the shuttle"
msgbox msg
pattern device
match substrate, substrate_x_init_pos, substrate_y_init_pos
match device, device_x_init_pos, device_y_init_pos
```

```
'The following set of commands creates and opens a data file, in
'which, the voltages applied to the tangential comb-drive actuator
'and the corresponding displacements of the tangential arm are
'stored
let fname = basename,"_fric_test.dat"
fopen fname
fprintf fname| "Voltage (V)"; "x_disp (microns)"; "y_disp (microns)"
```

```
'The following set of commands applies an increasing voltage to the
'tangential comb-drive actuator, determines the corresponding
'displacements of the tangential arm using the pattern matching
'technique and stores the applied voltage and displacements of the
'tangential arm in the data file opened previously.
for i = 0 to Vt i+1
{
  outv 2: i/gaino
  print "Vt = ", i
  delay 0.5
  snap
  match substrate, substrate_x_pos, substrate_y_pos
  match device, device_x_pos, device_y_pos
  let x_disp = device_x_pos - substrate_x_pos + substrate_x_init_pos
    - device_x_init_pos
```

```

let y_disp = device_y_pos - substrate_y_pos + substrate_y_init_pos
            - device_y_init_pos
print "x_disp = ", scale*x_disp, " microns, y_disp = ",
      scale*y_disp, " microns"
let voltage[i] = i
let x_pos[i] = x_disp*scale
let y_pos[i] = y_disp*scale
fprintf fname| voltage[i]; x_pos[i]; y_pos[i]
}

```

```

'The following command collects an optical image of the SFAT showing
'the sidewall interface after the completion of the friction test
wrtimgt basename,"_final_state.tif"
fclose fname

```

```

outv 2: 0
delay 1
outv 1: 0

```

```

'The following set of commands plots the voltages applied to pull
'drive of the tangential comb-drive actuator versus the
'corresponding x and y displacements of the tangential arm
for i = 0 to asize[voltage]-1 i+1
{
  chart voltage[i], x_pos[i], 1
  chart voltage[i], y_pos[i], 2
}

```

A.10 Script Name: SFAT Adhesion Test.stp

```

'The following set of commands declares the variables that can be
'inputted by the user

```

```

ustring basename, "Samplerefno", "Base of filenames"
uglobal push, 30, "No. of 1V increments to form the interface"
uglobal pull, 45, "No. of 1V increments to break the interface"
uglobal gaino, 20, "Gain of the voltage amplifier"

```

```

desc "This script applies an incr. vol. to the push"
desc "drive of the norm. arm to bring it in contact"
desc "with the tang. arm and then applies an incr. vol."
desc "to its pull drive to break the sid. interf."
desc "Used to determine adhesion between sidewalls."
desc "Created by Naveed - 06/24/09"

```

```

include init.mac

```

```

begin

call init

'The following set of commands declares the variables used in the
'script
alloc scale
alloc device_x_init_pos_normal
alloc device_y_init_pos_normal
alloc device_x_pos_normal
alloc device_y_pos_normal
alloc substrate_x_init_pos_normal
alloc substrate_y_init_pos_normal
alloc substrate_x_pos_normal
alloc substrate_y_pos_normal
alloc x_disp_normal
alloc y_disp_normal
alloc device_x_init_pos_tangential
alloc device_y_init_pos_tangential
alloc device_x_pos_tangential
alloc device_y_pos_tangential
alloc substrate_x_init_pos_tangential
alloc substrate_y_init_pos_tangential
alloc substrate_x_pos_tangential
alloc substrate_y_pos_tangential
alloc x_disp_tangential
alloc y_disp_tangential

string fname
string msg

array voltage
array x_pos_normal
array y_pos_normal
array x_pos_tangential
array y_pos_tangential
array voltage_pb
array x_pos_pb_normal
array y_pos_pb_normal
array x_pos_pb_tangential
array y_pos_pb_tangential

let scale = 0.465*10/mag
print "Scale = ", scale

```

```
'The following set of commands asks the user to select the anchored  
'and movable patterns that should be used to track the displacement  
'of the normal arm and determines their initial positions
```

```
snap
```

```
let msg = "Select anchor on normal arm"
```

```
msgbox msg
```

```
pattern substrate_normal
```

```
let msg = "Select shuttle on normal arm"
```

```
msgbox msg
```

```
pattern device_normal
```

```
match substrate_normal, substrate_x_init_pos_normal,
```

```
    substrate_y_init_pos_normal
```

```
match device_normal, device_x_init_pos_normal,
```

```
    device_y_init_pos_normal
```

```
'The following set of commands asks the user to select the anchored  
'and movable patterns that should be used to track the displacement  
'of the tangential arm and determines their initial positions
```

```
let msg = "Select anchor on tangential arm"
```

```
msgbox msg
```

```
pattern substrate_tangential
```

```
let msg = "Select shuttle on tangential arm"
```

```
msgbox msg
```

```
pattern device_tangential
```

```
match substrate_tangential, substrate_x_init_pos_tangential,
```

```
    substrate_y_init_pos_tangential
```

```
match device_tangential, device_x_init_pos_tangential,
```

```
    device_y_init_pos_tangential
```

```
'The following set of commands creates and opens a data file, in  
'which, the voltages applied to the push drive of the normal arm  
'and the corresponding displacements of its suspended shuttle are  
'stored. The displacements of the suspended shuttle of the  
'tangential arm due to the voltages applied to the push drive of  
'the normal arm are also stored in the data file
```

```
let fname = basename, "_push.dat"
```

```
fopen fname
```

```
fprint fname| "Voltage (V)"; "x_disp_normal (microns)";
```

```
    "y_disp_normal (microns)"; "x_disp_tangential(microns)";
```

```
    "y_disp_tangential (microns)"
```

```
'The following set of commands applies an increasing voltage to  
'the push drive of the normal arm, determines the  
'corresponding displacements of its suspended shuttle using the
```

```

'pattern matching technique and stores the applied voltage and
'shuttle displacements in the data file opened previously. It also
'determines the displacements of the suspended shuttle of the
'tangential arm caused by the voltages applied to the push drive
'of the normal arm and stores them in the data file opened
'previously
for i = 0 to push i+1
{
  outv 1: i/gaino
  delay 1
  snap
  match substrate_normal, substrate_x_pos_normal,
        substrate_y_pos_normal
  match device_normal, device_x_pos_normal, device_y_pos_normal
  match substrate_tangential, substrate_x_pos_tangential,
        substrate_y_pos_tangential
  match device_tangential, device_x_pos_tangential,
        device_y_pos_tangential
  let x_disp_normal = device_x_pos_normal - substrate_x_pos_normal +
                    substrate_x_init_pos_normal
                    - device_x_init_pos_normal
  let y_disp_normal = device_y_pos_normal - substrate_y_pos_normal +
                    substrate_y_init_pos_normal
                    - device_y_init_pos_normal
  print "Voltage = ", i
  print "x_disp_normal = ", scale*x_disp_normal, " microns,
        y_disp_normal = ", scale*y_disp_normal,
        " microns"

  let voltage[i] = i
  let x_pos_normal[i] = x_disp_normal*scale
  let y_pos_normal[i] = y_disp_normal*scale
  let x_disp_tangential = device_x_pos_tangential
                        - substrate_x_pos_tangential
                        + substrate_x_init_pos_tangential
                        - device_x_init_pos_tangential
  let y_disp_tangential = device_y_pos_tangential
                        - substrate_y_pos_tangential
                        + substrate_y_init_pos_tangential
                        - device_y_init_pos_tangential
  print "x_disp_tang = ", scale*x_disp_tangential, " microns,
        y_disp_tang = ", scale*y_disp_tangential, " microns"
  let x_pos_tangential[i] = x_disp_tangential*scale
  let y_pos_tangential[i] = y_disp_tangential*scale
  fprintf fname| voltage[i]; x_pos_normal[i]; y_pos_normal[i];
        x_pos_tangential[i]; y_pos_tangential[i]
}

```

```

}
fclose fname

let msg "Hit select to start the pull back cycle"
msgbox msg
wait

'The following set of commands creates and opens a data file, in
'which, the voltages applied to the pull drive of the normal arm
'and the corresponding positions of its suspended shuttle are
'stored. The displacements of the suspended shuttle of the
'tangential arm due to the voltages applied to the pull drive of
'the normal arm are also stored in the data file
let fname = basename, "_pull.dat"
fopen fname
fprintf fname| "Voltage_pb (V)"; "x_disp_pb_normal (microns)";
              "y_disp_pb_normal (microns)"; "x_disp_pb_tangential
              (microns)"; "y_disp_pb_tangential (microns)"

'The following set of commands applies an increasing voltage to
'the pull drive of the normal arm, determines the
'corresponding positions of its suspended shuttle using the
'pattern matching technique and stores the applied voltage and
'shuttle positions in the data file opened previously. It also
'determines the displacements of the suspended shuttle of the
'tangential arm caused by the voltages applied to the pull drive
'of the normal arm and stores them in the data file opened
'previously
for i = 0 to pull*5 i+1
{
  outv 2: i/gaino/5
  delay 1
  snap
  match substrate_normal, substrate_x_pos_normal,
        substrate_y_pos_normal
  match device_normal, device_x_pos_normal, device_y_pos_normal
  match substrate_tangential, substrate_x_pos_tangential,
        substrate_y_pos_tangential
  match device_tangential, device_x_pos_tangential,
        device_y_pos_tangential
  let x_disp_normal = device_x_pos_normal - substrate_x_pos_normal
                    + substrate_x_init_pos_normal
                    - device_x_init_pos_normal
  let y_disp_normal = device_y_pos_normal - substrate_y_pos_normal
                    + substrate_y_init_pos_normal

```

```

        - device_y_init_pos_normal
print "x_disp = ", scale*x_disp_normal, " microns, y_disp = ",
      scale*y_disp_normal, " microns"
let voltage_pb[i] = i/5
let x_pos_pb_normal[i] = x_disp_normal*scale
let y_pos_pb_normal[i] = y_disp_normal*scale
let x_disp_tangential = device_x_pos_tangential
                      - substrate_x_pos_tangential
                      + substrate_x_init_pos_tangential
                      - device_x_init_pos_tangential
let y_disp_tangential = device_y_pos_tangential
                      - substrate_y_pos_tangential
                      + substrate_y_init_pos_tangential
                      - device_y_init_pos_tangential
print "x_disp_tang = ", scale*x_disp_tangential, " microns,
      y_disp = ", scale*y_disp_tangential, " microns"
let x_pos_pb_tangential[i] = x_disp_tangential*scale
let y_pos_pb_tangential[i] = y_disp_tangential*scale
fprintf fname| voltage_pb[i]; x_pos_pb_normal[i]; y_pos_pb_normal[i];
          x_pos_pb_tangential[i]; y_pos_pb_tangential[i]
}

```

```

outv 1: 0
outv 2: 0
fclose fname

```

```

'The following set of commands plots the voltages applied to push
'drive of the normal arm versus the corresponding x and y
'displacements of its suspended shuttle
for i = 0 to asize[voltage]-1 i+1
{
  chart voltage[i], x_pos_normal[i], 1
  chart voltage[i], y_pos_normal[i], 2
}

```

```

'The following set of commands plots the voltages applied to pull
'drive of the normal arm versus the corresponding x and y
'displacements of its suspended shuttle
for i = 0 to asize[voltage_pb]-1 i+1
{
  chart voltage_pb[i], x_pos_pb_normal[i], 3
  chart voltage_pb[i], y_pos_pb_normal[i], 4
}

```

A.11 Script Name: Pattern Matching Technique Uncertainty.stp

```
'The following set of commands declares the variables that can be
'inputted by the user
ustring basename, "Testno_obj_lens_mag", "Base of filenames"
uglobal n, 1000, "No. of measurements"

desc "This script measures the distance"
desc "between two fixed points in a live"
desc "image n times & calculates the"
desc "rms error in the measurement."
desc " "
desc "Created by Naveed - 11/21/2010"

include init.mac

begin

call init

'The following set of commands declares the variables used in the
'script
alloc scale
alloc device_x_pos
alloc device_y_pos
alloc substrate_x_pos
alloc substrate_y_pos
alloc device_x_init_pos
alloc device_y_init_pos
alloc substrate_x_init_pos
alloc substrate_y_init_pos
alloc x_disp
alloc y_disp
alloc rms_err_x
alloc rms_err_y

string fname
string msg

array x_pos_err
array y_pos_err

let scale = 0.465*10/mag
print "Scale = ", scale
```

```

outv 0 : 3.45
fireset "shutter",300

'The following set of commands asks the user to select two anchored
'patterns and determines their initial positions
snap
let msg = "Select ROI1 & pattern1"
msgbox msg
pattern substrate
match substrate, substrate_x_init_pos, substrat_y_init_pos
let msg = "Select ROI2 & pattern2"
msgbox msg
pattern device
match device, device_x_init_pos, device_y_init_pos

'The following set of commands creates and opens a data file, in
'which, the errors in the determination of the relative x and y
'positions of the two anchored patterns are stored
let fname = basename,"_uncertainty_in_pattern_matching_technique_",
           @dn,".dat"
fopen fname
fprintf fname| "error_x (nm)"; "error_y (nm)"

'The following set of commands determines the relative x and y
'positions of the two anchored patterns n times, calculates the
'relative errors in their determination and stores the errors in the
'data file opened previously
for i = 0 to n i+1
{
  snap
  match substrate, substrate_x_pos, substrate_y_pos
  match device, device_x_pos, device_y_pos
  let x_disp = device_x_pos - substrate_x_pos + substrate_x_init_pos
              - device_x_init_pos
  let y_disp = device_y_pos - substrate_y_pos + substrate_y_init_pos
              - device_y_init_pos
  print "x_disp = ", scale*x_disp*1000," nm, y_disp = ",
        scale*y_disp*1000," nm"
  let x_pos_err[i] = x_disp*scale*1000
  let y_pos_err[i] = y_disp*scale*1000
  fprintf fname| x_pos_err[i]; y_pos_err[i]
  refresh
  delay 1
}

```

```
outv 1:0
outv 2:0
```

```
'The following set of commands charts the relative errors in the
'determination of the relative x and y positions of the two anchored
' patterns, calculates the rms errors in the determination of their
'relative x and y positions and stores the rms errors in the data
'file opened previously
let rms_err_x = 0
let rms_err_y = 0
for i = 0 to asize[x_pos_err]-1 i+1
{
  chart i, x_pos_err[i], 3
  chart i, y_pos_err[i], 4
  let rms_err_x = rms_err_x + (x_pos_err[i]*x_pos_err[i])
  let rms_err_y = rms_err_y + (y_pos_err[i]*y_pos_err[i])
}

let rms_err_x = rms_err_x/asize[x_pos_err]
let rms_err_y = rms_err_y/asize[y_pos_err]

let rms_err_x = sqrt(rms_err_x)
let rms_err_y = sqrt(rms_err_y)

print "RMS error in the measurement of x =", rms_err_x" nm"
fprintf fname| "RMS error in the measurement of x =", rms_err_x" nm"
print "RMS error in the measurement of y =", rms_err_y" nm"
fprintf fname| "RMS error in the measurement of y =", rms_err_y" nm"

fclose fname
```

A.12 Macro Name: init.mac

```
macro init
{
'The following command inputs the default magnification of the
'objective lens
  global mag
  let mag=10

'The following commands record the date and time of the commencement
'of execution of a script
  string startdate
  getdate startdate
```

```

string starttime
gettimel starttime

'The following command determines the size (in microns) of a pixel
'in the field of view
global scale
'For Firewire Camera
let scale = (0.465)*10/mag
'For NTSC B/W (2/3" CCD) Camera
'let scale = (1.35)*10/mag
'For NTSC Color (1/2" CCD) Camera
'let scale = 0.98*10/mag

'The following commands input the maximum number of x and y pixels
'in the field of view
global npix_x
global npix_y
'For Firewire Camera
let npix_x = 1280
let npix_y = 960
'For NTSC camera
'let npix_x = 640
'let npix_y = 480

global pi
let pi = 3.14159

'The following command inputs the gain of the voltage amplifier,
'which is used in line with a DAC to generate the voltages required
'to actuate the microinstruments
global amp_gain
let amp_gain = 20
global inv_amp_gain
let inv_amp_gain = 1/20

'The following command assigns a name piezo_chan to channel 7,
'which is the channel used to actuate the close-loop piezo used to
'modulate the length of the reference arm of the interferometer
global piezo_chan
let piezo_chan = 7
outv piezo_chan:0

'The following command inputs the value of v2pi, which is the
'voltage that should be applied to the close-loop piezo to cause a

```

```

'phase shift of 2pi in the reference light beam
global v2pi
'For open-loop piezo
'let v2pi=1.51
'For close-loop piezo
let v2pi=0.029544

'The following command inputs the wavelength (in nm) of light that
'gets transmitted through the monochromator installed in the
'interferometer and, is used for phase shifting interferometry
global lambda
let lambda = 532

'The following command inputs the gain of the piezo-controller,
'which is used in line with the DAC used to generate the voltages
'required to actuate the close-loop piezo
global piezo_gain
let piezo_gain = 1

'The following command assigns a name "led_chan" to channel 0, which
'is the channel used to power the illumination source (a green LED)
global led_chan
let led_chan = 0

'The following command causes the DAC to output 3.45 V at channel 6,
' which is the channel used to power an indicator light that is used
'to indicate operational status of the probe station
outv 6=3.45
print "init.mac was called successfully."
}

```

Appendix B

Derivations of the Equations Used to Determine ϕ and $\Delta\phi$

B.1 Derivation of the Equation Used to Determine ϕ : Sequence H

The self-calibrating five frame sequence (referred to as H) suggested by Hariharan *et al.* is given by Eqs. (B.1.1a - B.1.1e) shown below, where I_1, I_2, I_3, I_4 and I_5 are the intensity measurements made at phase steps of $\pm 2\alpha, \pm\alpha, 0, \mp\alpha, \mp 2\alpha$ respectively and ϕ is the original optical phase difference between the interfering beams [176].

$$I_1 = A + B + 2\sqrt{AB} \cos(\phi \pm 2\alpha) \quad (\text{B.1.1a})$$

$$I_2 = A + B + 2\sqrt{AB} \cos(\phi \pm \alpha) \quad (\text{B.1.1b})$$

$$I_3 = A + B + 2\sqrt{AB} \cos(\phi) \quad (\text{B.1.1c})$$

$$I_4 = A + B + 2\sqrt{AB} \cos(\phi \mp \alpha) \quad (\text{B.1.1d})$$

$$I_5 = A + B + 2\sqrt{AB} \cos(\phi \mp 2\alpha) \quad (\text{B.1.1e})$$

Subtracting Eq. B.1.1d from Eq. B.1.1b gives,

$$I_2 - I_4 = \pm 4\sqrt{AB} \sin(\phi) \sin(\alpha) \quad (\text{B.1.2})$$

Similarly,

$$2I_3 - I_1 - I_5 = 4\sqrt{AB} \cos(\phi)[1 - \cos(2\alpha)] \quad (\text{B.1.3})$$

Dividing Eq. B.1.2 by Eq. B.1.3 gives,

$$\frac{I_2 - I_4}{2I_3 - I_1 - I_5} = \pm \tan(\phi) \frac{\sin(\alpha)}{1 - \cos(2\alpha)} \quad (\text{B.1.4})$$

For $\alpha = 90^\circ$, Eq. B.1.4 gives,

$$\tan(\phi) = \pm \frac{2(I_2 - I_4)}{2I_3 - I_1 - I_5} \quad (\text{B.1.5})$$

B.2 Derivation of the Equation Used to Determine ϕ : Sequence NH

The class of five frame sequence (referred to as NH), which is mathematically equivalent to sequence H is represented by Eqs. (B.2.1a - B.2.1e) shown below, where I_1, I_2, I_3, I_4, I_5 are the intensity measurements made at phase steps of $0, \pm\alpha, \pm 2\alpha,$

$\pm 3\alpha, \pm 4\alpha$ respectively.

$$I_1 = A + B + 2\sqrt{AB} \cos(\phi) \quad (\text{B.2.1a})$$

$$I_2 = A + B + 2\sqrt{AB} \cos(\phi \pm \alpha) \quad (\text{B.2.1b})$$

$$I_3 = A + B + 2\sqrt{AB} \cos(\phi \pm 2\alpha) \quad (\text{B.2.1c})$$

$$I_4 = A + B + 2\sqrt{AB} \cos(\phi \pm 3\alpha) \quad (\text{B.2.1d})$$

$$I_5 = A + B + 2\sqrt{AB} \cos(\phi \pm 4\alpha) \quad (\text{B.2.1e})$$

Subtracting Eq. B.2.1d from Eq. B.2.1b gives,

$$I_2 - I_4 = \mp 4\sqrt{AB} \sin(\phi \pm 2\alpha) \sin(\alpha) \quad (\text{B.2.2})$$

Similarly,

$$2I_3 - I_1 - I_5 = 4\sqrt{AB} \cos(\phi \pm 2\alpha)[1 - \cos(2\alpha)] \quad (\text{B.2.3})$$

Dividing Eq. B.2.2 by Eq. B.2.3 gives,

$$\frac{I_2 - I_4}{2I_3 - I_1 - I_5} = \mp \tan(\phi \pm 2\alpha) \frac{\sin(\alpha)}{1 - \cos(2\alpha)} \quad (\text{B.2.4})$$

For $\alpha = 90^\circ$, Eq. B.2.4 gives,

$$\tan(\phi) = \mp \frac{2(I_2 - I_4)}{2I_3 - I_1 - I_5} \quad (\text{B.2.5})$$

B.3 Error Analysis of Sequence H

If a small error ϵ is present in the nominal phase step α , then, according to Eq. B.1.4,

$$\frac{I_2 - I_4}{2I_3 - I_1 - I_5} = \pm \tan(\phi) \frac{\sin(\alpha + \epsilon)}{1 - \cos[2(\alpha + \epsilon)]} \quad (\text{B.3.1})$$

Following Eq. B.1.4 and Eq. B.1.5,

$$\frac{I_2 - I_4}{2I_3 - I_1 - I_5} = \pm \frac{\tan(\phi')}{2} \quad (\text{B.3.2})$$

From Eqs. B.3.1 and B.3.2,

$$\frac{\tan(\phi')}{2} = \tan(\phi) \frac{\sin(\alpha + \epsilon)}{1 - \cos[2(\alpha + \epsilon)]} \quad (\text{B.3.3})$$

Now,

$$\frac{\sin(\alpha + \epsilon)}{1 - \cos[2(\alpha + \epsilon)]} = \frac{\sin(\alpha) \cos(\epsilon) + \cos(\alpha) \sin(\epsilon)}{1 - [\cos(2\alpha) \cos(2\epsilon) - \sin(2\alpha) \sin(2\epsilon)]} \quad (\text{B.3.4})$$

For $\alpha = 90^\circ$, Eq. B.3.4 becomes,

$$\frac{\sin(\alpha + \epsilon)}{1 - \cos[2(\alpha + \epsilon)]} = \frac{\cos(\epsilon)}{1 + \cos(2\epsilon)} \quad (\text{B.3.5})$$

$$= \frac{1}{2 \cos(\epsilon)} \quad (\text{B.3.6})$$

Since ϵ is small, neglecting ϵ^2 in Eq. B.3.6 gives,

$$\frac{\sin(\alpha + \epsilon)}{1 - \cos[2(\alpha + \epsilon)]} = \frac{1}{2 \cos^2(\epsilon/2)} \quad (\text{B.3.7})$$

$$= \frac{1}{2} \sec^2(\epsilon/2) \quad (\text{B.3.8})$$

$$= \frac{1}{2} (1 + \tan^2(\epsilon/2)) \quad (\text{B.3.9})$$

Since ϵ is small, $\tan(\epsilon/2) = \epsilon/2$, therefore, Eq. B.3.9 becomes,

$$\frac{\sin(\alpha + \epsilon)}{1 - \cos[2(\alpha + \epsilon)]} = \frac{1}{2} \left(1 + \frac{\epsilon^2}{4}\right) \quad (\text{B.3.10})$$

Substituting Eq. B.3.10 in Eq. B.3.3, we get,

$$\frac{\tan(\phi')}{2} = \frac{\tan(\phi)}{2} \left(1 + \frac{\epsilon^2}{4}\right) \quad (\text{B.3.11})$$

Rearranging Eq. B.3.11 gives,

$$\tan(\phi') - \tan(\phi) = \frac{\epsilon^2}{4} \tan(\phi) \quad (\text{B.3.12})$$

Rearranging Eq. B.3.12 and using Eq. B.3.11 gives,

$$\tan(\phi' - \phi) = \frac{\epsilon^2}{4} \frac{\tan(\phi)}{1 + \tan(\phi) \tan(\phi)(\epsilon^2/4 + 1)} \quad (\text{B.3.13})$$

Since ϵ is small, neglecting $\epsilon^2/4$ in Eq. B.3.13 gives,

$$\tan(\phi' - \phi) = \frac{\epsilon^2}{4} \frac{\tan(\phi)}{1 + \tan^2(\phi)} \quad (\text{B.3.14})$$

$$= \frac{\epsilon^2}{8} \sin(2\phi) \quad (\text{B.3.15})$$

Since $\phi' - \phi$ is small, $\tan(\phi' - \phi) = \phi' - \phi$, therefore, Eq. B.3.15 becomes,

$$\Delta\phi_H = \phi' - \phi = \frac{\epsilon^2}{8} \sin(2\phi) \quad (\text{B.3.16})$$

B.4 Error Analysis of Sequence NH

If a small error ϵ is present in the nominal phase step α , then, according to Eq. B.2.4,

$$\frac{I_2 - I_4}{2I_3 - I_1 - I_5} = \mp \tan[\phi \pm 2(\alpha + \epsilon)] \frac{\sin(\alpha + \epsilon)}{1 - \cos[2(\alpha + \epsilon)]} \quad (\text{B.4.1})$$

Following Eq. B.2.4 and Eq. B.2.5,

$$\frac{I_2 - I_4}{2I_3 - I_1 - I_5} = \mp \frac{\tan(\phi')}{2} \quad (\text{B.4.2})$$

From Eqs. B.4.1 and B.4.2,

$$\frac{\tan(\phi')}{2} = \tan[\phi \pm 2(\alpha + \epsilon)] \frac{\sin(\alpha + \epsilon)}{1 - \cos[2(\alpha + \epsilon)]} \quad (\text{B.4.3})$$

For $\alpha = 90^\circ$,

$$\tan[\phi \pm 2(\alpha + \epsilon)] \frac{\sin(\alpha + \epsilon)}{1 - \cos[2(\alpha + \epsilon)]} = \tan(\phi \pm 2\epsilon) \frac{\cos(\epsilon)}{1 + \cos(2\epsilon)} \quad (\text{B.4.4})$$

$$= \tan(\phi \pm 2\epsilon) \frac{1}{2 \cos(\epsilon)} \quad (\text{B.4.5})$$

Substituting Eq. B.3.10, Eq. B.4.5 in Eq. B.4.3, we get,

$$\frac{\tan(\phi')}{2} = \frac{\tan(\phi \pm 2\epsilon)}{2} \left(1 + \frac{\epsilon^2}{4}\right) \quad (\text{B.4.6})$$

Rearranging Eq. B.4.6 gives,

$$\tan(\phi') - \tan(\phi) = \pm \frac{\tan(2\epsilon)[1 + \tan^2(\phi)]}{1 \mp \tan(\phi) \tan(2\epsilon)} + \frac{\epsilon^2}{4} \tan(\phi \pm 2\epsilon) \quad (\text{B.4.7})$$

Rearranging Eq. B.4.7 gives,

$$\tan(\phi' - \phi) = \pm \frac{\tan(2\epsilon)[1 + \tan^2(\phi)]}{[1 \mp \tan(\phi) \tan(2\epsilon)][1 + \tan(\phi) \tan(\phi')]} + \frac{\epsilon^2}{4} \frac{\tan(\phi \pm 2\epsilon)}{1 + \tan(\phi) \tan(\phi')} \quad (\text{B.4.8})$$

Now since ϵ is very small,

$$\frac{\tan(2\epsilon)[1 + \tan^2(\phi)]}{[1 \mp \tan(\phi) \tan(2\epsilon)][1 + \tan(\phi) \tan(\phi')]} = 2\epsilon \quad (\text{B.4.9})$$

Substituting Eq. B.4.9 in Eq. B.4.8 gives,

$$\tan(\phi' - \phi) = \pm 2\epsilon + \frac{\epsilon^2}{4} \frac{\tan(\phi \pm 2\epsilon)}{1 + \tan(\phi)\tan(\phi')} \quad (\text{B.4.10})$$

$$= \cos^2(\phi) \left[\pm \frac{2\epsilon}{\cos^2(\phi)} + \frac{\epsilon^2}{4} \tan(\phi) \pm \frac{\epsilon^3}{2} \right] \quad (\text{B.4.11})$$

Since $2\epsilon/\cos^2(\phi) \gg (\epsilon^2/4)\tan(\phi)$ and $\epsilon^3/2$, Eq. B.4.11 becomes,

$$\tan(\phi' - \phi) = \pm 2\epsilon \quad (\text{B.4.12})$$

Since $\phi' - \phi$ is very small, $\tan(\phi' - \phi) = \phi' - \phi$, therefore, Eq. B.4.12 becomes,

$$\Delta\phi_{NH} = \phi' - \phi = \pm 2\epsilon \quad (\text{B.4.13})$$

Appendix C

List of Acronyms

AFM	Atomic Force Microscope/Microscopy
AuNP	Gold Nanoparticle
BOX	Buried Oxide
CA	Contact Angle
CAA	Contact Angle Analysis
CBA	Cantilever Beam Array
CPD	Critical Point Drying/Dried
CVD	Chemical Vapor Deposition/Deposited
DI	Deionized
DRIE	Deep Reactive Ion Etching
FTIR	Fourier Transformed Infra-red
GXL	Gas-expanded Liquid
HMDS	Hexamethyldisilazane
iMEMS ¹	Integrated Micro-Electro-Mechanical Systems
IPA	Isopropyl Alcohol
MST	Mechanical Stress Tester
MEMS	Microelectromechanical Systems
NP	Nanoparticle
OTS	Octadecyltrichlorosilane
RMS	Root Mean Square
RPM	Revolutions Per Minute
RST	Residual Stress Tester
SEM	Scanning Electron Microscope/Microscopy
SUMMiT ²	Sandia Ultra-planar Multi-level MEMS Technology
SBA	Sidewall Beam Array
SFAT	Sidewall Friction and Adhesion Tester
SFT	Sidewall Friction Tester
TEM	Transmission Electron Microscope/Microscopy
UHV	Ultra-high Vacuum
UVO	Ultra-violet-Ozone
XPS	X-ray Photoelectron Spectroscopy

¹Registered trademark of Analog Devices

²Registered trademark of Sandia National Laboratories